Mechanistic Investigations in Hybrid Advanced Oxidation Processes for Degradation of Recalcitrant Pollutants

A
Thesis
Submitted in
Partial Fulfillment of the
Requirements for the Degree of

DOCTOR OF PHILOSOPHY

By

Sankar Chakma

Department of Chemical Engineering
Indian Institute of Technology Guwahati
Guwahati – 781 039, Assam, India

August 2015

Dedicated

To

My Guide and My Family Members for

Their Supports and Encouragement

Throughout My Research Work

CERTIFICATE

It is certified that the work contained in the thesis entitled "**MECHANISTIC INVESTIGATIONS IN HYBRID ADVANCED OXIDATION PROCESSES FOR DEGRADATION OF RECALCITRANT POLLUTANTS**", by **Sankar Chakma** (Roll No. 11610705), has been carried out under my supervision and that this work has not been submitted elsewhere for a degree.

Date:06.08.2015

Prof. V. S. Moholkar
Department of Chemical Engineering
Indian Institute of Technology Guwahati
Guwaahti – 781 039, Assam, India

CONTENTS

LIST OF TABLES

Chapter 8

Chapter 9

भारतीय प्रौद्योगिकी संस्थान गुवाहाटी
Indian Institute of Technology Guwahati

LIST OF FIGURES

Chapter 3

Chapter 6

Chapter 7

Chapter 9

1

GENERAL INTRODUCTION AND LITERATURE REVIEW

CHAPTER 1

GENERAL INTRODUCTION AND LITERATURE REVIEW

1.1 INTRODUCTION

Waste effluent discharge from various process industries (such as textile industries, pharmaceutical industries etc.) contains several types of hazardous and recalcitrant organic pollutants, which are not easily biodegradable. Due to fast economic and industrial development around the world, emissions from these process industries have risen to daunting levels and have posed severe threat to environment. In the past few decades, numerous techniques for effective degradation and mineralization of the recalcitrant organic pollutants have been attempted, known as advanced oxidation process (AOP) or advanced oxidation technique (AOT). The basic principle of all these AOPs is the production of extremely energetic $^{\bullet}OH$ radicals with oxidation potential of 2.8 eV. On the basis of phases various components of reaction system, the AOPs are categorized as: (1) homogeneous and (2) heterogeneous. The most widely used homogeneous advanced oxidation techniques for wastewater treatment are: Fenton process (Fe^{2+}/H_2O_2), photolysis (UV/H_2O_2), ferrioxalate (Fe^{3+}–oxalate/UV), ozonation (O_3), persulfate process ($UV/S_2O_8^{2-}$ or $Fe^{2+}/S_2O_8^{2-}$). For certain pollutants, especially the textile dyes appearing in wastewater discharge from textile industries (which make second largest contribution to water pollution after agriculture),

enzymatic treatments with peroxidase enzymes, e.g. lignin peroxidase, manganese peroxidase, horseradish peroxidase or laccase, have also been used. Conventional heterogeneous advanced oxidation technique for wastewater treatment is photocatalysis, with catalyst in the form of metal oxides such as zinc or titanium, either with pure form or doped with transition metals such as Fe–, Ag–, Au–, Ag–, Ni– and Mg. Voluminous research has been published in recent past on development of new photocatalysts for application in degradation/ mineralization of variety of pollutants.

Several authors have also attempted use of combined (or hybrid) advanced oxidation techniques for wastewater treatment. Such hybrid techniques, in which two or more conventional advanced oxidation techniques are applied simultaneously, have been found to give more effective and efficient degradation/ mineralization of recalcitrant pollutants than the conventional individual techniques. The hybrid advanced oxidation techniques reported in literature in recent past are: photo–Fenton ($UV/Fe^{2+}/H_2O_2$), photocatalysis–Fenton (UV/TiO_2 and Fe^{2+}/H_2O_2), photo–Fenton–ferrioxalate (UV/Fe^{3+}–$Oxalate/H_2O_2$), UV/O_3, persulfate, ozone–microbubble system etc. (Monteagudo et al., 2008, 2013, 2015; Katsumata et al., 2010; Kusic et al., 2011; Pang and Abdullah, 2013; Nie et al., 2014; Giri and Golder, 2014; 2014; Khuntia et al., 2014; Ghafoori et al., 2015; Wang et al., 2015).

Sonolysis (or ultrasound treatment) is a relatively new advanced oxidation process that has attracted attention of researchers. This technique has been successfully applied for degradation of a large number of organic pollutants (Adewuyi, 2001, 2005a, 2005b). In this technique, the oxidizing radicals are produced through phenomenon of transient cavitation. Cavitation is essentially nucleation, growth and implosive collapse of tiny gas bubbles (with equilibrium size of few microns), which is driven by pressure variation induced by ultrasound. The implosive transient collapse of transient bubbles creates enormous energy concentration on extremely small spatial and temporal scale. The temperatures and pressures

inside the cavitation bubble reach extreme (~ 5000 K and 500 bar) at the moment of transient collapse (Suslick, 1990). At these extreme conditions, the thermal dissociation of gas and solvent vapor molecules inside the bubbles gives rise to formation of radical species such as $^{\bullet}O$, $^{\bullet}OH$, $HO_2^{\bullet}$ and $H^{\bullet}$. These species either diffuse out of the cavitation bubble (at the point of maximum compression or minimum radius) or get released into the bulk liquid medium as the bubble undergoes fragmentation at the point of maximum compression during radial motion. These radicals can induce/ accelerate numerous chemical reactions in the bulk liquid medium including oxidative degradation of the organic pollutants.

More recently, sono–hybrid techniques, in which sonolysis technique is coupled with conventional advanced oxidation techniques such as Fenton, photolysis, photocatalysis, persulfate, enzymatic process etc., have been applied for more effective and efficient degradation/ mineralization of bio–recalcitrant pollutants that include phenol and derivatives (Entezari and Pétrier, 2003, 2004, 2005; Mishra and Gogate, 2011; Kim et al., 2015), aniline (Chen et al., 2015), pharmaceutical drugs such as sulfamethoxazole and ciprofloxacin (Guo et al., 2015; Giri and Golder, 2014), azo and non-azo textile dyes (Byun and Kwak, 2005; Velegraki, 2006; Berberidou et al., 2007; Rehorek et al., 2007; Madhavan et al., 2010a, He et al., 2011; Patidar et al., 2012; Malani et al., 2014), plastic intermediate bisphenol-A (Chakma and Moholkar, 2014; Huang et al., 2012), chlorinated aromatic compounds (Peller et al., 2003), distillery wastewater (Sangave and Pandit, 2006), herbicide linuron and insecticide fenitrothion (Katsumata et al., 2010, 2011), non-steroidal anti-inflammatory drug diclofenac (Madhavan et a., 2010b; Bagal and Gogate, 2014a), copolymer styrene-acrylic acid (Saien et al., 2010), cholesterol (Sun et al., 2011) etc. These hybrid techniques have been termed as: sono–Fenton, sono–photolysis, sono–photocatalysis, sono–Ferrioxalate and sono–enzymatic (Tangestaninejad et al., 2008;Vinu and Madras, 2009; Jian et al., 2010; Madhavan et al., 2010a, 2010b; Patidar et al., 2012; Grcic et al., 2012; Xiong et al., 2012; Pang and Abdullah,

2012, 2013; Babuponnusami and Muthukumar, 2014; Bagal and Gogate, 2014a; Malani et al., 2014; Chakma and Moholkar, 2013a, 2015; Wang et al., 2015). Despite voluminous literature published in last one and half decade employing numerous sono–hybrid techniques, the exact mechanism of these techniques has remained largely unexplored. The exact mechanistic synergy between chemistry of the conventional process and the physical and chemical effects induced by ultrasound and cavitation, which leads to faster and higher degradation of the pollutant, has not been established yet. Most of the literature in this area is focused on results rather than rationale. Identifications of the interlinks between physics/chemistry of ultrasound and cavitation and the chemistry of the conventional AOP is crucial for not only research in the degradation of pollutants with sono–hybrid AOPs, but also important from view point of optimization and scale–up of wastewater treatment processes employing these hybrid AOPs. Fulfillment of this knowledge gap has been the principal aim with which this thesis work was undertaken.

As a preamble to the thesis, we have given in the next section the description of basic chemical mechanism of the individual AOPs. In addition, we have also presented an extensive literature review on degradation of different pollutant with application hybrid AOP with combination of that individual AOP with sonolysis.

1.2 CHEMICAL MECHANISMS AND LITERATURE REVIEW OF ADVANCED OXIDATION TECHNIQUES

All advanced oxidation techniques are essentially aimed at production of the $^{\bullet}OH$ and other oxidizing radicals for oxidative degradation of bio–recalcitrant pollutants. The hydroxyl radical has the highest oxidation potential of 2.8 eV and can attack organic molecules with a whopping rate constant of 10^6–10^9 mole^{-1} s^{-1} (Andreozzi et al., 1999). The other oxidizing radicals produced during advanced oxidation processes are $HO_2^{\bullet}$, $O^{\bullet}$ and $O_2^{\bullet-}$. Molecular

species such as O_3 and H_2O_2 produced from combination of these species also contribute to the oxidation and degradation of the pollutant. We describe below the basic chemistry of different advanced oxidation processes or the chemical mechanism through which different advanced oxidation processes lead to production of radicals. In the context of the theme of present thesis, we have also discussed coupling of these advanced oxidation processes with sonolysis and have given summary of literature employing such sono–hybrid advanced oxidation processes.

1.2.1 Sonolysis

As noted earlier, sonolysis or ultrasound assisted degradation is based on production of through transient cavitation bubbles. The vapor and gas molecules present in the bubble at the moment of transient collapse are subjected to extreme conditions generated inside the bubble. At these conditions, these molecules undergo thermal dissociation to generate numerous chemical species – some of which are radical species. This phenomenon is related to the transport of vapor molecules across bubble interface. During expansion of cavitation bubble in radial motion, evaporation of solvent at the bubble interface causes diffusion of vapor molecules towards bubble core. In the subsequent compression phase, not all of these vapor molecules can diffuse back at the bubble interface and undergo condensation. The "entrapped" vapor molecules are subjected to extreme conditions at transient collapse. The exact physics of this phenomenon is explained in greater detail in the next chapter along with a mathematical model. Usually, sonolysis treatments are carried out in water as the liquid medium. The radicals generated in the bubble through thermal dissociation of water molecules can undergo numerous reactions as follows (Lin et al., 2008):

$$H_2O \xrightarrow{US} HO^{\bullet} + H^{\bullet} \qquad (1.1)$$

$$HO^{\bullet} + H^{\bullet} \longrightarrow H_2O \qquad (1.2)$$

$$2\ HO^{\bullet} \longrightarrow O^{\bullet} + H_2O \quad (1.3)$$

$$2\ HO^{\bullet} \longrightarrow H_2O_2 \quad (1.4)$$

If the cavitation bubble contains oxygen (as in case of air bubbles) or if the liquid medium has dissolved oxygen present in it, several other reactions may also occur leading to production of ozone and hydrogen peroxide as follows (Neppolian et al., 2002):

$$O_2 \longrightarrow 2\ O^{\bullet} \quad (1.5)$$

$$O_2 + O^{\bullet} \longrightarrow O_3 \quad (1.6)$$

$$O_2 + H^{\bullet} \longrightarrow HO_2^{\bullet} \quad (1.7)$$

$$2\ HO_2^{\bullet} \longrightarrow H_2O_2 + O_2 \quad (1.8)$$

The nitrogen present in air bubbles can also give rise to numerous reactions, which are listed below. Some of these reactions have adverse effect on the oxidative degradation process, as these lead to scavenging of the oxidizing radicals by nitrogen – leading to formation of less reactive radicals (Chakma and Moholkar, 2013b).

$$N_2 + O^{\bullet} \rightleftharpoons N^{\bullet} + NO \quad (1.9)$$

$$N_2 + {}^{\bullet}OH \rightleftharpoons N_2H + O^{\bullet} \quad (1.10)$$

$$N_2 + {}^{\bullet}OH \rightleftharpoons N_2O + H^{\bullet} \quad (1.11)$$

$$N_2 + {}^{\bullet}OH \rightleftharpoons NH + NO \quad (1.12)$$

$$N_2 + H^{\bullet} \rightleftharpoons N_2H \quad (1.13)$$

$$N_2 + H^{\bullet} \rightleftharpoons NH + N^{\bullet} \quad (1.14)$$

$$N + {}^{\bullet}OH \rightleftharpoons NO + H^{\bullet} \quad (1.15)$$

$$N_2O + O^{\bullet} \rightleftharpoons 2\ NO \quad (1.16)$$

$$NO + {}^{\bullet}OH \rightleftharpoons NO_2 \quad (1.17)$$

$$NH + {}^{\bullet}OH \rightleftharpoons NH_2 + O^{\bullet} \quad (1.18)$$

$$NH_2 + O^{\bullet} \rightleftharpoons H^{\bullet} + HNO \quad (1.19)$$

$$HNO + O^{\bullet} \rightleftharpoons NH + O_2 \quad (1.20)$$

$$HNO + O^{\bullet} \rightleftharpoons NO + {}^{\bullet}OH \quad (1.21)$$

$$HNO + {}^{\bullet}OH \rightleftharpoons NO + H_2O \quad (1.22)$$

$$N + O_2 \rightleftharpoons NO + O^{\bullet} \quad (1.23)$$

$$NO + O_2 \rightleftharpoons NO_2 + O^{\bullet} \quad (1.24)$$

$$NH + O_2 \rightleftharpoons HNO + O^{\bullet} \quad (1.25)$$

$$NH + O_2 \rightleftharpoons NO + {}^{\bullet}OH \quad (1.26)$$

$$N_2 + O_2 \rightleftharpoons N_2O + O^{\bullet} \quad (1.27)$$

***Other mechanisms of sonolysis*:** It should be noted that degradation of pollutant in sonolysis can also occur by two other mechanisms than oxidative reactions induced by radicals. If the pollutant has sufficiently high vapor pressure at ambient conditions, it can evaporate inside the bubble along with liquid medium. The molecules of pollutant can also get entrapped inside the bubble and undergo thermal dissociation. The bubble interface (which is essentially a gas–liquid boundary) has hydrophobic character. Therefore, pollutants with strong hydrophobic character – such as aromatic or poly-aromatic hydrocarbons, can effectively "partition" between bulk liquid and the bubble interface. Some of these can even adsorb on the bubble interface. As the bubble wall rapidly recedes during compression phase, some of these adsorbed molecules can get "squeezed" inside the bubble and undergo thermal dissociation.

Secondly, the degradation of pollutant can also occur through thermal dissociation at

the interface of the bubble. At the moment of transient collapse, the temperature inside the bubble reaches extreme. Although the collapse of the bubble is extremely rapid (occurring in few tens of nanoseconds), and thus, adiabatic, some finite heat transfer may occur across bubble interface. This causes heating up of the thin liquid layer at the bubble interface to moderate temperatures of ~ 500–600^{o}C (Kotronarou et al., 1991). The pressure in this region may also rise due to rapid convergence of fluid elements. The pollutants molecules present in this region are subjected to these conditions. It could be possible that these molecules can undergo thermal dissociation and degradation.

1.2.2 Fenton Process

Fenton process is one of the easiest and simplest techniques for generation •OH radical for oxidation process, without using any specific chemicals or expensive method. The basic advantage of Fenton process is that it does not require any specific reactor nor specific conditions for production of oxidizing radicals, as in case of sonolysis. It can produce OH radicals at ambient temperature and pressure with fast kinetics. In this process, H_2O_2 is activated by ferrous ion (Fe^{2+}) known as Fenton's reagent. The generation of $^{\bullet}$OH radical through Fenton reaction is shown below (Brillas et al., 2009; Bagal and Gogate, 2014b):

$$Fe^{2+} + H_2O_2 \longrightarrow Fe^{3+} + OH^- + HO^{\bullet} \quad (1.28)$$

$$Fe^{3+} + H_2O_2 \longrightarrow Fe^{2+} + HO_2^{\bullet} + H^+ \quad (1.29)$$

$$Fe^{3+} + HO_2^{\bullet} \longrightarrow Fe^{2+} + O_2 + H^+ \quad (1.30)$$

A noticeable advantage of the Fenton process is that it has no adverse impact on environment; moreover, H_2O_2 is easy to handle. The several studies have demonstrated that numerous organic pollutants numerous organic compounds, including textile dyes and pesticides (Pang and Abdulla, 2012, 2013; Iglesias et al., 2015; Bocos et al., 2015) can be efficiently treated by Fenton's reagent.

Over the last few years, the basic Fenton process has been modified by numerous investigations. The modified Fenton processes include: UV/Fenton, O_3/Fenton, H_2O_2/FeOX and UV/Fe^{3+}–oxalate/H_2O_2 process. In photo–assisted Fenton systems (or photo–Fenton process), the reaction mixture is subjected to exposed to UV lights (generally, UVC = 254 nm and UVA = 365 nm) to accelerate the degradation process (Katsumata et al., 2011; Giri and Golder, 2014; Chakma and Moholkar, 2014; Rodríguez-Chueca et al., 2014) by producing more $^{\bullet}OH$ radicals. In photo–Fenton reaction, the iron species that make hydroxylated complex are further photo–reduced under UV light and produces extra •OH radicals in solution as shown below (Rodríguez et al., 2012; Monteagudo et al., 2013):

$$Fe^{3+} + H_2O \longrightarrow FeOH^{2+} \xrightarrow{hv} Fe^{2+} + {}^{\bullet}OH \qquad (1.31)$$

The iron–hydroxy complexes are able to absorb photons within broader wavelength of light (including visible range), which increases the energy efficiency of solar spectrum – as compared to convention UV–initiated photocatalysis.

Rodríguez et al. (2012) have observed in ozone (O_3)/Fenton process that the rate of removal of recalcitrant organic pollutants increases with increasing O_3 concentration. Higher ozone concentration not only leads to direct O_3 induced oxidation reactions, but also enhanced production of radicals ($^{\bullet}OH$, $O_3^{\bullet-}$) through following reactions (Rodríguez et al., 2012; Ziylan and Ince, 2015):

$$Fe^{2+} + O_3 \longrightarrow FeO^{2+} + O_2 \qquad (1.32a)$$

$$Fe^{2+} + O_3 \longrightarrow Fe^{3+} + O_3^{\bullet-} \qquad (1.32b)$$

$$Fe^{3+} + O_3 \longrightarrow FeO^{2+} + {}^{\bullet}OH + H^+ + OH^- \qquad (1.33)$$

$$FeO^{2+} + H_2O \longrightarrow Fe^{3+} + {}^{\bullet}OH + OH^- \qquad (1.34)$$

The Fe^{2+} formed from the photolysis of Fe^{3+} (shown in reaction Eq. 31) reacts with O_3 to yield FeO^{2+} that eventually gives hydroxyl radicals ($^{\bullet}OH$) and hydrogen peroxide (H_2O_2) in

the ionic form through reactions Eqs. 33 and 34.

The recent variants of the Fenton processes are sono–Fenton or sono–photo–Fenton (Segura et al., 2009). In last one decade, several studies have demonstrated that sono–Fenton and sono–photo–Fenton processes (Joseph et al., 2000; Neppolian et al., 2002; Ioan et al., 2007; Lin et al., 2008; Melero et al., 2008; Segura et al., 2009; Katsumata et al., 2011; Zhong et al., 2011; Grčić et al., 2012; Zhao et al., 2012; Monteagudo et al., 2014a, 2014b) give effective degradation of various types of pollutants. The mechanistic synergism between Fenton, photo–Fenton and sonolysis leads to higher production of oxidizing species that lead to faster and higher degradation of pollutants. A summary of published literature for wastewater treatment using are presented in Table 1.1.

1.2.3 Photo-Ferrioxalate System

In photo–ferrioaxalate process, ferrioxalate complexes ($[Fe(C_2O_4)_3]^{3-}$) are prepared by reacting of iron species and oxalate salts. This ferrioxalate complex has high photochemical activity near ultraviolet range (Arslan et al., 2000; Jeong and Yoon, 2004, 2005; Liu et al., 2006; Huang et al., 2007; Katsumata et al., 2010; Monteagudo et al., 2008, 2013), and can absorb the photons of solar spectrum up to the range of 450 nm (which is ~18% of total energy) (Monteagudo et al., 2008). The ferrioxalate complex undergoes a series of photochemical reactions through Ligand to Metal Charge Transfer reaction (LMCT) mechanism as follows (Jeong and Yoon, 2004, Zhou et al., 2004; Vedrenne et al., 2012) leading to production of three major oxidant radical species, viz. $^{\bullet}OH$, $HO_2^{\bullet}$ and $O_2^{\bullet-}$:

$$[Fe(C_2O_4)_3]^{3-} + h\nu \longrightarrow Fe^{2+} + 2\,C_2O_4^{2-} + C_2O_4^{\bullet-} \qquad (35)$$

$$C_2O_4^{\bullet-} + [Fe(C_2O_4)_3]^{3-} \longrightarrow Fe^{2+} + 3\,C_2O_4^{2-} + 2\,CO_2 \qquad (1.36)$$

$$C_2O_4^{\bullet-} \longrightarrow CO_2 + CO_2^{\bullet-} \qquad (1.37)$$

$$CO_2^{\bullet-} + O_2 \longrightarrow CO_2 + O_2^{\bullet-} \quad (1.38)$$

$$C_2O_4^{\bullet-} + O_2 \longrightarrow 2\,CO_2 + O_2^{\bullet-} \quad (1.39)$$

$$O_2^{\bullet-} + H^+ \longrightarrow HO_2^{\bullet} \quad (1.40)$$

$$HO_2^{\bullet} + HO_2^{\bullet} \longrightarrow H_2O_2 + O_2 \quad (1.41)$$

$$H_2O_2 + Fe^{2+} \longrightarrow Fe^{3+} + HO^{\bullet} + OH^- \quad (1.42)$$

$$Fe^{3+} + H_2O_2 \rightleftharpoons Fe^{2+} + HO_2^{\bullet} + H^+ \quad (1.43)$$

It could be seen that reactions Eqs. 1.42 and 1.43 are essentially the Fenton and Fenton–like reactions. However, the difference is that the H_2O_2 required for these reactions is produced in–situ (although external addition of H_2O_2 is also possible).

In air–saturated solution at pH 2–4, the intermediate oxalate radicals react with molecular oxygen (O_2) to generate superoxide radicals ($O_2^{\bullet-}$), which disproportionate to form H_2O_2 in subsequent reactions (Huang et al., 2007). The Fe^{2+} formed in the reactions (Eqs. 1.35 and 1.36) can react with this in–situ generated H_2O_2 to generate hydroxyl radicals through Fenton reaction mechanism. Therefore, the photolysis of ferrioxalate in the presence of O_2 is a continuous source of $^{\bullet}OH$ radical production via Fenton and Fenton–like reactions.

To enhance the production of $^{\bullet}OH$ radicals, photolysis of ferrioxalate complexes is carried out in presence of heterogeneous photocatalysts such as TiO_2 (Safarzadeh–Amiri et al., 1996) and hydrogen peroxide (Dong et al., 2007; Azami et al., 2012; Vedrenne et al., 2012; Fadzil et al., 2012). Ferrioxalate process is basically a Fenton–like reaction, and hence, the pH of the reaction medium plays an important role. The optimum pH for ferrioxalate has been found to be in the range of 2–4 (Arslan et al., 2000; Jeong and Yoon, 2004; Dong et al., 2007; Monteagudo et al., 2009; Rodríguez et al., 2011; Azami et al., 2012; Zhou et al., 2013). Another important parameter affecting efficiency of ferrioxalate process is the molar ratio of iron to oxalate. The optimum value of this parameter is reported to be 1:3 (Hatchard and

Parker, 1956; Arslan et al., 2000; Selvam et al., 2007).

Safarzadeh–Amiri et al. (1996) and Selvam et al. (2007) have applied ferrioxalate and photocatalysis processes simultaneously in the presence of solar light and UV (365 nm) light irradiation to degrade organic contaminants, *viz*. benzene, toluene, and xylene, and reactive orange 4; respectively. In the study by Safarzadeh–Amiri et al. (1996), it was revealed that ferrioxalate process yielded far higher (~25 times) mineralization than sunlight/TiO_2/H_2O_2 process. The intermediate of carbon dioxide radical anion ($CO_2^{\bullet-}$) plays dual role in photo–ferrioxalate process. Jeong and Yoon (2004) have demonstrated the role of this species in degradation of 2,4–dichlorophenoxyacetic acid (2,4–D). At high concentration of ferrioxalate complex, $CO_2^{\bullet-}$ reacts with complex to reduce Fe^{3+} to Fe^{2+}. At low concentration, $CO_2^{\bullet-}$ essentially contributes to *in–situ* formation of H_2O_2, as a result of its reaction with oxygen, which triggers the Fenton reactions. The dual activity of $CO_2^{\bullet-}$ is shown in reaction schemes below.

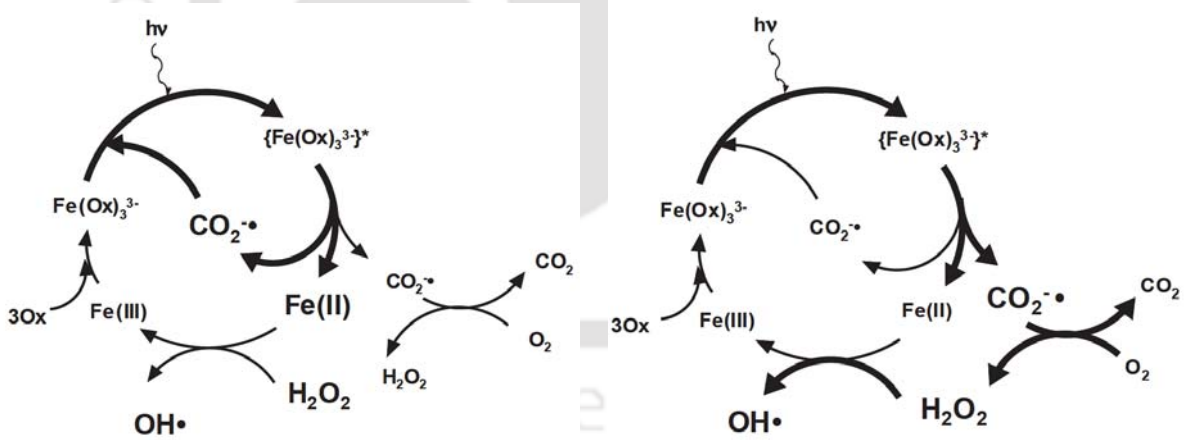

Figure 1.1: Dual reaction scheme of $CO_2^{\bullet-}$ in photo–ferrioxalate system: (A) reaction mechanism at high concentration of iron (Fe^{3+}), and (B) reaction mechanism at low concentration of iron (Fe^{3+}). (Adopted from Jeong and Yoon, 2004)

A summary of published literature on hybrid photo–ferrioxalate process is given in Table 1.2.

Table 1.1: Summary of literature on sono-Fenton and sono-photo-Fenton process for wastewater treatment

Hybrid-AOP	Pollutants	Process parameters	Results/ Max. degradation (%)	Reference
US/Fenton	Bisphenol-A (BPA)	f = 40 kHz, P = 100 W, BPA = 20 mg/L; Fe_3O_4 = 585 mg/L; H_2O_2 = 160 mM; pH = 3, 7 & 9; T = 35°C; t = 480 min	100% (1.39×10^{-4} s^{-1}) at pH 3 98.1% (1.33×10^{-4} s^{-1}) at pH 7 95.1% (9.4×10^{-5} s^{-1}) at pH 9	Huang et al. (2012)
US/Fenton (heterogeneous)	Sulfamethazine (SMZ)	f = 20 kHz (horn), P = 330W, SMZ = 25 mg/L, goethite = 0.5 g/L, Ox = 0.8 mM, UV = 1 × 9W (365 nm), pH = 3, T = 20°C, t = 60 min, Air = 1 L/min	60% (2.2×10^{-2} min^{-1}) TOC removal	Zhou et al. (2013)
US/Fenton	Acid Red B (ARB) Methylene blue (MB)	f = 40 kHz (bath), P = 200 W, ARB = 0.02 mM; MB = 0.032 mM; H_2O_2 = 600 mg/L; Fe^{2+} = 0.18 mM; pH = 2; T = 25°C; t = 60 min	Decolorization was faster and higher in non azo dyes. Maximum obtained decolorization was 91.8% (0.25 min^{-1}) for ARB and 100% (0.31 min^{-1}) for MB	Chakma and Moholkar (2013a)
US/ UV/ Fenton	Antipyrine (ANP)	f = 24 kHz (horn), P = 200 W, ANP = 50 mg/L, H_2O_2 = 1500 mg/L, Fe^{2+} = 12 mg/L, UV = 1 × 150 W (190-280 nm), pH = 2.7, T = 30°C, t = 50 min	92% TOC was removed in sono-photo-Fenton	Duran et al. (2013a)

Table 1.1 (*continued…*): Summary of literature on sono-Fenton (US/Fenton) and sono-photo-Fenton (US/UV/Fenton) process for wastewater treatment

Hybrid-AOP	Pollutants	Process parameters	Results/ Max. degradation (%)	Reference
US/Fenton US/UV/Fenton	Paracetamol (PCM)	f = 213 kHz (horn), P = 13.8 W, PCM = 0.09 mM, Fe^{3+}= 0.05 mM, UV = 1 × 450 W (≥ 320 nm), pH = 2.7, T = 25°C, t = 3 h	TOC removal were: >10% (26.1×10^{-7} M min^{-1}) in sono-Fenton and ~85% (46.7×10^{-7} M min^{-1}) in sono-photo-Fenton	Madhavan et al. (2013)
US/UV/Fenton	Reactive Blue 4 (RB4)	f = 24 kHz (horn), P = 200 W, RB4 = 30 mg/L (TOC), H_2O_2 = 500 mg/L, Fe^{2+} = 5 mg/L, UV = 1 × 15 W (254 nm), pH = 3, T = 30°C, t = 60 min	94% (0.0469 min^{-1}) TOC removal was achieved	Monteagudo et al. (2014b)
US/Fenton	Dichlorvos (DCV)	f = 36 kHz (horn), P = 150 W, DCV = 20 mg/L, H_2O_2 = 40 mg/L, Fe^{2+} = 40 mg/L, pH = 3, T = room, t = 75 min	81.19% degradation	Patil and Gogate (2014)
US/Fenton US/UV/Fenton	Bisphenol-A (BPA)	f = 40 kHz (bath), P = 200 W, BPA = 10 mg/L (0.043 mM); H_2O_2 = 7.85 mM; Fe^{2+} = 0.36 mM; UV = 1 × 160 W (365 nm), pH = 2; T = 25°C; t = 60 min	Sono-Fenton showed the highest degradation of 99% (9.22×10^{-3} s^{-1}), while use of UVA lamp causes the degradation rate in Sono–photo-Fenton of 86.5% (2.6×10^{-3} s^{-1})	Chakma and Moholkar (2014)

Table 1.2: Summary of literature on wastewater treatment using hybrid ferrioxalate system

Hybrid-AOP	Pollutants	Process parameters	Results/ Max. degradation (%)	Reference
US/UV/FeOX	Reactive Black 5 (RB5)	*f* = 20 kHz (horn type), P = 300W, UV source = 1 × 9 W (365 nm), RB5 = 20 mg/L, Fe^{3+} = 0.5 mM, Ox = 1 mM, pH = 3, T = 20°C, t = 60 min, Air = 1 L/min	~100% (3.62×10^{-2} min^{-1}) degradation and ~ 65% TOC removal in US/UV/Fe(III)-Ox	Zhou et al. (2011)
US/UV/FeOX	Sulfamethazine (SMZ)	*f* = 20 kHz (horn), P = 330W, SMZ = 25 mg/L, goethite = 0.5 g/L, Fe^{3+} = 250 μM, Ox = 0.8 mM, UV = 1 × 9 W (365 nm), pH = 3, T = 20°C, t = 60 min, Air = 1 L/min	64.4% (2.7×10^{-2} min^{-1}) TOC removal	Zhou et al. (2013)
Fenton/UV/FeOX	Methyl Orange (MO)	MO = 20 mg/L, Fe^{3+} = 2 mg/L, Ox = 6 mg/L, H_2O_2 = 5 mM, UV = 1 × 13W (100 – 280 nm), pH = 6, t = 90 min	67% decolorization achieved after 90 min	Fadzil et al., (2012)
Fenton/UV/FeOX	Methyl Orange (MO)	MO = 0.025 mM, Fe^{2+} = 0.3 mM, Ox = 6.5 mM, H_2O_2 = 11 mM, UV = ND, pH = 3.5, t = 65 min	92 – 100% color was removed after 65 min of treatment	Azami et al. (2012)

Table 1.2 (*continued…*): Summary of literature on wastewater treatment using hybrid ferrioxalate system

Hybrid-AOP	Pollutants	Process parameters	Results/ Max. degradation (%)	Reference
Fenton/UV/FeOX	Indigo dye (ID)	ID = 33.33 mg/L, Fe^{2+} = 1.87 mM, Ox = 65.45 mM, H_2O_2 = 1280 mg/L, UV = 290 nm, pH = 5-6, t = 180 min	73% (0.013 min^{-1}) TOC removal was obtained after 180 min of treatment	Vedrenne et al. (2012)
US/UV/FeOX	Ferinitrothion (FT)	Fe^{3+}= 0.5 mM, Ox = 5 mM, FT= 10 mg/L, pH= 6, T = 25°C	Complete degradation was achieved in ultrasound-assisted FeOX process	Katsumata et al. (2010)
UVA/TiO_2/FeOX	Bisphenol-A	BPA = 0.01 mM, Ox = 0.2 mM, H_2O_2 = 0.5 mM, T = 27°C, pH = 3, t = 90 min, UV = 1 × 15 W (365 nm)	80% reduction was seen in hybrid process	Rodríguez et al. (2011)
O_3/FeOX/UVA	Testosterone (TST) Bisphenol A (BPA) Acetaminophen (AAP)	TST = BPA = AAP =0.01 mM, O_3 = 0.25mM; TiO_2 = 0.1 g/L; Fe^{3+} = 0.05 mM, H_2O_2 = $5x10^{-4}$ M; Ox = 0.4 mM; citric acid = 0.4 mM; T = 22–25°C	~ 80% TOC removal was seen after 120 min of treatment	Rodríguez et al. (2012)
Fenton/FeOX	Orange II (OR)	OR = 20 mg/L; Fe^{2+} = 2 mg/L; Ox = 60 mg/L; Accumulated solar energy = 80 Wh; H_2O_2 flow rate = 0.5 mL/min; pH = 3; T = 24°C; air flow rate = 1.3 m^3/h	100% decoloration was achieved using hybrid process. TOC removal was 95% with continuous addition of H_2O_2 whereas TOC removal was 80% when H_2O_2 was added at the beginning	Monteagudo et al. (2009)

Ox - oxalate, FeOX – ferrioxalate, sono-FeOX – sono-ferrioxalate process (US/Fe^{3+}-Ox/UV)

1.2.4 Photolysis (US/H_2O_2/UV) Process

In photolysis of H_2O_2 (UV/H_2O_2 system), a molecule of H_2O_2 is decomposed under ultraviolet light leading to production of two $^{\bullet}OH$ radicals. As the molar extinction coefficient of H_2O_2 under UVA light (365 nm) is very low, photolysis of H_2O_2 needs to be carried out in UVC light (254 nm). Under UVC light, hydrogen peroxide decomposes to generate $^{\bullet}OH$ radicals as shown below:

$$H_2O_2 \xrightarrow{h\nu\ (254\ nm)} 2^{\bullet}OH \qquad (1.44)$$

The concentration of hydrogen peroxide is crucial parameter in photolysis of hydrogen peroxide process. Higher concentration of hydrogen peroxide may result in scavenging of the $^{\bullet}OH$ radicals before their reaction with organic pollutants. The reactions leading to scavenging are shown below (Mishra and Gogate, 2011; Chakma and Moholkar, 2015b).

$$^{\bullet}OH + H_2O_2 \longrightarrow H_2O + HO_2^{\bullet} \qquad (1.45)$$

$$^{\bullet}H + H_2O_2 \longrightarrow HO_2^{\bullet} + H_2 \qquad (1.46)$$

$$HO_2^{\bullet} + {}^{\bullet}OH \longrightarrow O_2 + H_2O \qquad (1.47)$$

Conventional photolysis process can also be combined with ultrasound for more effective degradation and mineralization of bio–recalcitrant pollutants. Hydrogen peroxide can also get decomposed under sonication resulting in production of $^{\bullet}OH$ radicals. Sonolysis of water hydrogen peroxide can also generate H_2O_2 in–situ through recombination of the $^{\bullet}OH$ radicals generated from thermal dissociation of water inside the cavitation bubble at transient collapse. This in–situ generated H_2O_2 can undergo photo–decomposition under UVC light to generate additional $^{\bullet}OH$ radicals. Presence of dissolved oxygen in liquid medium can also trigger additional chemical reactions leading to formation of $HO_2^{\bullet}$ and $^{\bullet}O$ radicals. The possible reactions in sono–photolysis process are shown below:

$$H_2O \xrightarrow{US} {}^{\bullet}OH + {}^{\bullet}H \quad (1.48)$$

$${}^{\bullet}OH + {}^{\bullet}OH \longrightarrow H_2O_2 \quad (1.49)$$

$${}^{\bullet}OH + O_2 \longrightarrow HO_2^{\bullet} + O^{\bullet} \quad (1.50)$$

pH of the solution is an important parameter affecting chemistry sono–photolysis. At low pH, H_2O_2 reacts with proton to generate oxonium ion ($H_3O_2^+$) (Daud et al. 2012): $H_2O_2 + H^+ \longrightarrow H_3O_2^+$; while at high pH (> pK_a), it undergoes dissociation to generate H^+ and HO_2^- species (Chang et al., 2010): $H_2O_2 \rightleftharpoons H^+ + HO_2^-$. However, the influence of pH in photolysis process is not much significant and it has been found the optimum pH for photolysis or sono–photolysis reactions is to be neutral (pH = 7). Table 1.3 presents the summary of literature on degradation of variety of pollutants employing sono–photolysis.

1.2.5 Persulfate Oxidation Process

Persulfate based oxidation systems for degradation of recalcitrant pollutants have been investigated by many researchers. Metal persulfates generate sulfate radicals that can effectively degrade a large variety of organic pollutants. Activation of persulfate anion gives rise to sulfate radical. The conventional activation methods for persulfate anion ($S_2O_8^{2-}$) are UVC (254 nm) activation, Fe^{2+} activation and thermal activation, described by reactions below (Monteagudo et al., 2015; Wang et al., 2015):

$$S_2O_8^{2-} \xrightarrow{UVC} 2\ SO_4^{\bullet-} \quad (1.51)$$

$$S_2O_8^{2-} \xrightarrow{Heat} 2\ SO_4^{\bullet-} \quad (1.52)$$

$$S_2O_8^{2-} + Fe^{2+} \longrightarrow Fe^{3+} + SO_4^{\bullet-} + SO_4^{2-} \quad (1.53)$$

The new activation method of persulfate is through sonolysis. In sonolysis, the activation persulfate anion can occur in the interfacial region of cavitation bubble, which gets

heated to moderate temperatures during transient collapse. The H$^{\bullet}$ and $^{\bullet}$OH radicals produced during transient cavitation can also activate the persulfate anion. The relevant activation reactions are given below (Wang et al., 2015, Roshani and vel Leitner, 2011; Kusic et al., 2011):

$$S_2O_8^{2-} \xrightarrow{US} 2\,SO_4^{\bullet-} \quad (1.54)$$

$$H_2O \xrightarrow{US} {}^{\bullet}OH + {}^{\bullet}H \quad (1.55)$$

$$S_2O_8^{2-} + {}^{\bullet}H \longrightarrow SO_4^{\bullet-} + H^+ + SO_4^{2-} \quad (1.56)$$

$$S_2O_8^{2-} + {}^{\bullet}OH \longrightarrow SO_4^{\bullet-} + HSO_4^- + 0.5O_2 \quad (1.57)$$

Some other reactions that can occur in the persulfate reaction system are as follows:

$$H_2O + SO_4^{\bullet-} \longrightarrow H^+ + SO_4^{2-} + {}^{\bullet}OH \quad (1.58)$$

$$S_2O_8^{2-} + {}^{\bullet}OH \longrightarrow OH^- + S_2O_8^{\bullet-} \quad (1.59)$$

$$S_2O_8^{2-} + SO_4^{\bullet-} \longrightarrow SO_4^{2-} + S_2O_8^{\bullet-} \quad (1.60)$$

$$SO_4^{\bullet-} + SO_4^{\bullet-} \longrightarrow S_2O_8^{2-} \quad (1.61)$$

$$Fe^{2+} + SO_4^{\bullet-} \longrightarrow Fe^{3+} + SO_4^{2-} \quad (1.62)$$

The last two reactions (either recombination of the sulfate radicals or scavenging of the sulfate radicals by Fe^{2+} ions) result in loss of oxidation potential. Table 1.4 presents summary of previous studies in degradation of different pollutants with persulfate based oxidation system.

Table 1.3: Summary of published literature on sono-photolysis (US/UV/H_2O_2) process for wastewater treatment

Hybrid-AOP	Pollutants	Process parameters	Results/ Max. degradation (%)	Reference
US/UV/H_2O_2	Phthalate acid esters (PAEs)	f = 400 kHz (bath), PAEs. = 0.01 mM (mix. of DMP, DEP, DBP, MMP), H_2O_2 = *in-situ* generated, UV sources = 6 nos (254 nm), pH = 6.5, T = 28^{o}C, t = 90 min	Degradation: ~82% for MMP (0.0238 min^{-1}) and ~100% for DMP (0.0293 min^{-1}, DEP (0.0387 min^{-1}) & DBP (0.0712 min^{-1}). TOC removal of PAEs was 17%	Xu et al. (2015)
US/UV/H_2O_2	Synthetic pharmaceutical wastewater (SPWW)	f = 20 kHz (bath), P = 140W, TOC = 12 mg/L, H_2O_2 = 1200 mg/L, UV sources = 1 × 13W (254 nm), pH = 3.9, T = ND, t = 120 min, Air = 2 L/min	Max. TOC removal was 98%	Ghafoori et al. (2015)
US/UV/H_2O_2	Atrazine (ATZ)	f = 20 (P = 375W) and 400 kHz (P = 120W) (bath), ATZ = 0.02 mM, H_2O_2 = 5.0×10^{-4} mM/min (in-situ), UV sources = 1 nos (254 nm), pH = 6.5, T = 28^{o}C, t = 60 min	~100% degradation was achieved with 60% of TOC removal	Xu et al. (2014)

Table 1.3 (*continued…*): Summary of published literature on sono-photolysis (US/UV/H_2O_2) process for wastewater treatment

Hybrid-AOP	Pollutants	Process parameters	Results/ Max. degradation (%)	Reference
US/UV/H_2O_2	Synthetic pharmaceutical wastewater (SPWW)	f = 20 kHz (horn type), P = 140W, Composition of SPWW (mg/L) = 4AMP (6.25), PCM (2.5), Ph (12.5), CLP (7.5), BA (6.25), SA (28.75), DCF (0.5), NB (7.5), H_2O_2 = 1750 mg/L, UV sources = 1 × 13 W (254 nm), pH = 2, T = 33.1^oC, t = 90 min, Air = 3 L/min	90% TOC after 180 min	Mowla et al. (2014)
US/UV/H_2O_2	Trihalomethanes (THMs)	f = 500 kHz (PZT transducer), P = 52.55 W, THMs = 10 mg/L, *in-situ* generated H_2O_2, UV sources = 4 × 10.5 W (254 nm), pH = 4.5, T = 25^oC, t = 60 min	100% degradation and 50% TOC were achieved at optimum conditions	Park et al. (2014)
US/UV/H_2O_2	Pharmaceutical wastewater (PW)	f = 24 kHz (horn), P = 200W, PW = 125 mg/L (TOC), H_2O_2 = 6500 mg/L, UV sources = 1 × 150 W (190-280 nm), pH = 7, T = 30^oC, t = 120 min	100% TOC reduction was achieved	Monteagudo et al. (2014a)

Table 1.3 (*continued…*): Summary of published literature on sono-photolysis (US/UV/H_2O_2) process for wastewater treatment

Hybrid-AOP	Pollutants	Process parameters	Results/ Max. degradation (%)	Reference
US/UV/H_2O_2	Food industry wastewater	f = 24 kHz (horn type), P = 200W, H_2O_2 = 11750 ppm, UV sources = 1 × 150 W (190-280 nm), pH = 8, T = 30°C, t = 180 min	TOC removal 60% after 60 min and 98% after 180 min	Duran et al. (2013b)
US/UV/H_2O_2	Dimethyl phthalate (DMP)	f = 400 kHz (bath), P = 120W, DMP = 0.05 mM, H_2O_2 = 9.75×10^{-4} mM/min (in-situ), UV sources = 6nos (254 nm), pH = 6.5, T = 28°C, t = 120 min	~100% degradation	Xu et al. (2013)
US alone UV alone US/UV/H_2O_2	Diethyl phthalate (DEP)	f = 283 kHz (horn type), DEP = 45 µM, H_2O_2 = 0.32 µM/min (*in-situ*), UV sources = 4 × 10 W (254 nm, UVC) or {(2 × 10 W, 254 nm, UVC) + (2 × 10 W, 185 nm, VUV)(185 nm + 254 nm)}, pH = 6.2-6.7, T = 15-18°C, t = 120 min	~92% (1.7×10^{-2} min^{-1}) degradation in US/UVC and ~90% (1.7×10^{-1} min^{-1}) in US/UVC/VUV. TOC removal: ~30% in US/UVC and ~90% in US/UVC/VUV. Positive synergy in sono-photolysis with UVC (SF=1.68) and UVC/VUV (SF=1.23)	Na et al. (2012a)

Table 1.3 (*continued…*): Summary of published literature on sono-photolysis (US/UV/H_2O_2) process for wastewater treatment

Hybrid-AOP	Pollutants	Process parameters	Results/ Max. Degradation (%)	Reference
US/UV/H_2O_2	Diethyl phthalate (DEP)	f = 283 kHz (bath), DEP = 45 μM, H_2O_2 = 0.32 μM/min (*in-situ*), TiO_2 = 450 mg/L, UV sources = 4 × 10.5 W (254 nm), pH = 6.2, T = 15-18^oC, t = 120 min	Sonophotolysis: ~85% (1.56×10^{-2} min^{-1}) degradation with synergy effect 1.95. Sonophotocatalysis: ~100% ($9:2\times 10^{-2}$ min^{-1}) degradation with synergy effect 1.29. TOC removal: ~18% in sonophotolysis and ~60% in sono-photocatalysis	Na et al. (2012b)
US alone UV alone US/UV/H_2O_2 (*in-situ* generated)	2,4,6-trichlorophenol (TCP)	f = 20 kHz (horn type), P = 750W, UV source = 1 × 8 W (365 nm), TCP = 50 mg/L, in-situ generated H_2O_2, pH = ND, T = 10 – 50^oC, t = 300 min	Positive synergistic effect was seen between 10-30^oC and an antagonistic effect between 40-50^oC Degradation: ~76% (7.99×10^{-5} s^{-1}) in (US+UV), ~72% (6.52×10^{-5} s^{-1}) with UV only, and ~68% (6.66×10^{-5} s^{-1}) with US alone	Joseph et al. (2011)

4AMP - 4-aminophenol, PCM - paracetamol, Ph - phenol, CLP - chloramphenicol, BA - benzoic acid, SA - salicylic acid, DCF - diclofenac sodium, NB – nitrobenzene, ND – not defined/ not determined, SF – synergy factor, SP – sono-photolysis, THMs = CF - chloroform, DCBM - dichlorobromomethane, CDBMM - chlorodibromomethane, BF – bromoform, PAEs = dimethyl phthalate (DMP), diethyl phtha-late (DEP), di-n-butyl phthalate (DBP) and monomethyl phthalate (MMP)

Table 1.4: Summary of published literature on sono-persulfate system for wastewater treatment

Hybrid-AOP	Pollutants	Process parameters	Results/ Max. Degradation (%)	Reference
US/PS US/EL/PS	Aniline (AN)	*f* = 160 kHz (PZT), P = 320 W, AN = 75 mg/L, PS = 2.5 wt% (1.88 mg/L), EP = 6 V, pH = 3, T = 45°C, t = 7 h, N_2 = 150 mL/min	TOC removal was ~25% in sono-persulfate process and ~92% in sonoelectro-persulfate. N_2 gas flow helps the TOC removal in sonoelectro-persulfate process nearly 100%	Chen and Huang (2015)
US/PS	Phenanthrene (PhN)	*f* = 20 kHz (bath), P = 90 W, PhN = 65, 390 and 816 mg/kg soil, PS = 0-100 g/L, [Fe(III)–EDTA] = 150 mg Fe/L, NaOH = 2M, pH = 5.8, T = 20°C, t = 30 min	100% degradation in 30 min of treatment in all concentration of PhN	Deng et al. (2015)
US/PS	Humic acid (HA)	*f* = 40 kHz (bath), P = 200 W, HA = 30 mg/L, PS = 100 mM, pH = 3, T = 40°C, t = 120 min	90% humic acid was removed in 2 h of treatment using US/PS	Wang et al. (2015)
US/PS	Ammonium perfluorooctanoate (APFO)	*f* = 20 kHz (bath), P = 300 W, APFO = 46.4 μmol/L, PS = 10 mM, pH = 6, T = 25°C, t = 120 min	51.2% APFO was removed after 120 min of treatment in presence of 20 kHz ultrasound frequency	Hao et al. (2014)

Table 1.4 (*continued…*): Summary of published literature on sono-persulfate system for wastewater treatment

Method	Pollutants	Process parameters	Results/ Max. Degradation (%)	Reference
US/PS US/Fe^0/PS	Acid Orange 7 (AO7)	*f* = 20 kHz (bath), P = 60 W, AO7 = 30 mg/L, PS = 300 mg/L, Fe0 = 500 mg/L, pH = 5.8, T = 22°C, t = 60 min	Maximum decolorization was achieved 10% in US/PS and 96.4% in US/Fe^0/PS	Wang et al. (2014)
US/PS US/Fe^0/PS	Sulfadiazine (SD)	*f* = 20 kHz (bath), P = 40 W, SD = 20 mg/L, PS = 1.84 mM, Fe0 = 0.92 mM, pH = 3-7, T = 25°C, t = 60 min	Degradation of SD was13.7% in US/PS and 95.7-98.4% in US/Fe0/PS in the pH range of 3-7	Zou et al. (2014)
US/PS/H_2O_2/Fe	Pharmaceutical effluent	*f* = 30 kHz (bath), COD = 10667 mg/L, PS = 5 g/L, H_2O_2 = 5 g/L, iron = 4 g/L, pH = 3, T = 30-50°C, t = 30 min	100% COD removal was achieved after 30 min of treatment, degradation increases with in temperature	Nachiappan and Muthukumar (2013)
US/PS	NFDOHA Perfluoroalkylether sulfonates (PFS)	*f* = 28 kHz (bath), P = 200W, NFDOHA ≈ 50 μM, PS = 10 mM, pH = ND, T = 28°C, t = 24 h	55.7% NFDOHA was decomposed after 24 h	Hori et al. (2012)

EP – electrode potential, US – ultrasound, PS – persulfate, NFDOHA - Perfluoroether carboxylic acids ($CF_3OC_2F_4OCF_2COOH$, $CF_3OC_2F_4OC_2F_4OCF_2COOH$, $CF_3OC_3F_6COOH$, $C_2F_5OC_2F_4OCF_2COOH$, $C_4F_9OC_2F_4OC_2F_4OCF_2COOH$)

1.2.6 H_2O_2 – Peroxidase System (Enzymatic process)

Enzymatic treatments have been widely applied in effective in decolorization of textiles dyes by either precipitation or transformation into other harmless products. Peroxidase enzymes, e.g. such as lignin peroxidase, manganese peroxidase, laccases and horseradish peroxidase have been mostly applied in these treatments. A distinct merit of enzymatic treatment is extremely selective and efficient action of enzyme, as compared to the other conventional techniques. A widely used peroxidase is the horseradish peroxidase (donor: hydrogen peroxide oxidoreductase, EC 1.11.1.7 HRP), which is quite versatile with potential applications in chemical, environmental, pharmaceutical and biotechnology industries. Peroxidases have been found ubiquitously in nature – in plants, microorganisms and animals. These enzymes catalyze oxidation of a variety of the substrates, utilizing H_2O_2 as an electron acceptor. Peroxidases contain a heme cofactor in their active sites, or redox–active cysteine or selenocysteine residues. Oxidation of the aromatic substrates by Horseradish peroxidase (HRP) is initiated by their binding to the exposed heme edge site. The nature of the electron donor is dependent on the structure of the enzyme. Horseradish peroxidase isoenzyme C (HRP C) contains a single polypeptide of 308 amino acid residues. The general chemistry of Horseradish peroxidase (and also other isoenzymes) catalyzed reactions is given as follows (Veitch, 2004; Patidar et al., 2012):

$$H_2O_2 + 2\,AH_2 \xrightarrow{\text{HRP C}} 2\,H_2O + 2\,AH^{\bullet} \qquad (1.63)$$

AH_2 and $AH^{\bullet}$ represent a reducing substrate and its radical product, respectively. Typical substrates for enzymatic oxidation are aromatic phenols, phenolic acids, indoles, amines and sulfonates. Enzymatic treatment processes have also been widely used for degumming (Mahmoodi et al., 2010), unhairing in leather industries (Jian et al., 2010) and degradation of many recalcitrant organic compounds (Entezari and Petrier, 2003, 2004, 2005, 2006; Tauber et al., 2008). Hydrogen peroxide may also be added during enzymatic treatment

process, which acts as a co–substrate to activate the enzymatic action. It contributes in the catalytic cycle of enzyme as shown in the Fig. 1.2 to oxidize the native enzyme to form enzyme intermediate (two–electron oxidation state of the enzyme, E1 and E2), which accepts the aromatic compound to carry out its oxidation to a free radical form (Mester and Tien, 2000):

$$E + H_2O_2 \longrightarrow E_1 + H_2O \quad (1.64)$$

$$E_1 + RH \longrightarrow E_2 + R^{\bullet} \quad (1.65)$$

$$E_2 + RH \longrightarrow E + R^{\bullet} + H_2O \quad (1.66)$$

Here, RH is a reducing substrate, R• is the reducing substrate after one electron oxidation. The catalytic activity cycle of horse radish peroxidase (HRP) enzyme with ferulate as reducing substrate is shown in Fig. 1.2 (Veitch, 2004).

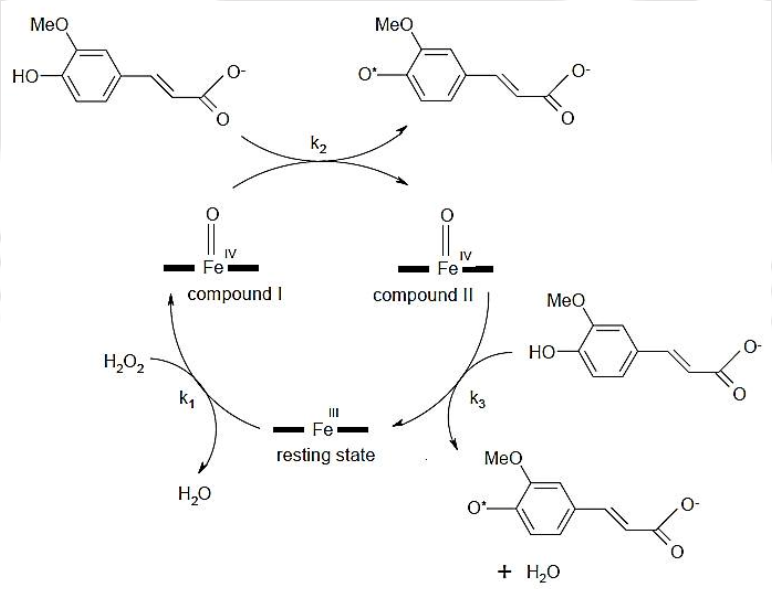

Figure 1.2: The catalytic cycle of horseradish peroxidase enzyme during the reaction with ferulate as reducing substrate. (Adopted from Veitch, 2004)

More recently, several authors have combined the enzymatic treatment with sonication, known as sono–enzymatic technique, for degradation of organic pollutants (Sutar

and Rathod, 2015; Malani et al., 2013, 2014; Entezari and Petrier, 2003, 2005). Focus of this hybrid treatment is on treatment of wastewater discharge from textile industries comprising textile dyes and highly hydrophobic polycyclic aromatic hydrocarbons (PAHs). The sono–enzymatic techniques have been found to give efficient decolorization as well as mineralization of the variety of organic pollutants. The important process parameters over which the performance of sono–enzymatic process depends are pH and temperature of the solution and concentration of H_2O_2 added to the dye solution. The optimum values of these factors are highly specific to type of the pollutant and the enzyme involved in the treatment (Entezari and Petrier, 2003, 2004, 2005, 2006; Malani et al., 2012; Mahmoodi et al., 2010; Jian et al., 2010; Tauber et al., 2008). Despite this specificity, the most common values of these parameters used during treatments are pH = 7 and temperature = 35^{o}C. Most of the peroxidase enzymes have high activity at these conditions. A summary of the literature on sono–enzymatic degradation of various organic pollutants is given in Table 1.5.

Table 1.5: Summary of sono–enzymatic process for treatment of wastewater

Method	Pollutants	Process parameters	Results/ Max. degradation (%)	Reference
Sono-enzymatic	Cetirizine dihydrochloride (CZ)	*f* = 25 kHz (bath), P = 100 W, CZ = 5 mg/L, H_2O_2 = ND, Laccase = 0.02% (w/v), pH = 6, T = 50 ^oC, t = 7 h, Stirring = 200 rpm	Maximum CZ degradation of 91% was obtained with ultrasound duty cycle of 50% with simultaneous agitation at 200 rpm	Sutar and Rathod (2015)
Sono-enzymatic	Acid red B (ARB)	*f* = 35 kHz (bath), P = 35W, ARB = 20 mg/L, H_2O_2 (30%) = 200 µL, HRP = 300 µL (2 U/mL), pH = 7 (10 mM), T = 15-30^oC, t = 60 min, P_o = 1 and 2 bar	Degradation of ARB was studied at different temperatures and pressures. Higher pressure eliminates cavitation resulting in lower degradation. The maximum degradation was 51-52% at atmospheric pressure at 25-30^oC	Malani et al. (2014)
Sono-enzymatic	Acid red B (ARB)	*f* = 35 kHz (bath), P = 35 W, ARB = 20 mg/L, H_2O_2 (30%) = 500 µL, HRP = 300 µL (2 U/mL), pH = 7 (10 mM), T = 25^oC, t = 60 min, PEG (380-420 g/mol) = 26.8 µL	Optimization and degradation was studied with free and immobilized HRP enzyme. Optimum conditions were pH 6.5 & 25^oC for immobilized HRP and pH 7 & 20-25^oC for free HRP. Max. degradation of 61.2% with immobilized and 49.4% with free HRP enzyme was achieved in presence of PEG	Malani et al. (2013)

Table 1.5 (*continued…*): Summary of sono–enzymatic process for treatment of wastewater

Method	Pollutants	Process parameters	Results/ Max. degradation (%)	Reference
Sono-enzymatic	Malachite green (MG) and Acid red B (ARB)	*f* = 35 kHz (bath), P = 35 W, MG or ARB = 12 and 25 mg/L, H_2O_2 (30%) = 200 μL, HRP = 300 μL (2 U/mL), pH = 6, T = 20°C, t = 60 min, PEG = 0.01 g/g dye	Max. degradation was seen at 2 bar pressure (55.56% (0.00619 min-1) for 12 mg/L and 59.64% (0.00521 min-1) for 25 mg/L of MG; and (67.14% (0.0192 min-1) for 12 mg/L, 65.41% (0.0196 min-1) for 25 mg/L of ARB	Patidar et al. (2012)
Sono-enzymatic	Cholesterol (CHL) in egg yolk	*f* = ND, P = 200 W (probe), Egg yolk = 10-50 g, CHLO= 0.6 U/g egg yolk, pH = 7, T = 37°C, t = 15 min	Optimum conditions were found to be 30g egg yolk, CHLO conc. of 0.6 U/g egg yolk, ultrasonication time of 15 min (20% amplitude) and incubation time of 10 h. At this conditions 91.68% yolk cholesterol was degraded	Sun et al. (2011)
Sono-enzymatic	Sericin removal from textile fibers	*f* = ND, P = 125 W, Alcalase or Savinase = 0.5-1 g/L, pH = 8-9, T = 55-60°C, t = 15 min	Degradation of sericin (or degumming of textile fibers) was investigated. Ultrasound enhanced the removal of sericin (21.02%.) by improving the properties of silk yarn such as strength and elongation	Mahmoodi et al. (2010)

Table 1.5 (*continued…*): Summary of sono–enzymatic process for treatment of wastewater

Method	Pollutants	Process parameters	Results/ Max. Degradation (%)	Reference
Sono-enzymatic	Unhairing of pigskins	*f* = 20 and 40 kHz; P = ND; Neutral Protease (NP) = 400 U/ml; Alkali Protease (AP) = 400 U/mL; Amylase (AM) = 40 U/mL; pH = 7.8 (NP), 9.5 (AP) and 6.5 (AM); T =32^{o}C, t = 8 h	Ultrasound enhances unhairing process by increasing the diffusion of enzymes through skins. Under the application of 20 kHz frequency ultrasound, amylase helps to release 5000 μg/mL protein and > 300 μg/mL saccharides, while protease helps to released > 9000 μg/mL protein and >400 μg/mL saccharides in the same conditions	Jian et al. (2010)
Sono-enzymatic	Acid Orange 5 Acid Orange 52 Direct Blue 71 Reactive Black 5 Reactive Orange 16 Reactive Orange 107	*f* = 850 kHz, P = 90 W, Dye conc. = 100 μM, Laccase = 5 nkat/mL, pH = 4.5, T = 30^{o}C	Depending on the dye's structure, the decolorization process takes different time. However, almost complete decolorization was achieved after 24 h of treatment with enzyme followed by 18-25 h of sonochemical treatment	Tauber et al. (2008)

Table 1.5 (*continued…*): Summary of sono–enzymatic process for treatment of wastewater

Method	Pollutants	Process parameters	Results/ Max. degradation (%)	Reference
Sono-enzymatic	Azo dyes (2,7-dihydroxy-1-phenylazo naphthaline-3,6-disulfonic acid)	*f* = 850 kHz, P = 61 W, Dye conc. = 200 μM, ENZ (Azoreductase or Laccase) = ND, pH = 6.5, T = 20°C, t = 6 h	Degradation of azo dyes and -H, -F, -Cl, -Br, $-CF_3$, $-NO_2$ and $-CH_3$ substituted azo dyes in ortho-, meta- and para-position were investigated. Ultrasonic treatment of o-, m-, and p-substituted azo compounds showed 1.5-50 times higher degradation rates. All derivatives were completely degraded after 6 h of treatment.	Rehorek et al. (2007)
Sono-enzymatic	Distillery wastewater	*f* = 22.5 kHz, P = ND, COD = 100-110 g/L, TOC = 55-56 g/L, Cellulase = 50 U, pH = 7.5, T = 50°C, t = 96.5-98 h (total required for US+E+AO)	The highest COD removal of >60% was achieved with 72 h of aerobic biological pretreatment followed by ultrasonic and enzymatic treatment. The best result was obtained with the following combination: (1) US [2h] + EZ [24h] + AO [72h], (2) US [30 min] + EZ [12h] + AO [72h]	Sangave and Pandit (2006)

Table 1.5 (*continued…*): Summary of sono–enzymatic process for treatment of wastewater

Method	Pollutants	Process parameters	Results/ Max. Degradation (%)	Reference
Sono-enzymatic	2-chlorophenol (2CLP)	f = 500 kHz, P = 15.1 W, 2CLP = 0.1 mM, HRP = 0.078 U/mL, H_2O_2 = 1 mM, pH = 7, T = 31^oC, t = 60 min	100% degradation of 2-chlorophenol was obtained after 30 min of treatment using sono-enzymatic process	Entezari et al. (2006)
Sono-enzymatic	(Phenol+ p-chlorophenol) (Phenol+ p-cresol) (Phenol + p-nitrophenol); (p-chlorophenol+ p-cresol)	f = 423 kHz, P = 5.5 W, Phenols = 0.8 mM, HRP = 0.8 μ/mL, H_2O_2 = 2 mM, pH = 7.2, T = 30^oC, t = 60 min	Degradation of substituted phenols from a mixture was easier than the phenol. Sono-enzymatic gave faster degradation and 100% degradation was achieved within 40 min.	Entezari and Pétrier (2005)
Sono-enzymatic	Phenol (Ph)	f = 423 kHz, P = 5.5 W, Ph = 1.6, 2.4 and 4 mM, HRP = 2.4 U/mL, H_2O_2 = 2 mM, pH = 7.2, T = 25^oC, t = 60 min, PEG = 0.77 mM	Investigated the sequence and method of addition of reagent. Rapid addition of HRP in the solution with H_2O_2 gave 60% removal of phenol; while drop wise or gradual addition (1 mL/10min) of HRP gave 80% degradation just in 20 min. However, complete degradation was with addition of PEG (0.77 mM)	Entezari and Pétrier (2004)

AO – aerobic biological oxidation, f – frequency (Hz), P – power (W), P_o – pressure (bar), T – temperature (^oC), t – time, HRP – horseradish peroxidise, CHLO – cholesterol oxidase

1.2.7 Photocatalysis Process

The conventional heterogeneous advanced oxidation technique is photocatalysis. In this process, semiconductor metal oxides such as TiO_2 or ZnO are used as catalyst along with O_2 as an oxidizing agent (Chakma and Moholkar, 2015; Kumar et al., 2015; Hu et al., 2014). In photo–generated catalysis process or photocatalysis process, the photocatalytic activity depends on the ability of the catalyst to create electron–hole pairs, which generates oxidizing (•OH) radicals. Among different photocatalysts, ZnO and TiO_2 are the most popular, as they have desired properties such as high stability, efficient performance and low cost. For a semiconductor catalyst (e.g. TiO_2 or ZnO), the threshold or ideal wavelength corresponding to the band–gap energy of ~ 3.2 eV is 387 nm (i.e. near–UV radiation). When TiO_2 is exposed to ultraviolet (or near to UV–light or sunlight), an electron (e^-) from the valence band (VB) is promoted to the conduction band (CB) resulting in the simultaneous generation of a positive oxidant hole (h^+) in the VB, i.e. creation of electron–hole pairs (Adewuyi, 2005b).

$$TiO_2 + h\nu(\geq 3.2\ \text{eV}, < 387\ \text{nm}) \longrightarrow h^+_{VB} + e^-_{CB} \qquad (1.67)$$

These photo–generated electron–hole pairs facilitate redox reactions through formation of adsorbed radicals on TiO_2 surfaces. The step of electron–hole formation is very fast (time constant ~10^{15} s^{-1}) in a well–illuminated reactor (Pareek and Adesina, 2004). TiO_2 exists in two phases, viz. anatase and rutile. Anatase phase exhibits a higher band gap (~ 3.2 eV) in comparison to rutile phase (~ 3.0 eV), and thus, can be excited by irradiation at longer wavelengths. Anatase phase generally exhibits superior photocatalytic activity as compared to rutile phase. Moreover, anatase phase of TiO_2 has significantly higher surface area, hence, greater extent of adsorption of radicals. The generation and interaction of radical species for various photocatalytic systems can be described with following reactions (Adewuyi, 2005a, 2005b).

(a) TiO_2–O_2 system

$$TiO_2 + h\nu\ (\geq 3.2\ eV, < 387nm) \longrightarrow h^+_{VB(TiO_2)} + e^-_{CB(TiO_2)} \quad (1.68)$$

$$h^+_{VB(TiO_2)} + e^-_{CB(TiO_2)} \longrightarrow TiO_2 + heat \quad (1.69)$$

$$h^+_{VB(TiO_2)} + H_2O_{ad} \longrightarrow HO^{\bullet}_{(TiO_2)} + H^+ \quad (1.70)$$

$$2\ h^+_{VB(TiO_2)} + 2\ H_2O \longrightarrow H_2O_2 + 2\ H^+ \quad (1.71)$$

$$h^+_{VB(TiO_2)} + OH^-_{ad} \longrightarrow HO^{\bullet} \quad (1.72)$$

$$e^-_{CB(TiO_2)} + O_{2(ad)} \longrightarrow O^{\bullet-}_{2(TiO_2)} \quad (1.73)$$

$$O_{2(ad)} + e^- + H^+ \longrightarrow HO^{\bullet}_2 \quad (1.77)$$

$$O^{\bullet-}_2 + H_2O_2 \longrightarrow HO^{\bullet} + OH^- + O_2 \quad (1.78)$$

$$2\ O^{\bullet-}_2 + 2\ H^+ \longrightarrow H_2O_2 + O_2 \quad (1.79)$$

$$O^{\bullet-}_2 + e^-_{CB(TiO_2)} + 2\ H^+ \longrightarrow H_2O_2 \quad (1.80)$$

$$O_{2(ad)} + 2\ e^- + 2\ H^+ \longrightarrow H_2O_{2(ad)} \quad (1.81)$$

(b) *TiO_2–H_2O_2 system*

$$H_2O_{2(ad)} + 2\ h^+ \longrightarrow O_2 + 2\ H^+ \quad (1.82)$$

$$H_2O_{2(ad)} + 2\ H^+ + 2\ e^- \longrightarrow 2\ H_2O \quad (1.83)$$

$$H_2O_{2(ad)} + h^+ \longrightarrow HO^{\bullet}_2 + H^+ \quad (1.84)$$

$$HO^{\bullet}_2 + HO^{\bullet}_2 \longrightarrow H_2O_2 + O_2 \quad (1.85)$$

$$O^{\bullet-}_2 + HO^{\bullet}_2 \longrightarrow HO^-_2 + O_2 \quad (1.86)$$

$$HO^-_2 + H^+ \rightleftharpoons H_2O_2 \quad (1.87)$$

$$e^{-}_{CB(TiO_2)} + H_2O_2 \longrightarrow HO^{\bullet}_{(TiO_2)} + OH^{-} \quad (1.88)$$

$$O^{\bullet -}_{2(TiO_2)} + H_2O_2 \longrightarrow HO^{\bullet}_{(TiO_2)} + OH^{-} + O_2 \quad (1.89)$$

$$H_2O_2 + h\nu \longrightarrow 2\,HO^{\bullet} \quad (1.90)$$

$$HO^{\bullet} + H_2O_2 \longrightarrow H_2O + HO^{\bullet}_2 \quad (1.91)$$

The electrons formed in the above reaction scheme reduce some metal and dissolved oxygen to form superoxide $O^{\bullet -}_2$ radical ion, while holes react with the water molecules adsorbed on the metal oxide surface to generate $^{\bullet}$OH radicals:

$$TiO_2(h^{+}) + H_2O_{ad} \longrightarrow TiO_2 + {}^{\bullet}OH_{ad} + H^{+} \quad (1.92)$$

$$TiO_2(h^{+}) + OH^{-}_{ad} \longrightarrow TiO_2 + {}^{\bullet}OH_{ad} \quad (1.93)$$

The concentration of adsorbed water is high, so the above two reactions generate large numbers of $^{\bullet}$OH radicals. In addition, the pollutant molecules adsorbed on the surface also get oxidized due to electron transfer:

$$TiO_2(h^{+}) + RX_{ad} \longrightarrow TiO_2 + RX^{\bullet}_{ad} \quad (1.94)$$

Transition and rare-earth metals doped catalysts: The conventional photocatalysts TiO_2 (anatase) and ZnO have large band gap energies. Hence, these catalysts do not show efficient photo–activity in visible light region (≥ 400 nm). For effective wastewater treatment using solar light energy, it is essential that absorption range of these photocatalyst be increased to the visible range. The catalyst can be made photoactive in visible light by decreasing the band gap energy between conduction band (CB) and valence band (VB). Doping of conventional photocatalysts with transition metal such as Fe–, Ag–, Au–, Mg–, Ni–, Co– etc. (Zaleska, 2008; Kudo and Miseki, 2009; Xu and Li, 2010; Yao et al., 2010; Etacheri et al., 2012; Ng et al., 2012; Dong et al., 2011; Samadi et al., 2012; Daghrir et al., 2013; Aydin et al., 2013; Pang and Abdullah, 2012, 2013; Guo et al., 2013; Chakma et al., 2013; Ba–Abbad et al.,

2013; Sathishkumar et al., 2014b), rare–earth elements such as Ce–, Er–, Yb–) (Shirsath et al., 2013; Reszczyńska et al., 2015), and in some cases non-metal such as N–, S– and F–doped photocatalyst (Qin et al., 2011; Zhu et al., 2013; Asiri et al., 2014) are also used to increase the absorption of photons. As the transition metal ions are incorporated into the semiconductor (e.g. TiO_2 or ZnO) lattice, impurity energy levels in the band gap of TiO_2 or ZnO are formed as follows (Ni et al., 2007):

$$M^{n+} + h\nu \longrightarrow M^{(n+1)+} + e^-_{cb} \quad \text{(cb – conduction band)} \quad (1.95)$$

$$M^{n+} + h\nu \longrightarrow M^{(n-1)+} + h^+_{vb} \quad \text{(vb – valence band)} \quad (1.96)$$

M and M^{n+} represent the metal and metal ion dopant. Further, the electron–hole transfer between photocatalyst (TiO_2 or ZnO) and metal ions (M^{n+}) can alter the electron–hole recombination as given by the following equations:

$$\text{Electron trap} : M^{n+} + e^-_{cb} \longrightarrow M^{(n-1)+} \quad (1.97)$$

$$\text{Hole trap} : M^{n+} + h^+_{vb} \longrightarrow M^{(n+1)+} \quad (1.98)$$

The energy level of $M^{n+}/M^{(n-1)+}$ is less negative than that of the energy level of the conduction band (CB) of original photocatalyst, while the energy level of $M^{n+}/M^{(n+1)+}$ is less positive than that of the energy level of valence band (VB) of original photocatalyst.

Given below is an illustrative analysis of Fe^{3+}–doped ZnO semiconductor photocatalyst. In this case, the low amount of Fe^{3+} ions inhibits the recombination of hole (h^+) – electron (e^-) and functions as hole and trap as shown in the equations given below (Chakma and Moholkar, 2015a):

$$ZnO + h\nu \longrightarrow e^- + h^+ \quad \text{(charge pair generation)} \quad (1.99)$$

$$Fe^{3+} + e^-_{cb} \longrightarrow Fe^{2+} \quad \text{(electron trap)} \quad (1.100)$$

$$Fe^{2+} + O_2(ads) \longrightarrow Fe^{3+} + O_2^{\bullet -} \quad \text{(electron release)} \quad (1.101)$$

$$Fe^{3+} + h^+_{vb} \longrightarrow Fe^{4+} \quad \text{(hole trap)} \quad (1.102)$$

$$Fe^{4+} + OH^- \longrightarrow Fe^{3+} + {}^{\bullet}OH \qquad \text{(hole release)} \qquad (1.103)$$

During the electron hole – trap process, Fe^{2+} and Fe^{4+} ions are formed by reacting Fe^{3+} ions with electron holes and trap. These ions are unstable as compared to Fe^{3+} and react with O_2 and OH^- adsorbed onto the surface of the catalyst. This results in production of ${}^{\bullet}OH$ radicals and $O_2^{\bullet -}$ radicals that degrade the organic recalcitrant pollutants. The rates of the degradation reactions at optimum concentration of Fe^{3+} ions are very fast. If the concentration of Fe^{3+} is higher than the optimum concentration, Fe^{4+} ions react with electrons ($Fe^{4+} + e^- \longrightarrow Fe^{3+}$) and reduce availability of the traps. As a result, Fe^{3+} ions act as recombination centers and reduce the activity of Fe–ZnO photocatalyst through the reactions:

$$Fe^{3+} + e^- \longrightarrow Fe^{2+} \qquad (1.104)$$

$$Fe^{2+} + h^+_{vb} \longrightarrow Fe^{3+} \qquad (1.105)$$

Combining of sonolysis with photocatalysis has been attempted by several authors for faster and higher degradation of variety of pollutants. There are essentially two process variants: combination of sonolysis with photocatalyst – without application of external UV light – known as sonocatalysis; and combination of sonolysis with photocatalyst with application of external UV light – known as sonophotocatalysis. Both of these hybrid advanced oxidation processes have been investigated. A summary of literature published employing both of these hybrid AOPs is given in Table 1.6 (sonocatalysis) and Table 1.7 (sonophotocatalysis).

Table 1.6: Summary of degradation of recalcitrant pollutants using sonocatalysis (US/catalyst) process

Hybrid-AOP	Pollutants	Process parameters	Results/ Max. degradation (%)	Reference
Sonocatalysis	Methyl orange (MO)	f = 42 kHz (bath), P = 170 W, MO = 20 mg/L, ZnO = 333 mg/L, T = 25^{o}C, t = 40 min, Air saturated	12.12% reduction in (US + ZnO + Air)	Kumar et al. (2015)
Sonocatalysis	Acid Orange 7 (AO7)	f = 40 kHz (bath), AO7 = 10 mg/L, CPP+TiO_2 = 5 g/L, pH = 4, T = 21-27 ^{o}C, t = 2.5 h	30% (3.13 × 10^{-3} min^{-1}) reduction	Markovic et al. (2015)
Sonocatalysis	Acid Red B (ARB) Methylene Blue (MB)	f = 40 kHz (bath), P = 200 W, ARB or MB = 20 mg/L, ZnO or Fe-ZnO = 0.5 g/L, pH = 7, T = 27^{o}C, t = 60 min	**ARB:** 50.21% (3.49 ×10^{-4} s^{-1}) with ZnO and 58.52% (7.24×10^{-4} s^{-1}) with Fe-ZnO. **MB:** 47.93% (5.42×10^{-4} s^{-1}) with ZnO and 55.46% (6.86×10^{-4} s^{-1}) with Fe-ZnO	Chakma and Moholkar (2015a)
Sonocatalysis	Rhodamine B (RhB)	f = 40 and 60 kHz (bath), P = 240W, RhB = 5 mg/L, $LuFeO_3$ = 4 g/L, pH = 6.5, T = 40^{o}C, t = 90 min	~ 90% with 40 kHz and ~ 100% with 60 kHz	Zhou et al. (2015)
Sonocatalysis	Paracetamol (PCT)	f = 861 kHz (bath), P = 120 W, PCT = 35µM, doped-TiO_2 = 1-50 mg/L, pH = 3, T = -- ^{o}C, t = 40 min	~100% removal of PCT with TOC reduction of 41% with Pd-TiO_2 and 54% with Pd/Au-TiO_2	Ziylan-Yavas et al. (2015)

Table 1.6 (*continued…*): Summary of degradation of recalcitrant pollutants using sonocatalysis (US/catalyst) process

Hybrid-AOP	Pollutants	Process parameters	Results/ Max. Degradation (%)	Reference
Sonocatalysis	Acid Blue 113 (AB113)	f = 42 kHz (bath), AB113 = 10^{-5} M, Pr^{3+}-TiO_2 = 1 g/LUV sources = 1 nos (≥ 420 nm), pH = 6, T = room temp., t = -- min	~35% TOC removal was achieved with Pr^{3+}-TiO_2	Sathishkumar et al. (2014a)
Sonocatalysis	Simazine (SZ)	f = 42 kHz (bath), SZ = 5 mg/L, Au-TiO_2 = 1.5 g/L UV sources = 1 nos (≥ 420 nm), pH = 6, T = ND, t = 7 h	31% TOC reduction (5.45×10^{-4} s^{-1})	Sathishkumar et al. (2014b)
Sonocatalysis	Direct Blue 71 (DB71)	f = 20 kHz (horn), P = 95 W, DB71 = 200 mg/L, ZnO = 2 g/L, H_2O_2 = 75 mg/L, pH = 2.5, T = 20°C, t = 20 min	~100% decolorization in both US+ZnO and US+ZnO+H_2O_2	Ertugay and Acar (2014)
Sonocatalysis	Rhodamine 6G (Rh6G)	f = 50 kHz (bath), P = 170 W, Rh6G = 10 mg/L, CuO = 1.5 g/L or TiO_2 = 4 g/L, UV sources = 1 × 9 W, pH = 12.5, T = ND, t = 3h	52.8% (7×10^{-3} min^{-1}) with CuO and 51.2% (6.8×10^{-3} min^{-1}) TiO_2	Bokhale et al. (2014)
Sonocatalysis	Rhodamine B (RhB)	f = 35 kHz (bath), P = 200 W, RhB = 20 mg/L, ZnO or ZnO/CNTs = 1 g/L, pH = ND, T = ND, t = 60 min	10 wt% CNTs-ZnO exhibits the max. degradation of 19% (0.0035 min^{-1}) with ZnO and 49% (0.011 min^{-1}) with ZnO/CNTs	Ahmad et al. (2014)

Table 1.6 (*continued…*): Summary of degradation of recalcitrant pollutants using sonocatalysis (US/catalyst) process

Hybrid-AOP	Pollutants	Process parameters	Results/ Max. Degradation (%)	Reference
Sonocatalysis	Acid Blue 113 (AB113)	f = 42 kHz (bath), AB113 = 10^{-5} M, Pure and doped-TiO_2 (Gd^{3+} or Nd^{3+} or Y^{3+}) = 1 g/L, pH = 6, T = room temp, t = 5h	Y^{3+}-TiO_2 showed the highest mineralization with TOC removal of~38% (8.8×10^{-5} s^{-1})	Sathishkumar et al. (2014c)
Sonocatalysis	Dichlorvos (DCV)	f = 36 kHz (horn), P = 150 W, DCV = 20 mg/L, TiO_2 = 0.01-0.2 g/L, pH = 3, T = room, t = 75 min	Only 7.45% degradation was achieved	Patil and Gogate (2014)
Sonocatalysis	Phenol (Ph)	f = 40 kHz (bath), P = 100 W, Ph = 40 mg/L, ZnO = 100 mg/L, H_2O_2 = 15 mg/L, pH = 5.5, T = 29°C, t = 120 min	13.7% in (US+ZnO) and 16.9% in (US+ZnO+H_2O_2)	Jyothi et al. (2014)
Sonocatalysis	Ofloxacin (OFX)	f = 20 kHz (probe), P = 400 W, OFX = 10 mg/L, TiO_2 = 1 g/L, pH = 6, T = 27°C, t = 120 min	62% (0.0203 min^{-1}) degradation of OFX was obtained	Hapeshi et al. (2013)
Sonocatalysis	Textile wastewater	f = 35 kHz (bath), P = 50 W, COD = 1600 mg/L, TOC = 522 mg/L, Fe^{3+}-TiO_2 = 6 g/L, H_2O_2 = 40 mM, pH = 3, T = 30 °C, t = 3h	Color removal = 79.9%, COD removal = 59.4% and TOC removal = 49.8%	Pang and Abdullah (2013)

Table 1.7: Degradation summary of recalcitrant pollutants using sono–photocatalysis (US/UV/catalysis) process

Hybrid-AOP	Pollutants	Process parameters	Results/ Max. degradation (%)	Reference
Sono-photocatalysis	Methyl orange (MO)	f = 42 kHz (bath), P = 170 W, MO = 20 mg/L, ZnO = 333 mg/L, UV sources = 1 × 125W (< 390 nm), T = 25^{o}C, t = 40 min, Air saturated	62.99% in (US + ZnO + UV) 99.45% in (US + ZnO + UV + Air)	Kumar et al. (2015)
Sono-photocatalysis	Acid Orange 7 (AO7)	f = 40 kHz (bath), AO7 = 10 mg/L, CPP+TiO_2 = 5 g/L, UV sources = 1 × 300 W, pH = 4, T = 21-27 ^{o}C, t = 150 min	100% (25.01 × 10^{-3} min^{-1}) degradation in (US+UV+Cat) with SF = 2.44	Markovic et al. (2015)
Sono-photocatalysis	Acid Red B (ARB) Methylene Blue (MB)	f = 40 kHz (bath), P = 200 W, ARB or MB = 20 mg/L, ZnO or Fe-ZnO = 0.5 g/L, UV sources = 1 × 160W (365 nm), pH = 7, T = 27^{o}C, t = 60 min	**ARB:** 80.98% (9.22×10^{-4} s^{-1}) with ZnO and 74.75% (1.13×10^{-3} s^{-1}) with Fe-ZnO. **MB:** 53.28% (6.39×10^{-4} s^{-1}) with ZnO and 67.55% (9.07×10^{-4} s^{-1}) with Fe-ZnO	Chakma and Moholkar (2015a)
Sono-photocatalysis	Acid Blue 113 (AB113)	f = 42 kHz (bath), AB113 = 10^{-5} M, RE-TiO_2 = 1 g/L, UV sources = 1 lamp (≥ 420 nm), pH = 6, T = room temp., t = 1h (deg.) and 5h (TOC)	Max. deg. of ~55% (1h) and ~55% TOC reduction (5h) with Pr^{3+}-TiO_2 Degradation follow the order of Pr^{3+}-TiO_2> Sm^{3+}-TiO_2> Er^{3+}-TiO_2> TiO_2	Sathishkumar et al. (2014a)

Table 1.7 (*continued…*): Degradation summary of recalcitrant pollutants using sono–photocatalysis (US//UV/catalysis) process

Hybrid-AOP	Pollutants	Process parameters	Results/ Max. Degradation (%)	Reference
Sono-photocatalysis	Simazine (SZ)	f = 42 kHz (bath), SZ = 5 mg/L, Au-TiO_2 = 1.5 g/L UV sources = 1 lamp (≥ 420 nm), pH = 6, T = ND, t = 420 min	43% TOC reduction (5.88×10^{-4} s^{-1})	Sathishkumar et al. (2014b)
Sono-photocatalysis	Rhodamine 6G (Rh6G)	f = 50 kHz (bath), P = 170 W, Rh6G = 10 mg/L, CuO = 1.5 g/L or TiO_2 = 4 g/L, UV sources = 1 × 9 W, pH = 12.5, T = ND, t = 180 min	60.8% (8.4×10^{-3} min^{-1}) with CuO, 63.3% (8.9×10^{-3} min^{-1}) with TiO_2	Bokhale et al. (2014)
Sono-photocatalysis	Diclofenac (DCF) and Ibuprofen (IBP)	f = 20 kHz (horn), DCF or IBP = 10 mg/L, TiO_2 = 0.5 g/L, UV sources = 1 × 9W (350-400 nm) or 1 × 1 kW (≥ 290 nm), pH = ND, T = 25°C, t = 120 min	96% (4.0×10^{-2} min^{-1}) DCF and 85% (4.9×10^{-2} min^{-1}) IBP	Michael et al. (2014)
Sono-photocatalysis	Rhodamine B (RhB)	f = 35 kHz (bath), P = 200 W, RhB = 20 mg/L, ZnO or ZnO/CNTs = 1 g/L, UV sources = Sunlight (1.213×10^5 Lux unit), pH = ND, T = ND, t = 60 min	ZnO with 10 wt% CNTs was the best and the individual degradation was as ~45% (0.01 min^{-1}) with ZnO and ~ 93% (0.045 min^{-1}) with ZnO/CNTs	Ahmad et al. (2014)

Table 1.7 (*continued…*): Degradation summary of recalcitrant pollutants using sono–photocatalysis (US//UV/catalysis) process

Hybrid-AOP	Pollutants	Process parameters	Results/ Max. Degradation (%)	Reference
Sono-photocatalysis	Acid Blue 113 (AB113)	f = 42 kHz (bath), AB113 = 10^{-5} M, Pure and doped-TiO_2 (Gd^{3+} or Nd^{3+} or Y^{3+}) = 1 g/L, UV sources = 1 nos (≥ 420 nm), pH = 6, T = room temp, t = 300 min	Y^{3+}-TiO_2 showed the highest catalytic activity with TOC removal of ~65% (18×10^{-5} s^{-1})	Sathishkumar et al. (2014c)
Sono-photocatalysis	Ofloxacin (OFX)	f = 20 kHz (probe), P = 400 W, OFX = 10 mg/L, TiO_2 = 1 g/L, UV sources = 1 × 9 W (350 – 400 nm), pH = 6, T = 27°C, t = 120 min	100% (0.1054 min^{-1}) degradation was achieved	Hapeshi et al. (2013)
Sono-photocatalysis	Paracetamol (PCM)	f = 213 kHz (horn), P = 13.8 W, PCM = 0.09 mM, TiO_2 = 1 g/L, UV sources = 1 × 450 W (≥ 320 nm), pH = 2.7, T = 25°C, t = 180 min	~80% (40.2×10^{-7} M min^{-1}) TOC reduction was achieved	Madhavan et al. (2013)
Sono-photocatalysis	Direct Blue 71 (DB71)	f = 20 kHz (horn), P = 95 W, DB71 = 200 mg/L, ZnO = 2 g/L, H_2O_2 = 75 mg/L, UV sources = 2 UV lamps (254 nm), pH = 2.5, T = 20°C, t = 20 min	~100% decolorization in 20 min	Ertugay and Acar (2014)

Table 1.7 (*continued…*): Degradation summary of recalcitrant pollutants using sono–photocatalysis (US/UV/catalysis) process

Hybrid-AOP	Pollutants	Process parameters	Results/ Max. Degradation (%)	Reference
Sono-photocatalysis	Dichlorvos (DCV)	*f* = 36 kHz (horn), P = 150 W, DCV = 20 mg/L, TiO_2 = 0.01-0.2 g/L, UV sources = Sunlight, pH = 3, T = room, t = 75 min	83.12% degradation in US/Solar/TiO_2	Patil and Gogate (2014)
Sono-photocatalysis	Trichloroacetic acid (TCA)	*f* = 30 kHz (probe), P = 80 W, TCA = 100 mg/L, TiO_2 = 62.5 mg/L, UV sources = 2 × 9 W (254 nm), pH = 5.8, T = 28^{o}C, t = 60 min, Air and O_2 bubbling	8.24% (air) and 14.37% (O_2) degradation were obtained with ~35% TOC removal	Hu et al. (2014)
Sono-photocatalysis	Phenol (Ph)	*f* = 40 kHz (bath), P = 100 W, Ph = 40 mg/L, ZnO = 100 mg/L, H_2O_2 = 15 mg/L, UV sources = 1 × 400 W (254 nm), pH = 5.5, T = 29^{o}C, t = 120 min	87.9% in (US+ZnO+UV) and 94.6% in (US+ZnO+H_2O_2+UV)	Jyothi et al. (2014)

CPP+TiO_2 - corona pre-treated polypropylene (CPP) supported TiO_2, RE-TiO_2– rare earth materials (Sm^{3+}, Pr^{3+} and Er^{3+}) doped TiO_2

1.3 SCOPE AND STRUCTURE OF THE THESIS

The preceding section has presented the basic chemistry of the conventional advanced oxidation processes which have been extensively investigated for degradation/ mineralization of variety of pollutants. The relatively new AOP of sonolysis has also shown high promise for effective degradation of pollutants. Although the principal chemical mechanism of all AOPs is oxidative degradation and mineralization through $^{\bullet}OH$ radicals, the chemical mechanism of production of these radicals differs significantly in each AOP. The hybrid AOPs combining sonolysis with conventional AOPs have also been investigated and the literature review on these hybrid AOPs presented in preceding sections shows high potential of the hybrid AOPs for more effective treatment of wastewater. Both kinetics of degradation and extent of complete mineralization shows significant rise with the hybrid AOP as compared with the individual AOPs.

However, as noted earlier, despite significant research on hybrid AOPs, the exact mechanism of these processes that lead to faster and higher degradation has not been fully explored. The exact interactions between individual mechanisms of the AOPs, described in the previous section, have not been identified. The present thesis is aimed at establishing the physical mechanism of the sono–hybrid AOPs. This would essentially mean identification of links between physics of ultrasound and cavitation and chemistry of degradation. The methodology, which we adopt for these investigations, is that of coupling results of simulations of cavitation bubble dynamics with experimental results on degradation of pollutant with specific protocols. The experimental protocols alter the characteristics of the ultrasound and cavitation phenomenon in the liquid. These alterations will be captured by simulations of the cavitation bubble dynamics, which will give magnitudes of the physical and chemical effects induced by cavitation bubbles under the applied protocols. Concurrent analysis of the experimental and simulations result reveal interesting mechanistic features of

the hybrid AOPs involving sonolysis and the conventional AOPs.

The model organic compounds that have been chosen for the mechanistic investigations are common pollutants appearing in wastewater discharge of petrochemical, pharmaceutical and textile industries. These model pollutants include azo and non–azo textile dyes (Acid Red B, Methylene blue and Blue HE2R), plastic intermediate of Bisphenol A and inflammatory and analgesic drug Ibuprofen.

The sono–hybrid processes that have been dealt with in this thesis are: (1) sono–photo–Fenton, (2) sono–Ferrioxalate, (3) sono–photolysis, (4) sono–persulfate, (5) sono–enzymatic and (6) sono–photocatalysis (using doped or dual activity catalysts). The thesis comprises of total 10 chapters (including the present one). A brief description of contents of each chapter is as follows:

Chapter 2 deals with investigation of physical mechanism of sono–Fenton process. In this study, the textile dyes of Acid Red B and Blue HE2R have been employed as model pollutants. Initially optimization of parameters such as concentrations of Fe2+, H2O2, pH, and initial dye concentration has been carried out. The experimental protocols include application of elevated static pressure and de–oxygenation of the liquid medium.

Chapter 3 describes investigations in the hybrid AOP of sono–photo–Fenton with Bisphenol A being employed as model pollutant. The experimental protocols used include application of individual techniques of Fenton, and Fenton/UV with mechanical agitation and also with sonication. The two Fenton reagents, viz. Fe^{2+} and H_2O_2, have also been individually applied with sonication. Comparative analysis of the Bisphenol A degradation and mineralization (using TOC removal) in these protocols helps in identification of exact role of ultrasound and cavitation in the process.

Chapter 4 deals with the hybrid AOP of sono–photo–ferrioxalate. Initially optimization of the process parameters (such as concentrations of Fe^{3+}, oxalate, molar ratio of

the two, pH, H_2O_2 addition etc) has been carried out. The experimental protocols include de–oxygenation of the solution and sparging of monatomic and diatomic gases. Two textile dyes, viz. azo dye of Acid Red B and non–azo dye of Methylene blue have been employed as model pollutants.

Chapter 5 presents investigations in hybrid AOP of sono–photolysis using azo dye of Acid Red B as model pollutants. The experimental protocols include application of individual AOPs of sonolysis and photolysis (with mechanical agitation), combination of ultrasound + H_2O_2 and ultrasound + H_2O_2 + UV. Arrhenius analysis of the three processes, viz. sonolysis, photolysis and sono–photolysis has also been done to assess variations in activation energy and frequency factor. Intensification of the sono–photolysis with addition of salt (or electrolyte) has also been investigated.

Chapter 6 describes the mechanistic investigations of sono–persulfate oxidation process using azo dye of Acid Red B as model pollutant. Different methods of activation of persulfate, viz. thermal activation, Fe^{2+} activation and UV–C activation, for degradation of the pollutants have been studied. These methods have been applied individually and in binary and ternary combinations. The variations in decolorization/ mineralization of Acid Red B in different experimental protocols have been assessed to identify synergistic effects of the three methods of persulfate activation.

Chapter 7 presents investigations in sono–enzymatic degradation of analgesic drug Ibuprofen using Horseradish peroxidase as the enzyme. The experimental protocols include application of sonolysis and enzymatic treatments individually. The hybrid sono–enzymatic treatment has been applied at atmospheric and elevated static pressure. Two ultrasound frequencies have been employed. GC–MS analysis of reaction solution has been carried out to identify the intermediate of degradation. Mineralization of the drug in various protocols has also been assessed with TOC analysis. Finally, the degradation of Ibuprofen has also been

assessed with kinetic and thermodynamic analysis to determine Arrhenius parameters of activation energy and frequency factor, and thermodynamic parameters of enthalpy, entropy and Gibbs energy change.

Chapter 8 presents investigations in heterogeneous sono–hybrid AOP of sono–catalysis and sono–photocatalysis. The photocatalyst employed is ZnO either in pure form and doped with Fe^{3+}. Doping has been carried out with sonication in presence and absence of surfactant. Azo dye of Acid Red B and non–azo dye of methylene blue have been used as model pollutants. Extensive characterization of the photocatalysts has been carried out prior to experiments. The experimental protocols include application of individual AOP of sonolysis and photocatalysis, and hybrid AOP of sono–photocatalysis with oxygenated and de–oxygenated liquid medium.

Chapter 9 describes investigations in sonochemical synthesis of new catalyst of zirconium ferrite, which has dual activity of photocatalysis and Fenton due to presence of $\alpha - Fe_2O_3$ phase. Experimental protocols employed in this study are same as that in previous chapter. The efficacy of zirconium ferrite in degradation/ mineralization of the azo dye has been compared with conventional photocatalyst of TiO_2 synthesized through sonochemical route. The effect of UV source, either UV–A or combination of UV–A & UV–C, on degradation/ mineralization has also been assessed.

Chapter 10 gives an overview of all results on degradation/ mineralization of various pollutants using different sono–hybrid AOPs. The similarity in trends of degradation/ mineralization seen with similar experimental protocols under different sono–hybrid AOPs – despite significantly different individual chemical mechanisms of the individual AOPs and different chemical structure of the pollutant – has been identified. These similarities are essentially manifestations of similar physics of reaction systems despite different chemistry. All results when viewed together help in discerning the exact role of ultrasound and

cavitation in the hybrid AOPs. Some suggestions for future investigations (through mechanistic viewpoint) in sono–hybrid AOPs have also been made.

REFERENCES

Adewuyi Y, Sonochemistry in environmental remediation. 1. Combinative and hybrid sono-photochemical oxidation processes for the treatment of pollutants in water, Environ. Sci. Technol. 39 (2005a) 3409–3420.

Adewuyi Y, Sonochemistry in environmental remediation-2: Heterogeneous sono-photocatalytic oxidation processes for the treatment of pollutants in water, Environ. Sci. Technol. 39 (2005b) 8557−8570.

Adewuyi Y, Sonochemistry: Environmental science and engineering applications, Ind. Eng. Chem. Res. 40 (2001) 4681–4715.

Ahmad M, Ahmed E, Hong ZL, Ahmed W, Elhissi A, Khalid NR, Photocatalytic, sonocatalytic and sonophotocatalytic degradation of Rhodamine B using ZnO/CNTs composites photocatalysts, Ultrason. Sonochem. 21 (2014) 761–773.

Andreozzi R, Caprio V, Insola A, Marotta R, Advanced oxidation processes (AOP) for water purification and recovery, Catal. Today 53 (1999) 51–59.

Arslan I., Balcioğlu I. A., Bahnemann D. W., Advanced chemical oxidation of reactive dyes in simulated dyehouse effluents by ferrioxalate-Fenton/UV-A and TiO_2/UV-A processes, Dyes and Pigments 47 (2000) 207–218.

Asiri AM, Al-Amoudi MS, Bazaid SA, Adam AA, Alamry KA, Anandan S, Enhanced visible light photodegradation of water pollutants over N-, S-doped titanium dioxide and n-titanium dioxide in the presence of inorganic anions, J. Saudi Chem. Soc. 18 (2014) 155-163.

Aydın C, El–sadek MSA, Zheng K, Yahia IS, Yakuphanoglu F, Synthesis, diffused

reflectance and electrical properties of nanocrystalline Fe–doped ZnO via sol–gel calcination technique, Optic. Laser Technol. 48 (2013) 447–452.

Azami M, Bahram M, Nouri S, Naseri A, A central composite design for the optimization of the removal of the azo dye, methyl orange, from waste water using the Fenton reaction, J. Serb. Chem. Soc. 77 (2012) 235–246.

Ba–Abbad MM, Kadhum AAH, Mohamad AB, Takriff MS, Sopian K, Visible light photocatalytic activity of Fe^{3+}–doped ZnO nanoparticle prepared via sol–gel technique, Chemosphere 91 (2013) 1604–1611.

Babuponnusami A, Muthukumar K, Advanced oxidation of phenol: A comparison between Fenton, electro-Fenton, sono-electro-Fenton and photo-electro-Fenton processes, Chem. Eng. J. 183 (2012) 1– 9.

Bagal MV, Gogate PR, Degradation of diclofenac sodium using combined processes based on hydrodynamic cavitation and heterogeneous photocatalysis, Ultrason. Sonochem. 21 (2014a) 1035–1043.

Bagal MV, Gogate PR, Wastewater treatment using hybrid treatment schemes based on cavitation and Fenton chemistry: A review, Ultrason. Sonochem. 21 (2014b) 1-14.

Berberidou C, Poulios I, Xekoukoulotakis NP, Mantzavinos D, Sonolytic, photocatalytic and sonophotocatalytic degradation of malachite green in aqueous solutions, Appl. Catal. B: Environ. 74 (2007) 63–72.

Bocos E, Fernández-Costas C, Pazos M, Sanromán MA, Removal of PAHs and pesticides from polluted soils by enhanced electrokinetic-Fenton treatment, Chemosphere 125 (2015) 168-174.

Bokhale NB, Bomble SD, Dalbhanjan RR, Mahale DD, Hinge SP, Banerjee BS, Mohod AV, Gogate PR, Sonocatalytic and sonophotocatalytic degradation of rhodamine 6G containing wastewaters, Ultrason. Sonochem. 21 (2014) 1797–1804.

Brillas E, Sires I, Oturan MA, Electro-Fenton process and related electrochemical technologies based on fenton's reaction chemistry, Chem. Rev. 109 (2009) 6570–6631

Byun K-T, Kwak H-Y, Degradation of methylene blue under multibubble sonoluminescence condition, J. Photochem. Photobio. A: Chem. 175 (2005) 45–50.

Chakma S, Bhasarkar JB, Moholkar VS, Preparation, characterization and application of sonochemically doped Fe^{3+} into ZnO nanoparticles, Int. J. Res. Eng. Tech. 2 (2013) 177-183.

Chakma S, Moholkar VS, Intensification of wastewater treatment using sono-hybrid processes: An overview of mechanistic synergism, Indian Chem. Eng. (2015b) 1–23. http://dx.doi.org/10.1080/00194506.2015.1026948

Chakma S, Moholkar VS, Investigation in mechanistic issues of sonocatalysis and sonophotocatalysis using pure and doped photocatalysts, Ultrason. Sonochem. 22 (2015a) 287−299.

Chakma S, Moholkar VS, Investigations in synergism of hybrid advanced oxidation processes with combinations of sonolysis + Fenton process + UV for degradation of bisphenol–A, Ind. Eng. Chem. Res. 53 (2014) 6855–6865.

Chakma S, Moholkar VS, Numerical simulation and investigation of system parameters of sonochemical process, Chinese J. Eng. 2013 (2013b) 1–14.

Chakma S, Moholkar VS, Physical mechanism of sono–Fenton process, AIChE J. 59 (2013a) 4303 – 4313.

Chang M-W, Chung C-C, Chern J-M, Chen T-S, Dye decomposition kinetics by UV/H_2O_2: Initial rate analysis by effective kinetic modelling methodology, Chem. Eng. Sci. 65 (2010) 135-140.

Chen W-S, Huang C-P, Mineralization of aniline in aqueous solution by electro-activated persulfate oxidation enhanced with ultrasound, Chem. Eng. J. 266 (2015) 279–288.

Daghrir R, Drogu P, Robert D, Modified TiO_2 for environmental photocatalytic applications: a review, Ind. Eng. Chem. Res. 52 (2013) 3581−3599.

Daud NK, Akpan UG, Hameed BH, Decolorization of Sunzol Black DN conc. in aqueous solution by Fenton oxidation process: effect of system parameters and kinetic study, Desalin. Water Treat. 37 (2012) 1–7.

Deng D, Lin X, Ou J, Wang Z, Li S, Deng M, Shu Y, Efficient chemical oxidation of high levels of soil-sorbed phenanthrene by ultrasound induced, thermally activated persulfate, Chem. Eng. J. 265 (2015) 176–183.

Dong S, Xu K, Liu J, Cui H, Photocatalytic performance of ZnO:Fe array films under sun light irradiation, Physica B 406 (2011) 3609–3612.

Dong X, Ding W, Zhang X, Liang X, Mechanism and kinetics model of degradation of synthetic dyes by UV-vis/H_2O_2/Ferrioxalate complexes, Dyes and Pigments 74 (2007) 470-476.

Duran A, Monteagudo JM, Sanmartín I, García-Díaz A, Sonophotocatalytic mineralization of antipyrine in aqueous solution, Appl. Catal. B Environ. 138– 139 (2013a) 318–325.

Duran A, Monteagudo JM, Sanmartín I, Gómez P, Homogeneous sonophotolysis of food processing industry wastewater: Study of synergistic effects, mineralization and toxicity removal, Ultrason. Sonochem. 20 (2013b) 785–791.

Entezari MH, Mostafai M, Sarafraz-Yazdi A, A combination of ultrasound and a bio-catalyst: removal of 2-chlorophenol from aqueous solution, Ultrason. Sonochem. 13 (2006) 37–41.

Entezari MH, Petrier C, A combination of ultrasound and oxidative enzyme: sono-enzyme degradation of phenols in a mixture, Ultrason. Sonochem. 12 (2005) 283–288.

Entezari MH, Petrier C, A combination of ultrasound and oxidative enzyme: sono-biodegradation of phenol, Appl. Catal. B Environ. 53 (2004) 257–263.

Entezari MH, Pétrier C, A combination of ultrasound and oxidative enzyme: sono-

biodegradation of substituted phenols, Ultrason. Sonochem. 10 (2003) 241–246.

Ertugay N, Acar FN, The degradation of Direct Blue 71 by sono, photo and sonophotocatalytic oxidation in the presence of ZnO nanocatalyst, Appl. Surf. Sci. 318 (2014) 121–126.

Etacheri V, Roshan R, Kumar V, Mg−doped ZnO nanoparticles for efficient sunlight−driven photocatalysis, ACS Appl. Mater. Interfaces 4 (2012) 2717–2725.

Fadzil NAM, Zainal Z, Abdullah AH, Ozone-assisted decolorization of methyl orange via homogeneous and heterogeneous photocatalysis, Int. J. Electrochem. Sci. 7 (2012) 11993–12003.

Ghafoori S, Mowla A, Jahani R, Mehrvar M, Chan PK, Sonophotolytic degradation of synthetic pharmaceutical wastewater: Statistical experimental design and modelling, J. Environ. Manage. 150 (2015) 128-137.

Giri AS, Golder AK, Ciprofloxacin degradation from aqueous solution by Fenton oxidation: reaction kinetics and degradation mechanisms, RSC Adv. 4 (2014) 6738-6745.

Grcic I, Sipic A, Koprivanac N, Vrsaljko D, Global parameter of ultrasound exploitation (GPUE) in the reactors for wastewater treatment by sono-Fenton oxidation, Ultrason. Sonochem. 19 (2012) 270–279.

Guo M, Zhao J, Xu X, Yu W, Wang X, Preparation of Fe-doped ZrO_2 nanotube arrays by anodization of Zr–Fe alloy and their magnetic properties, Mater. Lett. 111 (2013) 93–96.

Guo W-Q, Yin R-L, Zhou X-J, Du J-S, Cao H-O, Yang S-S, Ren N-Q, Sulfamethoxazole degradation by ultrasound/ozone oxidation process in water: Kinetics, mechanisms, and pathways, Ultrason. Sonochem. 22 (2015) 182–187.

Hao F, Guo W, Wang A, Leng Y, Li H, Intensification of sonochemical degradation of ammonium perfluorooctanoate by persulfate oxidant, Ultrason. Sonochem. 21 (2014) 554–558.

Hapeshi E, Fotiou I, Fatta-Kassinos D, Sonophotocatalytic treatment of ofloxacin in secondary treated effluent and elucidation of its transformation products, Chem. Eng. J. 224 (2013) 96–105.

He Y, Grieser F, Ashokkumar M, The mechanism of sonophotocatalytic degradation of methyl orange and its products in aqueous solutions, Ultrason. Sonochem. 18 (2011) 974–980.

Hori H, Nagano Y, Murayama M, Koike K, Kutsuna S, Efficient decomposition of perfluoroether carboxylic acids in water with a combination of persulfate oxidant and ultrasonic irradiation, J. Fluorine Chem. 141 (2012) 5–10.

Hu B, Wu C, Zhang Z, Wang L, Sonophotocatalytic degradation of trichloroacetic acid in aqueous solution, Ceramics Int. 40 (2014) 7015–7021.

Huang R, Fang Z, Yan X, Cheng W, Heterogeneous sono–fenton catalytic degradation of bisphenol A by Fe_3O_4 magnetic nanoparticles under neutral condition, Chem. Eng. J. 197 (2012) 242-249.

Huang Y-H, Tsai S-T, Huang Y-F, Chen C-Y, Degradation of commercial azo dye reactive Black B in photo/ferrioxalate system, J. Hazard. Mater. 140 (2007) 382–388.

Iglesias O, Fernández de Dios MA, Tavares T, Sanromán MA, Pazos M, Heterogeneous electro-Fenton treatment: preparation, characterization and performance in groundwater pesticide removal, J. Ind. Eng. Chem. (2015). doi:10.1016/j.jiec.2014.12.044

Ioan I, Wilson S, Lundanes E, Neculai A, Comparison of Fenton and sono-Fenton bisphenol A degradation, J. Hazard. Mater. 142 (2007) 559–563.

Jeong J, Yoon J, Dual roles of $CO_2^{\bullet-}$ for degrading synthetic organic chemicals in the photo/ferrioxalate system, Water Res. 38 (2004) 3531–3540.

Jeong J, Yoon J, pH effect on $^{\bullet}OH$ radical production in photo/ferrioxalate system, Water Res. 39 (2005) 2893–2900.

Jian S, Wenyi T, Wuyong C, Studies on the application of ultrasound in leather enzymatic unhairing, Ultrason. Sonochem. 17 (2010) 376–382.

Joseph CG, Puma GL, Bono A, Taufiq-Yap YH, Krishnaiah D, Operating parameters and synergistic effects of combining ultrasound and ultraviolet irradiation in the degradation of 2,4,6-trichlorophenol, Desalination 276 (2011) 303–309.

Joseph JM, Destaillats H, Hung H-M, Hoffmann MR, The sonochemical degradation of azobenzene and related azo dyes: rate enhancements via Fenton's reactions, J. Phys. Chem. A 104 (2000) 301–307.

Jyothi KP, Yesodharan S, Yesodharan EP, Ultrasound (US), Ultraviolet light (UV) and combination (US + UV) assisted semiconductor catalysed degradation of organic pollutants in water: Oscillation in the concentration of hydrogen peroxide formed in situ, Ultrason. Sonochem. 21 (2014) 1787–1796.

Katsumata H, Kobayashi T, Kaneco S, Suzuki T, Ohta K, Degradation of linuron by ultrasound combined with photo-Fenton treatment, Chem. Eng. J. 166 (2011) 468–473.

Katsumata H, Okada T, Kaneco S, Suzuki T, Ohta K, Degradation of fenitrothion by ultrasound/ ferrioxalate/ UV system, Ultrason. Sonochem. 17 (2010) 200-206.

Khuntia S, Majumder SK, Ghosh P, Oxidation of As(III) to As(V) using ozone microbubbles, Chemosphere 97 (2014) 120-124.

Kim K, Cho E, Thokchom B, Cui M, Jang M, Khim J, Synergistic sonoelectrochemical removal of substituted phenols: Implications of ultrasonic parameters and physicochemical properties, Ultrason. Sonochem. 24 (2015) 172–177.

Kotronarou A, Mills G, Hoffmann MR, Ultrasonic irradiation of p-nitrophenol in aqueous solution J. Phys. Chem. 95 (1991) 3630–3638.

Kudo A, Miseki Y, Heterogeneous Photocatalyst Materials for Water Splitting, Chem. Soc. Rev. (2009) 253−278.

Kumar R, Kumar G, Akhtar MS, Umar A, Sonophotocatalytic degradation of methyl orange using ZnO nano-aggregates, J. Alloys Compd. 629 (2015) 167–172.

Kusic H, Peternel I, Ukic S, Koprivanac N, Bolanca T, Papic S, Bozic AL, Modeling of iron activated persulfate oxidation treating reactive azo dye in water matrix, Chem. Eng. J. 172 (2011) 109– 121.

Lin J-J, Zhao X-S, Liu D, Yu Z-G, Zhang Y, Xu H, The decoloration and mineralization of azo dye C.I. Acid Red 14 by sonochemical process: Rate improvement via Fenton's reactions, J. Hazard. Mater. 157 (2008) 541–546.

Liu C, Li F, Li X, Zhang G, Kuang Y, The effect of iron oxides and oxalate on the photodegradation of 2-mercaptobenzothiazole, J. Mol. Catal. A Chem. 252 (2006) 40–48.

Madhavan J, Grieser F, Ashokkumar M, Sonophotocatalytic degradation of paracetamol using TiO_2 and Fe^{3+}, Sep. Purif. Technol. 103 (2013) 114–118.

Madhavan J, Satishkumar PS, Anandan S, Grieser F, Ashokkumar M, Degradation of acid red 88 by the combination of sonolysis and photocatalysis, Separation and Purification Technology 74 (2010a) 336–341.

Madhavan J, Satishkumar PS, Anandan S, Zhou M, Grieser F, Ashokkumar M, Ultrasound assisted photocatalytic degradation of diclofenac in an aqueous environment, Chemosphere 80 (2010b) 747–752.

Mahmoodi NM, Arami M, Mazaheri F, Rahimi S, Degradation of sericin (degumming) of Persian silk by ultrasound and enzymes as a cleaner and environmentally friendly process, J. Clean. Prod. 18 (2010) 146–151.

Malani RS, Khanna S, Chakma S, Moholkar VS, Mechanistic insight into sono–enzymatic degradation of organic pollutants with kinetic and thermodynamic analysis, Ultrason. Sonochem. 21 (2014) 1400–1406.

Malani RS, Khanna S, Moholkar VS, Sonoenzymatic decolourization of an azo dye employing immobilized horse radish peroxidase (HRP): A mechanistic study, J. Hazard. Mater. 256– 257 (2013) 90–97.

Markovic D, Saponjic Z, Radoicic M, Radetic T, Vodnik V, Potkonjak B, Radetic M, Sonophotocatalytic degradation of dye C.I. Acid Orange 7 by TiO_2 and Ag nanoparticles immobilized on corona pretreated polypropylene non-woven fabric, Ultrason. Sonochem. 24 (2015) 221–229.

Melero JA, Martinez F, Molina R, Effect of ultrasound on the properties of heterogeneous catalysts for sono-Fenton oxidation processes, J. Adv. Oxid. Technol. 11 (2008) 75–83.

Mester T, Tien M, Oxidation mechanism of ligninolytic enzymes involved in the degradation of environmental pollutants, International Biodeterioration & Biodegradation 46 (2000) 51-59.

Michael I, Achilleos A, Lambropoulou D, Torrens VO, Pérez S, Petroviće M, Barceló́e D, Fatta-Kassinos D, Proposed transformation pathway and evolution profile of diclofenac and ibuprofen transformation products during (sono)photocatalysis, Appl. Catal. B Environ. 147 (2014) 1015–1027.

Mishra KP, Gogate PR, Intensification of sonophotocatalytic degradation of p-nitrophenol at pilot scale capacity, Ultrason. Sonochem. 18 (2011) 739–744.

Monteagudo JM, Durán A, Culebradas R, San Martín I, Carnicer A, Optimization of pharmaceutical wastewater treatment by solar/ferrioxalate photo-catalysis, J. Environ. Manag. 128 (2013) 210 - 219.

Monteagudo JM, Durán A, González R, Expósito AJ, In situ chemical oxidation of carbamazepine solutions using persulfate simultaneously activated by heat energy, UV light, Fe^{2+} ions, and H_2O_2, Appl. Catal. B Environ. 176–177 (2015) 120-129.

Monteagudo JM, Durán A, López-Almodóvar C, Homogeneus ferrioxalate-assisted solar photo-Fenton degradation of Orange II aqueous solutions, App. Catal. B: Environ. 83 (2008) 46–55.

Monteagudo JM, Durán A, San Martín I, Aguirre M, Effect of continuous addition of H_2O_2 and air injection on ferrioxalate-assisted solar photo-Fenton degradation of Orange II, Appl. Catal. B: Environ. 89 (2009) 510–518.

Monteagudo JM, Duran A, San Martín I, García S, Ultrasound-assisted homogeneous photocatalytic degradation of Reactive Blue 4 in aqueous solution, Appl. Catal. B Environ. 152–153 (2014b) 59–67.

Monteagudo JM, Duran A, San Martín I, Mineralization of wastewater from the pharmaceutical industry containing chloride ions by UV photolysis of H_2O_2/Fe(II) and ultrasonic irradiation, J. Environ. Manage. 141 (2014a) 61-69.

Mowla A, Mehrvar M, Dhib R, Combination of sonophotolysis and aerobic activated sludge processes for treatment of synthetic pharmaceutical wastewater, Chem. Eng. J. 255 (2014) 411–423.

Na S, Ahn Y-G, Cui M, Khim J, Significant diethyl phthalate (DEP) degradation by combined advanced oxidation process in aqueous solution, J. Environ. Manage. 101 (2012b) 104-110.

Na S, Jinhua C, Cui M, Khim J, Sonophotolytic diethyl phthalate (DEP) degradation with UVC or VUV irradiation, Ultrason. Sonochem. 19 (2012a) 1094–1098.

Nachiappan S, Muthukumar K, Treatment of pharmaceutical effluent by ultrasound coupled with dual oxidant system, Environ. Technol. 34 (2013) 209–217.

Neppolian B, Jung H, Choi H, Lee JH, Kang J-W, Sonolytic degradation of methyl tert-butyl ether: the role of coupled Fenton process and persulphate ion, Wat. Res. 36 (2002) 4699–4708.

Ng CM, Chen P−C, Sivakumar M, Hydrothermal crystallization of titania on silver nucleation sites for the synthesis of visible light nano-photocatalysts-enhanced photoactivity using Rhodamine 6G, Appl. Catal. A General 433–434 (2012) 75–80.

Ni M, Leung MKH, Leung DYC, Sumathy K, A review and recent developments in photocatalytic water–splitting using TiO_2 for hydrogen production, Renew. Sustain. Energ. Rev. 11 (2007) 401–425.

Nie M, Yang Y, Zhang Z, Yan C, Wang X, Li H, Dong W, Degradation of chloramphenicol by thermally activated persulfate in aqueous solution, Chem. Eng. J. 246 (2014) 373–382.

Pang YL, Abdullah AZ, Effect of low Fe^{3+} doping on characteristics, sonocatalytic activity and reusability of TiO_2 nanotubes catalysts for removal of Rhodamine B from water, J. Hazard. Mater. 235– 236 (2012) 326– 335.

Pang YL, Abdullah AZ, Fe^{3+} doped TiO_2 nanotubes for combined adsorption–sonocatalytic degradation of real textile wastewater, Appl. Catal. B Environ. 129 (2013) 473–481.

Pareek V.K., Adesina A.A, Light intensity distribution in a photocatalytic reactor using finite volume, AIChE J. 50 (2004) 1273–1288.

Park B, Cho E, Son Y, Khim J, Distribution of electrical energy consumption for the efficient degradation control of THMs mixture in sonophotolytic process, Ultrason. Sonochem. 21 (2014) 1982–1987.

Patidar R, Khanna S, Moholkar VS, Physical features of ultrasound assisted enzymatic degradation of recalcitrant organic pollutants, Ultrason. Sonochem. 19 (2012) 104–118.

Patil PN, Gogate PR, Degradation of dichlorvos using hybrid advanced oxidation processesbased on ultrasound, J. Water Process Eng. (2014). http://dx.doi.org/10.1016/ j.jwpe.2014.10.012

Peller J, Wiest O, Kamat PV, Synergy of combining sonolysis and photocatalysis in the Degradation and mineralization of chlorinated aromatic compounds, Environ. Sci.

Technol. 37 (2003) 1926–1932.

Qin H, Li W, Xia Y, He T, Photocatalytic activity of heterostructures based on ZnO and N−doped ZnO, ACS Appl. Mater. Interfaces 3 (2011) 3152–3156.

Rehorek A, Hoffmann P, Kandelbauer A, Gubitz GM, Sonochemical substrate selectivity and reaction pathway of systematically substituted azo compounds, Chemosphere 67 (2007) 1526–1532.

Reszczyńska J, Grzyb T, Sobczak JW, Lisowski W, Gazda M, Ohtani B, Zaleska A, Visible light activity of rare earth metal doped (Er^{3+}, Yb^{3+} or Er^{3+}/ Yb^{3+}) titania photocatalysts, Appl. Catal. B Environ. 163 (2015) 40−49.

Rodríguez E.M., Fernández G., Álvarez P.M., Hernández R., Beltrán F.J., Photocatalytic degradation of organics in water in the presence of iron oxides: Effects of pH and light source, Appl. Catal. B: Environ. 102 (2011) 572–583.

Rodríguez EM, Fernández G, Alvarez PM, Beltrán FJ, TiO_2 and Fe (III) photocatalytic ozonation processes of a mixture of emergent contaminants of water, Water Res. 46 (2012) 152-166.

Rodríguez-Chueca J, Polo-López MI, Mosteo R, Ormad MP, Fernández-Ibáñez P, Disinfection of real and simulated urban wastewater effluents using a mild solar photo-Fenton, Appl. Catal. B Environ. 150–151 (2014) 619-629.

Roshani B, vel Leitner NK, The influence of persulfate addition for the degradation of micropollutants by ionizing radiation, Chem. Eng. J. 168 (2011) 784–789.

Safarzadeh-Amiri A, Bolton JR, Cater SR, Ferrioxalate-mediated solar degradation of organic contaminants in water, Solar Energ. 56 (5) (1996) 439–443.

Saien J, Delavari H, Solymani AR, Sono-assisted photocatalytic degradation of styrene-acrylic acid copolymer in aqueous media with nano titania particles and kinetic studies, J. Hazard. Mater. 177 (2010) 1031–1038.

Samadi M, Asghari Shivaee H, Zanetti M, Ali P, Moshfegh A, Visible light photocatalytic activity of novel MWCNT–doped ZnO electrospun nanofibers, J. Mol. Catal. A: Chem. 359 (2012) 42–48.

Sangave PC, Pandit AB, Ultrasound and enzyme assisted biodegradation of distillery wastewater, J. Environ. Manage. 80 (2006) 36–46.

Sathishkumar PS, Mangalaraja RV, Rozas O, Mansilla HD, Gracia-Pinilla MA, Meléndrez MF, Anandan S, Sonophotocatalytic degradation of Acid Blue 113 in the presence of rare earth nanoclusters loaded TiO_2 nanophotocatalysts, Sep. Purif. Technol. 133 (2014a) 407–414.

Sathishkumar PS, Mangalaraja RV, Rozas O, Mansilla HD, Gracia-Pinilla MA, Anandan S, Sonophotocatalytic (42 kHz) degradation of Simazine in the presence of Au–TiO_2 nanocatalysts, Appl. Catal. B Environ. 160–161 (2014b) 692–700.

Sathishkumar PS, Mangalaraja RV, Rozas O, Mansilla HD, Gracia-Pinilla MA, Anandan S, Low frequency ultrasound (42 kHz) assisted degradation of Acid Blue 113 in the presence of visible light driven rare earth nanoclusters loaded TiO_2 nanophotocatalysts, Ultrason. Sonochem. 21 (2014c) 1675–1681.

Segura Y, Molina R, Martínez F, Melero JA, Integrated heterogeneous sono–photo Fenton processes for the degradation of phenolic aqueous solutions, Ultrason. Sonochem. 16 (2009) 417–424.

Selvam K, Muruganandham M, Sobana N, Swaminathan M, Enhancement of UV-assisted photo-Fenton degradation of reactive orange 4 using TiO_2-P25 nanoparticles, Sep. Purif. Technol. 54 (2007) 241–247.

Shirsath SR, Pinjari DV, Gogate PR, Sonawane SH, Pandit AB, Ultrasound assisted synthesis of doped TiO_2 nano−particles: Characterization and comparison of effectiveness for photocatalytic oxidation of dyestuff effluent, Ultrason. Sonochem. 20 (2013) 277–286.

Sun Y, Yang H, Zhong X, Zhang L, Wang W, Ultrasound-assisted enzymatic degradation of cholesterol in egg yolk, Innovative Food Science and Emerging Technologies 12 (2011) 505–508.

Suslick KS, Sonochemistry, Science 247 (1990) 1439–1445.

Sutar RS, Rathod VK, Ultrasound assisted enzyme catalyzed degradation of cetirizine dihydrochloride, Ultrason. Sonochem. 24 (2015) 80–86.

Tangestaninejad S, Moghadam M, Mirkhani V, Mohammadpoor-Baltork I, Salavati H, Sonochemical and visible light induced photochemical and sonophotochemical degradation of dyes catalyzed by recoverable vanadium–containing poly-phosphomolybdate immobilized on TiO_2 nanoparticles, Ultrason. Sonochem. 15 (2008) 815–822.

Tauber MM, Gubitz GM, Rehorek A, Degradation of azo dyes by oxidative processes – Laccase and ultrasound treatment, Biores. Technol. 99 (2008) 4213–4220.

Vedrenne M, Vasquez–Medrano R, Prato–Garcia D, Frontana–Uribe BA, Hernandez–Esparza M, de Andrés JM, A ferrous oxalate mediated photo–Fenton system: Toward an increased biodegradability of indigo dyed wastewaters, J. Hazard. Mater. 243 (2012) 292–301.

Velegraki T., Poulios I., Charalabaki M., Kalogerakis N., Samaras P., Mantzavinos D., Photocatalytic and sonolytic oxidation of acid orange 7 in aqueous solution, Appl. Catal. B: Environ. 62 (2006) 159–168.

Vinu R, Madras G, Kinetics of sonophotocatalytic degradation of anionic dyes with nano−TiO_2, Environ. Sci. Technol. 43 (2009) 473–479.

Wang S, Zhou N, Wu S, Zhang Q, Yang Z, Modeling the oxidation kinetics of sono-activated persulfate's process on the degradation of humic acid, Ultrason. Sonochem. 23 (2015) 128–134

Wang X, Wang L, Li J, Qiu J, Cai C, Zhang H, Degradation of Acid Orange 7 by persulfate activated with zero valent iron in the presence of ultrasonic irradiation, Sep. Purif. Technol. 122 (2014) 41–46.

Xiong SF, Yin ZL, Yuan ZF, Yan WB, Yang WY, Liu JJ, Zhang F, Dual-frequency (20/40 kHz) ultrasonic assisted photocatalysis for degradation of methylene blue effluent: Synergistic effect and kinetic study, Ultrason. Sonochem. 19 (2012) 756–761.

Xu L, Li X, Influence of Fe–doping on the structural and optical properties of ZnO thin films prepared by sol–gel method, J. Crystal Growth 312 (2010) 851–855.

Xu LJ, Chu W, Graham N, Atrazine degradation using chemical-free process of USUV: Analysis of the micro-heterogeneous environments and the degradation mechanisms, J. Hazard. Mater. 275 (2014) 166–174.

Xu LJ, Chu W, Graham N, Sonophotolytic degradation of dimethyl phthalate without catalyst: Analysis of the synergistic effect and modelling, Water Research 47 (2013) 1996–2004.

Xu LJ, Chu W, Graham N, Sonophotolytic degradation of phthalate acid esters in water and wastewater: Influence of compound properties and degradation mechanisms, J. Hazard. Mater. 288 (2015) 43–50.

Yao Z, Jia F, Tian S, Li CX, Jiang Z, Bai X, Microporous Ni−doped TiO_2 film photocatalyst by plasma electrolytic oxidation, ACS Appl. Mater. Interfaces 2 (2010) 2617–2622.

Zaleska A, Doped−TiO_2: A Review, Recent Pat. Eng. 2 (2008) 157−164.

Zhao D, Ding C, Wu C, Xu X, Kinetics of ultrasound-enhanced oxidation of p-nitrophenol by fenton's reagent, Energy Procedia 16 (2012) 146–152.

Zhong X, Royer S, Zhang H, Huang Q, Xiang L, Valange S, Barrault J, Mesoporous silica iron-doped as stable and efficient heterogeneous catalyst for the degradation of C.I. Acid Orange 7 using sono–photo-Fenton process, Sep. Purif. Technol. 80 (2011) 163–171.

Zhou D, Wu F, Deng N, Xiang W, Photooxidation of bisphenol A (BPA) in water in the presence of ferric and carboxylate salts, Wat. Res. 38 (2004) 4107–4116.

Zhou M, Yang H, Xian T, Li RS, Zhang HM, Wang XX, Sonocatalytic degradation of RhB over $LuFeO_3$ particles under ultrasonic irradiation, J. Hazard. Mater. 289 (2015) 149–157.

Zhou T, Lim T-T, Wu X, Sonophotolytic degradation of azo dye reactive black 5 in an ultrasound/ UV/ ferric system and the roles of different organic ligands, Water Res. 45 (2011) 2915 – 2924.

Zhou T, Wu X, Zhang Y, Li J, Lim T-T, Synergistic catalytic degradation of antibiotic sulfamethazine in a heterogeneous sonophotolytic goethite/oxalate Fenton-like system, Appl. Catal. B Environ. 136–137 (2013) 294–301.

Zhu L−P, Wang L−L, Bing N−C, Huang C, Wang L−J, Liao G−H, Porous fluorine−doped $\gamma - Fe_2O_3$ hollow spheres: synthesis, growth mechanism, and their application in photocatalysis, ACS Appl. Mater. Interfaces 5 (2013) 12478−12487.

Ziylan A, Ince NH, Catalytic ozonation of ibuprofen with ultrasound and Fe-based catalysts, Catal. Today 240 (2015) 2–8.

Ziylan-Yavas A, Mizukoshi Y, Maeda Y, Ince NH, Supporting of pristine TiO_2 with noble metals to enhance the oxidation and mineralization of paracetamol by sonolysis and sonophotolysis, Appl. Catal. B: Environ. 172 (2015) 7–17.

Zou X, Zhou T, Mao J, Wu X, Synergistic degradation of antibiotic sulfadiazine in a heterogeneous ultrasound-enhanced Fe^0/persulfate Fenton-like system, Chem. Eng. J. 257 (2014) 36–44.

भारतीय प्रौद्योगिकी संस्थान गुवाहाटी
Indian Institute of Technology Guwahati

2

PHYSICAL MECHANISM OF SONO–FENTON PROCESS

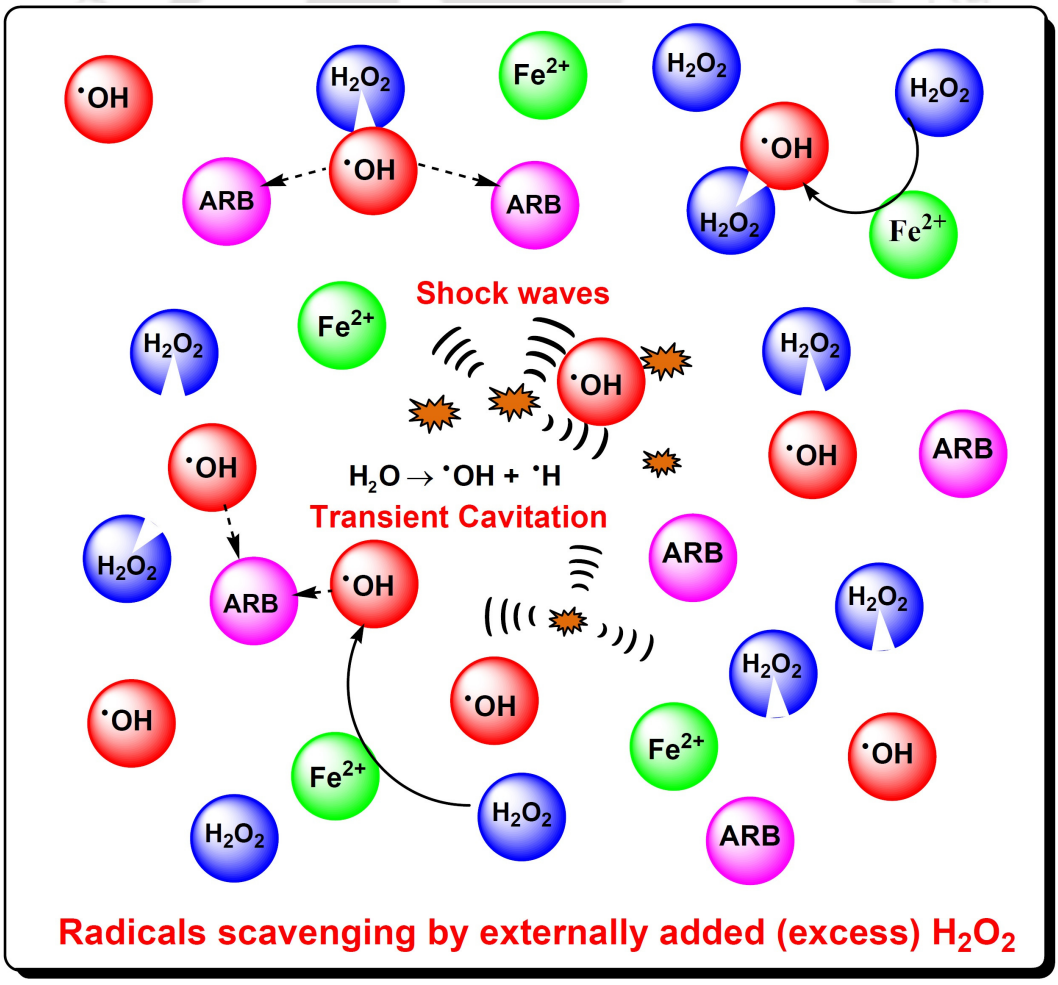

CHAPTER 2

PHYSICAL MECHANISM OF SONO–FENTON PROCESS

2.1 INTRODUCTION

Use of synthetic organic dyes by the textile industries has increased significantly in recent years and many of these dyes are toxic organic pollutants. Based on their chemical structure, the synthetic dyes are categorized into various classes like acidic, basic, azo, non–azo etc. Among these classes, use of azo dyes has been the maximum (~70%) (Peralta–Zamora et al., 1998). These dyes appear in the wastewater discharge from textile industries. The degradation (or decolorization) of these dyes using conventional biological techniques is very difficult due to their complex structure. Globally, approximately 10,000 types of dyes and pigments are produced annually, and about 20% of these are discharged as textile industrial effluents without any pretreatment. For the effective decolorization of the synthetic dyes, advanced oxidation processes (AOPs) have been widely employed as alternative methods. These techniques include Fenton, ozonation, photocatalytic techniques, peroxide treatment, sonolysis, enzyme treatments etc. Literature published in last one decade includes more than 100 papers that report use of these techniques for decolorization of textile wastewater containing wide range of dyes belonging to the different classes mentioned above. For further boosting the efficiency of AOPs, hybrid methods have also been widely

used that simultaneously employ two or more AOPs mentioned above, and voluminous literature has also been published in this area in past one decade. The combinations of AOPs that have been used includes sono–Fenton, sono–photocatalysis, sono–enzymatic treatments, photo–Fenton techniques, UV/H_2O_2, UV/ozone, ozone/H_2O_2 etc. (Lin et al., 2008; Wu, 2008; Papić et al., 2009; Patidar et al., 2012). An excellent review of the individual as well as hybrid AOP techniques for treatment of wastewater has been given by Gogate and Pandit (Gogate and Pandit, 2004a, 2004b). The hybrid techniques have been reported to enhance the decolorization kinetics as well as yield. Most of the literature in the area of hybrid AOPs is focused on results than rationale. Although in many studies an attempt is made to quantify the enhancement factor for the decolorization (or degradation) with reference to one of the AOPs, only a few studies have attempted to deduce the exact mechanism of the synergism between the individual AOP. In this chapter, we have addressed this basic issue in the context of a widely used hybrid AOP, i.e. sono–Fenton process. Several recent studies report employment of sono–Fenton processes for degradation of different organic pollutants (Segura et al., 2008, 2012; Huang et al., 2012; Babuponnusami and Muthukumar, 2012; Grčić et al., 2012; Oezdemir et al., 2011a, 2011b; Zhong et al., 2011;;Sundararaman et al., 2009; Bremner et al., 2009; Molina et al., 2006; Bianchi et al., 2006). We have used two dyes, viz. Acid red B (an azo dye, abbreviated hereafter as ARB) and Blue HE2R (a non–azo dye, abbreviated hereafter as BLH), as model pollutants in this study in view of the large pollution generated by effluent from textile industry, as mentioned earlier. Our approach for identifying the mechanism of the synergism between sonolysis and Fenton process is two–fold, i.e. to couple experiments with simulations of cavitation bubble dynamics. In the next section, we present our contemplations and conjectures, on which the methodology and protocols of this study are based.

2.2 CONTEMPLATIONS AND CONJECTURES

The degradation (or oxidation or decolorization) efficiency of an advanced oxidation process such as sonolysis or Fenton reagent is characterized by the production of $^{\bullet}OH$ radical, which is a powerful oxidizing agent with an oxidation potential of 2.8 V. The $^{\bullet}OH$ radicals are extremely reactive species, and the typical rate constant of their reaction with organic compounds ranges between 10^6–10^9 mol^{-1} s^{-1} (Andreozzi et al., 1999). However, the basic mechanism (either physical or chemical) through which $^{\bullet}OH$ radicals are produced in these techniques is completely different. In sonolysis, the radicals are produced through transient cavitation, which is a phenomenon comprising essentially of 3 phases, viz. nucleation, growth and an adiabatic implosive collapse of a gas or vapor bubble (Shah et al., 1999). These phases are driven by pressure variation induced in the liquid medium (or solvent) due to propagation of the ultrasound wave. Gas pockets trapped in the crevices of solid boundaries of the reaction system constitute the nuclei for cavitation. The growth of the bubble is accompanied by evaporation of large amount of solvent at the bubble interface (or bubble wall), and diffusion of solvent vapor towards the core of the bubble. During the ensuing collapse phase, not all of the vapor molecules can diffuse back to the bubble wall and condense (Storey and Szeri, 2000). A significant fraction of vapor remains inside the bubble when the bubble motion reaches extremely fast during the final moments of compression. The bubble collapse occurs within as small time as 50 ns, and it is almost adiabatic. The temperature and pressure condition inside the bubble reaches extreme, typically excessive of 5000 K and 500 bar, respectively (Hart and Henglein, 1987; Suslick, 1990). The entrapped solvent vapor inside the bubble is subjected to these extreme conditions and undergoes thermal dissociation resulting in very many chemical species, some of which are radical species. The solvent used in majority of the sonochemical processes is water, and 8 species could result out of thermal dissociation of water, *viz*. H_2, O_2, H_2O_2, O_3, $^{\bullet}OH$, $H^{\bullet}$, $O^{\bullet}$, $HO^{\bullet}_2$. The predominant radical

species is $^{\bullet}OH$ (Storey and Szeri, 2000; Hart and Henglein, 1987; Suslick, 1990). As the bubble reaches minimum radius during the radial motion, these species can either diffuse out of the bubble, or with fragmentation of the bubble these get released and mixed into the medium.

$^{\bullet}OH$ radical production through Fenton process is known to occur through the well known reactions as follows (Andreozzi et al., 1999):

$$Fe^{2+} + H_2O_2 \longrightarrow Fe^{3+} + OH^- + HO^{\bullet} \qquad (2.1)$$

$$Fe^{3+} + H_2O_2 \longrightarrow Fe^{2+} + HO_2^{\bullet} + H^+ \qquad (2.2)$$

$$Fe^{3+} + HO_2^{\bullet} \longrightarrow Fe^{2+} + O_2 + H^+ \qquad (2.3)$$

When the techniques of sonolysis and Fenton are applied together, there are several means through which they can assist / oppose each other's mechanism. One obvious mechanism through which the two AOPs can interact is the formation and utilization of $^{\bullet}OH$ radicals. These radicals are formed at the location of bubble collapse and can independently decolorize the dye molecules. However, being extremely reactive, these radicals do not penetrate or diffuse through the bulk medium. If the concentration of pollutant in the solution is small, the probability of interaction between the radical and pollutant molecule is also small, and under these circumstances it is very likely that the $^{\bullet}OH$ radicals would recombine ($^{\bullet}OH + {}^{\bullet}OH \rightleftharpoons H_2O_2$) to give H_2O_2, which is a loss of oxidation potential. However, with Fe^{2+} being present in the medium, $^{\bullet}OH$ radicals can get regenerated from the H_2O_2 (formed due to recombination) through Fenton reactions. Any mechanical agitation applied to the medium can enhance the probability of radical–pollutant interaction, which in turn results in enhancement of degradation / decolorization. Ultrasound and cavitation also generate intense micro–mixing in the medium through different mechanisms such as micro–turbulence due to cavitation bubbles and micro–streaming (i.e. oscillatory velocity of fluid elements due

to ultrasound propagation) (Shah et al., 1999). This micro–mixing can increase the probability of interaction of radical and pollutant molecules, resulting in better utilization of the radicals (generated from either Fenton process or from the cavitation bubbles) for purpose of decolorization. If, however, H_2O_2 added externally to the medium (as one of the Fenton reagents) is in excess, it would evaporate into the cavitation bubble generating additional $^{\bullet}OH$ radicals, which could enhance the extent of decolorization. The extent of production of radicals through cavitation bubbles depends on three factors (Sivasankar et al., 2007): (1) the bubble population in the medium, (2) extent of evaporation of H_2O_2, which in turn depends on the concentration of H_2O_2 in the solution and its partial pressure, and (3) peak temperature and pressure reached in the bubble at transient collapse, which in turn depends on frequency and pressure amplitude of the ultrasound wave. It should be noted that excess concentration of H_2O_2 in the medium could have adverse effect on degradation /decolorization as the $^{\bullet}OH$ radicals generated by either cavitation bubbles or Fenton reactions can get converted to molecular species due to scavenging action of H_2O_2 through following reactions (Gri–Mech, http://www.me.berkeley.edu/gri–mech/data/frames.html):

$$^{\bullet}OH + H_2O_2 \longrightarrow H_2O + HO_2^{\bullet} \qquad (2.4)$$

$$^{\bullet}OH + HO_2^{\bullet} \longrightarrow O_2 + H_2O \qquad (2.5)$$

The dissolved oxygen in the medium also plays a critical role in the decolorization process due to the conservation of radicals, as has been demonstrated in our earlier works (Sivasankar and Moholkar, 2009a, 2009b). The dissolved oxygen can help conservation of the $^{\bullet}OH$ radicals generated through Fenton reactions as well as cavitation bubbles through following reaction:

$$^{\bullet}OH + O_2 \longleftrightarrow O^{\bullet} + HO_2^{\bullet} \qquad (2.6)$$

The physical mechanism of synergy between sonolysis and Fenton reactions can be deduced by discriminating between the physical and chemical effects of ultrasound and

cavitation, each of which has distinct beneficial influence on the Fenton process. The question that we try to answer is that what is the individual contribution of these effects, and which of these effects is more beneficial for the hybrid process of sono–Fenton. Moreover, we also try to identify the role played by secondary factors such as concentration of H_2O_2 in the medium and extent of dissolved oxygen content in the medium. As stated previously, we have adopted an approach of coupling experimental results with simulations of bubble dynamics for this purpose.

2.3 MATERIALS AND METHODS

This study aimed at elucidating the physical mechanism of the sono–Fenton process, i.e. identifying the inter–connections between cavitation physics and Fenton chemistry. The textile dyes used in this work are only model or representative pollutants. The degradation of these dyes with sono–Fenton process has been previously reported in literature with identification of the degradation intermediates (Lin et al., 2008). In view of this, we have not included identification of degradation intermediates (with proposition of the degradation mechanism) in the experimental scope of present study. Experiments have been designed so as to vary the characteristics of cavitation phenomenon in the medium. The decolorization of original dye solution has been used as yardstick for illuminating the physical mechanism and synergy of the sono–Fenton process.

2.3.1 Materials

Following chemicals have been used in this study: ARB dye, BLH dye, ferrous sulfate heptahydrate ($FeSO_4 \cdot 7H_2O$), hydrogen peroxide (30% v/v), sulfuric acid (97%), sodium hydroxide (pellets). All the chemicals were purchased from Merck India Ltd. and used as received without any further pretreatment. For all experiments, Milli–Q water from Milli–Q

Synthesis unit (Millipore®, USA) was used as the liquid medium.

2.3.2 Experimental setup

A schematic of the experimental setup is shown in Fig. 2.1. Sonication experiments were carried out in a conical flask (250 mL) made of borosilicate glass. Experiments were carried out with either mechanical stirring of the solution or sonication. For mechanical stirring, a magnetic stirrer (Remi Equipments, Model: LZMS3969) was used. An ultrasound bath (JeioTech, South Korea, Model: UC–10, Capacity: 10 L) with frequency of 40 kHz and power of 200 W was used for sonication the medium. The bath was filled with 10 L of water as the sonication medium. This water was replaced with fresh water in every 10 min to maintain bulk liquid medium at constant temperature during the experiment. The average temperature of the bath, and hence, the reaction solution inside the flask, varied by less than 3^{o}C due to this procedure. Prior to experiments, the sonication bath was characterized with calorimetric measurements for actual power dissipation and the distribution of acoustic pressure amplitude (Sivasankar and Moholkar, 2007; Chakma and Moholkar, 2011). The ultrasound intensity (and hence the ultrasound pressure amplitude) in the bath shows significant spatial variation. In order to avoid the variation in the ultrasound pressure amplitude in different experiments (which could give rise to artifacts), the conical flask containing dye solution was placed at the center of the sonication bath, and its position was carefully maintained constant in all experiments. All sonication experiments were conducted in the same flask so as to have same ultrasound pressure amplitude and power dissipation in the reaction mixture in all experiments. Moreover, sonication experiments were carried out at two static pressures, *viz*. atmospheric (101.3 kPa) static pressure and elevated static pressure of 200 kPa (or 2 bar). The rationale underlying raised static pressure to the system during sonication of reaction mixture has been described by Moholkar et al. (2004), and will also be

explained in this chapter subsequently. A simple procedure was used to raise the static pressure of the medium. The neck of the conical flask used in the experiments was closed using a rubber stopper with metal tube pierced in it. The outer end of the metal tube was connected to a nitrogen cylinder through two–stage pressure regulator. The pressure of the outlet gas from cylinder, and hence, the static pressure on the dye solution could be controlled through this regulator.

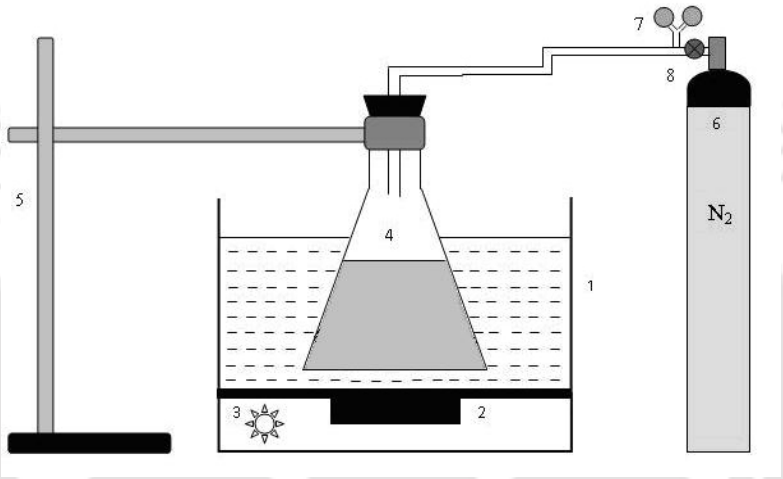

Figure 2.1: A schematic diagram of experimental setup. (1) ultrasound bath (2) transducer (3) timer or regulator (4) desorption mixture (5) burette stand to hold the flask (6) nitrogen gas cylinder (7) pressure gauge (8) two–stage regulator to control the pressure.

2.3.3 Experimental procedure

A 100 mg/L stock solution of the dye (both ARB and BLH) was prepared and stored at 4^{o}C. The major experimental parameters that influence the decolorization process are: (1) composition of the Fenton reagent (i.e. the ratio of Fe^{2+}/H_2O_2), (2) the initial concentration of dye, (3) pH of the solution. To assess the optimum values of these parameters, we conducted preliminary experiments with ARB dye, which have been described in the preliminary experimental section.

For all experiments, 50 mL of dye solution of concentration 10 mg/L was prepared by

taking an appropriate amount of stock solution and diluting it with Milli–Q water. The experiments were carried out in 7 categories for both dyes with different conditions, as described in Table 2.2. Prior to the main set of experiments, we conducted several preliminary experiments in which the influence of parameters such as initial dye concentration, ratio of Fenton reagents (i.e. H_2O_2 and $FeSO_4 \cdot 7H_2O$) and pH of the solution was assessed. The optimum value of each parameter was decided on the basis of these preliminary experiments and was further used for the main set of experiments. To monitor the progress of decolorization of dye solution, aliquots of 1 mL were withdrawn from the reaction mixture every 10 min and the total time of treatment of dye solution in each category of experiments was 60 min. During the withdrawal of the aliquot, the pressure in the conical flask was released. The pressure was restored prior to commencement of sonication. After withdrawal of aliquot, the Fenton reaction was terminated by adjusting the pH 7.5 – 8.0 with NaOH stock solution (5 N), which also resulted in Fe(III) floc formation. The samples were then filtered through 0.22 μm filter to remove the Fe(III) floc and the filtrate was analyzed for the concentration of dye using UV–Visible spectrophotometer (Varian Carry 50). The maximum absorbance wavelength (λ_{max}) of ARB and BLH were determined at 512 nm and 586 nm, respectively, by scanning the UV–Vis spectra from 200 to 800 nm. Figs. 2.2A and 2.2B depict the UV–vis spectra of samples of the dye solutions withdrawn from the reaction mixtures at different time intervals. The decolorization efficiency in different experimental categories was determined as: $\eta\ (\%) = (C_o - C)/C_o \times 100$; where, C_o is the initial concentration of dye, and C is the concentration of dye at any time t (min). In each of the seven categories of experiments for both dyes, experimental runs were taken in triplicate to check the reproducibility of the results. The mean value of the three experimental runs was used for evaluation of kinetics of decolorization and the final yield.

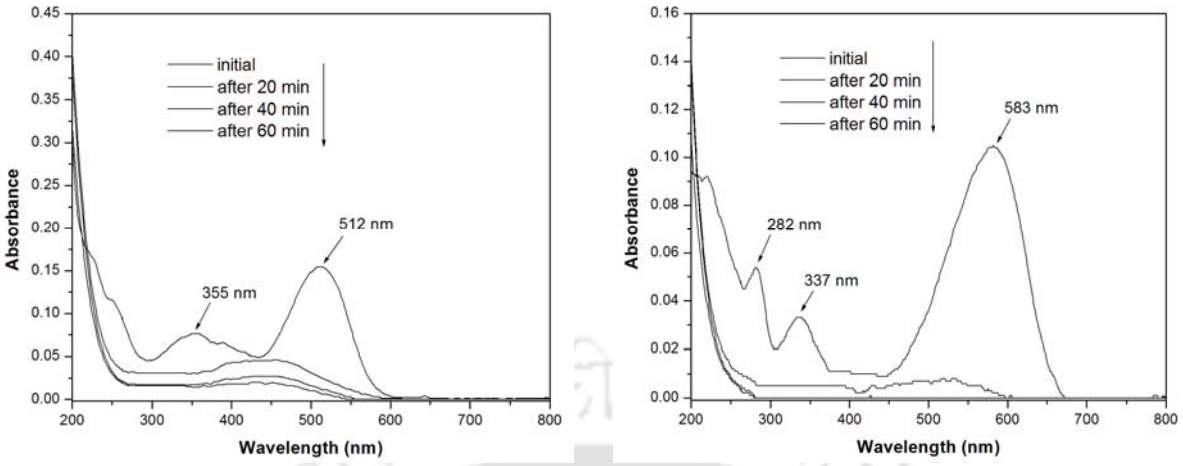

(A) (B)

Figure 2.2: (A) UV–Visible spectra of ARB for different samples withdrawn at different time interval during Fenton reaction. (B) UV–Visible spectra of Blue–HE2R for different samples withdrawn at different time interval during Fenton reaction.

2.4 ULTRASOUND AND BUBBLE DYNAMICS PHENOMENA

Cavitation is essentially the nucleation, growth and implosive collapse of gas/ vapor bubbles (or more generally, the radial motion or volume oscillations of the bubble) driven by bulk pressure variation induced by ultrasound. Occurrence of cavitation in liquid medium requires presence of "nuclei" for the same in the bulk liquid medium. These nuclei could be gas pockets trapped in the crevices of the solid boundaries in the reaction system (such as reactor wall or crevices in the sonicator surface) or solid particles present in the liquid, or these could be freely floating tiny bubble already present in the liquid. Ultrasound passes through the medium in the form of longitudinal wave comprising compression and rarefaction half cycles. This induces period (usually sinusoidal) variation in the static pressure of the liquid medium. As the static pressure in the medium falls during the rarefaction half cycle of ultrasound wave, the cavitation nuclei undergo expansion to form cavitation bubbles. These bubbles undergo compression in the ensuing compression half

cycle. Depending on the pressure amplitude of the ultrasound wave and static pressure in the medium, the radial motion of the bubble is characterized as stable cavitation and transient cavitation. During its radial motion under influence of pressure variation induced by ultrasound, the bubble is acted upon by two forces, *viz*. pressure force and inertial force. The dominant force among these two is governed by the expansion of the bubble in the rarefaction half cycle, which in turn is governed by the amplitude of the ultrasound wave. For sufficiently high pressure amplitude of ultrasound wave (typically greater than the static pressure in the bulk liquid medium), the bubble expands to more than double of its original size. In the ensuing compression phase, the compression of the bubble is dominated by inertial force. The spherical convergence of fluid elements imparts higher and higher kinetic energy to the bubble, due to which bubble undergoes a "transient collapse" and gets compressed to extremely small size. The transient collapse of the bubble is extremely fast and adiabatic during which the bubble wall velocity reaches (or even exceeds) the sonic speed in the liquid medium. The bubble can get compressed to extremely small size (typically $1/10^{th}$ to $1/100^{th}$ of original size), and temperature and pressure in it can reach extreme (~ 5000 K, ~ 500 bar). This essentially creates energy concentration in the medium on extremely small spatial and temporal scale, as the bubble collapse occurs in a few tens of nanoseconds. During the transient collapse, the bubble contents (which is a mixture of gas and vapor of bulk liquid medium) are subjected to extreme conditions generated in the bubble and can get dissociated to form various species, some of which are radical species. The most common liquid medium used for cavitation assisted reactions is water and the species arising out of dissociation of water contain many radicals such as $H^{\bullet}$, $O^{\bullet}$ and $^{\bullet}OH$. For small bubbles of few microns size and frequencies in the range of 20–100 kHz, transient cavitation is seen for ultrasound pressure amplitudes greater than the static pressure on the medium. If the static pressure of the medium is raised to moderate levels, keeping the acoustic pressure amplitude

constant, the transient cavitation events get eliminated as the static pressure exceeds the ultrasound pressure amplitude. In such cases, the bubble undergoes stable, small–amplitude oscillatory motion. The temperature and pressure inside the bubble remains almost ambient. The ultrasound wave (which is a longitudinal wave comprising of alternate compression / rarefaction cycles) also induces high velocity oscillatory motion of the fluid elements, commonly known as micro–streaming. However, the liquid properties such as density and compressibility are not a strong function of pressure, and hence, the velocity of micro–streaming is not altered by rise in the static pressure on the liquid medium.

The principal chemical effect of cavitation, popularly known as the *sonochemical effect* is generation of highly reactive radicals such as $^{\bullet}H$, $^{\bullet}O$, $^{\bullet}OH$ and $HO_2^{\bullet}$. These radicals render several beneficial effects on a reaction system such as induction of stubborn chemical reaction, acceleration of the reaction kinetics, reduction in the number of steps in a synthesis or sometimes a switch of reaction pathway. The principal physical effect of cavitation is generation of strong convection in the medium due to five phenomena, *viz*. ultrasound oscillatory velocity, micro–convection (or micro–turbulence), micro–streaming, shock waves and micro–jets. As both physical and chemical effects of cavitation occur on extremely small spatial and temporal scale, a direct measurement or quantification of these effects would require highly sophisticated equipment. However, a much easier (and cheaper) method to get a fairly accurate estimate of the magnitudes of physical and chemical effects of cavitation is numerical simulations of the bubble dynamics equation, which we rely upon in this study. Modeling of cavitation bubble dynamics is an active area of research for past three decades and various authors have addressed the matter with different approaches. For greater details, we refer the readers to the earlier studies by Krishnan et al. (2006). We have used the diffusion limited ordinary differential equation (ODE) model using boundary layer approximation proposed by Toegel et al. (2000) for our analysis, which is based on the

comprehensive PDE model of Storey and Szeri (2000), who showed that vapor entrapment in the cavitation bubble, leading to formation of radicals is essentially a diffusion limited process. Large amount of evaporation occurs at the bubble interface during the expansion phase of bubble motion, and vapor molecules enter and diffuse towards the bubble core. In the subsequent compression phase, the same vapor diffuses back and condenses at the bubble wall. However, in the final moments of bubble compression, velocity of the bubble interface (or bubble wall) becomes extremely fast and the time scale of bubble motion becomes smaller than the time scale of vapor diffusion to bubble wall as well as time scale of condensation (or phase change) at the bubble wall. As a result, not all of the vapor that has entered the bubble during expansion can escape during compression, and gets "entrapped" in the bubble. Another factor that also contributes to entrapment of vapor in the bubble is non–equilibrium phase change at the bubble interface in the final moments of collapse of the bubble. In this case, since the bubble interface moves with extremely high velocity, not all of the vapor molecules that diffuse towards the interface stick to it, which gives rise to "non–equilibrium phase change". A parameter that represents this process is "accommodation coefficient", which represents the fraction of the vapor molecules that stick to the surface. The time scale of condensation varies inversely with the accommodation coefficient. The smaller the value of accommodation coefficient the larger the extent of non–equilibrium phase change and higher the entrapment of the bubble. Storey and Szeri (2000) have used a value of 0.14 for accommodation coefficient.

The entrapped vapor is subjected to conditions of extreme pressure and temperature reached during collapse. Dissociation of the vapor molecules occurs at these conditions resulting in generation of radicals. This model has been extensively described in previous studies by Sivasankar and Moholkar (2008), and Kumar and Moholkar (2007). For the convenience of the reader, we reproduce here only the main components of the model and

relevant data / boundary conditions. For greater details on this model, we refer the reader to the studies reported by Sivasankar and Moholkar (2008) and Kumar and Moholkar (2007); as well as the original paper of Toegel et al. (2000) and Storey and Szeri (2000).

The essential equations and thermodynamic data of this model have been summarized in Tables 2.1A and 2.1B. The main components of the model are:

(1) Keller–Miksis equation for the radial motion of the bubble (Keller and Miksis, 1980).

(2) Equation for the diffusive flux of water vapor and heat conduction through bubble wall.

(3) Overall energy balance treating the cavitation bubble as an open system.

The transport parameters for the heat and mass transfer (thermal conductivity and diffusion coefficient) are determined using Chapman–Enskog theory using Lennard–Jones 12–6 potential at the bulk temperature of the liquid medium. Thermal and diffusive penetration depths are estimated using dimensional analysis. Diffusion of gas across bubble interface is ignored in the present model as the time scale for the diffusion of gases is much higher than the time scale for the radial motion of bubble. The set of four ODEs described in Table 2.1 was solved simultaneously using Runge–Kutta adaptive step size method (Press et al., 1992).

We have considered an air bubble (for aerated solutions) and a nitrogen bubble (for de–aerated solution using nitrogen sparging) as the cavitation nuclei for simulations of cavitation bubble dynamics in the dye solution. The condition for bubble collapse is taken as the first compression after an initial expansion. Various parameters used in the simulation of bubble dynamics equation and their numerical values are as follows: Ultrasound frequency (f) = 40 kHz; Ultrasound pressure amplitude (P_A) = 200 kPa; Equilibrium bubble radius (R_o) = 5 μm; Vapor pressure of liquid medium (water) = 2500 Pa (calculate using Antoine type correlation). Various physical properties of water are as follows: density (ρ_L) = 1000 kg/m^3, kinematic viscosity (ν) = 10^{-6} Pa–s, surface tension (σ) = 0.072 N/m and velocity of sound (c) = 1481 m/s. Since the dyes as well as other components of reaction mixture (H_2O_2,

$FeSO_4 \cdot 7H_2O$) are present in very small quantities, we have ignored the change in the physical properties of water with addition of these chemicals.

Table 2.1: (A) Model equation for cavitation bubble dynamics

Model Component	Equation	Initial Value
1. Radial motion of the cavitation bubble	$\left(1-\frac{dR/dt}{c}\right)R\frac{d^2R}{dt^2}+\frac{3}{2}\left(1-\frac{dR/dt}{3c}\right)\left(\frac{dR}{dt}\right)^2 = \frac{1}{\rho_L}\left(1+\frac{dR/dt}{c}\right)(P_i-P_t)+\frac{R}{\rho_L c}\frac{dP_i}{dt}-4\nu\frac{dR/dt}{R}-\frac{2\sigma}{\rho_L R}$ Internal pressure in the bubble: $P_i = \frac{N_{tot}(t)\,kT}{\left[4\pi\left(R^3(t)-h^3\right)/3\right]}$ Pressure in bulk liquid medium: $P_t = P_0 - P_A \sin(2\pi ft)$	At $t = 0$, $R = R_o$ $dR/dt = 0$
2. Diffusive flux of water molecules	$\frac{dN_W}{dt} = 4\pi R^2 D_W \left.\frac{\partial C_W}{\partial r}\right\|_{r=R} \approx 4\pi R^2 D_W \left(\frac{C_{W,R}-C_W}{l_{diff}}\right)$ Instantaneous diffusive penetration depth: $l_{diff} = \min\left(\sqrt{\frac{RD_w}{\lvert dR/dt\rvert}}, \frac{R}{\pi}\right)$	At $t = 0$, $N_w = 0$
3. Heat conduction across bubble wall	$\frac{dQ}{dt} = 4\pi R^2 \lambda \left.\frac{\partial T}{\partial r}\right\|_{r=R} \approx 4\pi R^2 \lambda \left(\frac{T_0-T}{l_{th}}\right)$ Thermal diffusion length: $l_{th} = \min\left(\sqrt{\frac{R\kappa}{\lvert dR/dt\rvert}}, \frac{R}{\pi}\right)$	At $t = 0$, $Q = 0$
4. Overall energy balance	$C_{V,mix}\,dT/dt = dQ/dt - P_i dV/dt + (h_W - U_W)\,dN_W/dt$ Mixture heat capacity: $C_{V,mix} = \sum C_{V,i} N_i$ (i = N_2/O_2/H_2O) Molecular properties of water: Enthalpy: $h_w = 4kT_o$ Internal energy: $U_W = N_W kT\left(3+\sum_{i=1}^{3}\frac{\theta_i/T}{\exp(\theta_i/T)-1}\right)$ Heat capacity of various species (i = N_2/O_2/H_2O): $C_{V,i} = N_i k\left(f_i/2+\sum\left((\theta_i/T)^2\exp(\theta_i/T)\Big/\left(\exp(\theta_i/T)-1\right)^2\right)\right)$	At $t = 0$, $T = T_0$

(B) Thermodynamic data for the model

Species	Degrees of freedom (translational + rotational) (f_i)	Lennard–Jones force constants		Characteristic vibrational temperatures θ (K)
		σ (10^{-10} m)	ε/k (K)	
N_2	5	3.68	92	3350
O_2	5	3.43	113	2273
H_2O	6	2.65	380	2295, 5255, 5400

Data taken from Hirschfelder et al. (1954), Condon and Odishaw (1958), Reid et al. (1987)

Notations for Table 2.1: R – radius of the bubble; dR/dt – bubble wall velocity; c – velocity of sound in bulk liquid medium; ρ_L – density of the liquid; ν – kinematic viscosity of liquid; σ – surface tension of liquid; λ – thermal conductivity of bubble contents; κ – thermal diffusivity of bubble contents; θ – characteristic vibrational temperature(s) of the species; N_w – number of water molecules in the bubble; N_{N2} – number of nitrogen molecules in the bubble; N_{O2} – number of oxygen molecules in the bubble; t – time, D_w – diffusion coefficient of water vapor; C_w – concentration of water molecules in the bubble; $C_{w,R}$ – concentration of water molecules at the bubble wall or gas–liquid interface; Q – heat conducted across bubble wall; T – temperature of the bubble contents; T_o – ambient (or bulk liquid medium) temperature; k – Bolzmann constant; h_w – molecular enthalpy of water; U_w – internal energy of water molecules; f_i – translational and rotational degrees of freedom; $C_{V,i}$ – heat capacity at constant volume for species i; N_{tot} – total number of molecules (gas + vapor) in the bubble; h – van der Waal's hard core radius; P_o – ambient (bulk) pressure in liquid; P_A – pressure amplitude of ultrasound wave; f – frequency of ultrasound wave.

2.4.1 Estimation of physical and chemical effects of cavitation

***Sonochemical effect (radical generation by cavitation bubbles)*:** Using the numerical solution of bubble dynamics model, one can estimate the composition of the bubble contents at the collapse. While calculating the composition of the bubble at the time of collapse, we assume that thermodynamic equilibrium is attained (Krishnan et al., 2006). This assumption is justified in terms of very high concentrations of different chemical species in the bubble at the point of minimum radius (or maximum compression) during radial motion. The bubble gets compressed to about 1/100th of original size, and thus, the concentrations of various chemical species are of the order of 100 mol/cm^3 (Krishnan et al., 2006). Secondly, the specific rate constants of many reactions among the species formed out of thermal dissociation are of the order of 10^7 or 10^8 cm^3/mol·s. As an approximation, if the time–scale of reaction is considered as inverse of specific kinetic constant, it is at least an order of

magnitude higher than the time scale of radial motion of the bubble. Finally, the temperature inside the bubble is extremely high at the moment of transient collapse. This also makes the kinetics of different reactions among chemical species generated in the bubble very fast. As a result of all these factors, the bubble contents are likely to be in thermal equilibrium at all times during the radial motion of the bubble (Brenner et al., 2003).

The equilibrium mole fraction of the various species in the bubble at the conditions of temperature and pressure at first the compression of the bubble can be calculated using free–energy minimization technique (Chemical Equilibrium Calculation, http://navier.engr. colostate.edu/ ~dandy/code/code–4/index.html).

***Sonophysical effect of cavitation*:** As noted earlier, the principal physical effect of cavitation is generation of convection in the bulk medium through two phenomena, viz. micro–convection (or micro–turbulence) and shock or acoustic waves. Micro–convection is the oscillatory motion of liquid in the close vicinity of the bubble, which induced by volume oscillations of the bubble. Shock waves (or acoustic waves) are generated due to reflection of the converging fluid elements from bubble interface – when the bubble comes to a sudden halt during compression phase of radial motion. This phenomenon is typical for cavitation bubbles that contain non–condensable gas. As the bubble is compressed, the pressure inside the bubble rises drastically. At certain point of time, when the inertial force of fluid elements outside the bubble and the pressure force of non–condensable gas inside the bubble balance, the bubble comes to a sudden halt. However, the fluid elements outside the bubble are still converging towards the bubble interface at very high speed. These fluid elements are reflected back from the bubble interface, which gives rise to a “shock” or “acoustic” wave with high pressure amplitude. These waves have several effects, especially in liquid–liquid or solid–liquid heterogeneous reaction systems, which help in enhancement of the kinetics of

the process. For liquid–liquid heterogeneous system, the shock waves can give fine emulsification between phases, while for solid–liquid system, the shock waves can give particle size reduction or cleaning of the catalyst surface by desorption of product / catalyst poison from the surface.

The magnitudes of both micro–turbulence and shock waves can be calculated from numerical result of bubble dynamics model as follows (Leighton, 1994; Grossmann et al., 1997; Moholkar and Warmoeskerken, 2003):

Micro–convection: $V_{turb}(r,t) = \frac{R^2}{r^2}\left(\frac{dR}{dt}\right)$

Shock Waves (or Acoustic Waves): $P_{AW}(r,t) = \frac{\rho}{4\pi r}\frac{d^2V_b}{dt^2} = \rho\frac{R}{r}\left[2\left(\frac{dR}{dt}\right)^2 + R\frac{d^2R}{dt^2}\right]$

where V_b is the volume of the bubble. A representative value of r is taken as 1 mm.

Micro–streaming due to ultrasound: The small amplitude of yet rapid oscillatory motion of fluid elements as ultrasound wave propagates through the medium is called micro–streaming. This phenomenon also gives rise to intense micro–mixing in the medium. The magnitude of the micro–streaming velocity (u) is dependent on the pressure amplitude (P_A) of the ultrasound wave as: $u = P_A/\rho c$. In the present study, substituting values of P_A as 200 kPa, ρ = 1000 kg/m^3, and c = 1481 m/s, gives u = 0.135 m/s.

Simulations have been conduced for following 4 conditions: (1) Air bubble, atmospheric static pressure; (2) Air bubble, elevated static pressure; (3) Nitrogen bubble, atmospheric static pressure; (4) Nitrogen bubble, elevated static pressure.

2.5 PRELIMINARY EXPERIMENTAL RESULTS

As mentioned in earlier section, we have conducted initial experiments with Acid Red B (ARB) dye to assess the optimum values of process parameters that influence the

decolorization efficiency through sono–Fenton technique. The results of these preliminary experiments are given below:

***Effect of iron catalyst addition*:** To study the effect of this parameter, experiments were carried out with different amounts of $FeSO_4 \cdot 7H_2O$ and H_2O_2 in the ARB dye solution with initial concentration of 30 mg/L (0.06 mM). The effect of variation of dosages of $FeSO_4 \cdot 7H_2O$ (added in the form of solution in Milli–Q water) on decolorization of ARB for a constant concentration of 600 mg/L (5.292×10^{-3} M) of H_2O_2 is shown in Fig. 2.3A. The amount of $FeSO_4 \cdot 7H_2O$ is varied in the range 20 – 600 mg/L (corresponding to concentration of 7.193×10^{-5} M – 2.158×10^{-3} M as Fe^{2+} ion). As the amount of Fe^{2+} catalyst increases, the decolorization rate initially remains almost same, but a small increase in rate was observed with 600 mg/L (2.158×10^{-3} M as Fe^{2+} ion) addition of iron catalyst. The optimum degradation of ARB was obtained at minimum dosage of 50 mg/L (1.798×10^{-4} M as Fe^{2+} ion) iron catalyst.

***Effect of H_2O_2 concentration*:** The dependence of ARB decolorization on H_2O_2 concentration is shown in Fig. 2.3B. The sono–Fenton process was carried out with different H_2O_2 concentration over a range of 200–1400 mg/L to investigate the optimum condition for decolorization of ARB dye solution with concentration of 30 mg/L (0.06 mM). The experimental results reveal that after a certain concentration of H_2O_2, the degradation rate decreases, as H_2O_2 acts as a radical scavenger, which was also reported by Mishra and Gogate (2011). However, the optimum concentration of 600 mg/L (5.292×10^{-3} M) H_2O_2 was obtained with an initial dye concentration of 30 mg/L (0.06 mM).

***Effect of initial dye concentration*:** The effect of this parameter on decolorization was

assessed using different ARB concentrations (in the range 10–30 mg/L), and the results are shown in Fig. 2.3C. Although the percentage decolorization at all three initial concentrations was similar, for higher initial concentrations of dye, a greater portion of the dye is left in the solution. This essentially means that to achieve same absolute decolorization of solutions, more sonication time is required for higher dye concentrations. On the basis of these results, a dilute concentration of 10 mg/L (0.02 mM) was decided as optimum.

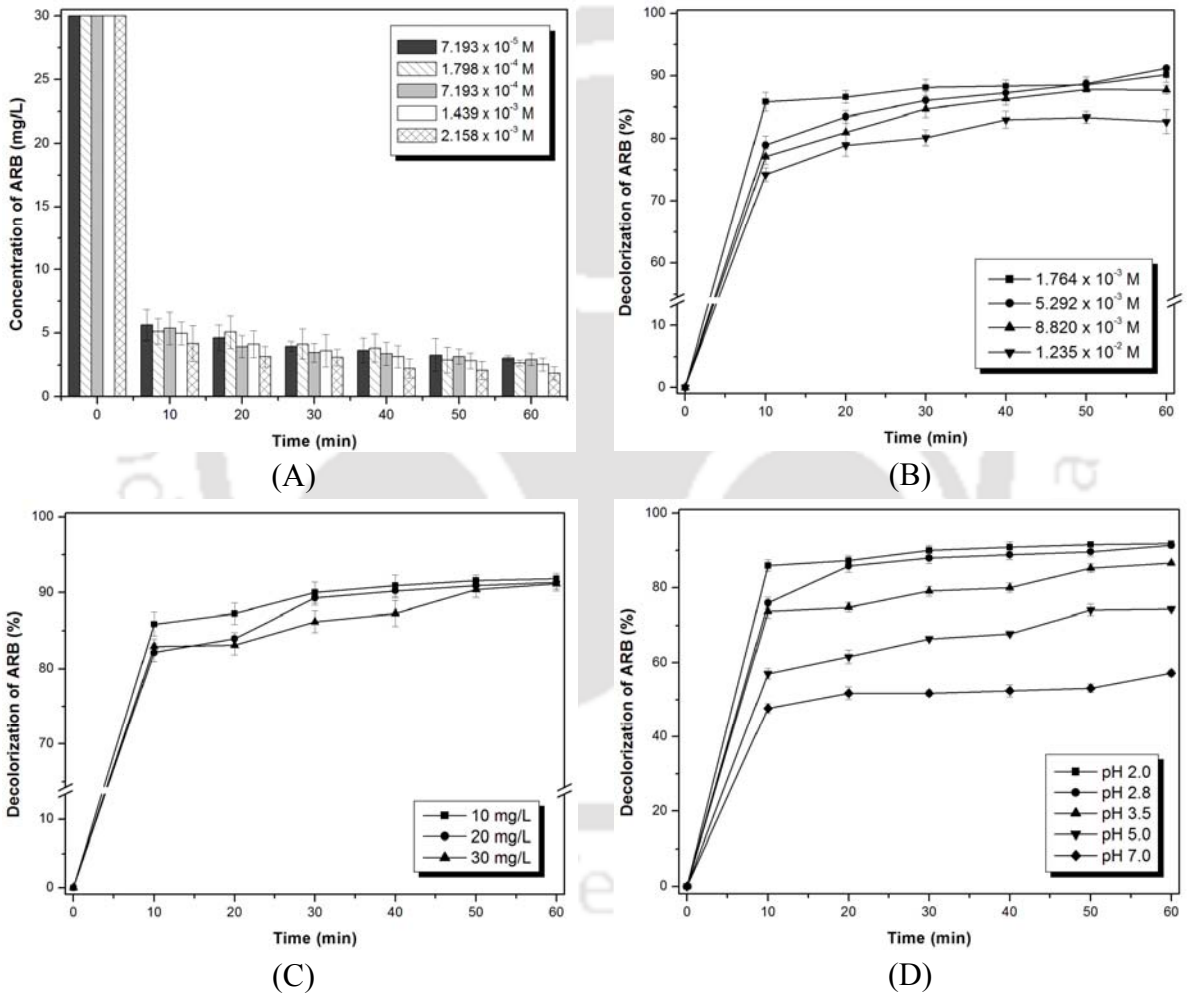

Figure 2.3: Effect of various parameters in sono–Fenton process for dye decolorization. (A) Effect of iron catalyst addition, (B) effect of H_2O_2 concentration, (C) effect of initial dye concentration, and (D) effect of pH on decolorization using sono–Fenton process

***Effect of pH on Fenton reaction*:** A major factor affecting the yield of Fenton reaction is the pH of the medium. The effect of pH on decolorization of ARB is shown in the Fig. 2.3D. At

higher pH value of the reaction mixture, the degradation of ARB decreases as the Fenton reaction is unfavorable at higher pH (due to reduced regeneration of Fe^{2+} ions). At lower pH (pH 2.0 ± 0.1), the maximum degradation was obtained (91.8%), while at higher pH (pH 7) the degradation was only around 57.2% with an initial dye concentration of 10 mg/L. On the basis of these results, the optimum pH value for sono–Fenton experiments was decided as 2.

2.6 RESULTS AND DISCUSSION

2.6.1 Experimental results

The time history of decolorization of ARB and BLH dyes during 60 min of reaction is shown in Figs. 2.4 & 2.5, respectively. The decolorization reaction is very fast and it could be seen from Figs. 2.4 & 2.5 that for both dyes, most of the decolorization was achieved in the first 10 min of treatment in the categories involving Fenton reagent. Therefore, in Figs. 2.4 & 2.5, we have separately depicted the trends in decolorization of both dyes for the first 10 min in Figs. 2.4(A.2), 2.4(B.2), 2.5(A.2) and 2.5(B.2), with analysis of samples that were withdrawn every 2 min. The summary of the decolorization experiments is given in Table 2.2, which gives the extent of decolorization at the end of 10 min as well as 60 min. The time history of decolorization in the first 10 min was fitted to pseudo 1^{st} order kinetics to determine the kinetic constant of decolorization. We would like to state that we have not explicitly determined the order of the decolorization reaction. The decolorization process (which essentially is the oxidation of the dye molecules induced by radicals produced during sonication and Fenton reaction) occurs through series of reactions with several intermediates. Each of the reaction in decolorization chain will have its own order and rate constant.

In view of this difficulty, and the limitations of instrumentation used in the study, we have made a simple approximation of 1^{st} order overall reaction behavior, to get a relative idea of the kinetics of decolorization under different experimental conditions. Since most of the

decolorization in experiments employing Fenton reagent occurred within first 10 min, the 1st order kinetic constant for these experiments was calculated only with the decolorization data for 10 min. The fitness of the pseudo 1st order kinetic model to the experimental data is represented by the regression coefficient (R^2), which is also mentioned in Table 2.2. For most cases, the value of R^2 was greater than 0.8, which indicates suitability of the pseudo 1st order kinetics for the time data of decolorization.

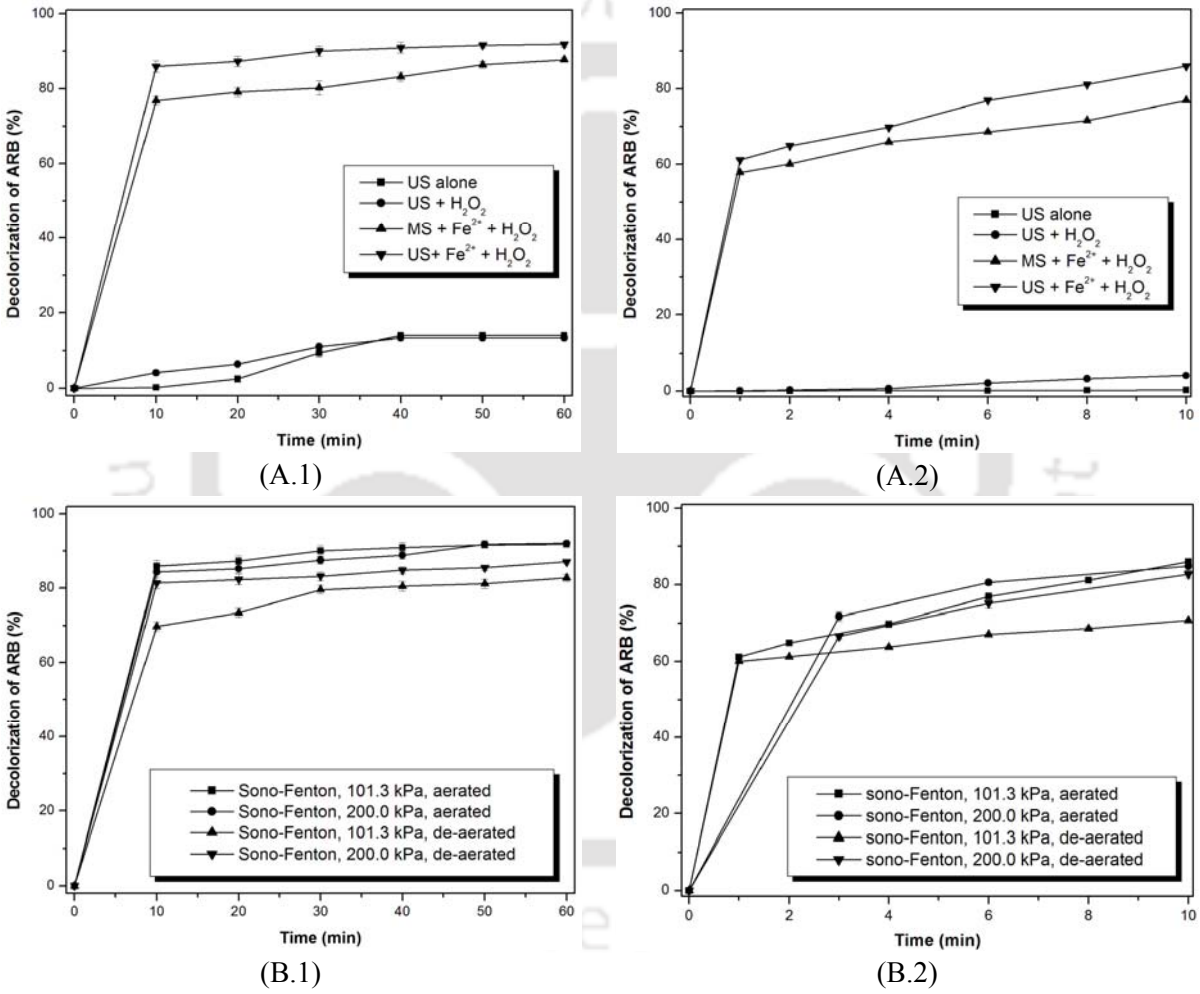

Figure 2.4: Experimental results for decolorization of ARB dye solution (10 mg/L). (A) Decolorization under different combinations of ultrasound and Fenton reagents at atmospheric static pressure (A.1 – the time history of total 60 min reaction, A.2 – trends of decolorization in the initial 10 min). (B) Effect of static pressure on decolorization by sono–Fenton process (B.1 – the time history of total 60 min reaction, B.2 – trends of decolorization in the initial 10 min).

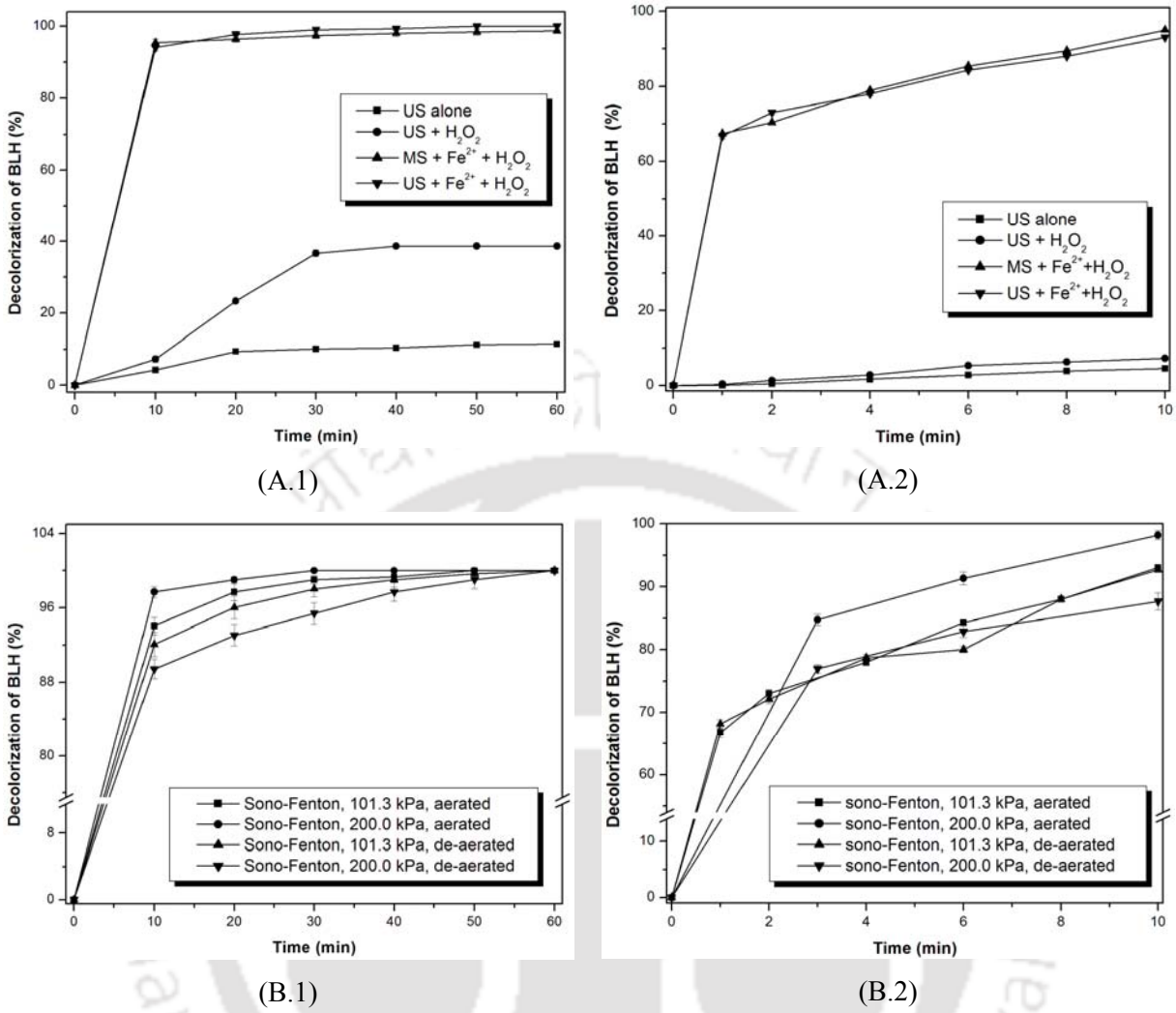

Figure 2.5: Experimental results for decolorization of BLH dye solution (10 mg/L). (A) Decolorization under different combinations of ultrasound and Fenton reagents at atmospheric static pressure (A.1 – the time history of total 60 min reaction, A.2 – trends of decolorization in the initial 10 min). (B) Effect of static pressure on decolorization by sono–Fenton process (B.1 – the time history of total 60 min reaction, B.2 – trends of decolorization in the initial 10 min).

For categories involving only sonication or sonication with H_2O_2, the rate of degradation/ decolorization was linear up to 30 min of treatment, and reduced to zero thereafter. Some other observations are as follows:

- Comparing between the two dyes in all categories of experiments, we see higher decolorization for the BLH dye, which is a non–azo category dye.

- The total decolorization obtained for both dyes for categories involving Fenton reagents was significantly higher than the categories where either sonication alone or sonication with H_2O_2 was applied.
- The decolorization kinetics as well as total decolorization obtained with Fenton reagent coupled with either mechanical stirring or ultrasound was similar.
- In case of sonication experiments, addition of H_2O_2 to the dye solution alone does not seem to cause any major change in extent of decolorization of the ARB dye, although a marginal enhancement in decolorization of the BLH dye is seen.

For the sono–Fenton process in aerated dye solution (i.e. category 4 and 5 of experiments), the extent of decolorization for both dyes is same for both atmospheric as well as elevated static pressure. Quite interestingly, in experimental categories 6 and 7, the extent of decolorization by the sono–Fenton process (at both atmospheric and elevated static pressure) reduces marginally with de–aeration (or essentially de–oxygenation) of the medium for the ARB dye. On the other hand, the decolorization of the BLH dye remains unaffected by the de–aeration of the medium.

Table 2.2: Summary of experimental results of dye decolorization

Experimental categories and conditions / composition of reaction mixture in each category	ARB dye (10 mg/L)			BLH dye (10 mg/L)		
	η (%)*		k_1 (min^{-1})	η (%)*		k_1 (min^{-1})
	10 min	60 min		10 min	60 min	
(1) Sonication alone (50 mL dye solution of concn.10 mg/L, P_o = 101.3 kPa)	0.20 ± 0.14	14.04 ± 0.04	0.0003 (R^2 = 0.96)	4.24 ± 0.38	11.43 ± 0.38	0.0047 (R^2 = 0.98)
(2) Stirring + Fenton (50 mL dye solution of concn. 10 mg/L + 2.5 mg $FeSO_4{\cdot}7H_2O$ + 27 µL 30% H_2O_2, P_o = 101.3 kPa)	76.81 ± 1.20	87.72 ± 0.68	0.2 (R^2 = 0.65)	95.38 ± 0.99	98.68 ± 0.38	0.33 (R^2 = 0.87)
(3) Sonication + H_2O_2 (50 mL dye solution of 10 mg/L concn. + 27 µL 30% H_2O_2, P_o = 101.3 kPa)	4.12 ± 0.70	13.35 ± 0.37	0.004 (R^2 = 0.91)	7.24 ± 0.94	38.59 ± 0.29	0.0079 (R^2 = 0.98)
(4) Sonication + Fenton (50 mL dye solution of 10 mg/L concn. + 2.5 mg $FeSO_4{\cdot}7H_2O$ + 27 µL 30% H_2O_2, P_o = 101.3 kPa)	85.9 ± 1.55	91.81 ± 0.73	0.25 (R^2 = 0.77)	94.06 ± 0.91	100.0 ± 0	0.31 (R^2 = 0.81)
(5) Sonication + Fenton (50 mL dye solution of 10 mg/L concn. + 2.5 mg $FeSO_4{\cdot}7H_2O$ + 27 µL 30% H_2O_2, P_o = 200 kPa)	84.31 ± 1.43	92.04 ± 0.53	0.24 (R^2 = 0.81)	97.69 ± 0.58	100.0 ± 0	0.42 (R^2 = 0.96)
(6) Sonication + Fenton (deaerated solution#, 50 mL dye solution of 10 mg/L concn. + 2.5 mg $FeSO_4{\cdot}7H_2O$ + 27 µL 30% H_2O_2, P_o = 101.3 kPa)	69.76 ± 1.21	82.72 ± 0.93	0.2 (R^2 = 0.51)	92.08 ± 1.3	100.0 ± 0	0.31 (R^2 = 0.8)
(7) Sonication + Fenton (deaerated solution#, 50 mL dye solution of 10 mg/L concn. + 2.5 mg $FeSO_4{\cdot}7H_2O$ + 27 µL 30% H_2O_2, P_o = 200 kPa)	81.35 ± 1.52	87.04 ± 0.53	0.21 (R^2 = 0.85)	89.44 ± 1.07	100.0 ± 0	0.27 (R^2 = 0.79)

* Initial pH of dye solution in all experiments was 2.0. The decolorization efficiency (η in %, as defined in subsection Experimental Procedure) and the kinetic constant for each experimental category refers to the mean value ± standard deviation of the three experimental runs in that category. # – De–aeration to 2 mg/L of dissolved oxygen achieved using sparging the dye solution with nitrogen at flow rate of 40 lit/h. P_o – static pressure on the medium. k_1 – pseudo 1st order kinetic constant calculated on the basis of decolorization obtained in the first 10 min of the reaction. R^2 – the regression coefficient

2.6.2 Simulations results

As stated earlier, the simulations were carried out for four conditions for air and nitrogen bubble. Representative simulations results for air bubble at atmospheric static pressure are shown in Figs. 2.6–2.9. The summary of the simulations results is given in Table 2.3 that lists the peak conditions of temperature and pressure reached in the bubble at moment transient collapse, the magnitudes of the micro–convection velocity and the acoustic wave generated by the cavitation bubble, and the equilibrium composition of chemical species generated from dissociation of gas and water vapor inside the bubble at the moment of transient collapse. From these results, we can identify some peculiar features of the cavitation bubble dynamics at the conditions used in the experiments.

(1) Both air and nitrogen bubbles undergo intense collapse at atmospheric static pressure. The peak conditions reached in the nitrogen bubble are more intense than air bubble. The velocity of micro–convection generated by both bubbles is similar, but the acoustic waves emitted by nitrogen bubble are stronger than those by the air bubble. The extent of water vapor entrapment in nitrogen bubble is higher than air bubble.

(2) Quite interestingly, although the peak conditions of temperature and pressure reached during transient collapse of air bubbles are lower than nitrogen bubble, the radical production by air bubble is higher. The number of oxidizing radicals ($^{\bullet}O$, $HO_2^{\bullet}$ and $^{\bullet}OH$) produced by the air bubble at least two fold higher. We attribute this result to the presence of oxygen in air bubble that conserves the radicals formed out of dissociation of water vapor (Sivasankar and Moholkar, 2009a, 2009b).

(3) With rise in static pressure to 200 kPa (or 2 bar), both chemical and physical effects of cavitation bubbles get eliminated. The radical production in both bubbles becomes practically nil, and the magnitudes of the micro–convection velocity and pressure amplitude of the acoustic wave reduces drastically. This essentially means that the contribution of

transient cavitation to the overall decolorization process is eliminated with rise in static pressure. Application of high static pressure in the medium (greater or equal to the acoustic pressure amplitude) can help in segregation of the effects of ultrasound and transient cavitation in the medium.

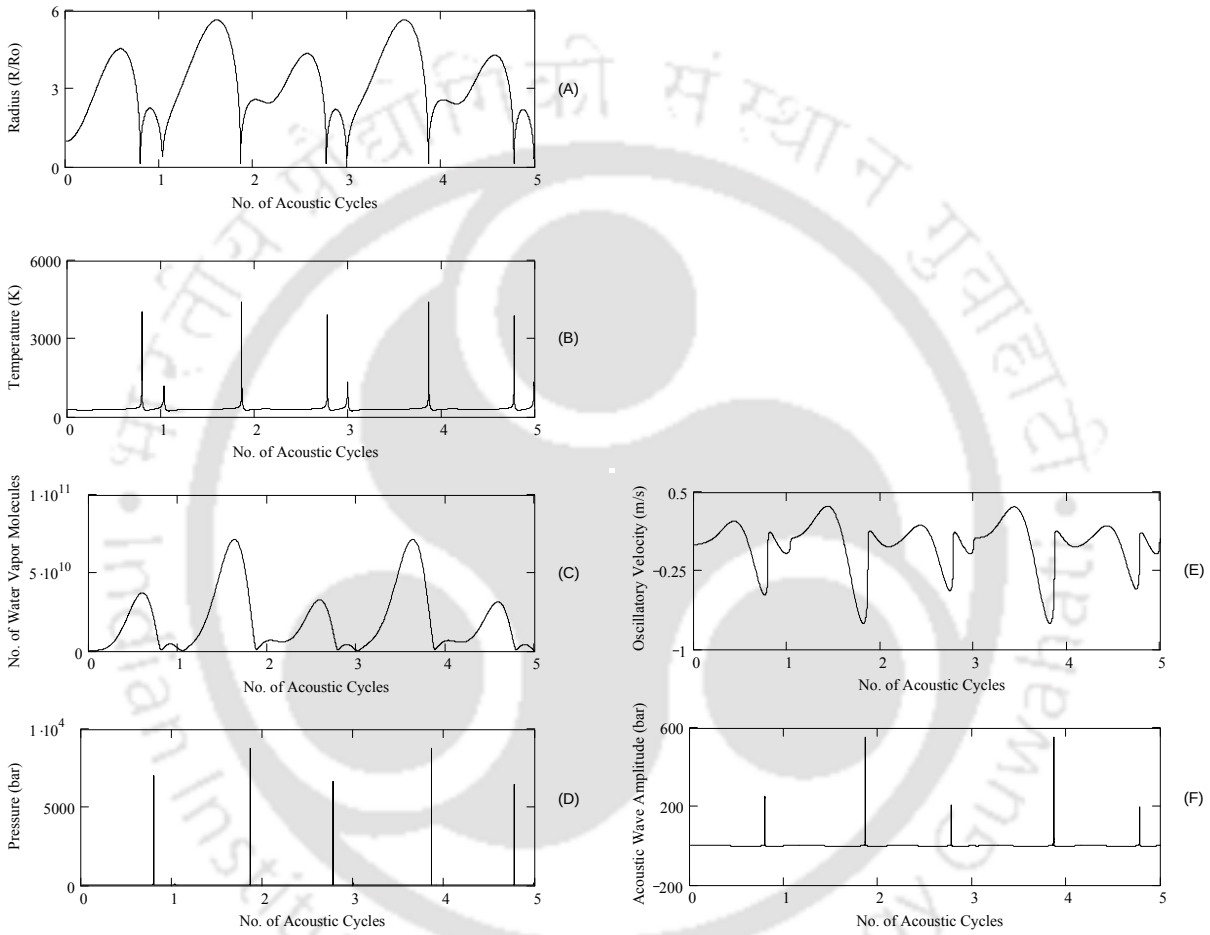

Figure 2.6: Simulations of radial motion of a 5 μm air bubble in water. f = 40 kHz, P_A = 190 kPa, P_o = 101.3 kPa (atmospheric). Time history of (A) radius of the bubble, (B) temperature inside the bubble, (C) water vapor evaporation in the bubble, (D) pressure inside the bubble, (E) micro–turbulence generated by the bubble, and (F) acoustic waves emitted by the bubble.

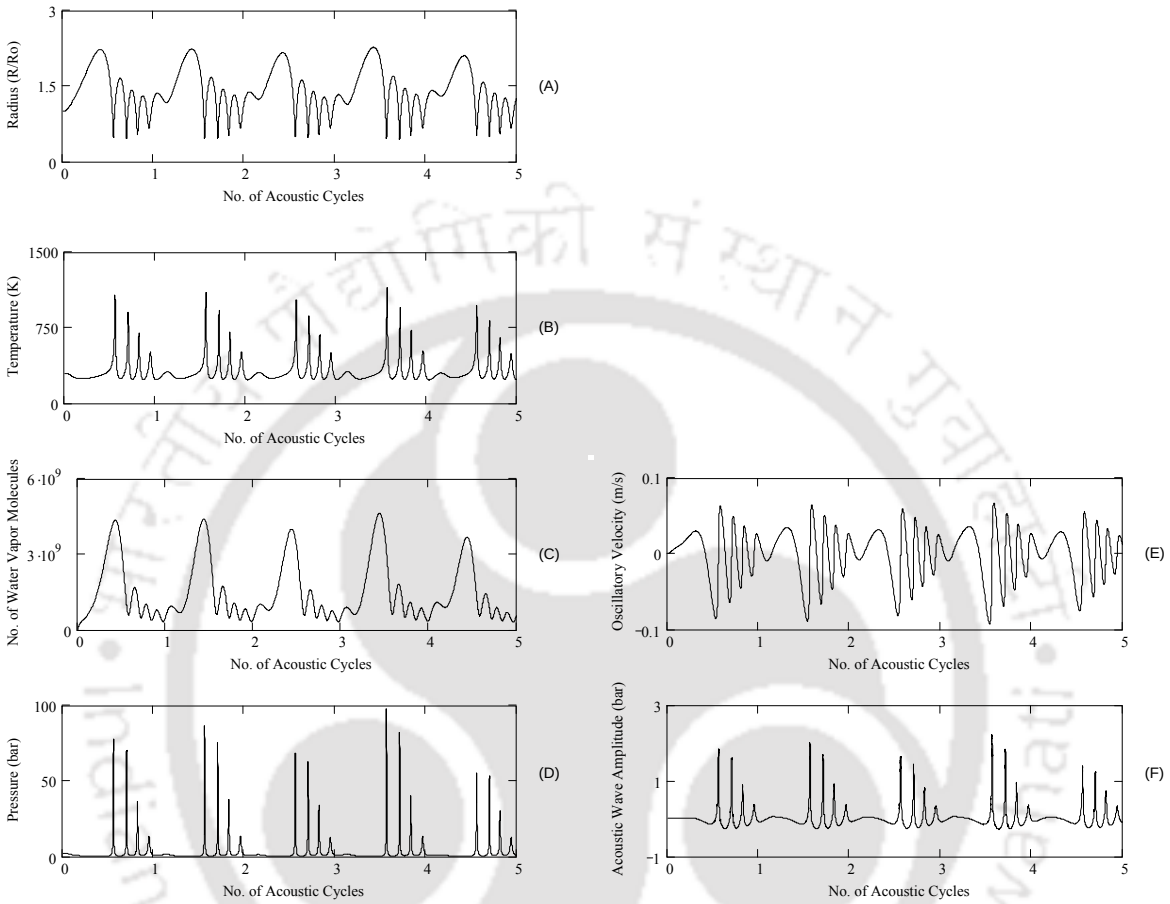

Figure 2.7: Simulations of radial motion of a 5 μm air bubble in water. f = 40 kHz; P_A = 190 kPa; P_o = 200 kPa (elevated). Time history of (A) radius of the bubble; (B) temperature inside the bubble; (C) water vapor evaporation in the bubble; (D) pressure inside the bubble (E) microturbulence generated by the bubble; (F) acoustic waves emitted by the bubble.

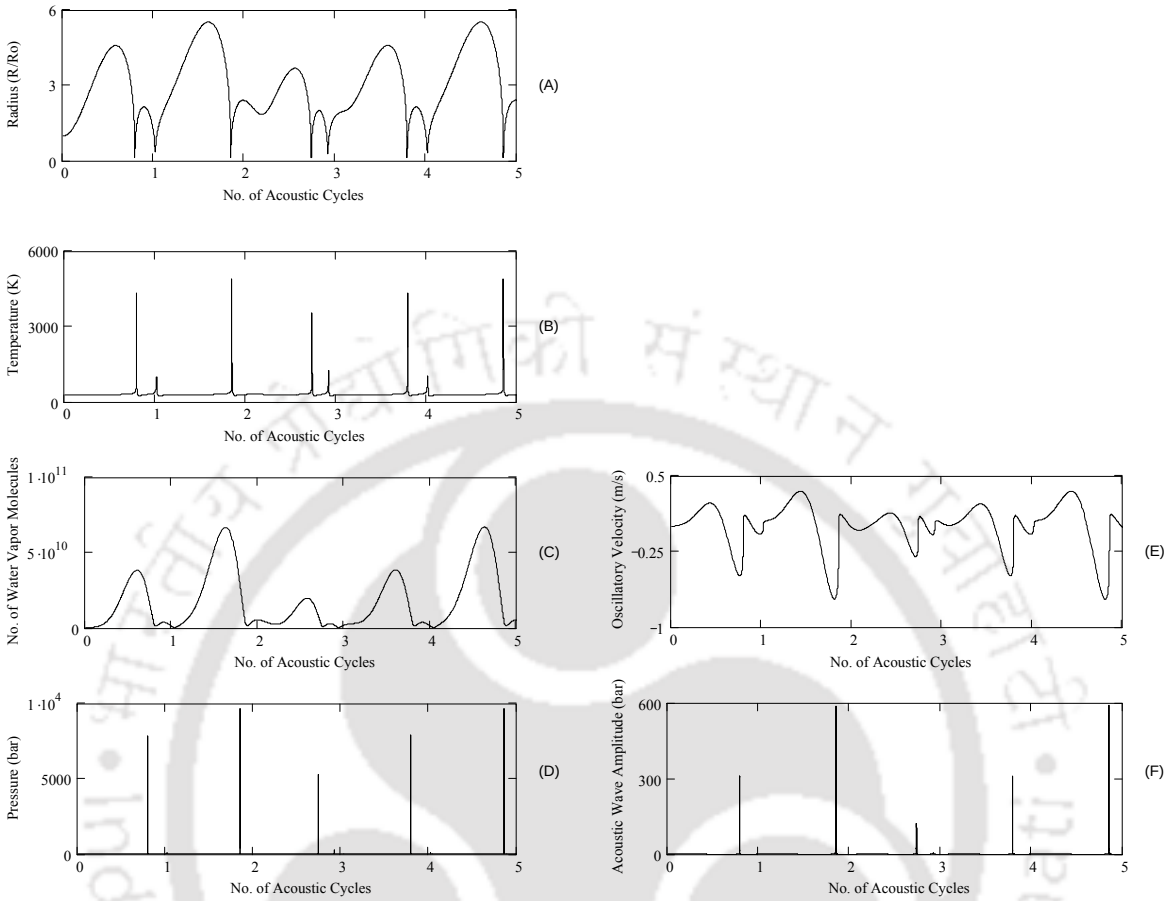

Figure 2.8: Simulations of radial motion of a 5 μm nitrogen bubble in water. f = 40 kHz; P_A = 190 kPa; P_o = 101.3 kPa (atmospheric). Time history of (A) radius of the bubble; (B) temperature inside the bubble; (C) water vapor evaporation in the bubble; (D) pressure inside the bubble (E) microturbulence generated by the bubble; (F) acoustic waves emitted by the bubble.

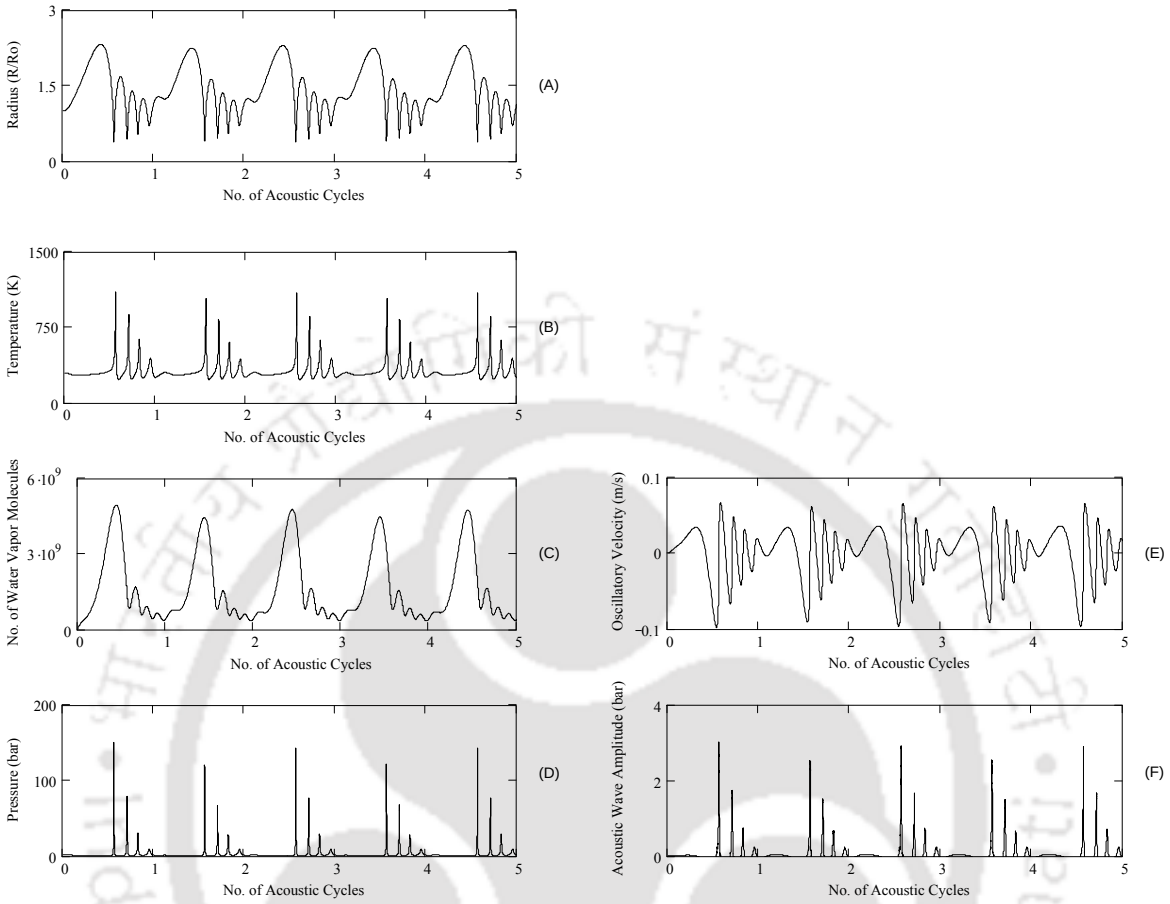

Figure 2.9: Simulations of radial motion of a 5 μm nitrogen bubble in water. f = 40 kHz; P_A = 190 kPa; P_o = 200 kPa (elevated). Time history of (A) radius of the bubble; (B) temperature inside the bubble; (C) water vapor evaporation in the bubble; (D) pressure inside the bubble, (E) microturbulence generated by the bubble; (F) acoustic waves emitted by the bubble.

Table 2.3: (A) Summary of the simulation results (Air and N_2 Bubbles)

	Parameters for simulations			
	Air bubble R_o = 5 μm P_o = 101.3 kPa	Air bubble R_o = 5 μm P_o = 200 kPa	Nitrogen bubble R_o = 5 μm P_o = 101.3 kPa	Nitrogen bubble R_o = 5 μm P_o = 200 kPa
	Conditions at the first collapse of the bubble			
Species	T_{max} = 4013 K P_{max} = 705.6 MPa V_{turb} = 0.056 m/s P_{AW} = 2.53 MPa	T_{max} = 1075 K P_{max} = 7.78 MPa V_{turb} = 0.008 m/s P_{AW} = 0.22 MPa	T_{max} = 4345 K P_{max} = 786.6 MPa V_{turb} = 0.054 m/s P_{AW} = 5.89 MPa	T_{max} = 1106 K P_{max} = 15 MPa V_{turb} = 0.008 m/s P_{AW} = 0.3 MPa
	N_{N2} = 1.306E+10 N_{O2} = 3.471E+9 N_W = 2.026E+9	N_{N2} = 1.306E+10 N_{O2} = 3.471E+9 N_W = 9.03E+8	N_{N2} = 1.653E+10 N_W = 2.872E+9	N_{N2} = 1.653E+10 N_W = 1.28E+9
	Equilibrium composition of species in the bubble at collapse			
N_2	6.52E–01	7.49E–01	8.26E–01	9.28E–01
O_2	1.30E–01	1.99E–01	2.29E–03	0.
H_2O	9.21E–02	5.20E–02	1.08E–01	7.20E–02
H	8.15E–04	0.	5.08E–03	0.
O	6.50E–03	0.	1.47E–03	0.
OH	2.56E–02	1.12E–07	1.42E–02	0.
HO_2	1.11E–03	0.	8.12E–05	0.
H_2O_2	1.69E–04	0.	3.65E–05	0.
O_3	1.67E–05	0.	5.75E–08	0.
H_2	1.79E–03	0.	2.68E–02	6.74E–08
NO	8.79E–02	7.13E–05	1.61E–02	3.11E–08
NO_2	1.67E–03	1.98E–05	3.76E–05	0.
HNO	1.55E–04	0.	1.18E–04	0.
HNO_2	1.16E–05	0.	8.73E–07	0.
HNO_3	1.58E–06	0.	1.48E–08	0.
NH_3	1.89E–06	0.	1.24E–04	0.

(B) Net production of various oxidizing species per bubble

Parameter	**Air bubble (P_o = 101.3 kPa)**	**Air bubble (P_o = 200 kPa)**	**N_2 bubble (P_o = 101.3 kPa)**	**N_2 bubble (P_o = 200 kPa)**
N_{OH}	4.75E+08	1.95E+3	2.75E+08	0.
N_O	1.2E+08	0.	2.85E+07	0.
N_{HO2}	2.06E+07	0.	1.58E+06	0.
N_{H2O2}	3.14E+06	0.	7.08E+05	0.

Notation for Table 2.3: 4.75E+08 should read as 4.75×10^8, P_o – static pressure in the liquid medium; R_o – initial radius of the cavitation bubble; V_{turb} – average velocity of the micro–turbulence in the medium generated by ultrasound and cavitation in the medium (estimated at 1 mm distance from bubble center); P_{AW} – pressure amplitude of the acoustic wave generated by the cavitation bubble; T_{max} – temperature peak reached in the bubble at the time of first collapse; P_{max} – pressure peak reached in the bubble at the time of first collapse; N_W – number of water molecules trapped in the bubble; N_{N2} – number of N_2 molecules in the bubble; N_{O2} – number of

oxygen molecules in the bubble; N_{OH} – number of •OH radicals present in the bubble at transient collapse; N_H – number of H radicals present in the bubble at transient collapse; N_O – number of O radicals present in the bubble at transient collapse; N_{HO2} – number of HO_2 radicals present in the bubble at transient collapse; N_{H2O2} – number of H_2O_2 molecules present in the bubble at transient collapse

2.6.3 Analysis and discernment of the synergy in sono–Fenton process

Analysis of the experimental and simulation results concurrently helps us to discern the mechanism of the hybrid sono–Fenton process, and also identify the links between individual (and seeming independent) mechanism of sonochemical and Fenton processes. Comparison of results of categories 1 and 2, where the two techniques were applied separately, shows that contribution of Fenton process to overall decolorization is much higher than sonolysis. Comparison of decolorization obtained in categories 2 and 4 indicates a very small rise in decolorization with sono–Fenton process, as compared to Fenton process alone. Practically same decolorization as in category 4 is obtained in category 5, in which the contribution of transient cavitation effect is eliminated at elevated static pressure. These results are clearly indicative of the dominant role played by Fenton process over the sonochemical process. The most probable cause leading to this effect is scavenging of the $^{\bullet}OH$ radicals generated by the cavitation bubbles by the H_2O_2 through following reactions,[26] which leads to formation of molecular species causing reduction in the oxidation or decolorization potential.

$$^{\bullet}OH + H_2O_2 \longrightarrow H_2O + HO_2^{\bullet} \qquad (2.7)$$

$$H^{\bullet} + H_2O_2 \longrightarrow HO_2^{\bullet} + H_2 \qquad (2.8)$$

$$HO_2^{\bullet} + {}^{\bullet}OH \longrightarrow O_2 + H_2O \qquad (2.9)$$

The synergy in sonochemical and Fenton process thus seems to be negative.

Another factor leading to smaller contribution of sonolysis in the sono–Fenton process is the discrete nature of production of $^{\bullet}OH$ radicals by cavitation bubbles. The population or number density of cavitation bubbles in the medium is not likely to be uniform

volumetrically, and so is the production of $^{\bullet}OH$ radicals through transient cavitation events. The concentration of dye molecules in the solution is relatively small (10 mg/L), and hence, the probability of dye–radical interaction also comes into picture. Discrete production of $^{\bullet}OH$ radicals in the reaction volume, together with low concentration of dye can lead to lower utilization of the radicals produced by transient cavitation events for decolorization. The dissolved oxygen in the medium is revealed to play major role. The oxygen can conserve $^{\bullet}OH$ radicals to generate other oxidizing species like $^{\bullet}O$ and $^{\bullet}HO_2$ through reaction (Gri–Mech, http://www.me.berkeley.edu/gri–mech/data/frames.html):

$$^{\bullet}OH + O_2 \longrightarrow HO_2^{\bullet} + O^{\bullet} \qquad (2.10)$$

At lower concentration of dissolved oxygen (with de–aeration of the medium), as in experimental category 6 & 7, the conservation action is reduced, which eventually results in loss of radicals resulting in lower decolorization.

2.7 CONCLUSION

In this study, we have attempted to discern the mechanism of the hybrid sono–Fenton process for decolorization of the textile dyes. The concurrent analysis of experimental results with the simulations of cavitation bubble dynamics reveals the links and interactions between the individual mechanism of sonolysis and Fenton process. H_2O_2 added to the medium as one of the Fenton reagent scavenges the $^{\bullet}OH$ radicals produced by cavitation bubbles, which nullifies their effect, giving a negative synergy between sonolysis and Fenton process. Mere addition of H_2O_2 to the medium during sonolysis does not give much enhancement to decolorization, which is attributed to lower vapor pressure of H_2O_2 due to which it does not evaporate and dissociate inside the bubble (to generate additional $^{\bullet}OH$ radicals). Fenton reagent (Fe^{2+} + H_2O_2), on the other hand, gives volumetrically more uniform production of $^{\bullet}OH$ radicals in the solution, and hence, has a dominating contribution to decolorization in the

hybrid process. The role of ultrasound and cavitation in the hybrid sono–Fenton process is simply physical, i.e. causing intense mixing in the medium. Radical conservation due to dissolved oxygen is also revealed to play a major role in effective utilization of $^{\bullet}OH$ radicals for decolorization.

REFERENCES

Andreozzi R, Caprio V, Insola A, Marotta R, Advanced oxidation processes (AOP) for water purification and recovery, Catal. Today 53 (1999) 51–59.

Babuponnusami A, Muthukumar K, Advanced oxidation of phenol: A comparison between Fenton, electro–Fenton, sono–electro–Fenton and photo–electro–Fenton processes, Chem. Eng. J. 183 (2012) 1–9.

Bianchi CL, Pirola C, Ragaini V, Selli E, Mechanism and efficiency of atrazine degradation under combined oxidation processes, Appl. Catal. B Environ. 64 (2006) 131–138.

Bremner DH, Molina R, Martínez F, Melero JA, Segura Y, Degradation of phenolic aqueous solutions by high frequency sono–Fenton systems (US–Fe_2O_3/SBA–15–H_2O_2), Appl. Catal. B Environ. 90 (2009) 380–388.

Brenner M, Hilgenfeldt S, Lohse D, Single–bubble sonoluminescence. Rev. Mod. Phys. 74 (2002) 425–484.

Chakma S, Moholkar VS, Mechanistic features of ultrasonic desorption of aromatic pollutants, Chem. Eng. J. 175 (2011) 356– 367.

Chemical Equilibrium Calculation (Bioanalytical Microfluidics Program, Colorado State University). Website: http://navier.engr.colostate.edu/~dandy/code/code–4/index.html (accessed January 2013).

Condon EU, Odishaw H, Handbook of Physics, New York: McGraw Hill, 1958.

Gogate PR, Pandit AB, A review of imperative technologies for wastewater treatment I:

oxidation technologies at ambient conditions, Adv. Environ. Res. 8 (2004a) 501–551.

Gogate PR, Pandit AB, A review of imperative technologies for wastewater treatment II: hybrid methods, Adv. Environ. Res. 8 (2004b) 553–597.

Grčić I, Šipić A, Koprivanac N, Domagoj V, Global parameter of ultrasound exploitation (GPUE) in the reactors for wastewater treatment by sono–Fenton oxidation, Ultrason. Sonochem. 19 (2012) 270–279.

Gri–MechTM, Reaction rate coefficients (Authors: M. Frenklach, T. Bowman, G. Smith, B. Gardiner), Website: http://www.me.berkeley.edu/gri–mech/data/frames.html), accessed January 2013.

Grossmann S, Hilgenfeldt S, Zomack M, Lohse D, Sound radiation of 3 MHz driven gas bubbles, J. Acoust. Soc. Am. 102 (1997) 1223–1227.

Hart EJ, Henglein A, Sonochemistry of aqueous solutions: hydrogen–oxygen combustion in cavitation bubbles, J. Phys. Chem. 91 (1987) 3654–3656.

Hirschfelder JO, Curtiss CF, Bird RB, Molecular theory of gases and liquids, New York: Wiley, 1954.

Huang R, Fang Z, Yan X, Cheng W, Heterogeneous sono–Fenton catalytic degradation of bisphenol A by Fe_3O_4 magnetic nanoparticles under neutral condition, Chem. Eng. J. 197 (2012) 242–249.

Keller JB, Miksis MJ, Bubble oscillations of large amplitude, J. Acoust. Soc. Am. 68 (1980) 628–633.

Krishnan JS, Dwivedi P, Moholkar VS, Numerical investigation into the chemistry induced by hydrodynamic cavitation, Ind. Eng. Chem. Res. 45 (2006) 1493–1504.

Kumar KS, Moholkar VS, Conceptual design of a novel hydrodynamic cavitation reactor, Chem. Eng. Sci. 62 (2007) 2698–2711.

Leighton TG, *The Acoustic Bubble*, San Diego: Academic Press, 1994.

Lin JJ, Zhao XS, Liu D, Yu ZG, Zhang Y, Xu H, The decoloration and mineralization of azo dye C.I. Acid Red 14 by sonochemical process: Rate improvement via Fenton's reactions, J. Hazard. Mater. 157 (2008) 541–546.

Mishra KP, Gogate PR, Intensification of degradation of aqueous solutions of rhodamine B using sonochemical reactors at operating capacity of 7 L, J. Environ. Manage. 92 (2011) 1972–1977.

Moholkar VS, Warmoeskerken MMCG, Integrated approach to optimization of an ultrasonic processor, AIChE J. 49 (2003) 2918–2932.

Moholkar VS, Warmoeskerken MMCG, Ohl CD, Prosperetti A, Mechanism of mass–transfer enhancement in textiles by ultrasound, AIChE J. 50 (2004) 58–64.

Molina R, Martínez F, Melero JA, Bremner DH, Chakinala AG, Mineralization of phenol by a heterogeneous ultrasound/ Fe–SBA–15/H_2O_2 process: Multivariate study by factorial design of experiments, Appl. Catal. B Environ. 66 (2006) 198–207.

Oezdemir C, Oeden MK, Sahinkaya S, Kalipci E, Color removal from synthetic textile wastewater by sono–Fenton process, Clean: Soil, Air, Water (2011a) 39:60–67.

Ozdemir C, Oden MK, Sahinkaya S, Guclu D. Guclu, The sonochemical decolorization of textile azo dye CI reactive orange 127, Color Technol. 127 (2011b) 268–273.

Papic S, Vujevć D, Koprivanac N, Šinko D, Decolorization and mineralization of commercial reactive dyes by using homogeneous and heterogeneous Fenton and UV/Fenton process, J. Hazard. Mater. 164 (2009) 1137–1145.

Patidar R, Khanna S, Moholkar VS, Physical features of ultrasound assisted enzymatic degradation of recalcitrant organic pollutants, Ultrason. Sonochem. 19 (2012) 104–118.

Peralta–Zamora P, Kunz A, de Moraes SG, Pelegrini R, de Campos Moleiro P, Reyes J, Duran N, Degradation of reactive dyes I. A comparative study of ozonation, enzymatic and photochemical processes, Chemosphere 38 (1998) 835–852.

Press WH, Teukolsky SA, Flannery BP, Vetterling WT, *Numerical Recipes*, New York: Cambridge University Press, 1992.

Reid RC, Prausnitz JM, Poling BE, Properties of Gases and Liquids, New York: McGraw Hill, 1987.

Segura Y, Martinez F, Melero JA, Molina R, Chand R, Bremner DH, Enhancement of the advanced Fenton process (Fe^0/H_2O_2) by ultrasound for the mineralization of phenol, Appl. Catal. B Environ. 113–114 (2012) 100–106.

Segura Y, Molina R, Martinez F, Melero JA, Integrated heterogeneous sono–photo Fenton processes for the degradation of phenolic aqueous solutions, Ultrason. Sonochem. 16 (2008) 417–424.

Shah YT, Pandit AB, Moholkar VS, *Cavitation Reaction Engineering*, New York: Plenum Press/ Kluwer Academic, 1999.

Sivasankar T, Moholkar VS, Mechanistic approach to intensification of sonochemical degradation of phenol, Chem. Eng. J. 49 (2009a) 57–69.

Sivasankar T, Moholkar VS, Mechanistic features of the sonochemical degradation of organic pollutants, AIChE J. 54 (2008) 2206–2219.

Sivasankar T, Moholkar VS, Physical insights into the sonochemical degradation of recalcitrant organic pollutants with cavitation bubble dynamics, Ultrason. Sonochem. 16 (2009b) 769–781.

Sivasankar T, Paunikar AW, Moholkar VS, Mechanistic approach to enhancement of the yield of a sonochemical reaction, AIChE J. 53 (2007) 1132–1143.

Storey BD, Szeri AJ, Water vapor, sonoluminescence and sonochemistry, Proc. R. Soc. Lond. Ser. A 456 (2000) 1685–1709.

Sundararaman TR, Ramamurthi V, Partha N, Decolorization and COD removal of Reactive yellow 16 by Fenton oxidation and comparison of dye removal with photo Fenton and

sono Fenton process, Mod. Appl. Sci. 3 (2009) 15–22.

Suslick KS, Sonochemistry, Science 247 (1990) 1439–1445.

Toegel R, Gompf B, Pecha R, Lohse D, Does water vapor prevent upscaling sonoluminescence?, Phys. Rev. Lett. 85 (2000) 3165–3168.

Wu CH, Decolorization of C.I. Reactive Red 2 in O_3, Fenton–like and O_3/Fenton–like hybrid systems, Dyes Pigm. 77 (2008) 24–30.

Zhong X, Royer S, Zhang H, Huang Q, Xiang L, Valange S, Barrault J, Mesoporous silica iron–doped as stable and efficient heterogeneous catalyst for the degradation of C.I. Acid Orange 7 using sono–photo–Fenton process, Sep. Purif. Technol. 80 (2011) 163–171.

3

PHYSICAL MECHANISM OF HYBRID AOP SONOLYSIS + FENTON + UV

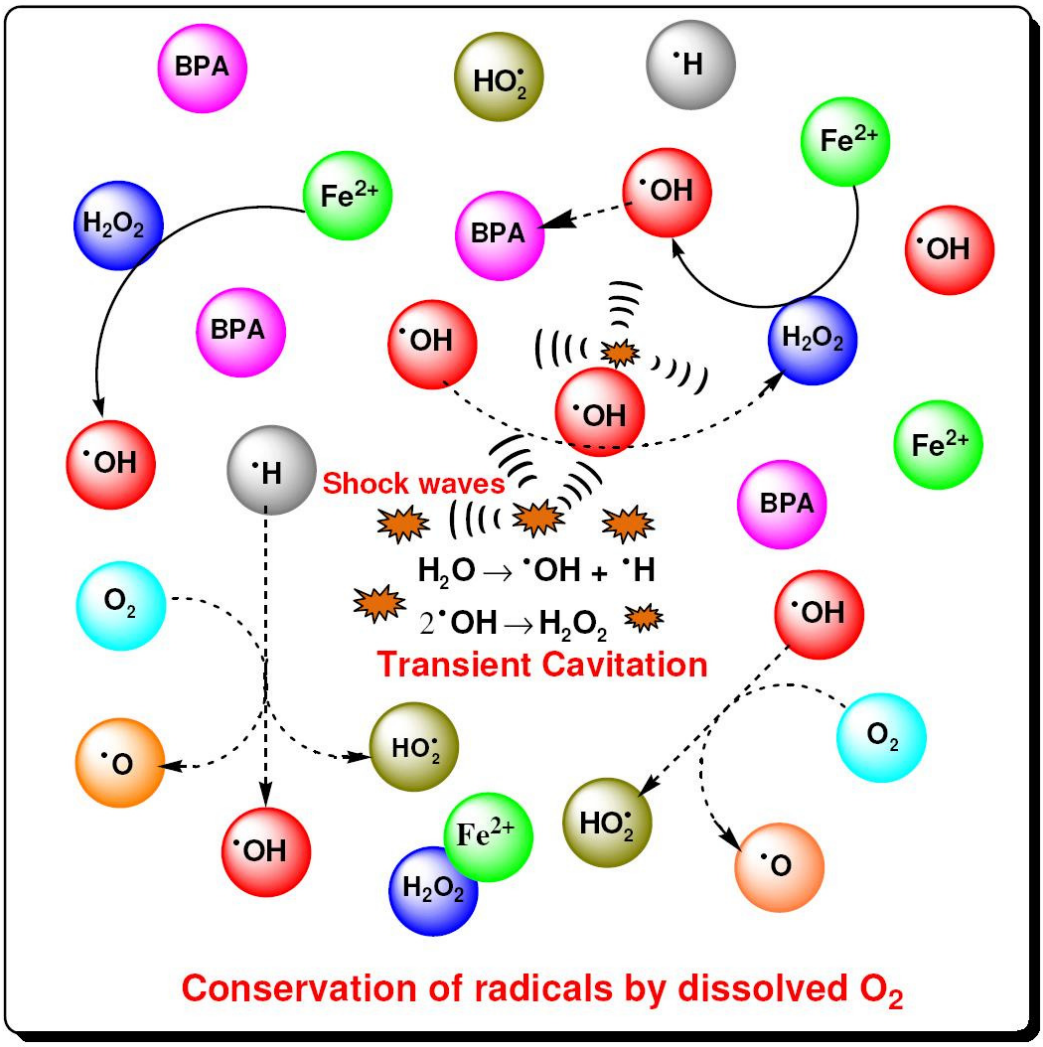

CHAPTER 3

PHYSICAL MECHANISM OF HYBRID AOP SONOLYSIS + FENTON + UV

3.1 INTRODUCTION

In the previous chapter, we presented investigations in physical mechanism of the hybrid AOP of sono-Fenton. This chapter extends this theme with investigations in the synergistic physical mechanisms of different hybrid advanced processes with combination of sonolysis, Fenton reaction and UV irradiation. The hydroxyl-complexes of Fe, which may form during sono-Fenton process are photoactive. Thus, addition of UV to the sono-Fenton helps in utilization of the photo-activity of these complexes for further enhancement of degradation. Bisphenol–A (BPA) has been chosen as the model pollutant. BPA is a highly versatile hydrocarbon molecule that forms major feedstock for epoxy and polycarbonate resins. Epoxy resins are used in surface coatings, laminates, adhesives and composites, while polycarbonates find use in communications and electronics, compact disks and associated equipment and appliances. Due to this ubiquitous application, BPA is released into the environment through many outlets such as landfill leachates and wastewater discharge from paper and plastics industries. According to US Environmental Protection Agency report, the total release of BPA is 1,132,062 pounds; of which 122,965 pounds are released to air, 6,246 pounds to water directly, 14,972 pounds released on-site to land, and 684,638 pounds

transferred off-site to land (Bisphenol-A action plan, 2010). Presence of BPA in landfills and in water bodies like rivers and lakes is of growing concern as BPA can interfere with hormonal activities leading to detrimental effects on the ecosystem and human health. Being a phenolic compound, BPA is not easily degraded by conventional biological processes. With experiments that alter the characteristics of the ultrasound and cavitation phenomena, we have attempted to elucidate the links between the individual mechanisms of the sonolysis and Fenton process coupled with UV irradiation.

3.2 MATERIALS AND METHODS

3.2.1 Materials

The following chemicals have been used in this present study: bisphenol–A, ferrous sulfate heptahydrate ($FeSO_4 \cdot 7H_2O$), hydrogen peroxide (30% v/v), sulfuric acid (98%), titanium dioxide, sodium hydroxide pellets (NaOH), acetonitrile (HPLC grade). All the chemicals were purchased from Merck India and used as received without any further treatment. Ultrapure water (≥ 18 MΩ–cm resistivity at 25^{o}C) from Milli–Q Synthesis unit (Millipore®, USA) was used for preparation of solutions in all experiments.

3.2.2 Experimental setup

The experimental setup for the sono–Fenton process (either at atmospheric or elevated static pressure) was the same as used in our previous studies (Chakma and Moholkar, 2013a, 2011). The experiments with sono–photo–Fenton process were carried out using a 250 mL beaker made of borosilicate glass (height – 116 mm, OD – 62 mm, thickness – 1.5 mm). A blended high pressure mercury UV lamp (Starlite, 160 W) was used for the UV–assisted experiments. This lamp had a maximum peak emission wavelength at 365 nm (UV–A category). However, it also had emissions at other wavelengths. A typical energy distribution

spectrum of a high pressure mercury UV–A lamp (similar to the one used in the present study) is shown in Fig.3.1.

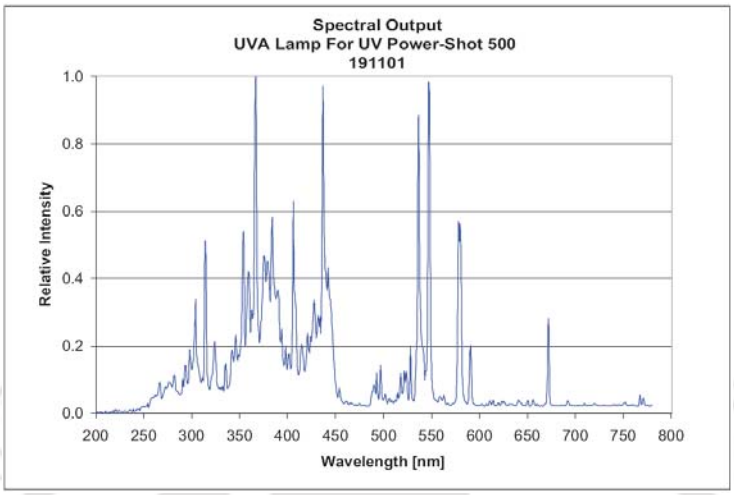

Figure 3.1: Typical spectral energy distribution for the UV lamp of category UV–A. [Source: CureUV.com, http://lib.store.yahoo.net/lib/yhst-12627748266280/dwg-uva-lamp-spectral-output.pdf]

The schematic diagram of the experimental setup is given in Fig. 3.2. The control (or base case) experiments were carried out using a mechanical stirrer operated at 300 rpm. An ultrasound bath (JeioTech, Model: UC–10, Dimensions (LH):) with frequency of 40 kHz and theoretical power of 200 W was used for sonication of the medium. The reaction beaker was placed at the exact center of the bath. Thus, the average distance of the beaker wall from the sides of the bath was 9 cm and 12 cm each. The distance of the beaker from the bottom of the bath was 7 cm. As the acoustic and cavitation intensity in the bath shows significant spatial variation (Gogate et al., 2002), the above parameters were scrupulously maintained constant in all experiments, which would avoid the artifacts. The UV lamp was positioned on the top of the reaction beaker, as shown in the schematic diagram in Fig. 3.2. The distance between the lamp and the surface of the reaction solution in the beaker was 14 cm. We would like to specify that due to relatively smaller reaction volume and also the geometric constraints, the usual arrangement of immersing the UV lamp in the reaction solution in a quartz sleeve could

not be followed. Arrangement of the UV lamp used in the present study may result in relatively small access of UV radiation. However, this effect is uniform in all experiments, and thus, does not affect the relative trends in BPA degradation in different experimental categories.

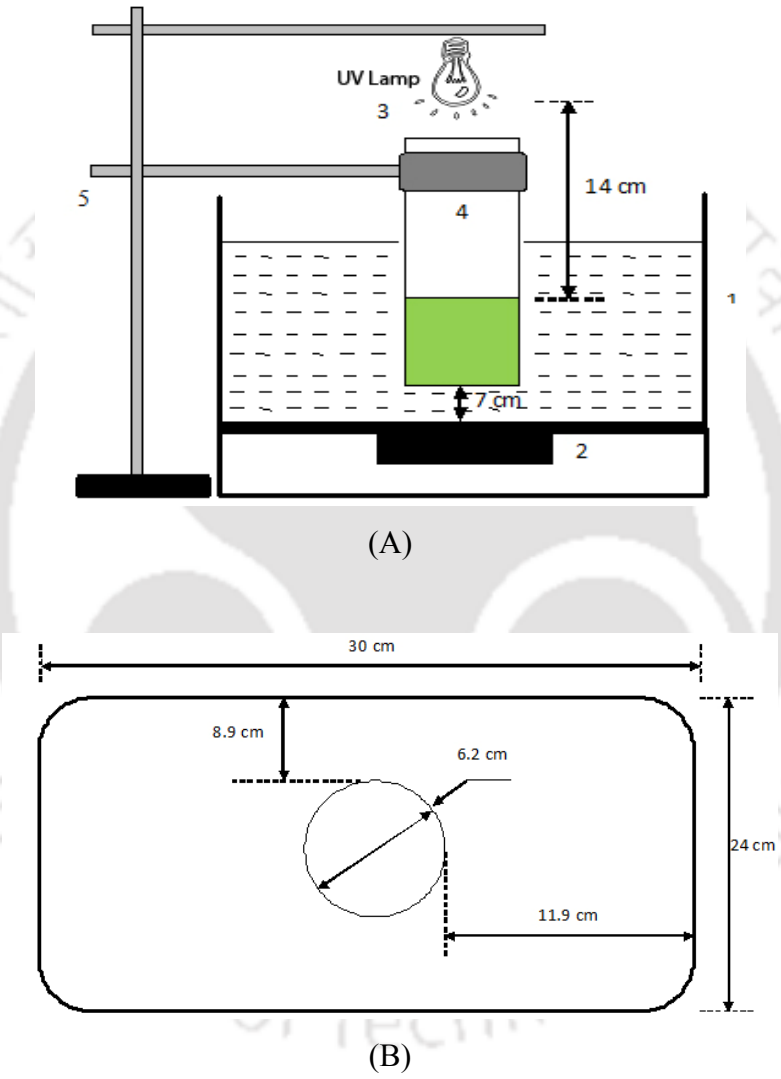

Figure 3.2: Schematic diagram of experimental setup for degradation of Bisphenol–A using sono–Fenton+UV hybrid process. (A) Front view and (B) Top view of the experimental setup. (1) Ultrasound bath, (2) transducer, (3) high pressure mercury UV lamp, (4) beaker for reaction solution, (5) burette stand

The bath was filled with 7 L water that acted as bulk medium for ultrasound. This water was replaced every 10 min to control rise in temperature during sonication. With this

procedure the temperature of the bulk medium was maintained at 25°C (± 2°C) in all experiments. For experiments under an unsaturated or de–aerated medium, the unsaturation was done by the method described by Chakma and Moholkar (2011). For this purpose, the medium (water) was subjected to vacuum for 60 min using a Riviera vacuum pump (Model: TID–25–S) producing a vacuum of 600 mm Hg (or 160 mm Hg pressure) with intense stirring. The acoustic pressure amplitude of the ultrasound waves generated by transducers in the bath was determined using calorimetric technique as ~ 190 kPa or 1.9 bar. This corresponds to the acoustic energy intensity of 1.2 W/cm^2 and a volumetric energy dissipation of 8.71 W/L. The exact calculations of these parameters are given in Annexure-I. Typically, only the cavitation bubbles with initial size much smaller than the resonance size corresponding to the ultrasound frequency of 40 kHz (i.e. 83 μm) undergo transient motion. The initial size of the cavitation bubbles varies significantly. Usually, the cavitation bubbles with initial size in the range of 2 to 10 μm undergo transient motion. Bubbles bigger than these sizes attain buoyancy during their growth in radial motion, and escape the medium; and thus, do not contribute to the sonochemical effect. For bubbles with initial size much smaller than the resonant size, the transient cavitation threshold (i.e. the minimum pressure amplitude of ultrasound wave required for occurrence of transient radial motion) is the static pressure of the medium (Leighton, 1994). Rise in the static pressure of the medium above the pressure amplitude of the ultrasound wave can thus eliminate transient cavitation in the medium. This forms the rationale underlying the experimental category of elevated static pressure, as explained in the subsequent section.

3.2.3 Experimental protocols and analysis

A 100 mg/L stock solution of BPA was prepared and stored in a refrigerator not more than one week. The reaction solution (50 mL) in all experiments was prepared by diluting this

stock solution to 10 mg/L (or 4.3×10^{-2} mM). Experiments were carried out in 10 categories with different protocols, as described in Table 3.1. Prior to the main set of experiments, we have conducted several preliminary experiments, in which the influence of parameters such as initial concentration of Fe^{2+}, initial concentration of H_2O_2 and method of addition of H_2O_2 in the reaction mixture was investigated. On the basis of these experiments, the optimum values of these parameters were decided as: $[Fe^{2+}]$ = 0.36 mM, $[H_2O_2]$ = 7.85 mM. The optimum value of H_2O_2 was limited by the scavenging of the radicals by the excess H_2O_2, while the optimum concentration of Fe^{2+} was decided on the basis of plateau obtained in the extent of degradation with increasing Fe^{2+} concentration. More details about the preliminary experiments are given in the next section (preliminary experimental result). pH value of the reaction mixture was fixed as 2 for Fenton, sono–Fenton or sono–photo–Fenton categories of experiments on the basis of our previous study (Chakma and Moholkar, 2013a). For photo–Fenton and sono–photo–Fenton categories; the UV lamp was placed right above the reaction beaker. Moreover, the whole experimental setup was placed in a black box to avoid light radiation diffusion. Before initiation of UV assisted experiments, the UV lamp was kept switched on for 15 min to establish a uniform UV field in the black box. In the first set of experiments, the degradation of BPA was monitored by withdrawing 1 mL aliquots of reaction mixture every 10 min. However, it was observed that the rate of degradation was very fast in the initial reaction period of 10 min. Hence, in the second set of experiments, the degradation in the initial 10 min was monitored more closely with sample withdrawal period reduced to 2 min. The total time of treatment of BPA solution in all categories of experiments was 60 min. For experiments with elevated static pressure, the pressure in the reaction flask was released during the withdrawal of aliquots of reaction mixture. The pressure was restored prior to re–commencement of sonication. The pH of the aliquots of reaction mixture was adjusted to 7.5–8 so as to terminate the Fenton reaction. This also resulted in formation of

floc of Fe(III). This iron–floc was filtered through a 0.22 μm filter paper for further analysis of BPA. The method for determination of hydrogen peroxide (H_2O_2) generated by cavitation is described in the next section.

Table 3.1: Summary of experimental results

Category of experiment ##		η (%)		k (s^{-1})	R^2
		10 min	60 min		
1	Sonolysis (base case)	4.3 ± 0.38	19.9 ± 0.67	7.66×10^{-5}	0.96
2	Sonolysis + H_2O_2	6.1 ± 3.54	20.0 ± 0.71	1.09×10^{-4}	0.88
3	Sonolysis + Fe^{2+}	16.3 ± 0.53	33.9 ± 1.87	3.18×10^{-4}	0.98
4	MS-Fenton	79.1 ± 0.35	91.2 ± 0.35	3.39×10^{-3}	0.89
5	Sono-Fenton (aerated solution)	89.9 ± 2.24	98.7 ± 1.04	9.22×10^{-3}	0.90
6	Sono-Fenton (de-aerated solution)	86.5 ± 1.1	98.7 ± 1.09	4.98×10^{-3}	0.98
7	Sono-Fenton (aerated solution, P_o = 200 kPa)	87.6 ± 2.77	98.7 ± 0.35	3.67×10^{-3}	0.99
8	Sono-Fenton (de-aerated solution, P_o = 200 kPa)	87.3 ± 0.63	95.2 ± 0.40	3.2×10^{-3}	0.99
9	MS-Fenton + UV*	76.5 ± 3.38	91.9 ± 1.86	4.76×10^{-3}	0.95
10	Sono-Fenton + UV*	62.7 ± 3.21	86.5 ± 0.93	2.6×10^{-3}	0.84

Experimental conditions: [BPA] = 10 mg/L (4.3×10^{-2} mM), [Fe^{2+}] = 0.36 mM, H_2O_2 = 7.85 mM,

Notations: η – degradation efficiency in (%) at pH 2; k – pseudo 1st order kinetic constant (s^{-1}) calculated using reaction data for 10 min; R^2 – regression coefficient; ## – All experiments conducted at atmospheric static pressure (P_o = 101.3 kPa) unless otherwise stated.

* In addition to these experiments with application of UV, we have also conducted experiments in the category of sonolysis + UV, H_2O_2+UV (with mechanical stirring) and H_2O_2+sonolysis+UV. The results of these experiments are given in the Annexure-II. However, the net degradation of BPA obtained for these experimental categories was small (in the range of 10–20% only). Since the peak emission wavelength of the UV source in this study was 365 nm, which is far away from the peak absorption wavelength of 254 nm for H_2O_2, the net utilization of UV irradiation for photochemical cleavage of H_2O_2 is limited, which is manifested in smaller degradation for these experimental categories.

3.2.4 Determination of H_2O_2 formation as dosimeter of transient cavitation

The amplitude of the ultrasound wave in the bath used in our experiments was 1.9 bar. For atmospheric static pressure (1 bar), this pressure amplitude is sufficient for occurrence of

transient cavitation in the medium, which induces the sonochemical effect. However, in order to further ensure this, we have assessed the formation of H_2O_2 with ultrasound irradiation (or sonication) using water as the liquid medium. The thermal dissociation of water in the cavitation bubble during transient collapse causes formation of $^{\bullet}OH$ radicals, which are released into the medium. These radicals can combine to form H_2O_2. Thus, formation of H_2O_2 with ultrasound irradiation is an indication of occurrence of transient cavitation. Fig. 3.3 depicts the formation of hydrogen peroxide during sonication of water taken in the reaction beaker.

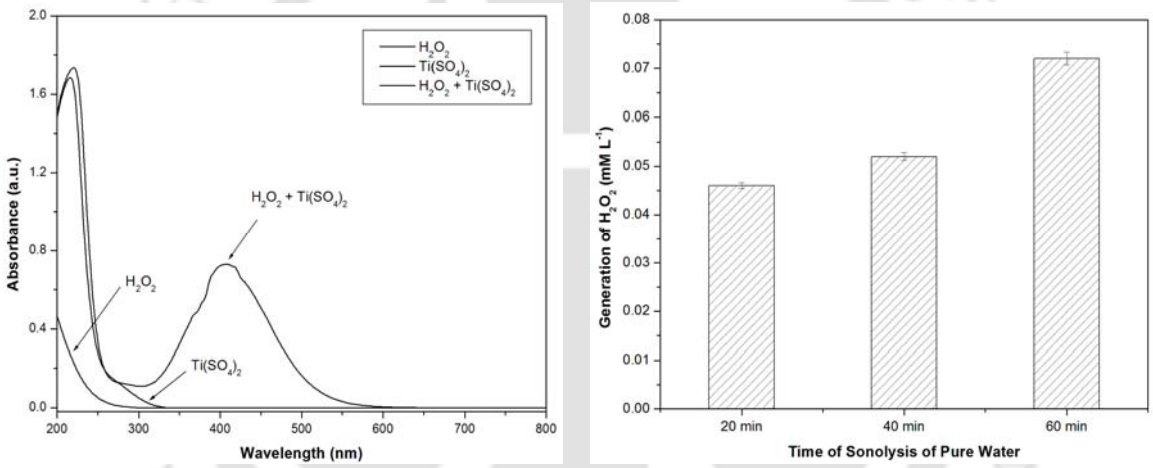

(A) (B)

Figure 3.3: Corroboration of occurrence of transient cavitation in reaction beaker with H_2O_2 dosimeter (Generation of H_2O_2 during sonolysis of ultrapure water (50 mL) at frequency of 40 kHz and temperature of 25°C)

Hydrogen peroxide was determined spectrophotometrically as yellow pertitanic acid, $TiO_2 \cdot H_2O_2$, from its reaction with an excess of aqueous Ti^{4+}, as described by Eisenberg (1943). For convenience of the reader, we briefly outline it as follows: 1 g of anhydrous TiO_2 is digested in 100 mL of concentrated sulfuric acid for 18 h at a temperature of 160°C. The solution is then cooled down to room temperature and diluted using ultrapure water to make a final volume of 500 mL. The final solution is filtered through a 0.22 µm filter paper to

separate any particles. To determine the hydrogen peroxide, a standard plot with different concentrations of H_2O_2 was prepared. In this procedure, 1 mL of titanium sulfate reagent is added to 10 mL of H_2O_2 solution, which gives a yellow color instantly with stability of 6 h.[41] The yellow color appearing after the addition of titanium sulfate is due to the formation of pertitanic acid ($TiO_2 \cdot H_2O_2$) (Treadwell and Hall, 1935). The formation of pertitanic acid through reaction of titanium sulfate with hydrogen peroxide is as follows (Eisenberg, 1943):

$$Ti^{4+} + H_2O_2 + 2H_2O \longrightarrow TiO_2 \cdot H_2O_2 + 4H^+ \qquad (3.1)$$

This pertitanic acid ($TiO_2 \cdot H_2O_2$) shows a maximum absorbance at a wavelength of 407 nm under a UV–Vis spectrophotometer.

3.2.5 Analytical technique for BPA

The filtrate was analyzed for residual BPA using HPLC (Shimadzu, Model: SPD–20A) with UV detector at 276 nm. The HPLC was equipped with a reverse phase C–18 column (250 mm × 4.6 mm, 5 µm). The mobile phase was a mixture of acetonitrile and water (70:30 v/v) with a flow rate of 0.5 mL/min. In addition, removal of total organic carbon (TOC) in the reaction solution with mineralization was analyzed using an Aurora TOC analyzer (O–I–Analytical, Model: 1030).

The intermediate species of the BPA degradation were identified using a mass spectrophotometer (Waters Q–Tof Premier & Aquity UPLC). A representative mass spectrum of the aliquot of reaction mixture (drawn after 10 min) for sono–photo–Fenton treatment is given in Fig. 3.4. Comparative analysis of this spectrum vis–à–vis the spectra reported in published literature helps to identify some of the intermediates of the BPA degradation (Poerschmann et al., 2010; Molkenthin et al., 2013). The chemical structures of intermediates identified in our analysis along with molecular weights are listed in Table 3.2.

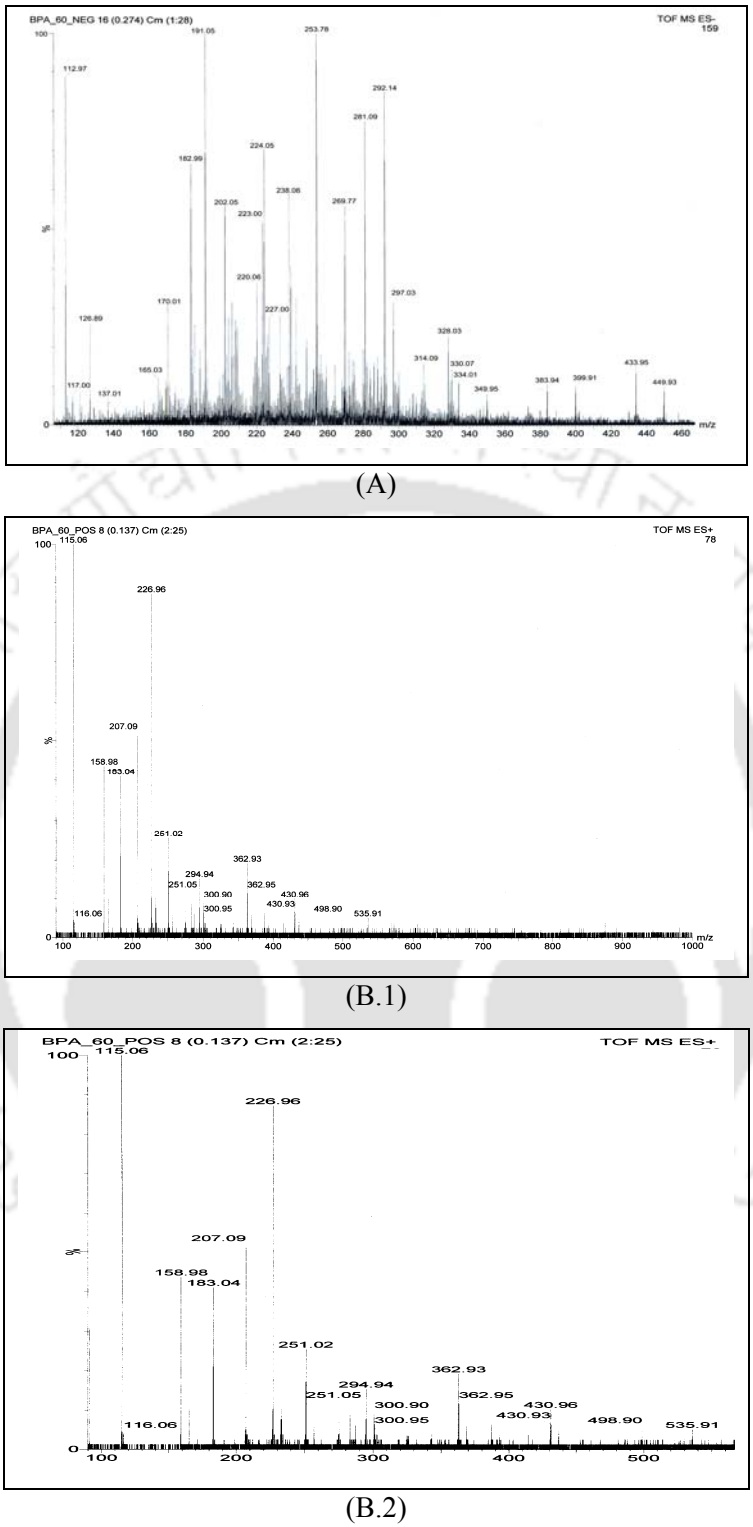

Figure 3.4: Mass spectrum of the reaction mixture for sono–photo–Fenton process for BPA degradation. (A) ES– spectrum, (B.1) ES+ complete spectrum and (B.2) enlarge version for m/z in ES+ mode

Table 3.2: Intermediates with structures and molecular weight detected during (sono–Fenton + UV) degradation of BPA

Mol. Wt.	Chemical Structure	Reference
118 [a]	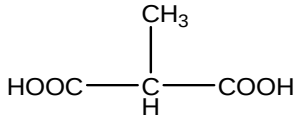	Poerschmann et al. (2010)
128 [a]	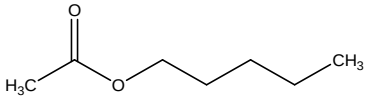	Molkenthin et al. (2013)
138 [a]	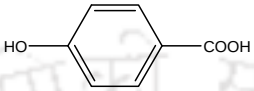	Poerschmann et al. (2010)
226 [b]	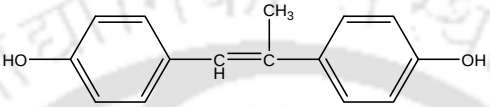	Poerschmann et al. (2010)
228 [a]	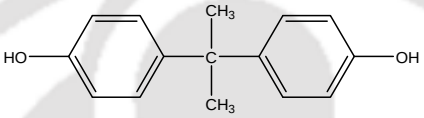	--
270 [a]	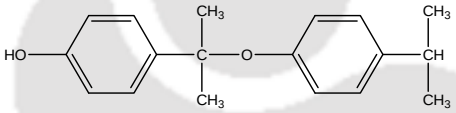	Poerschmann et al. (2010)
335 [a]	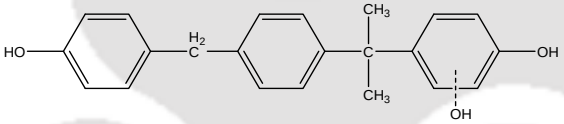	Poerschmann et al. (2010)
351 [a]	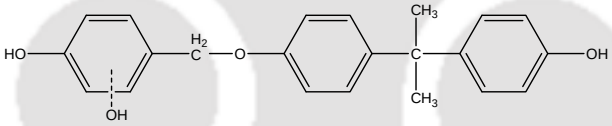	Poerschmann et al. (2010)
362 [b]	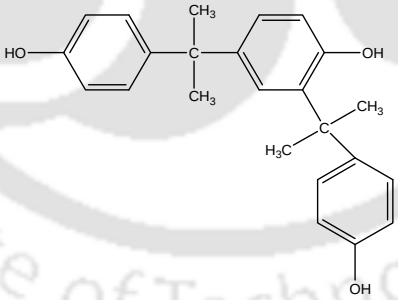	Poerschmann et al. (2010)

[a] – intermediates detected in ES– mode, [b] – intermediate detected in ES+ mode

It should be specifically mentioned that the main objective of this study is to establish the physical mechanism, and not to establish the chemical mechanism or pathway of the degradation of BPA in hybrid advanced oxidation processes. Therefore, we have not given significant emphasis to determine of all the intermediates. The intermediates detected in our experiments essentially indicate that the degradation of BPA is induced by the $^{\bullet}$OH radicals,

which corroborates the chemical mechanism of BPA degradation reported by numerous earlier authors. As far the objectives of the present study are concerned, this corroboration is sufficient for the interpretation and analysis of the results. Interested readers are requested to refer to the papers published by Katsumata et al. (2004), Inoue et al. (2008), and Torres et al. (2007, 2008) for more detail about the intermediates of BPA degradation and the dominant chemical pathway of degradation.

3.3 PRELIMINARY EXPERIMENTAL RESULTS

***Determination of optimum H_2O_2 concentration*:** The Fenton reagent consists of Fe^{2+} and H_2O_2. The amount of H_2O_2 present in the Fenton reagent (whether sub–stoichiometric or stoichiometric or above–stoichiometric with respect to the Fe^{2+} ions) plays an important role in the Fenton process. To determine the optimum amount of H_2O_2 in the Fenton process for degradation of bisphenol–A (BPA) with an initial concentration of 10 mg/L (4.3×10^{-2} mM), different amounts of H_2O_2 were added to the reaction mixture with a fixed quantity of $FeSO_4{\cdot}7H_2O$ (20 mg/L or 7.2×10^{-5} M as Fe^{2+} ions). The addition of H_2O_2 (30% v/v) in the mixture was in the range of 10 – 60 μL (corresponding values 1.96–11.75 mM). The results of degradation are shown in Fig. 3.5A. Initially, the degradation rate is proportional to the concentration of H_2O_2. But at the highest concentration of H_2O_2 (11.75 mM) in the reaction mixture, the degradation rate decreases. A plausible cause leading to this effect is scavenging of radicals by excess H_2O_2 instead of production of additional $^{\bullet}OH$ radical in the system. In the previous chapter, we have discussed this effect in greater detail. The optimum concentration of H_2O_2 is thus determined to be 7.85 mM for degradation of 10 mg/L (4.3×10^{-2} mM) Bisphenol–A. This has been used in the main experiments reported in this chapter.

***Determination of optimum Fe^{2+} concentration*:** As stated in the above section, Fe^{2+} is the

second component of the Fenton reagent. To investigate the effect of Fe^{2+} ions in the sono–Fenton process, the amount of Fe^{2+} in the Fenton reagent was varied between 0.036 and 0.72 mM, while keeping the amount of optimum value of H_2O_2 at 7.85 mM, as determined in the previous section. The experimental results are shown in Fig. 3.5B. It could be seen that as the concentration of Fe^{2+} in the reaction mixture increases, the degradation rate also increases. For Fe^{2+} concentration at 0.72 mM, almost 100% degradation was achieved. Although the rate of degradation increased with higher concentration of Fe^{2+}, the total extent of degradation of BPA was almost same for Fe^{2+} concentrations of 0.36 and 0.72 mM. With these results, the optimum concentration of Fe^{2+} ions was fixed at 0.36 mM with corresponding H_2O_2 concentration being 7.85 mM.

***Methods of introduction of H_2O_2 in reaction mixture and their consequences*:** In the two preceding sections, it has been shown that the degradation efficiency of BPA decreases with excess H_2O_2. This essentially is the effect of radical scavenging by H_2O_2. In order to investigate this effect, we have also conducted experiments with stepwise addition of H_2O_2 at different time intervals. The total amount of hydrogen peroxide (30% v/v) to be added to the reaction solution was 40 µL, which make the concentration of H_2O_2 in the reaction solution as 7.85 mM. The addition of this quantity of H_2O_2 was done with three different techniques: (A) entire 40 µL (30% v/v) was added at the start of experiment, (B) two step addition, i.e. 20 µL of 30% v/v H_2O_2 was added initially followed by an equal amount addition after 30 min of reaction, and (C) three step addition, i.e. 20 µL of 30% v/v H_2O_2 was added initially, and 10 µL of 30% v/v H_2O_2 added after each 20 min of reaction. The trends in BPA degradation with these techniques of H_2O_2 addition are shown in Fig. 3.5C. Although, the total degradation of BPA obtained with three techniques was almost the same, a higher initial degradation rate was seen for category B.

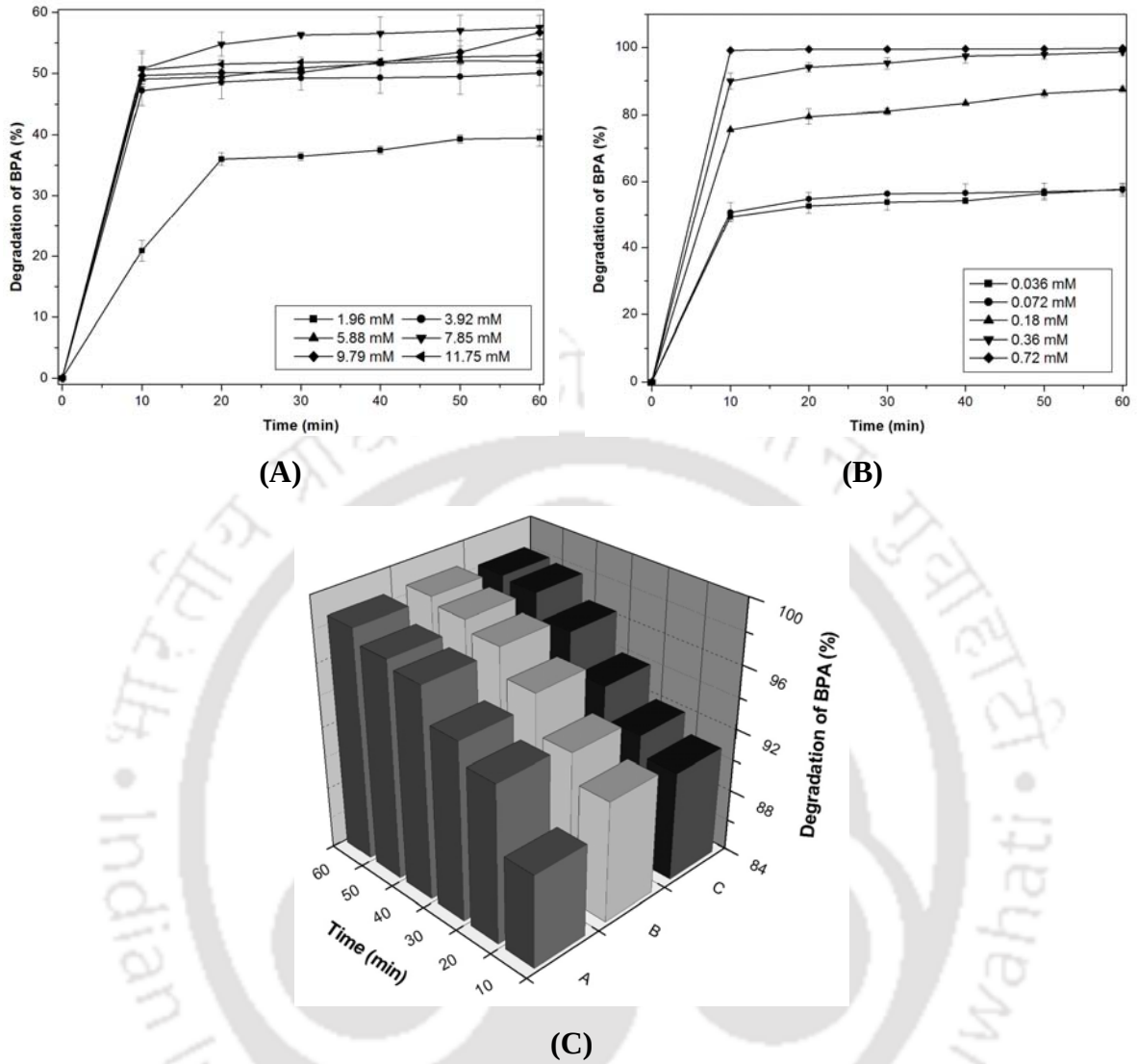

Figure 3.5: (A) Effect of H_2O_2 concentration on degradation of Bisphenol–A. Experimental conditions: $[Fe^{2+}]_0$ = 7.2 × 10^{-2} mM, $[BPA]_0$ = 4.3 × 10^{-2} mM; pH = 2; (B) Effect of Fe^{2+} concentration. Experimental conditions: $[H_2O_2]_0$ = 7.85 mM, $[BPA]_0$ = 4.3 × 10^{-2} mM; pH = 2; (C) Effects of H_2O_2 addition. Experimental conditions: $[Fe^{2+}]_0$ = 0.36 mM and $[BPA]_o$ = 4.3×10^{-2} mM, $[H_2O_2]_0$ = total 40 µL of 30% v/v added to 50 mL. A – Total initial addition of 40 µL of 30% v/v H_2O_2; B – 20 µL of 30% v/v H_2O_2 addition initially, followed by an equal amount added after 30 min of reaction, C – 20 µL of 30% v/v H_2O_2 addition initially, and 10 µL of 30% v/v H_2O_2 added after each 20 min of reaction.

3.4 SYNERGISM EFFECTS IN HAOPS: SOME CONJECTURES AND CONTEMPLATIONS

Prior to presentation of the experimental results and the analysis for determination of the physical mechanism of BPA degradation, a preamble is presented below that tries to identify possible synergies between the mechanism of sonolysis and Fenton process coupled with UV irradiation.

***Sonolysis + UV*:** In sonolysis, the water vapor entrapped in the cavitation bubble undergoes thermal dissociation to produce numerous radicals like $^{\bullet}H$, $^{\bullet}OH$, $^{\bullet}O$ and $HO_2^{\bullet}$. These radicals are released into the medium with fragmentation of the bubble during transient collapse, where they react with pollutant molecules to induce oxidation reactions that lead to degradation of the pollutant. However, for dilute concentration of the pollutants, the probability of interaction of radicals and pollutant molecule is low. Under such circumstances, the radicals may recombine. Combination of $^{\bullet}OH$ radicals (with oxidation potential of 2.8 eV) generates H_2O_2 (with oxidation potential of 1.77 eV), which is a loss of oxidation potential. UV irradiation of the reaction mixture can cause re–splitting of this H_2O_2 that regenerates the $^{\bullet}OH$ radicals: $H_2O_2 + h\nu \longrightarrow 2^{\bullet}OH$. In addition to H_2O_2 generated through transient cavitation, external addition of H_2O_2 to the reaction mixture enhances the efficiency of photolysis. The peak absorption wavelength of H_2O_2 is 254 nm. In the context of present study, the peak emission wavelength of the UV source is 365 nm, but it still has finite (yet reduced) emissions at 254 nm (Fig. 3.1). Therefore, synergy between sonolysis and UV is possible in our experiments.

***Sonolysis–Fenton process*:** The chemistry of the Fenton process is well known. In this case, the $^{\bullet}OH$ radicals are generated by reaction of Fe^{2+} and H_2O_2 with oxidation of Fe^{2+} to Fe^{3+}.

Simultaneously, reduction of Fe^{3+} ions by $HO_2^{\bullet}$ radicals regenerates Fe^{2+}. As noted earlier, in dilute solution of the pollutants, recombination of $^{\bullet}OH$ radicals formed during transient bubble collapse leads to formation of H_2O_2. The Fe^{2+} ions can react with H_2O_2 generated through cavitation bubbles to form $^{\bullet}OH$ radicals (even in the absence of externally added H_2O_2). Moreover, the $HO_2^{\bullet}$ radicals generated through collapse of transient cavitation bubbles can also help regeneration of Fe^{2+} ions. If H_2O_2 is externally added to the reaction mixture, as a component of the Fenton reagent, it may also evaporate into the bubble and be dissociated to $^{\bullet}OH$ radicals during transient collapse. However, in our previous studies (Chakma and Moholkar, 2013a; Bhasarkar et al., 2013), we have noticed that excess concentration of H_2O_2 in the reaction mixture can result in scavenging of radicals through reactions:

$$^{\bullet}OH + H_2O_2 \longrightarrow H_2O + HO_2^{\bullet} \qquad (3.2)$$

$$^{\bullet}OH + HO_2^{\bullet} \longrightarrow O_2 + H_2O \qquad (3.3)$$

***Fenton process + UV*:** Hydrolysis of Fe^{3+} in aqueous solution leads to formation of several Fe(III)–hydroxy complexes. Under irradiation by UV–light, these complexes can break down to regenerate Fe^{2+} with formation of additional $^{\bullet}OH$ radicals. Some reactions in this category (for medium pH ≤ 5) are as follows (Feng and Nansheng, 2000):

$$Fe^{3+} + H_2O \longrightarrow Fe(OH)^{2+} + H^{+} \qquad (3.4)$$

$$Fe^{3+} + 2H_2O \longrightarrow Fe(OH)_2^{+} + 2H^{+} \qquad (3.5)$$

$$Fe^{3+} + 2H_2O \longrightarrow Fe_2(OH)_2^{4+} + 4H^{+} \qquad (3.6)$$

In addition to the above, formation of $Fe(H_2O)_6^{3+}$ species has also been reported (Langford and Carey, 1975; Benkelberg and Warneck, 1995). The photolysis of the $Fe(OH)^{2+}$ complex can occur in following way (Baxendale and Magee, 1955; Faust and Hoigne, 1990):

$$Fe(OH)^{2+} + h\nu \longrightarrow Fe^{2+} + {}^{\bullet}OH \qquad (3.7)$$

Feng and Nansheng (2000) have calculated the distribution of hydrolytic Fe(III) salts in aqueous solutions at pH ≤ 5. For a low solution pH of 2, as used in this study, the dominant hydrolytic species are $Fe(OH)^{2+}$ and $Fe(H_2O)_6^{3+}$. The peak absorption wavelengths of these complexes are 297 and 240 nm, respectively. The UV source used in this study has finite (yet reduced) emissions in these wavelengths. Hence, the photolytic decomposition of hydrolytic Fe(III) complexes can occur in the reaction system of the present study. This is a possible synergy between techniques of Fenton process and UV. It should be mentioned, however, that H_2O_2 added to the reaction medium can also absorb UV radiation and undergo splitting to form $^{\bullet}OH$ radicals. This process would reduce the H_2O_2 utilization in the Fenton process. However, as mentioned earlier, the peak emission wavelength of UV source used in the present study is 365 nm, which is far removed from the peak absorption wavelength of 254 nm for H_2O_2. Thus, due to relatively lower energy intensity of 254 nm emission for the UV source used in this study, the photochemical cleavage of H_2O_2 to $^{\bullet}OH$ radicals is likely to be insignificant. Hence, the predominant utilization of externally added H_2O_2 is for the Fenton process. With this preamble, we now present and discuss our results.

3.5 RESULTS

The results of the experiments are described in Figs. 3.6–3.8, which show the degradation profile of BPA with time in different experimental protocols. Fig. 3.9 shows the percentage of TOC removal (or fraction of initial BPA completely mineralized) after 60 min of treatment. One peculiar feature of the rate of degradation in all experimental categories is the non–uniformity of degradation with respect to time. The rate of degradation is much faster in the initial 10 min and a significant fraction of total degradation occurs in this period only. The rate of degradation decreases markedly thereafter. As stated earlier, we have

monitored the degradation of BPA more closely for the initial 10 min. The degradation profile for the initial 10 min has been shown separately in Figs. 3.6–3.8, besides the total degradation profile for 60 min.

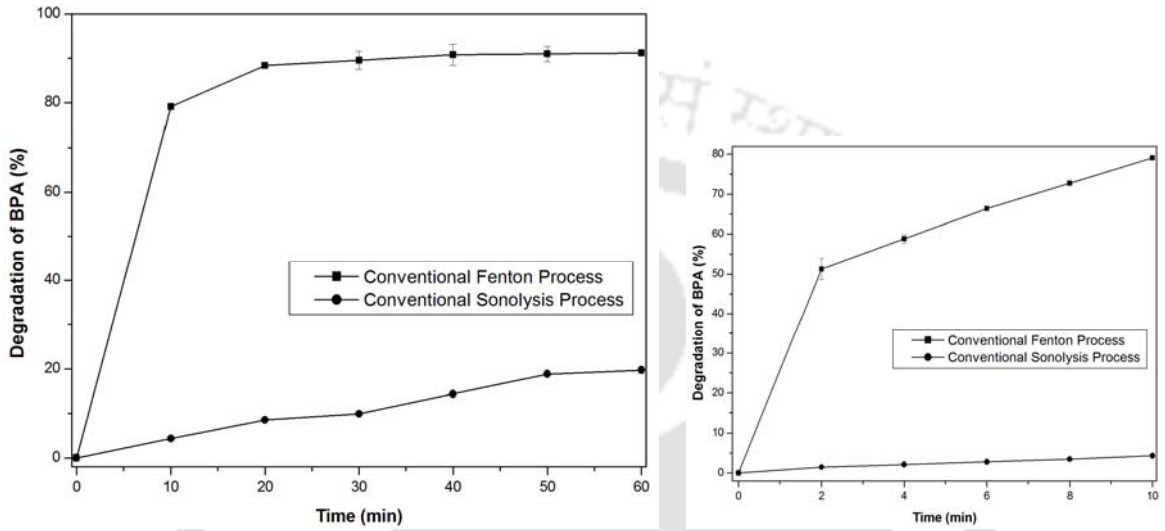

(A) (B)

Figure 3.6: Degradation profile of BPA with time in individual advanced oxidation processes. (A) Degradation profile for total 60 min reaction, and (B) Degradation profile in the initial 10 min. Experimental conditions: f = 40 kHz, $[Fe^{2+}]_0$ = 0.36 mM, $[H_2O_2]_0$ = 7.85 mM, $[BPA]_0 = 4.3 \times 10^{-2}$ mM.

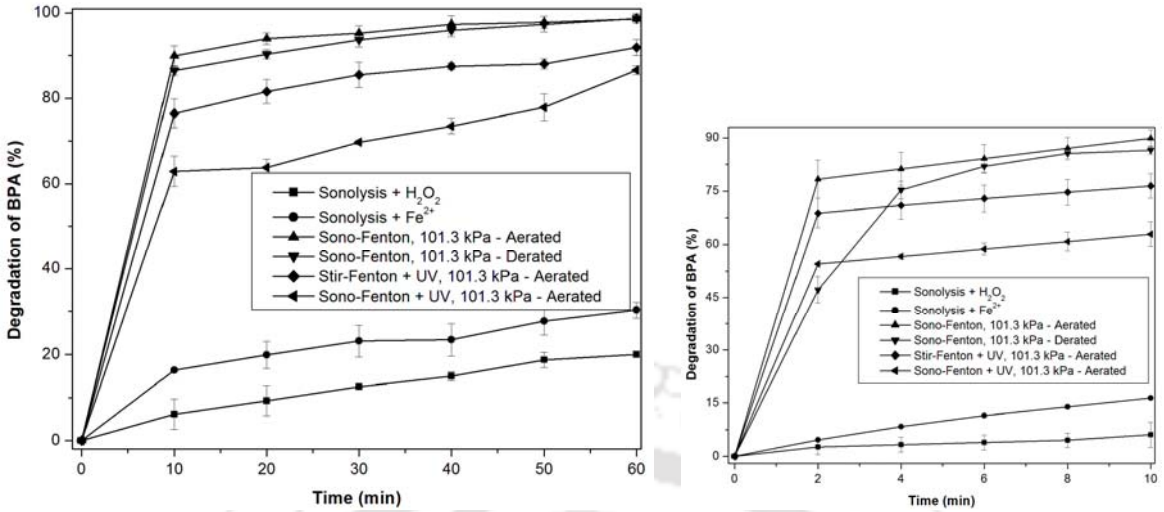

Figure 3.7: Degradation profile of BPA in different combinations of sonolysis and Fenton process coupled with UV. (A) Degradation profile for total 60 min reaction, and (B) Degradation profile in the initial 10 min. Experimental conditions: f = 40 kHz, $[Fe^{2+}]_0$ = 0.36 mM, $[H_2O_2]_0$ = 7.85 mM, $[BPA]_0$ = 4.3×10^{-2} mM

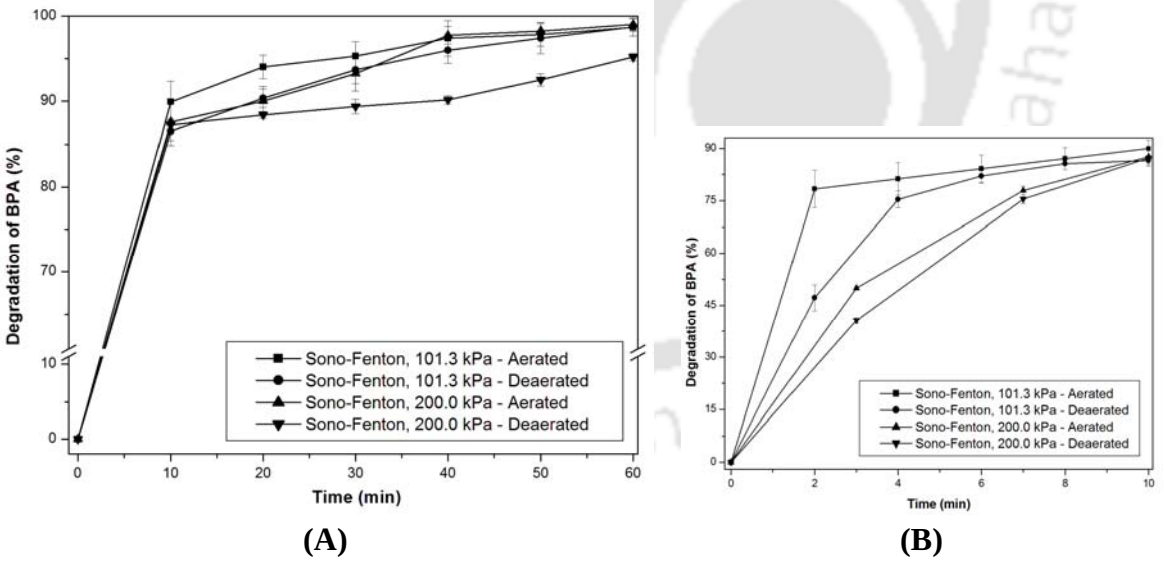

Figure 3.8: Degradation profile of BPA in sono–Fenton process at atmospheric and elevated static pressure. **(A)** Degradation profile for total 60 min reaction, and **(B)** Degradation profile in the initial 10 min. Experimental conditions: $[Fe^{2+}]_0$ = 0.36 mM, $[H_2O_2]_0$ = 7.85 mM, $[BPA]_0$ = 4.3×10^{-2} mM.

The summary of results of the degradation experiments, i.e. degradation achieved in the first 10 min of treatment and overall treatment of 60 min, is given in Table 3.1. Also given in Table 3.1 is the pseudo 1st order kinetic constant for degradation. This constant has been calculated using the degradation data obtained for the first 10 min only. We would like to specifically mention that reason underlying this approach of calculation of kinetic constant is the non–uniformity of degradation with time, as noted above. The salient features of the experimental results as observed from Figs. 3.6–3.8 and Table 3.1 are as follows:

(1) The extent of degradation for sonolysis and sonolysis + H_2O_2 is practically the same, while a significant rise in degradation is seen for the category sonolysis + Fe^{2+}.

(2) Practically same degradation is seen for categories of Fenton process and Fenton + UV process with mechanical stirring.

(3) The total degradation of BPA (in 60 min of treatment) obtained in 4 categories of sono–Fenton (with combinations of aeration/ de–aeration and atmospheric/ elevated static pressure) is practically the same. Moreover, it is only slightly higher (~ 8%) than the Fenton process with mechanical stirring. However, as compared to the degradation with sonolysis as an individual process, there are ~ 5× enhancements in degradation. The pseudo first order kinetic constant for BPA degradation in the 4 categories of sono–Fenton process shows significant variation. The highest kinetic constant (9.22×10^{-3} s^{-1}) is for the aerated solution at atmospheric static pressure. With de–aeration of the solution, this constant reduces by ~ 45%. With elevation of static pressure, the kinetic constant reduces by more than 50%. Interestingly, for both aerated and de–aerated solutions at elevated static pressure, the kinetic constant is very similar.

(4) Comparison of BPA degradation for the hybrid process of Fenton + UV with individual Fenton process (with mechanical stirring) shows practically similar values of total degradation in 60 min. However, a significant rise of ~40% is seen in the pseudo first order

kinetic constant of degradation.

(5) Finally, BPA degradation obtained with a triple combination of (sonolysis + Fenton + UV) process is faster than individual degradation obtained for sonolysis, but it is slower than the degradation for the Fenton process (with mechanical stirring). The same argument holds true for the pseudo first order kinetic constant for these processes. Comparison of the degradation for (sonolysis + Fenton + UV) process with sono–Fenton process (with all 4 versions with aerated/de–aerated solution and atmospheric/elevated static pressure) reveals reduction of total degradation as well as the pseudo first order rate constant.

3.6 DISCUSSION

Analysis of the experimental results vis–à–vis the possible synergies between the individual AOPs of Fenton process and sonolysis coupled with UV irradiation mentioned in section 3 help us to discern the mechanism of the hybrid AOPs. As far as individual effectiveness of sonolysis and Fenton process is concerned, Fenton is 4× more efficient than sonolysis. It should be noted that the pK_a value of BPA is in between 9.6 and 11. The pH of BPA solution in all experiments was 2. Thus, BPA exists in molecular (or un–dissociated) form in all experiments in the solution. As in the analysis of the physical mechanism of the sonochemical degradation of recalcitrant organic pollutants reported by Sivasankar and Moholkar (2009), the predominant location of degradation of BPA will be the bulk solution. Three factors that contribute to this effect are: low vapor pressure of BPA (~ 5 mPa at 295 K) due to which its evaporation in the cavitation bubble is negligible, molecular form of BPA at the solution pH of 2, and the –OH groups present in BPA, which can impart polar and hydrophilic character to the molecules, due to which they prefer to stay in the bulk region – rather than at the bubble interface (which has a hydrophobic character).

(1) The possible cause underlying the negligible difference between sonolysis and

sonolysis+H_2O_2 could be the scavenging effect of H_2O_2. Evaporation of H_2O_2 into the cavitation bubble leads to generation of additional $^{\bullet}OH$ radicals, but at the same time H_2O_2 present in the reaction mixture may scavenge it, hampering its utilization for BPA degradation.

(2) Significant rise in BPA degradation for category (sonolysis + Fe^{2+}) as compared to sonolysis alone is clearly attributed to regeneration of $^{\bullet}OH$ radicals by reaction of Fe^{2+} and H_2O_2 generated due to recombination of radicals generated by transient cavitation. More than 4–fold enhancement in BPA degradation in for sonolysis + Fe^{2+} category as compared to sonolysis alone is clearly attributed to marked enhancement in $^{\bullet}OH$ radical regeneration by Fenton reaction.

(3) In sono-Fenton process (at atmospheric static pressure), the oxidation radicals are generated by both cavitation bubbles as well as Fenton reactions. However, large rise in the extent of BPA degradation in sono-Fenton process, as compared to sonolysis alone clearly indicates dominant generation of $^{\bullet}OH$ radicals through Fenton route than sonolysis.

Comparison of kinetics of the BPA degradation with sono–Fenton under aerated (or oxygenated) or de–aerated (or de–oxygenated) condition reveals a significant role of dissolved oxygen in the process. Presence of dissolved oxygen in the reaction solution can help conservation of $H^{\bullet}$, $^{\bullet}OH$ and $HO_2^{\bullet}$ radicals (generated through dissociation of water vapor during transient cavitation) through various reactions given below (Sivasankar and Moholkar, 2009), which results in generation of alternative oxidizing radical species:

$$^{\bullet}OH + O_2 \rightleftharpoons O^{\bullet} + HO_2^{\bullet} \quad (3.8)$$

$$H^{\bullet} + O_2 \rightleftharpoons HO_2^{\bullet} \quad (3.9)$$

$$H^{\bullet} + O_2 \rightleftharpoons O^{\bullet} + {}^{\bullet}OH \quad (3.10)$$

$$^{\bullet}OH + {}^{\bullet}OH \rightleftharpoons H_2O_2 \quad (3.11)$$

$$H_2O_2 + O_2 \rightleftharpoons 2HO_2^{\bullet} \qquad (3.12)$$

Radical generation by transient cavitation is not uniform throughout the volume of the reaction medium, but rather discrete (i.e. only at the site of transient bubble collapse). The radicals generated from bubbles are highly unstable; and hence, do not diffuse into the medium. They react with pollutant molecules, if present in the close vicinity of site of bubble collapse. Or alternatively, these radicals simply recombine to form molecular species like O_2, H_2O and H_2O_2. This recombination is a loss of oxidation potential. The conservation of the radicals by dissolved oxygen through reactions mentioned above helps reduce the loss of oxidation potential due to recombination of the radicals. This process also increases the probability of interaction between radical and BPA molecule. In the present situation, however, the probability of radical–BPA molecule interaction can be assumed to be high due to the strong convection generated in the solution by the ultrasound waves and transient cavitation. As a consequence of all of these effects, the kinetic constant of BPA degradation for aerated solution is significantly higher than for the de-aerated solution.

Comparing between the sono–Fenton process at atmospheric and elevated static pressures, the effect of dissolved oxygen is more marked at atmospheric pressure, as transient cavitation occurs in the medium. With rise in the static pressure, the transient cavitation is eliminated and so is the production of radicals through cavitation bubbles. In this case, $^{\bullet}OH$ radical production occurs through the Fenton process. However, this radical production is rather uniform throughout the reaction volume (since the reagents Fe^{2+} and H_2O_2 are uniform throughout the volume), and hence, presence of dissolved oxygen does not contribute much to the net utility of the $^{\bullet}OH$ radicals. Thus, the rise in the kinetic constant of the sono–Fenton process for the aerated medium is relatively smaller as compared to the de–aerated medium at elevated static pressure.

Practically the same total degradation of BPA (in 60 min of treatment) with the sono–

Fenton process under atmospheric and elevated pressure shows a dominant contribution of the Fenton process as compared to sonolysis. At elevated static pressure, transient cavitation is eliminated, and thus, there is no contribution to generation of $^{\bullet}OH$ radicals by cavitation bubbles. To support this argument, we have given the results of simulations of cavitation bubble dynamics (using the diffusion limited model, described by Chakma and Moholkar (2013b) and Krishnan et al. (2006)) at atmospheric and elevated static pressure in Annexure-II, which show the temperature and pressure peaks reached in the bubble at transient collapse and the equilibrium composition of different species formed from dissociation of solvent vapor and gas molecules. Therefore, all degradation obtained at elevated static pressure is attributed to the Fenton process. The slight increase in BPA degradation with the sono–Fenton process as compared to Fenton alone is attributed to stronger convection generated by ultrasound and cavitation due to which the probability of radical – BPA molecule interaction increases.

(4) Comparison of the degradation result for the categories Fenton process (with mechanical stirring) and Fenton process + UV reveals negligible effect of UV irradiation on total BPA degradation achieved in 60 min treatment. However, the kinetic constant of degradation for Fenton + UV process is higher than for only the Fenton process. This essentially indicates that additional $^{\bullet}OH$ radicals generated from H_2O_2 photolytic cleavage (in addition to the radicals generated by the Fenton process) in the initial stage of degradation could have contributed to enhancement of the degradation kinetics in the first 10 min of treatment. However, the concentration of H_2O_2 decreases as the reaction proceeds, and so does the generation of additional radicals due to photolytic cleavage. Thus, the total degradation obtained in 60 min of treatment is practically same for the Fenton process with mechanical stirring and the Fenton process coupled with UV irradiation.

(5) The most interesting result of our study is the negative synergy of UV irradiation with

the sono–Fenton process. This is evident from comparison of degradation obtained in categories sono–Fenton and (sono–Fenton + UV). A probable cause for this effect is the improper utilization of H_2O_2 by sonication or Fenton process in presence of UV irradiation. As noted earlier, the UV irradiation independently splits the H_2O_2 molecules into $^{\bullet}OH$ radicals and this pathway competes with the Fenton process and sonolysis. Moreover, due to low concentration of H_2O_2 coupled with relatively low emission intensity at H_2O_2 absorption wavelength of 254 nm, the quantum of $^{\bullet}OH$ radical generation through UV–mechanism is rather low to yield an effective degradation, as noted earlier. These are, however, only conjectures and more detailed investigations are needed to discern the mechanism of negative synergy of UV irradiation on sono–Fenton system.

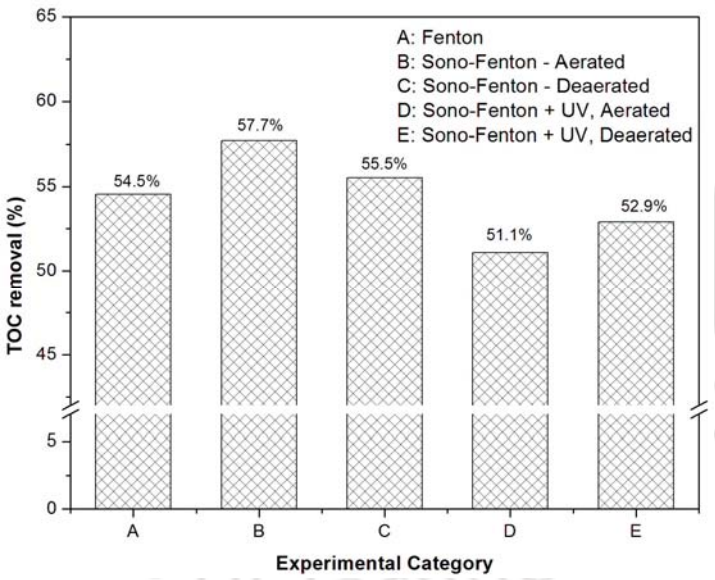

Figure 3.9: Percentage of TOC removal (or fractional mineralization of BPA) in 60 min of treatment in different experimental categories. Experimental condition: f = 40 kHz, λ_{max} = 365 nm, $[Fe^{2+}]_0$ = 0.36 mM, $[H_2O_2]_0$ = 7.85 mM, $[BPA]_0 = 4.3 \times 10^{-2}$ mM

(6) The total mineralization of the BPA in various experimental categories has also been assessed, with results depicted in Fig. 3.9. TOC reduction in different treatments (at

atmospheric static pressure) shows the following trend: sono–Fenton (aerated) > sono–Fenton (de-aerated) > Fenton process > sono–Fenton + UV (de-aerated) > sono–Fenton + UV (aerated). These trends clearly reveal the positive synergy between sonolysis and Fenton process, the supporting role of dissolved oxygen, and the negative effect of UV irradiation on the sono–Fenton system, as outlined earlier.

3.7 CONCLUSION

In this chapter, we have explored the mechanistic synergies for the hybrid advanced oxidation processes with combination of sonolysis and Fenton process coupled with UV irradiation. The categories for which positive synergies are obtained are: (1) Sonolysis alone and Sonolysis+Fe^{2+}, (2) Sonolysis & sono–Fenton, (3) Fenton & sono–Fenton. The static pressure on the reaction mixture in the sono–Fenton process does not show any influence on the extent of degradation. The category with no synergy is: Fenton and Fenton+UV. The category with negative synergy is: Fenton process and sono–Fenton+UV. We believe that results of this study will form useful input for further research in BPA degradation with hybrid advanced oxidation processes. The experimental framework used in this study can also be extended for study of degradation of other pollutants with hybrid advanced oxidation processes.

ANNEXURE-I

CALCULATION OF ACOUSTIC PRESSURE AMPLITUDE (P_{AW})

The acoustic pressure amplitude generated by transducers attached to the bottom of the ultrasound bath was calculated using a calorimetric method. This method is based on the assumption that the entire energy of ultrasound waves generated by the transducers is finally dissipated in the form of heat. The ultrasound bath was filled with 7 L of water as the medium, and sonication of this water was carried out until its temperature increased by 1°C. This temperature rise was achieved after 8 min of sonication. On the basis of these results, the total energy dissipation in the medium during sonication is determined as:

$$\frac{mC_p\Delta T}{t} = \frac{7\text{ kg} \times 4180\text{ J/kg-}^\circ\text{C} \times 1^\circ\text{C}}{8\text{ min} \times 60\text{ s/min}} = 60.96\text{ J/s} = 60.96\text{ W}$$

The ultrasound bath used in the experiment was equipped with 4 transducers of dia 40 mm. The intensity of the ultrasound (or the acoustic intensity) can then be calculated as:

$$\text{I} = \frac{\text{Actual power (W)}}{\text{Area of transducer (m}^2\text{)}} = \frac{60.96}{4 \times \frac{\pi}{4}(40 \times 10^{-3})^2}\text{ W/m}^2 = 12127.28\text{ W/m}^2$$

The relation between acoustic intensity and acoustic pressure amplitude is given as (Mason and Lorimer, 2002): $I = P_A^2/2\rho c$, where I = acoustic intensity, P_A = acoustic pressure amplitude, ρ = density of the medium, and c = speed of sound in the medium. Substituting values: ρ = 1000 kg/m^3, c = 1481 m/s, and I = 12127.28 W/m^2 gives acoustic pressure amplitude as:

$$P_A = \sqrt{2 \times 12127.28 \times 1481 \times 1000} = 1.895 \times 10^5\text{ Pa} \approx 190\text{ kPa (1.9 bar)}$$

ANNEXURE – II

Table 3.S1: Results for sonolysis+UV, photolysis (H_2O_2/UV) and sono+H_2O_2+UV and sono–photo–Fenton processes

Category of experiment ##	η (%)		k (s^{-1})	R^2
	10 min	60 min		
1. Sonolysis + UV	6.24 ± 1.74	19.62 ± 1.33	1.17×10^{-4}	0.96
2. Stirring + H_2O_2 + UV (photolysis)	1.22 ± 1.38	6.47 ± 0.19	2.46×10^{-5}	0.92
3. Sonolysis + H_2O_2 + UV (sono–photolysis)	4.52 ± 1.07	10.34 ± 1.32	7.09×10^{-5}	0.97

Notations: η – degradation efficiency in (%) at pH 2; k – pseudo 1st order kinetic constant (s^{-1}) calculated using reaction data for 30 min; R^2 – regression coefficient; # # – All experiments conducted at atmospheric (101.3 kPa) static pressure unless otherwise stated

Table 3.S2: (A) Summary of the simulation results (Air Bubbles)

	Parameters for simulations	
	R_o = 5 μm P_o = 101.3 kPa	R_o = 5 μm P_o = 200 kPa
	Conditions at the first collapse of the bubble	
	T_{max} = 4013 K P_{max} = 705.6 MPa V_{turb} = 0.056 m/s P_{AW} = 2.53 MPa	T_{max} = 1075 K P_{max} = 7.78 MPa V_{turb} = 0.008 m/s P_{AW} = 0.22 MPa
	N_{N2} = 1.306E+10 N_{O2} = 3.471E+9 N_W = 2.026E+9	N_{N2} = 1.306E+10 N_{O2} = 3.471E+9 N_W = 9.03E+8
Species	**Equilibrium composition of species in the bubble at collapse**	
N_2	6.52E–01	7.49E–01
O_2	1.30E–01	1.99E–01
H_2O	9.21E–02	5.20E–02
H	8.15E–04	0.
O	6.50E–03	0.
OH	2.56E–02	1.12E–07
HO_2	1.11E–03	0.
H_2O_2	1.69E–04	0.
O_3	1.67E–05	0.
H_2	1.79E–03	0.
NO	8.79E–02	7.13E–05
NO_2	1.67E–03	1.98E–05
HNO	1.55E–04	0.
HNO_2	1.16E–05	0.
HNO_3	1.58E–06	0.
NH_3	1.89E–06	0.

(B) Net production of various oxidizing species per bubble

Parameter	P_o = 101.3 kPa	P_o = 200 kPa
N_{OH}	4.75E+8	1.95E+3
N_O	1.2E+8	0.
N_{HO2}	2.06E+7	0.
N_{H2O2}	3.14E+6	0.

Notations: 4.75E+8 should read as 4.75×10^8, P_o – static pressure in the liquid medium; R_o – initial radius of the cavitation bubble; V_{turb} – average velocity of the micro–turbulence in the medium generated by ultrasound and cavitation in the medium (estimated at 1 mm distance from bubble center); P_{AW} – pressure amplitude of the acoustic wave generated by the cavitation bubble; T_{max} – temperature peak reached in the bubble at the time of first collapse; P_{max} – pressure peak reached in the bubble at the time of first collapse; N_W – number of water molecules trapped in the bubble; N_{N2} – number of N_2 molecules in the bubble; N_{O2} – number of oxygen molecules in the bubble; N_{OH} – number of OH radicals present in the bubble at transient collapse; N_H – number of H radicals present in the bubble at transient collapse; N_O – number of O radicals present in the bubble at transient collapse; N_{HO2} – number of HO_2 radicals present in the bubble at transient collapse; N_{H2O2} – number of H_2O_2 molecules present in the bubble at transient collapse

REFERENCES

Baxendale JH, Magee J, The photochemical oxidation of benzene in aqueous solution by ferric ion, Trans. Faraday Soc. 51 (1955) 205-213.

Benkelberg HJ, Warneck P, Photodecomposition of iron(III) hydroxo and sulfato complexes in aqueous solution: wavelength dependence of OH and SO_4 quantum yields, J. Phys. Chem. 99 (1995) 5214-5221.

Bhasarkar JB, Chakma S, Moholkar VS, Mechanistic features of oxidative desulfurization using sono–fenton–peracetic acid (Ultrasound/Fe^{2+}–CH_3COOH–H_2O_2) system, Ind. Eng. Chem. Res. 52 (2013) 9038-9047.

Bisphenol A Action Plan (CASRN 80-05-7), US Environmental Protection Agency (2010), Washington D.C., USA.

Chakma S, Moholkar VS, Mechanistic features of ultrasonic desorption of aromatic pollutants, Chem. Eng. J. 175 (2011) 356-367.

Chakma S, Moholkar VS, Numerical simulation and investigation of system parameters of

sonochemical process, Chinese J. Eng. 2013 (2013b) 1-14.

Chakma S, Moholkar VS, Physical mechanism of sono–fenton process, AIChE J. 59 (2013a) 4303-4313.

Eisenberg G, Colorimetric determination of hydrogen peroxide, Ind. Eng. Chem. Anal. Ed. 15 (1943) 327-328.

Faust BC, Hoigne J, Photolysis of Fe(III)–hydroxy complexes as source of OH radicals in clouds, fog and rain, Atmos. Environ. 24A (1990) 79-89.

Feng W, Nansheng D, Photochemistry of hydrolytic iron (III) species and photo-induced degradation of organic compounds: A mini review, Chemosphere 41 (2000) 1137-1147.

Gogate PR, Tatake PA, Kanthale PM, Pandit AB, Mapping of sonochemical reactors: Review, analysis, and experimental verification, AIChE J. 48 (2002) 1542-1560.

Inoue M, Masuda Y, Okada F, Sakurai A, Takahashi I, Sakakibara M, Degradation of Bisphenol-A using sonochemical reactions, Water Res. 42 (2008) 1379-1386.

Katsumata H, Kawabe S, Kaneco S, Suzuki T, Ohta K, Degradation of Bisphenol-A in water by the photo–Fenton reaction, J. Photoch. Photobio. A 162 (2004) 297-305.

Krishnan SJ, Dwivedi P, Moholkar VS, Numerical investigation into the chemistry induced by hydrodynamic cavitation, Ind. Eng. Chem. Res. 45 (2006) 1493-1504.

Langford CH, Carey JH, The charge transfer photochemistry of the hexaaquoironIII ion, the chloropentaaquoiron(III) ion, and the μ–dihydroxo dimer explored with tert–butyl alcohol scavenging, Can. J. Chem. 53 (1975) 2430-2435.

Leighton TG, The Acoustic Bubble, Academic Press: London, 1994.

Mason TJ, Lorimer JP, Applied sonochemistry: The uses of power ultrasound in chemistry and processing, Wiley–VCH, Coventry, 2002.

Molkenthin M, Olmez–Hanci T, Jekel MR, Arslan–Alaton I, Photo–Fenton–like treatment of BPA: Effect of UV light source and water matrix on toxicity and transformation products,

Water Res. 47 (2013) 5052-5064.

Poerschmann J, Trommler U, Górecki T, Aromatic intermediate formation during oxidative degradation of Bisphenol A by homogeneous sub–stoichiometric Fenton reaction, Chemosphere 79 (2010) 975-986.

Sivasankar T, Moholkar VS, Mechanistic approach to intensification of sonochemical degradation of phenol, Chem. Eng. J. 149 (2009) 57-69.

Torres RA, Abdelmalek F, Combet E, Pétrier C, Pulgarin C, A comparative study of ultrasonic cavitation and Fenton's reagent for Bisphenol A degradation in deionised and natural waters, J. Hazard. Mater. 146 (2007) 546-551.

Torres RA, Pétrier C, Combet E, Carrier M, Pulgarin C, Ultrasonic cavitation applied to the treatment of Bisphenol A. Effect of sonochemical parameters and analysis of BPA by–products, Ultrason. Sonochem. 15 (2008) 605-611.

Treadwell FP, Hall WT, Analytical Chemistry (vol. 2), Quantitative Analysis (8th ed.), John Wiley & Sons: New York, pp. 288, 1935.

भारतीय प्रौद्योगिकी संस्थान गुवाहाटी
Indian Institute of Technology Guwahati

4

MECHANISTIC ANALYSIS OF HYBRID SONO–PHOTO–FERRIOXALATE SYSTEM

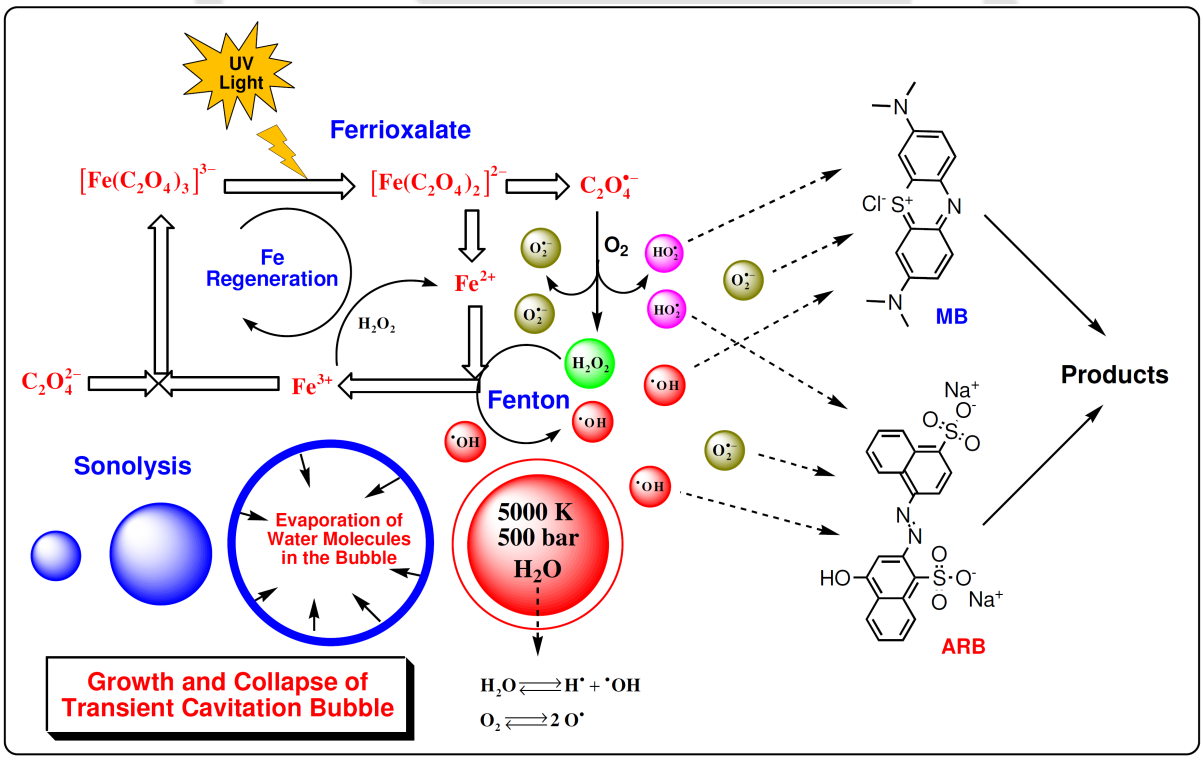

Reaction meachnisms in sono-Fenton-photo-ferrioxalate system

CHAPTER 4

MECHANISTIC ANALYSIS OF HYBRID SONO–PHOTO–FERRIOXALATE SYSTEM

4.1 INTRODUCTION

The previous two chapters explored the physical mechanism of hybrid AOP of sono-Fenton and sono-Fenon-UV (or sono-photo-Fenton). The main objective underlying the latter AOP was to utilize photo-activity of hydroxyl complexes of Fe. Extending the same theme, we have investigated the physical mechanism sono-photo-Ferrioxalate system. The oxalate complexes of Fe are highly photoactive with absorption range up to 450 nm (constituting 18% of total energy of solar spectrum) (Monteagudo et al., 2008). Ferrioxalate system also generates in-situ hydrogen peroxide which induces Fenton reactions. Due to these features, the ferrioxalate system gives substantial improvement in the sono-photo-Fenton process.

We have chosen two popular dyes applied widely in industry, *viz*. the azo dye Acid Red B (ARB) and a non–azo dye Methylene Blue (MB), as model pollutants. Experiments have been conducted so as to identify contribution of each pathway (*viz*. sonolysis, Fenton and ferrioxalate), and interactions among these pathways leading to higher overall degradation. The experimental results have been analyzed vis–à–vis simulations of cavitation bubble dynamics, which quantitatively predicts the physical and chemical effects induced by transient cavitation. Before proceeding to the experimental and results section, we briefly

outline the individual chemistry of each AOP in the next section. This mechanism was earlier described in chapter 1; however, for convenience of reader, it is reproduced here again.

4.2 CHEMICAL MECHANISMS OF SONOLYSIS, FENTON AND PHOTO–FERRIOXALATE AOPS

In this section, we have described the chemical mechanism of the individual AOPs of sonolysis, Fenton (including Fenton like) and photo–ferrioxalate. This forms basis for the discussion and analysis of our results with hybrid AOP.

Sonolysis: In sonolysis, the mechanism of radical production is through thermal dissociation of the solvent (usually water) and gas (usually air) molecules present in the bubble at the moment of transient collapse. A brief description of this phenomenon is as follows: During the expansion of cavitation bubble in rarefaction half cycle of the ultrasound, significant amount of solvent vapor evaporates at the bubble interface and diffuses towards the bubble center. In the ensuing compression cycle, this vapor diffuses back to the bubble interface and undergoes condensation. However, at the final moments of bubble collapse, the bubble wall velocity becomes very high (equal to or even higher than sonic velocity), and not all of the vapor that has entered the bubble can escape back to the liquid. At this stage, the time scale of bubble dynamics becomes smaller than time scales of vapor diffusion as well as condensation (Storey and Szeri, 2000). The entrapped solvent vapor along with gas in the bubble is subjected to extreme conditions of temperature and pressure (~ 5000 K, 500 bar) generated during transient collapse (Hart and Henglein, 1985, 1987). The typical reactions of dissociation of the entrapped water vapor and air molecules (either among themselves or with the dissolved oxygen in the bulk liquid medium) can be represented as follows (Eqs. 4.1-4.8):

$$H_2O \rightleftarrows H^{\bullet} + {}^{\bullet}OH \qquad (4.1)$$

$$O_2 \rightleftarrows 2\,O^{\bullet} \qquad (4.2)$$

$$O^{\bullet} + H_2O \rightleftharpoons 2\ {}^{\bullet}OH \quad (4.3)$$

$$H^{\bullet} + O_2 \rightleftharpoons O^{\bullet} + {}^{\bullet}OH \quad (4.4)$$

$$H^{\bullet} + O_2 \rightleftharpoons HO_2^{\bullet} \quad (4.5)$$

$${}^{\bullet}OH + {}^{\bullet}OH \rightleftharpoons H_2O_2 \quad (4.6)$$

$$H_2O_2 + O_2 \rightleftharpoons 2\ HO_2^{\bullet} \quad (4.7)$$

$${}^{\bullet}OH + O_2 \rightleftharpoons HO_2^{\bullet} + O^{\bullet} \quad (4.8)$$

Fenton process: In Fenton process, Fe^{2+} and H_2O_2 react to yield ${}^{\bullet}OH$ radical and oxidized Fe^{3+} ion (Eq. 4.9). At low pH of about < 3, the reduction of Fe^{3+} to Fe^{2+} occurs via another reaction with H_2O_2 with generation of hydroperoxy radicals (Eq. 4.10). The $HO_2^{\bullet}$ radical can also reduce Fe^{3+} to Fe^{2+} further (Eq. 4.11).

$$Fe^{2+} + H_2O_2 \longrightarrow Fe^{3+} + OH^- + {}^{\bullet}OH \quad (4.9)$$

$$Fe^{3+} + H_2O_2 \rightleftharpoons Fe^{2+} + HO_2^{\bullet} + H^+ \quad (4.10)$$

$$Fe^{3+} + HO_2^{\bullet} \longrightarrow Fe^{2+} + O_2 + H^+ \quad (4.11)$$

Photo–Ferrioxalate system: The photolysis of H_2O_2 is not very efficient, as due to lower molar extinction, H_2O_2 is able to absorb photons only below 350 – 400 nm, which constitute only 3% of solar radiation. The ferrioxalate complex ($[Fe(C_2O_4)_3]^{3-}$) is far more photosensitive, and is able to absorb photons of solar spectrum up to range of 450 nm (constituting 18% of total energy) (Monteagudo et al., 2008). Thus, the ferrioxalate system gives substantial improvement in the efficiency of conventional solar–Fenton process. Decomposition of ferrioxalate complex results in formation of Fe^{2+}, oxalate anion ($C_2O_4^{2-}$) and oxalate radicals ($C_2O_4^{\bullet -}$). The oxalate radical can combine with dissolved oxygen to generate two oxidizing radical species, viz. $O_2^{\bullet -}$ and $HO_2^{\bullet}$. The $HO_2^{\bullet}$ can combine to produce

H_2O_2, which can react with Fe^{2+} (generated from decomposition of $[Fe(C_2O_4)_3]^{3-}$) to yield $^{\bullet}OH$ radicals. The overall chemistry of ferrioxalate system is described below (Eqs. 4.12–4.23) (Jeong and Yoon, 2004, Zhou et al., 2004; Vedrenne et al., 2012).

$$Fe_2(SO_4)_3 \rightleftharpoons 2\,Fe^{3+} + 3\,SO_4^{2-} \quad (4.12)$$

$$KHC_2O_4 \rightleftharpoons K^+ + H^+ + C_2O_4^{2-} \quad (4.13)$$

$$Fe^{3+} + 3C_2O_4^{2-} \longrightarrow \left[Fe(C_2O_4)_3\right]^{3-} \quad (4.14)$$

$$[Fe(C_2O_4)_3]^{3-} \xrightarrow{h\nu} Fe^{2+} + 2\,C_2O_4^{2-} + C_2O_4^{\bullet-} \quad (4.15)$$

$$C_2O_4^{\bullet-} + [Fe(C_2O_4)_3]^{3-} \longrightarrow Fe^{2+} + 3\,C_2O_4^{2-} + 2\,CO_2 \quad (4.16)$$

$$C_2O_4^{\bullet-} \longrightarrow CO_2 + CO_2^{\bullet-} \quad (4.17)$$

$$C_2O_4^{\bullet-} + O_2 \longrightarrow 2\,CO_2 + O_2^{\bullet-} \quad (4.18)$$

$$CO_2^{\bullet-} + O_2 \longrightarrow CO_2 + O_2^{\bullet-} \quad (4.19)$$

$$O_2^{\bullet-} + H^+ \longrightarrow HO_2^{\bullet} \quad (4.20)$$

$$HO_2^{\bullet} + HO_2^{\bullet} \longrightarrow H_2O_2 + O_2 \quad (4.21)$$

$$Fe^{2+} + H_2O_2 \longrightarrow Fe^{3+} + {}^{\bullet}OH + OH^- \quad (4.22)$$

$$Fe^{3+} + H_2O_2 \rightleftharpoons Fe^{2+} + HO_2^{\bullet} + H^+ \quad (4.23)$$

For high concentration of ferrioxalate complex in the system, $CO_2^{\bullet-}$ can also react with ferrioxalate complex in presence of H_2O_2 (either in–situ generated or externally added) to generate extra •OH radicals as per the following reaction (Eqs. 4.24–4.25) (Monteagudo et al., 2013):

$$CO_2^{\bullet-} + [Fe(C_2O_4)_3]^{3-} \longrightarrow Fe^{2+} + CO_2 + 3\,C_2O_4^{2-} \quad (4.24)$$

$$Fe^{2+} + 3\,C_2O_4^{2-} + H_2O_2 \longrightarrow [Fe(C_2O_4)_3]^{3-} + OH^- + {}^{\bullet}OH \quad (4.25)$$

In presence of externally added H_2O_2, free Fe^{3+} (uncombined with oxalate ions) can undergo Fenton–like reactions ($Fe^{3+} + H_2O_2 \rightleftharpoons Fe^{2+} + HO_2^{\bullet} + H^+$) to generate Fe^{2+}, which can further produce •OH radicals through Fenton mechanism at low pH as described above.

4.3 MATERIALS AND METHODS

4.3.1 Materials

Methylene Blue ($C_{16}H_{18}N_3SCl$), ferric sulfate anhydrous ($Fe_2(SO_4)_3$) and potassium oxalate ($K_2C_2O_4$) were purchased from Loba Chemie India Ltd. H_2O_2 (30% v/v), NaOH, HCl were purchased from Merck India Ltd. Acid Red B ($C_{20}H_{12}N_2Na_2O_7S_2$) was procured from a.b. Chemicals and Instruments, Guwahati, India. All the chemicals were used as received without any further purification. All solutions were prepared using ultrapure water (resistivity of ≥ 18 MΩ·cm at 25°C) from Milli–Q synthesis Unit (Millipore®, USA).

4.3.2 Experimental setup

Reactions were carried out in a 200 mL beaker made of borosilicate glass. For experiments with mechanical stirring, a magnetic stirrer plate was used with agitation provided at 300 rpm by a magnetic needle. For experiments with sonication, an ultrasound bath (JeioTech, South Korea, capacity: 10 L, frequency: 40 kHz, power: 200 W) was used for sonication of the reaction mixture. The bath was filled with water as the medium, and the reaction beaker was placed at the center using a burette stand. The beaker was immersed to about 3/4th of its height in the water in bath. The temperature of the sonication medium, and hence, the reaction solution in the beaker was maintained constant at 25±1°C using circulation of cooling water from a water circulating bath (Amkette Analytics, Model: WB2000). To avoid any artifact due to spatial variation of the ultrasound intensity and local acoustic pressure amplitude in the reaction solution/ medium (Gogate et al., 2002; Moholkar

et al., 2004), all reactions were carried out in the same beaker, and the position of the beaker in the bath was carefully maintained same in all experiments. Actual acoustic power dissipation in the ultrasound bath, and the corresponding acoustic pressure amplitude in the system (generated by transducers attached to the bottom of ultrasound bath) was measured as 1.9 bar using calorimetric method (Bhasarkar et al., 2013; Chakma and Moholkar, 2014). The ultrasound pressure amplitude in the reaction mixture in the beaker was also determined as 1.9 bar using calorimetric method. These measurements indicated negligible attenuation of ultrasound waves through the walls of beaker. The intensity of the acoustic energy emitted by transducers was 1.2 W/cm^2 with volumetric energy dissipation of 8.71 W/L. The schematic of the experimental setup is available in our previous study (Chakma and Moholkar, 2014) as well as in previous chapter (Chapter 3).

For UV assisted experiments, a blended high pressure mercury UV lamp (Starlite, 160 W) with a maximum peak emission wavelength at 365 nm was used. The UV lamp was placed exactly above the mouth of the beaker containing the reaction mixture, and the whole set up was placed in a black box to avoid diffusion/ interference of surrounding light radiation. The UV lamp was kept switched on for 15 min to obtain a proper diffusion of ultraviolet light irradiation inside the box. Experiments in all categories were repeated twice to assess reproducibility. Average values of textile dye degradation/ decolorization are considered for analysis in any experimental category.

4.3.3 Experimental procedure

Experiments were carried out in nine categories with permutation/ combination of following experimental conditions: (1) individual AOP of Fenton–like system; (2) individual AOP of photo–ferrioxalate system; (3) individual AOP of sonolysis; (4) saturation level of the medium (either saturated medium with dissolved oxygen concentration of 8 ppm or

unsaturated or degassed medium with dissolved oxygen content reduced to 3 ppm); and (5) sono-hybrid AOP with sparge gas. Each of these techniques alters the predominant physical and chemical mechanism of the textile dye decolorization system. The procedure used for degassing (or de–oxygenation), gas sparging in the medium and the rational underlying these techniques will be explained later.

In each experiment, 50 mL of dye solution with an initial dye concentration of 20 ppm (corresponding to concentrations of 0.04 mM and 0.063 mM for ARB and MB dye, respectively) was used. Other conditions and parameters of dye decolorization experiments, *viz*. pH and concentrations of Fe^{3+}, $C_2O_4^{2-}$ and H_2O_2, have been optimized in several sets of preliminary experiments (results are shown in preliminary experimental section) and optimized values were found to be $[Fe^{3+}]$ = 0.2 mM, $[C_2O_4^{2-}]$ = 0.6 mM, $[H_2O_2]$ = 5 mM and pH = 3. During the treatment of the dye solution with either mechanical stirring or sonication in any experimental category, small aliquots (1 mL) of reaction mixture were withdrawn at regular time intervals. After withdrawal of the sample, pH was adjusted to 7.5–8 using 4N NaOH solution to quench the oxidation reactions. Raising of the pH of aliquot results in precipitation of Fe(III), which was separated by filtration of the sample using 0.22 μm filter paper. The residual concentration of dye in the filtrate was analyzed using UV–Vis spectrophotometer (Model: Lambda 35, Perkin Elmer) at wavelengths of 512 nm and 663 nm for the ARB and MB dye, respectively. The percentage efficiency (η%) of dye decolorization was defined as: $(C_o - C_t)/C_o \times 100$, where, C_o is the initial concentration of dye, and C_t is the concentration of dye at time t (min).

For experiments with unsaturated medium (or reduced dissolved oxygen content of the medium), water used for preparing dye solution was subjected to a vacuum of ~ 600 mm Hg (or absolute pressure of 160 mm Hg) using a vacuum pump (Make: Riviera, Model: TID–25–S). To ensure effective degassing (or de-oxygenation), water was heated to 70°C with

continuous vigorous stirring after vacuum treatment. The concentration of dissolved oxygen in the solution was determined using Winkler titration method. This procedure lowered the dissolved oxygen content of the medium to 3 ppm.

4.3.4 Kinetics of decolorization

The degradation pathway of both ARB and MB dye has complex chemistry involving formation of numerous intermediates. Several earlier authors have dealt with this matter (for example: Thiam et al., 2015; Xia et al., 2014; Yu and Chuang, 2008; Houas et al., 2001; Wang et al., 2014). The main chemical mechanism of degradation is hydroxylation / oxidation induced by $^{\bullet}OH$ and $HO_2^{\bullet}$ radicals formed by AOPs. Many of these intermediates are unstable and difficult to monitor using standard techniques like GC or HPLC. In view of this difficulty, we have assumed that overall kinetics of dye degradation follows pseudo 1st order kinetics with respect to dye concentration. As stated in the tables of experimental results, description of dye degradation / decolorization profile using pseudo 1st order kinetic model has yielded regression coefficients > 0.85, indicating excellent fit of this model to the decolorization process.

4.4 CAVITATION BUBBLE DYNAMICS MODEL

As noted earlier, ultrasound, and its secondary effect, cavitation give rise to physical and chemical effects that contribute to enhancement of the kinetics of the reaction system. We have estimated the magnitudes of these effects using a mathematical model for cavitation bubble dynamics. Before description of this model, we would like to discuss the rational underlying the technique of variation in dissolved gas content and addition of alcohol in the medium employed in experiments.

In the present study, the three experimental techniques employed are: (1) degassing

(or de-oxygenation) of the medium, (3) sparging of gas through the reaction mixture, and (2) addition of alcohols to reaction mixture. All of these techniques have implication on the cavitation phenomenon. For occurrence of cavitation phenomenon in liquid, nuclei are needed. These nuclei could be the gas pockets trapped in the crevices of solid boundaries in the medium or they could be tiny gas bubbles freely floating in the liquid. Degassing of the medium (by subjecting the medium to vacuum or heating of the medium) reduces both free and dissolved gas content of the medium, and increases the intensity of cavitation phenomena. In the context of present study, degassing of the medium also reduces the dissolved oxygen in the medium. As noted in section 2, chemical mechanisms of both sonolysis and photo–ferrioxalate system involve reactions with dissolved oxygen. Hence, variation in the dissolved oxygen content also affects the chemical mechanism dye decolorization / degradation. With sparging of gas through reaction mixture during treatment, additional nuclei get seeded in the medium, which increase the cavitation intensity. Sparging of gas also leaves the reaction mixture saturated with the gas – stripping away the dissolved oxygen in the medium. Depletion of dissolved oxygen in the medium affects the photo–ferrioxalate pathway, in which the $CO_2^{\bullet-}$ radical reacts with dissolved oxygen to yield $O_2^{\bullet-}$ and $HO_2^{\bullet}$ radical species, which lead to formation of H_2O_2 and Fenton–reaction.

Alcohol molecules are efficient radical scavenger. In the present context, there are two sources of radicals in the reaction mixture, viz. sonolysis and photo–ferrioxalate pathway. Addition of alcohols in the system can scavenge radicals produced through both pathways. As far as sonolysis is concerned, addition of alcohol in the system can also affect production of radicals. Alcohol molecules can adversely affect generation as well as of utilization of $^{\bullet}OH$ radicals, in the reaction mixture. As shown by Ashokkumar et al. (1997), alcohol molecules have tendency to adsorb onto the gas/ liquid interface of the bubble. These interfacially adsorbed molecules are able to evaporate into the bubble core during collapse.

During the compression phase of radial bubble motion, as the size of the bubble (and hence the area of bubble interface) reduces at fast rate, lateral interaction between the adsorbed alcohols molecules causes expulsion of some molecules in the bulk solution, while some molecules get evaporated into the bubble core. This phenomenon causes "quenching" effect in the transient collapse of bubble that reduces the intensity of the temperature and pressure peak reached in the bubble. However, the physical effects induced by transient cavitation, i.e. micro–turbulence and shock waves, remain unaffected. Addition of alcohols in the reaction mixture thus gives a means of discriminating between the relative influence of physical and chemical effects of cavitation on the reaction.

In the present study, the diffusion limited model for cavitation bubble dynamics has been used (Toegel et al., 2000). This model is based on hypothesis that solvent vapor entrapment in the bubble during transient collapse is diffusion–limited process. A brief description of this hypothesis is as follows: the expansion of the bubble in the rarefaction half cycle of ultrasound is accompanied by evaporation of the solvent at the bubble interface. Vapor molecules diffuse towards the bubble core. In the subsequent compression phase, the vapor molecules diffuse towards the bubble interface and condense. However, in the final moments of bubble collapse, the velocity of the bubble wall (or bubble interface) becomes extremely fast, i.e. equal to or even greater than the velocity of sound in the medium. At this condition, the time scale of the bubble motion becomes smaller than the time scale of diffusion of vapor molecules. This essentially means that the vapor molecules do not have sufficient time to diffuse towards the bubble interface and undergo condensation. Thus, the solvent vapor gets entrapped in the bubble. Moreover, the vapor molecules that have diffused to the bubble interface also cannot completely stick to the surface to undergo phase change. This phenomenon also causes non–equilibrium phase change in the bubble and entrapment of the vapor molecules. The compression of the bubble is extremely fast and adiabatic. The

temperature and pressure inside the bubble reach extreme (5000 K and 500 bar) and the vapor entrapped in the bubble undergoes thermal dissociation at these conditions. A wide variety of species are formed out of dissociation, some of which are radical species. At the point of maximum compression (or minimum bubble radius) the bubble may get fragmented and the bubble contents are released into the bulk liquid. The radicals released from the bubble can induce reactions in the liquid medium.

The diffusion limited bubble dynamics model comprises of 4 equations that take into account essential physics and chemistry of bubble dynamics using boundary layer approximation (Storey and Szeri, 2000), *viz*. (1) Keller–Miksis equation for the radial motion of the bubble; (2) Equation for the diffusive flux of water vapor through bubble wall, (3) Equation for heat conduction through bubble wall; and (4) Overall energy balance treating the cavitation bubble as an open system. The essential equations (along with relevant boundary conditions) and thermodynamic data of this model are given in Tables 2.1A & 2.1B (in Chapter 2). Equations for diffusive flux and conductive heat transfer requires thermal conductivity and diffusion coefficient (i.e. transport parameters). These are determined at the bulk temperature of the liquid medium using Chapman–Enskog theory that employs Lennard–Jones 12–6 potential. Dimensional analysis has been used to estimate thermal and diffusive penetration depths. During the bubble expansion, the gas dissolved in the liquid can also diffuse inside the bubble. However, gas diffusion is a much slower process than cavitation bubble dynamics. Typically, the time scale for the diffusion of gases is of the order of milliseconds, while the time scale for the radial motion of bubble is of the order of microseconds. Thus, diffusion of gas across bubble interface for a period of few tens of acoustic cycles is negligible. The equations of diffusion–limited model of cavitation bubble dynamics can be solved simultaneously using Runge–Kutta adaptive step size method (Press et al., 1992).

Some experimental categories (viz. categories 4A, B and C) of present study make use of sparge gas. For these categories, the cavitation bubble is considered to be made up of sparge gas. For other categories, an air bubble is considered as the cavitation bubble. The bubble collapse (or essentially the bubble fragmentation) is assumed to occur at the first compression after an initial expansion. The thermodynamic parameters for gases and wter were taken from Hirschfelder et al. (1954) Condon and Odishaw (1958) and Reid et al. (1987). Other numerical values of different parameters used in the simulation of bubble dynamics equation are: ultrasound frequency (f) = 40 kHz; ultrasound pressure amplitude (P_A) = 190 kPa (determined using calorimetric techniques); vapor pressure of liquid medium (water) = 2500 Pa (calculate using Antoine type correlation), density of water (ρ_L) = 1000 kg/m^3, kinematic viscosity of water (ν) = 10^{-6} Pa–s, surface tension of water (σ) = 0.072 N/m, sonic velocity in water (c) = 1481 m/s. The equilibrium bubble radius (R_o) is difficult to measure experimentally and usual approach is to assume a representative value for the same. Larger bubbles (size > 50 microns) have sufficient buoyancy to rise to surface of the liquid and escape. Therefore, we have considered bubble sufficiently small to undergo transient collapse at the conditions of frequency or ultrasound pressure amplitude present in the sonication bath used in this study. Typically, for the ultrasound frequencies in the range of 20–100 kHz, and (modest) ultrasound pressure amplitudes in the range of 1.5–2.5 bar, bubbles with initial radii < 10 μm undergo transient motion (Mettin et al., 1997). Considering this, an equilibrium bubble size of R_o = 10 μm has been assumed for simulations.

4.4.1 Physical and chemical effects of transient cavitation

***Sonochemical effect or quantification of radical generation by cavitation bubbles*:** The gas and vapor content of the cavitation bubble at the moment of transient collapse can be determined using numerical solution of cavitation bubble dynamics model. As note earlier,

the temperature and pressure in the bubble reaches extreme at the moment of transient collapse causing thermal dissociation of solvent vapor. The species generated out of solvent dissociation undergo reaction among themselves. Due to very small volume of the bubble at the point of maximum compression and very high temperature inside the bubble, the rates of reactions occurring among different chemical species present in the bubble are expected to be extremely fast. As a consequence, the bubble contents are likely to remain at thermodynamic equilibrium all through the radial motion of the cavitation bubble (Brenner et al., 2004). The equilibrium composition of the bubble contents at the conditions of transient collapse has been determined using non–stoichiometric model for equilibrium employing Gibbs free–energy minimization technique (www.factsage .com).

***Sonophysical effect of cavitation*:** In addition to the chemical effects stated above, radial motion of cavitation bubbles also induces several physical effects in the liquid medium through two phenomena, *viz*. micro–convection and shock or acoustic waves. The first phenomenon is essentially the oscillatory motion of liquid induced by volume oscillations of the bubble. The second phenomenon occurs due to reflection of converging fluid elements of the bulk liquid from the bubble interface as it comes to a sudden halt at the point of minimum radius during radial motion. The numerical solution of cavitation bubble dynamics model gives time history of bubble radius (R), bubble wall velocity (dR/dt) and bubble wall acceleration (d^2R/dt^2). Magnitudes of micro–convection velocity as well as acoustic (shock) waves can be calculated as follows (Leighton, 1994; Grossmann et al., 1997; Moholkar and Warmoeskerken, 2003):

Micro–convection: $$V_{turb}(r,t) = \frac{R^2}{r^2}\left(\frac{dR}{dt}\right)$$

Shock Waves (or Acoustic Waves): $$P_{AW}(r,t) = \frac{\rho}{4\pi r}\frac{d^2V_b}{dt^2} = \rho\frac{R}{r}\left[2\left(\frac{dR}{dt}\right)^2 + R\frac{d^2R}{dt^2}\right]$$

where V_b is the volume of the bubble. A representative value of r is taken as 1 mm.

4.5 PRELIMINARY EXPERIMENTAL RESULTS

As noted earlier, the experiments have been carried out in five categories. However, prior to main experiments, optimization of some parameters was done in preliminary experiments (with initial concentration of ARB dyes as 20 ppm), the results of which are described below:

***pH of the reaction medium*:** Fig. 4.1A shows the results of optimization of pH for fixed concentration of Fe^{3+} as 0.4 mM and oxalate concentration of 1.2 mM. Maximum color removal efficiency was seen at pH of 3. Reduction in color removal efficiency below pH 3 can be explained in terms of scavenging of the hydroxyl radicals by H^+ ions (Eq. 4.26):

$$^{\bullet}OH + H^+ + e^- \longrightarrow H_2O \qquad (4.26)$$

At lower pH, the reaction between H_2O_2 and Fe^{2+} also slows down due to higher stability of H_2O_2 by solvating a proton, which forms oxonium ion ($H_3O_2^+$) in the reaction medium (Eq. 4.27). $H_3O_2^+$ makes H_2O_2 electrophilic by enhancing its stability that results in reduction in its reactivity with Fe^{2+} ions (Daud et al., 2012).

$$H_2O_2 + H^+ \longrightarrow H_3O_2^+ \qquad (4.27)$$

On the other hand, for pH above 5, Fe^{3+} precipitates as oxyhydroxide, due to which radical production, via Fenton–like oxidation reactions are affected adversely. This phenomenon also causes reduction in decolorization efficiency. On the basis of these results, the optimum pH for decolorization was determined as 3.

***Molar ratio of Fe^{3+}–Oxalate*:** The results of effect of molar ratio of Fe^{3+} to oxalate ions on

decolorization of ARB dye (at concentration of Fe^{3+} = 0.4 mM, and pH = 3) are shown in Fig. 4.1B. As per the stoichiometry of $Fe_2(C_2O_4)_3^{3-}$ complex formation, 3 moles of $C_2O_4^{2-}$ combine with 2 moles of Fe^{3+}. Concurrent with this result, the decolorization efficiency increases with addition of oxalate ions till the ratio of $C_2O_4^{2-}/Fe^{3+}$ is 3. This essentially implies that layer and layer fraction of Fe^{3+} present in the reaction mixture forms a complex with oxalate, which undergoes dissociation in presence of UV radiation to generate radicals. The decolorization efficiency reduces as the oxalate/Fe^{3+} ratio either rises above or falls below 3. For $C_2O_4^{2-}/Fe^{3+} < 3$, some of the Fe^{3+} ions form hydroxyl – complexes, $Fe(OH)_3$, and precipitate. This phenomenon hinders the $^{\bullet}OH$ radical formation via both ferrioxalate pathway and Fenton–like pathway. For $C_2O_4^{2-}/Fe^{3+}$ ratios higher than 3, some oxalate remains unreacted in the system, and can scavenge the $^{\bullet}OH$ radicals generated in the system (Eq. 4.28) (Vedrenne et al., 2012; Monteagudo et al., 2013), which results in reduction in decolorization efficiency.

$$C_2O_4^{2-} + {}^{\bullet}OH \longrightarrow CO_2 + CO_2^{\bullet-} + OH^- \qquad (4.28)$$

***Concentration of Fe^{3+} in reaction mixture*:** The influence of amount of Fe^{3+} present in reaction mixture (for a fixed $C_2O_4^{2-}/Fe^{3+}$ ratio of 3) on extent of decolorization is shown in Fig. 4.1C. The $C_2O_4^{2-}/Fe^{3+}$ concentration ratio was fixed at 3, while the pH of the reaction mixture was also maintained at 3. The decolorization of ARB dye increased with Fe^{3+} till concentration of 0.2 mM. This result is attributed to greater extent of formation of $Fe_2(C_2O_4)_3^{3-}$ complex, which decomposes to generate Fe^{2+} and $C_2O_4^{\bullet-}$ radical. Thus, increase in Fe^{3+} concentration in the reaction mixture also causes a surge Fe^{2+} concentration. The Fe^{2+} ions can scavenge the $^{\bullet}OH$ radicals formed out of photo–ferrioxalate pathway as follows (Eq. 4.29) (Lucas and Peres, 2007):

$$Fe^{2+} + {}^{\bullet}OH \longrightarrow Fe^{3+} + HO^- \qquad (4.29)$$

The scavenging of $^{\bullet}OH$ radicals by Fe^{2+} causes reduction in the decolorization efficiency,

after the concentration of Fe^{3+} exceeds 0.2 mM. At higher concentration of Fe^{3+} and oxalate, the formation of ferrioxalate complex also increases and it can react with $CO_2^{\bullet-}$ (which plays an important role in generation of H_2O_2 through photo–ferrioxalate process) as shown in the below reaction (Eq. 4.30). This results reduction of *in–situ* H_2O_2 generation as described in earlier section, and hence, rate of decolorization.

$$CO_2^{\bullet-} + [Fe(C_2O_4)_3]^{3-} \longrightarrow Fe^{2+} + CO_2 + 3C_2O_4^{2-} \qquad (4.30)$$

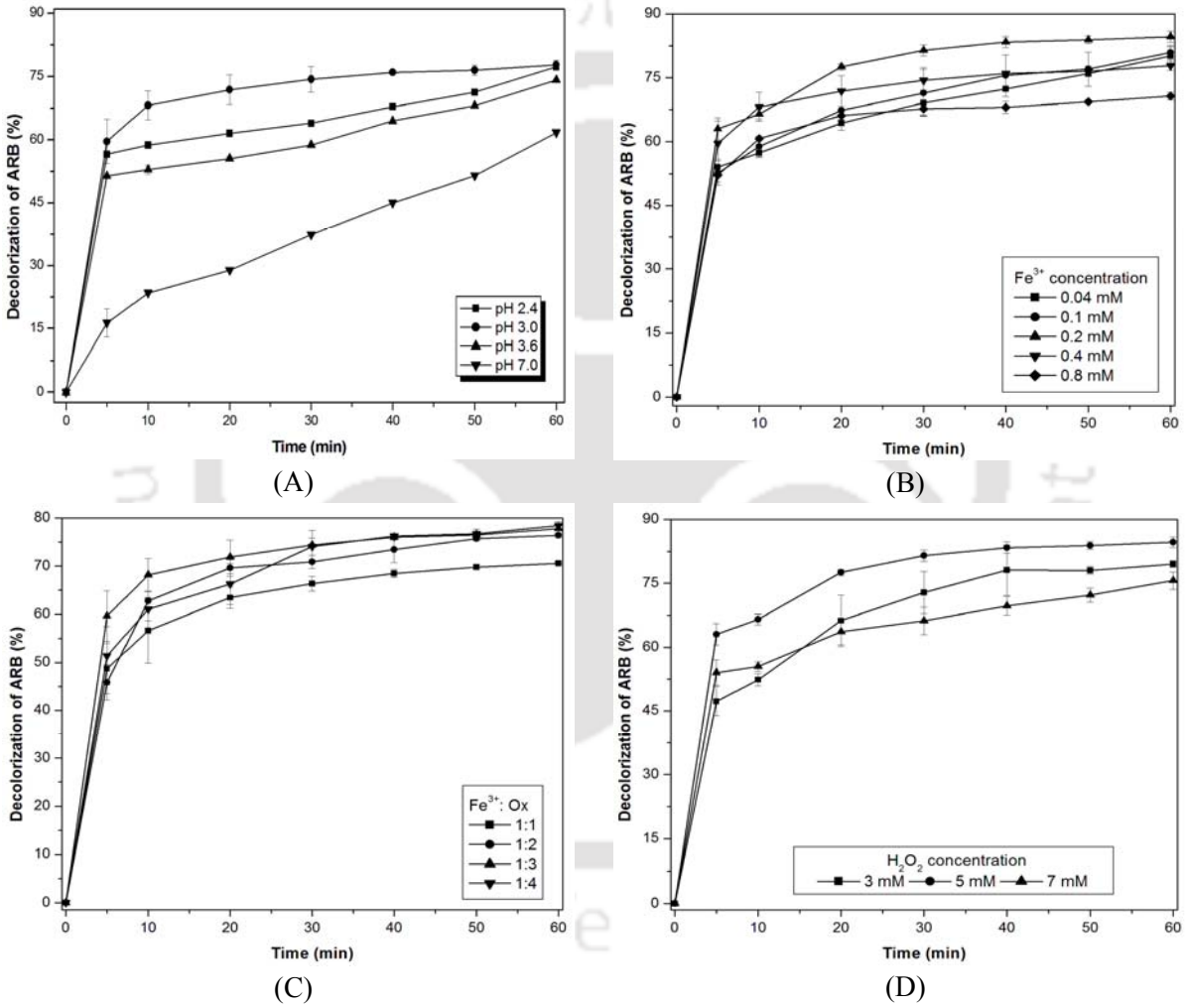

Figure 4.1: Results of preliminary experiments for optimization of decolorization of ARB dye. (A) Influence of pH on decolorization by sono–photo–ferrioxalate process. (B) Effect of Fe^{3+} ions on decolorization for molar ratio Fe^{3+}:Ox = 1:3. (C) Effect of Fe^{3+} to oxalate ions molar ratios on decolorization. (D) Effect of H_2O_2 concentration on decolorization.

***Concentration of H_2O_2 in reaction mixture*:** Addition of external H_2O_2 in the reaction

mixture has interesting effects on the decolorization process, as depicted in Fig. 4.1D. Addition of external H_2O_2 in the medium triggers Fenton–like reaction of Fe^{3+} with H_2O_2 that run simultaneously with the ferrioxalate reaction system. This phenomenon results in generation of additional $^{\bullet}OH$ radicals, and higher extent of decolorization. Therefore, rise in decolorization is observed as the H_2O_2 dosage increases from 3 to 5 mM. However, with further increase in the H_2O_2 concentration to 7 mM, the excess H_2O_2 scavenges the $^{\bullet}OH$ radicals produced in the system through following reaction (Eqs. 4.31 and 4.32); which causes reduction in decolorization (Chakma and Moholkar, 2013, 2014).

$$H_2O_2 + {}^{\bullet}OH \longrightarrow H_2O + HO_2^{\bullet} \qquad (4.31)$$

$$HO_2^{\bullet} + {}^{\bullet}OH \longrightarrow H_2O + O_2 \qquad (4.32)$$

Thus, the optimum concentration of H_2O_2 in the process was found to be 0.2 mM.

4.6 RESULTS AND DISCUSSION

4.6.1 Results of dye decolorization experiments

The results of dye decolorization in nine experimental categories for azo dye of ARB and non–azo dye of MB are given in Tables 4.1 & 4.2, respectively. The time profiles of dye decolorization in nine experimental categories are shown in Figs. 4.2–4.4 for both dyes. Representative results of simulations of cavitation bubble dynamics are given in Fig. 4.5A for a 5 μm air bubble and Fig. 4.5B for 10 μm argon gas bubble, which shows time histories of radius of the bubble, temperature and pressure inside the bubble, extent of solvent vaporization in the bubble, the micro–convection and shock (or acoustic) waves generated by the bubble. The summary of the simulation results for saturated and unsaturated medium is presented in Table 4.3. The summary of experimental results obtained in presence and absence of sparge gases and alcohols are presented in Fig. 4.6 and Tables 4.4 & 4.5**.** It could be seen that the smaller bubble of 5 μm (representing unsaturated liquid medium) undergoes

more intense collapse, with higher peaks of temperature and pressure attained during collapse, than the 10 μm bubble (representing saturated medium). This essentially means that the sonochemical effect of radical production is higher in unsaturated medium, as represented by mole fractions of ˙OH and ˙O radicals for 5 μm bubble, which are one order of magnitude higher than those for 10 μm bubble. Quite interestingly, the physical effect of micro–turbulence shows an inverse trend. In this case, the magnitude of micro–convection velocity generated by the 10 μm bubble is greater than 5 μm. Nonetheless, the pressure amplitude of the acoustic waves generated by 5 μm bubble is higher than the 10 μm bubble.

It is generally accepted that sonochemical effect (i.e. attack of •OH radicals generated by transient cavitation) contributes to degradation of organic pollutant. However, in the context of present study, in which dye decolorization is used as model reaction, both physical and chemical effects of cavitation can be of relevance. Saharan et al. (2012) have demonstrated that high shear generated by micro–convection and acoustic waves can break the chromophores of the dye molecules, leading to decolorization. This, of course, is the initial step in decolorization, and does not lead to complete mineralization. The complete mineralization is achieved by reactions induced by oxidizing radicals.

Table 4.1: Decolorization of Acid red B (ARB) dye in different experimental categories

Experimental category		Decolorization of ARB (η%)		k (s^{-1})	R^2
		5 min	60 min		
1	US alone	2.02 ± 0.28	14.76 ± 0.78	3.73E–05	0.89
2	MS + FeOX + UVA	39.14 ± 0.47	68.14 ± 0.19	1.01 E–03	0.88
3	MS + Fenton like	49.87 ± 0.89	66.36 ± 1.86	1.66E–03	0.90
4	US + FeOX + UVA	34.75 ± 0.70	71.74 ± 0.54	1.16E–03	0.88
5	US + Fenton like	53.08 ± 2.64	68.94 ± 3.34	1.78E–03	0.88
6	MS + Fenton like+ FeOX + UVA – Saturated	59.36 ± 4.0	86.53 ± 0.19	2.03E–03	0.89
7	US + Fenton like+ FeOX + UVA – Saturated	63.04 ± 2.52	85.87 ± 1.90	2.27E–03	0.87
8	MS + Fenton like+ FeOX + UVA – Unsaturated	58.65 ± 4.31	86.31 ± 0.58	2.04E–03	0.89
9	US + Fenton like+ FeOX + UVA – Unsaturated	55.74 ± 1.67	84.63 ± 1.24	1.80E–03	0.88

Table 4.2: Decolorization of Methylene blue (MB) dye in different experimental categories

Experimental Category		Decolorization of MB (η%)		k (s^{-1})	R^2
		5 min	60 min		
1	US alone	1.01 ± 0.4	6.84 ± 0.56	2.70E–05	0.98
2	MS + FeOX + UVA	44.81 ± 2.04	56.71 ± 3.37	1.31E–03	0.83
3	MS + Fenton like	96.48 ± 1.36	99.40 ± 1.40	1.11E–02	0.99
4	US + FeOX + UVA	47.53 ± 0.34	65.65 ± 0.11	1.45E–03	0.84
5	US + Fenton like	98.81 ± 0.96	99.65 ± 0.49	1.47E–02	0.99
6	MS + Fenton like + FeOX + UVA – Saturated	77.61 ± 1.05	98.64 ± 0.02	4.71E–03	0.99
7	US + Fenton like + FeOX + UVA – Saturated	78.05 ± 0.88	96.39 ± 0.27	4.74E–03	0.99
8	MS + Fenton like + FeOX + UVA – Unsaturated	65.72 ± 2.19	99.02 ± 0.28	3.24E–03	0.99
9	US + Fenton like + FeOX + UVA – Unsaturated	69.55 ± 1.70	98.73 ± 0.68	3.67E–03	0.99

Note for Tables 4.1 & 4.2: 2.70E–05 should read as 2.70×10^{-5}, US – ultrasound, MS – mechanical stirring, k –pseudo 1st order kinetic constant calculated on the basis of 30 min of experimental data, R^2 –regression coefficient, FeOX – ferrioxalate ($Fe^{3+} + C_2O_4^{2-}$), Fenton like – ($Fe^{3+} + H_2O_2$)

Table 4.3: Summary of the simulations of cavitation bubble dynamics

Species	Bulk liquid medium: water	
	Air bubble (R_o = 5 μm)	Air bubble (R_o = 10 μm)
	T_{max} = 3878 K P_{max} = 6549 bar V_{turb} = 0.051 m/s P_{AW} = 48.27 bar	T_{max} = 2827 K P_{max} = 1905 bar V_{turb} = 0.156 m/s P_{AW} = 4.65 bar
	x_{N2} = 0.711 x_{O2} = 0.189 x_W = 0.099	x_{N2} = 0.715 x_{O2} = 0.19 x_W = 0.095
	Equilibrium mole fraction	
N_2	7.21E–01	6.97E–01
O_2	1.51E–01	1.70E–01
NO	9.07E–02	3.38E–02
H_2O	1.85E–02	9.21E–02
OH	1.03E–02	5.01E–03
O	5.60E–03	5.71E–04
NO_2	1.89E–03	7.79E–04
N_2O	3.73E–04	6.96E–05
HO_2	6.12E–04	2.59E–04
H_2	2.66E–04	1.25E–04
H	2.59E–04	2.30E–05
HNO_2	1.98E–04	9.94E–05
HNO	5.88E–05	7.45E–06
H_2O_2	2.36E–05	2.07E–05
O_3	1.72E–05	2.07E–06
N	1.18E–05	–
NH	1.32E–06	–

Notation: 1.32E–06 should read as 1.32×10^6, R_o – initial radius of the cavitation bubble; T_{max} – temperature peak reached in the bubble at the time of first collapse; P_{max} – pressure peak reached in the bubble at the time of first collapse, V_{turb} – average velocity of the micro–turbulence generated by cavitation bubble (estimated at 1 mm distance from bubble center); P_{AW} – pressure amplitude of the acoustic wave generated by the cavitation bubble; x_W – mole fraction of water vapor in the bubble; x_{N2} – mole fraction of nitrogen in the bubble; x_{O2} – mole fraction of oxygen in the bubble

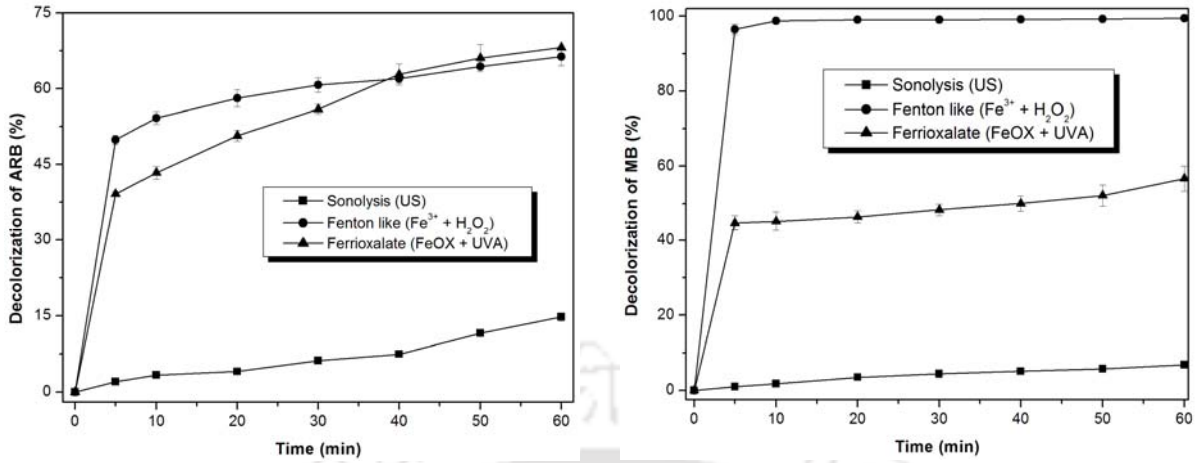

(A) (B)

Figure 4.2: Time histories of decolorization of the textile dyes with individual AOPs. (A) Decolorization of ARB dye. (B) Decolorization of MB dye. Experimental conditions: [ARB] = 0.04 mM, [MB] = 0.063 mM, $[Fe^{3+}]$ = 0.2 mM, $[C_2O_4^{2-}]$ = 0.6 mM, $[H_2O_2]$ = 5 mM, pH = 3, T = 298 K

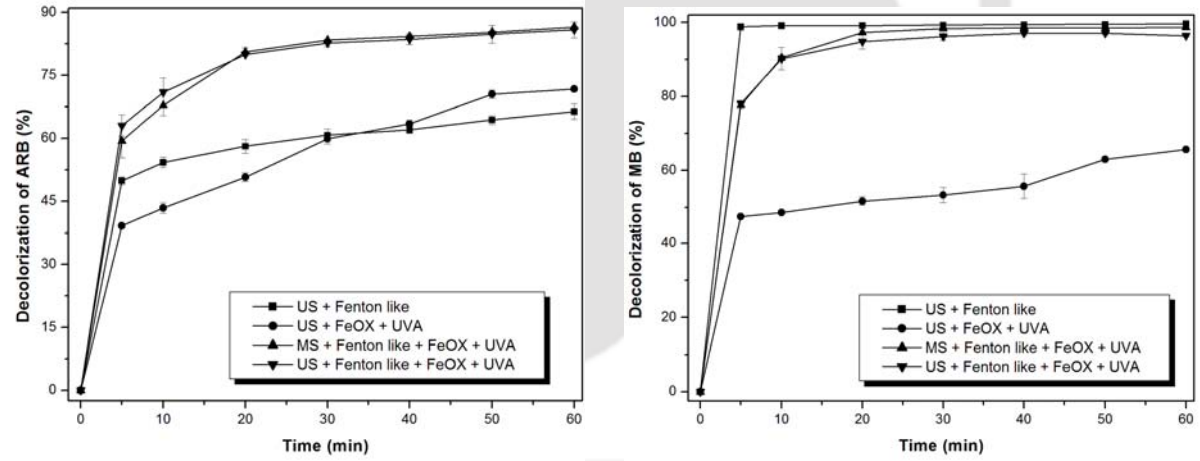

(A) (B)

Figure 4.3: Time histories of decolorization of the textile dyes with hybrid AOPs. (A) Decolorization of ARB dye. (B) Decolorization of MB dye. [ARB] = 0.04 mM, [MB] = 0.063 mM, $[Fe^{3+}]$ = 0.2 mM, $[C_2O_4^{2-}]$ = 0.6 mM, $[H_2O_2]$ = 5 mM, pH = 3, f = 40 kHz, T = 298 K

In Figs. 4.2–4.4, the extent of dye decolorization in the first five minutes of treatment, and complete treatment of 60 min has been given separately. As seen from the dye decolorization profiles given in Figs. 4.2–4.4, a major fraction of total decolorization (in 60

min of treatment) was achieved in first 30 min itself; and hence, the pseudo 1st order kinetic constant for dye decolorization has been determined using decolorization data for this period only. Some distinct features of dye decolorization that can be perceived from data presented in Tables 4.1–4.2 and the profiles shown in Figs. 4.2–4.4 are as follows:

(1) Trends in extent of decolorization with different experimental categories are similar for both dyes, although actual quantitative values of decolorization are different for ARB and MB dyes. The discrepancy of dissimilar extent of degradation is linked to the differences in chemical structure and the prevalent chemical mechanism of degradation of the two dyes. However, the qualitative similarity in trends in extent of decolorization is highlights resemblance of the physical mechanism of degradation of the two dyes.

(2) Among the individual AOPs, sonolysis gives least decolorization for both dyes. For the other two AOPs, photo–ferrioxalate and Fenton–like systems, significant decolorization is observed in 60 min treatment. Almost total decolorization of MB is achieved in 60 min of treatment with Fenton–like system. The least decolorization for sonolysis can be explained as follows:

The radicals formed inside the cavitation bubble during transient collapse get released into the bulk medium with fragmentation of the bubble at the instance of maximum compression. However, these radicals are extremely unstable and do not diffuse into the liquid medium from the point of bubble collapse. This puts a strong limitation on the interaction between the radicals and the molecules – which could further lead to hydroxylation/ oxidation reactions. Only those dye molecules that are in close vicinity of the bubble interface are likely to intercept the radicals released from the bubble. Due to rather small concentration of the dye in the reaction mixture (20 ppm), the probabilities of presence of dye molecules at the bubble interface, and the interception of radicals by them are small, which leads to low extent of dye decolorization. Moreover, occurrence of transient cavitation

events is a highly sporadic phenomenon in space as well as time domain. As stated earlier, cavitation phenomenon induced by the gas nuclei present in the liquid medium, which are contributed by freely suspended bubbles and gas pockets trapped in the crevices of the solid boundaries in reaction system. The volumetric distribution of these nuclei in the reaction mixture is not likely to be uniform. As a consequence, production of oxidizing radicals through sonolysis is also not uniform phenomenon, which puts a severe limit on the yield (or extent of dye decolorization, in the present context) of the sonolysis process.

(3) Almost similar extent of dye decolorization in categories 2 and 4, in which individual AOP of photo–ferrioxalate with mechanical stirring and hybrid AOP of sono–photo–ferrioxalate was applied, indicates that contribution of chemical effect of sonolysis in the hybrid AOPs trivial. Most of the decolorization is achieved via the photo–ferrioxalate route, with ultrasound and cavitation contributing only in terms of physical effect of generating convection (or stirring) in the medium. This result is consistent for decolorization of both ARB and MB dye.

(4) Similar arguments also hold for categories 3 and 5, in which individual Fenton–like and the hybrid sono–Fenton–like systems have been applied. The extent of decolorization in these categories is almost similar, confirming only physical role of ultrasound and cavitation in the hybrid AOP. Again, this result is consistent for both ARB and MB dyes.

(5) Trivial role of sonolysis in the hybrid AOP is also evident from the extent of dye decolorization in categories 6 & 7 and 8 & 9. Application of sonolysis in addition to the Fenton–like system and photo–ferrioxalate results in minuscule rise in decolorization. The extent of decolorization obtained with binary AOP of Fenton–like + photo–ferrioxalate system is almost similar as for the ternary AOP of sonolysis + Fenton–like + photo–ferrioxalate system. This result is consistent for reaction systems with saturated and unsaturated media. As seen from the results of simulation of cavitation bubble dynamics, the

intensity of transient cavitation increases with unsaturation. Despite this, the contribution of chemical effect of sonolysis to the overall decolorization is trivial, for the reasons explained earlier.

(6) The relative contributions of Fenton–like and photo–ferrioxalate pathways in the binary hybrid AOPs applied in categories 6 and 8 can also be determined on the basis of chemical mechanism of the individual AOPs given in section 2. In these categories, H_2O_2 is added in excess, while oxalate addition is in stoichiometry, with respect to the Fe^{3+}. In such situation, Fe^{3+} is competitively consumed by H_2O_2 and $C_2O_4^{2-}$. Reaction of Fe^{3+} with H_2O_2 generates Fe^{2+}, which can further react with H_2O_2 through regular Fenton reactions to produce $^{\bullet}OH$ radicals. Thus, the pathways of photo–ferrioxalate system and Fenton–like system hinder each other, which results in negative or adverse synergy between these systems. Although extent of decolorization of both dyes with individual Fenton–like and photo–ferrioxalate systems is greater than 50%, the total decolorization with both AOPs applied together is less than 100%. This indicates negative synergy in the binary AOP. For both dyes, the extent of decolorization is almost similar for saturated medium as well as unsaturated medium, in which the dissolved oxygen content of the medium is lowered. The chemical mechanism of the Fenton–like AOP does not involve dissolved oxygen. In the chemical mechanism of photo–ferrioxalate pathway, however, combination of oxalate radical (produced from photo decomposition of $Fe_2(C_2O_4)_3^{3-}$) with dissolved oxygen produces radical species of $O_2^{\bullet-}$ and $^{\bullet}OH$ that contribute to decolorization / degradation of dye. Therefore, the extent of decolorization through photo–ferrioxalate pathway is expected to reduce with depletion of dissolved oxygen in unsaturated medium.

If the decolorization in categories 6 and 8 are compared for both dyes, we find negligible change in total decolorization for both dyes, although the kinetic constant for the MB dye reduces slightly with unsaturation. These results essentially indicate that contribution

of the photo–ferrioxalate pathway to the overall decolorization is relatively lesser than the Fenton–like pathway.

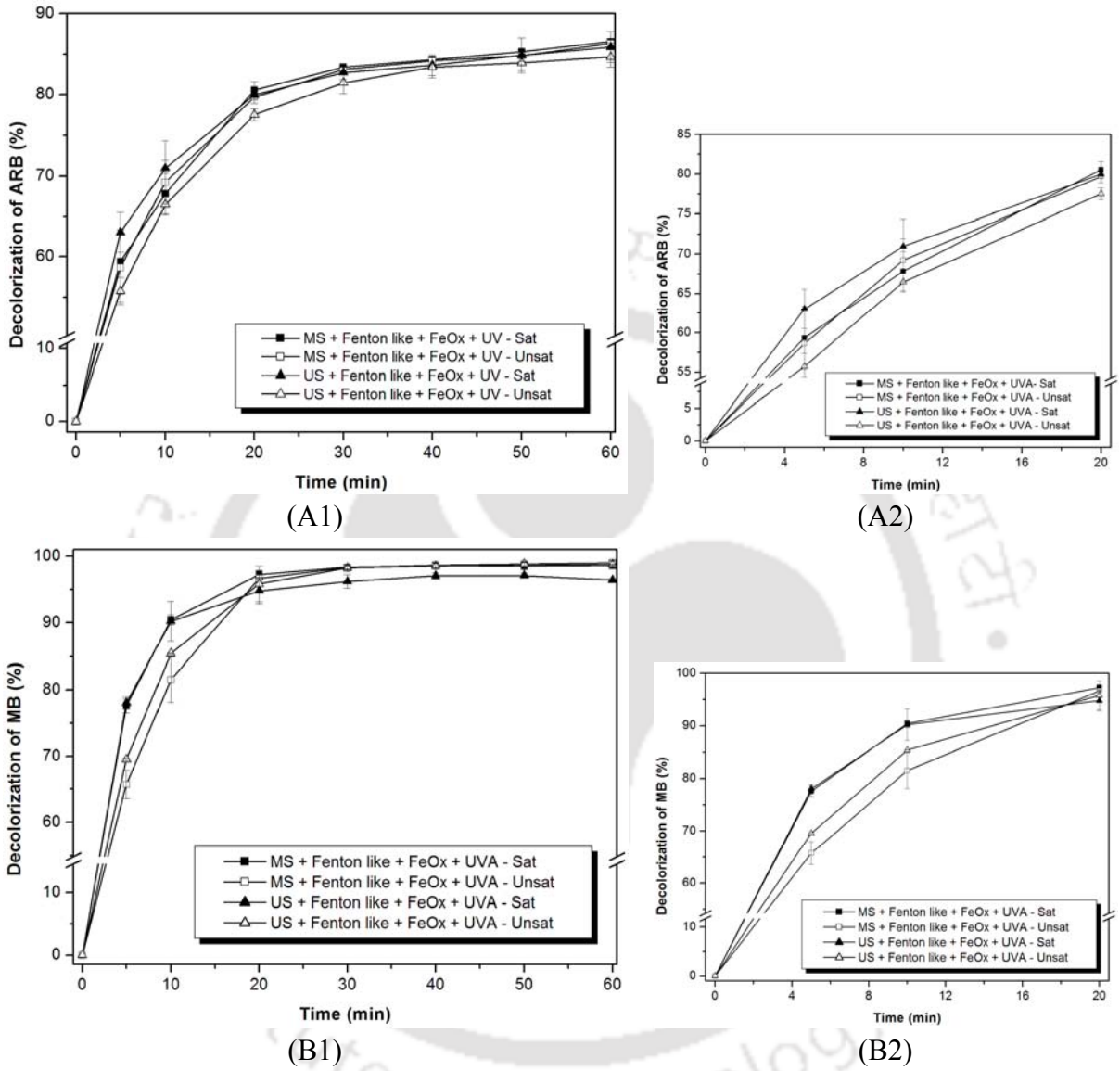

Figure 4.4: Influence of saturation level of the liquid medium on decolorization profiles of textile dyes in ternary hybrid AOP of (US+Fenton–like+Ferrioxalate). (A) Decolorization profiles of ARB dye. (A.1) Total decolorization profile (up to 60 min), (A.2) Enlarged view of the initial decolorization profile (for first 20 min). (B) Decolorization profiles for MB dye. (B.1) Total decolorization profile (up to 60 min), (B.2) Enlarged view of the initial decolorization profile (for first 20 min). Experimental conditions: [ARB] = 0.04 mM, [MB] = 0.063 mM, $[Fe^{3+}]$ = 0.2 mM, $[C_2O_4^{2-}]$ = 0.6 mM, $[H_2O_2]$ = 5 mM, pH = 3, f = 40 kHz, T = 298 K.

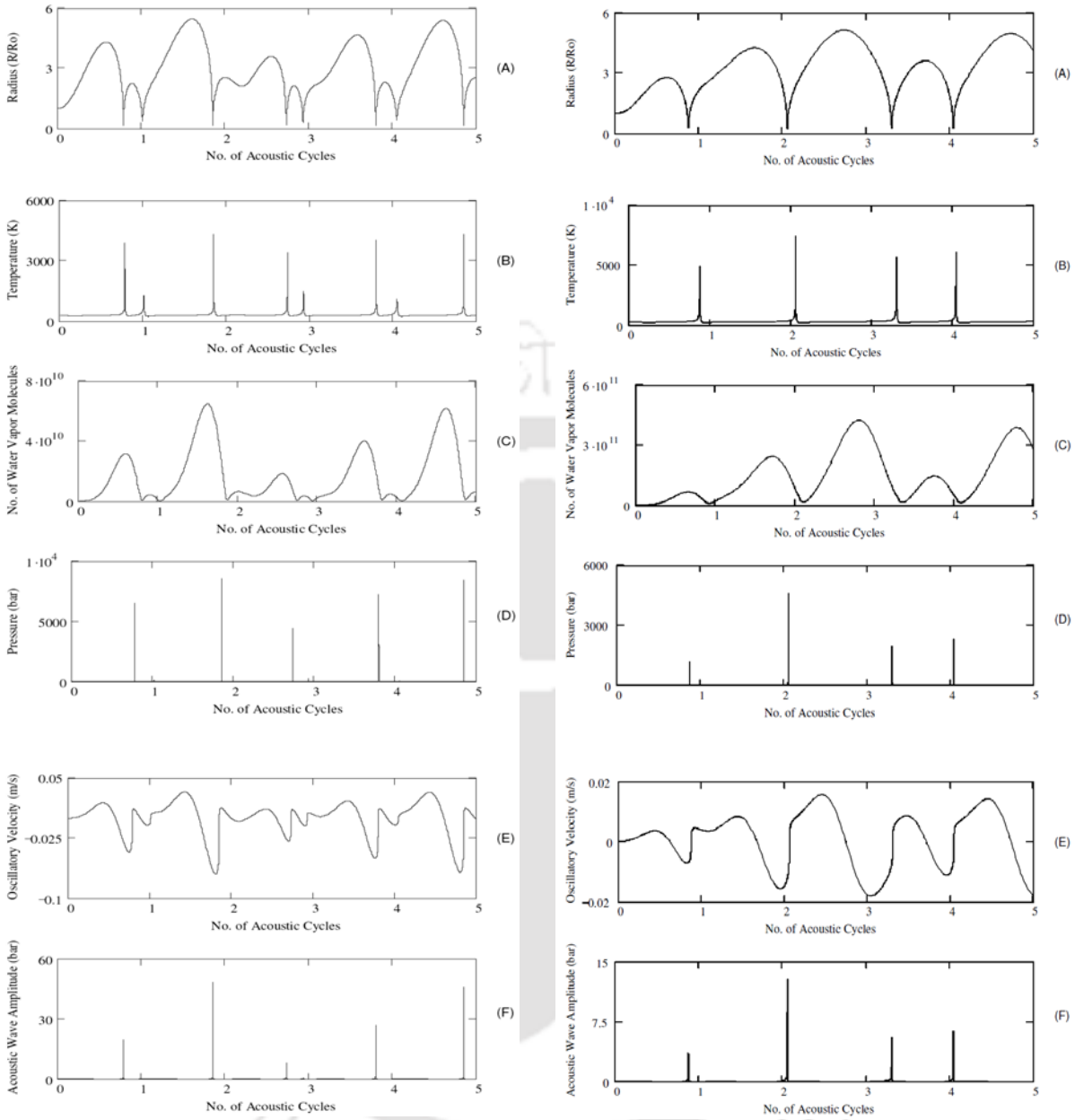

Figure 4.5: Simulations of cavitation bubble dynamics for a 5 μm air bubble and 10 μm argon bubble in water (f = 40 kHz, P_{AW} = 1.9 bar). Time history of (A) radius of the bubble; (B) temperature in the bubble; (C); water vapor molecules in the bubble (D) pressure in the bubble; (E) microturbulence generated by the bubble; (F) acoustic waves emitted by the bubble.

(7) Among all four gases, argon bubble undergoes most intense collapse with peak temperature of 4932 K reached inside the bubble. Oxygen bubble has the lowest temperature

at transient collapse. This result is attributed to lowest heat capacity of argon, which is a monatomic gas, as compared to nitrogen, oxygen and air which are diatomic gases. On the other hand, the pressure peak attained inside argon bubble is significantly smaller than the other three gases. In category 10, in which sparge gas was used, the maximum enhancement in decolorization, as compared to category 7, was obtained for argon (Ar). This result can very well be explained on the basis of simulation results. The temperature peak obtained at transient collapse, and the production of oxidizing radicals, is highest for argon. Therefore, the cavitation intensity in the medium shows highest rise for argon. The extent of increase in decolorization obtained for oxygen and nitrogen is lesser due to lower extent of radical production. Among these two gases, oxygen gives higher decolorization due to more radical production.

Nonetheless, comparing the extent of decolorization is category 10 for all sparge gases with that of category 7, a modest enhancement of only ~ 5–15% is seen. This result also confirms the subordinate contribution of sonolysis to dye decolorization in hybrid advanced oxidation processes.

(8) Addition of alcohol to reaction mixture (category 11) has two important consequences, viz. scavenging of the $^{\bullet}OH$ radicals and quenching (i.e. reduction in temperature and pressure peak reached in the bubble at the instance of collapse) of the transient cavitation, as explained in section on cavitation bubble dynamics. The photo–ferrioxalate pathway of decolorization involves several oxidizing radicals such as $O_2^{\bullet-}$, $^{\bullet}OH$ and $HO_2^{\bullet}$. Stylidi et al. (2004) have reported photocatalytic degradation of the azo dye Acid Orange 7, and have proposed a reaction pathway for degradation. The degradation of the dye molecule begins with cleavage of the molecules in vicinity of the azo bond chromophore with formation of intermediates with naphthalenic rings. These intermediates are attacked by three oxidizing species, *viz*. $O_2^{\bullet-}$, $^{\bullet}OH$ and $HO_2^{\bullet}$ to yield intermediates such as benzoic acid, 2–

methyl benzoic acid, phenol and benzoquinone. A similar chemical mechanism for degradation of Acid Red B (the model in present study) is also reported by Gao et al. (2012).

Alcohol addition to the reaction mixture helps in discriminating the contribution of and role of $^{\bullet}OH$ radical in chemical pathway of decolorization. Alcohols scavenge the $^{\bullet}OH$ radicals generated by sonolysis, Fenton reactions (or Fenton–like reactions) induced by externally added H_2O_2 with Fe^{3+}. In addition, the H radicals produced by cavitation bubbles are also effectively scavenged by alcohol molecules. The typical reactions in this case are (Janata, 2002): (1) $^{\bullet}OH + RH \rightarrow R^{\bullet} + H_2O$; (2) $H^{\bullet} + RH \rightarrow R^{\bullet} + H_2$; and (3) $R^{\bullet} + R^{\bullet} \rightarrow$ Products. Significant decolorization observed in presence of both alcohols, viz. methanol and 2–propanol, confirms dominant role of superoxide $O_2^{\bullet-}$ and hydroperoxy $HO_2^{\bullet}$ radicals in the chemistry of decolorization as compared to $^{\bullet}OH$ radical.

Among the two alcohols used for scavenging of $^{\bullet}OH$ radicals, higher reduction of decolorization is obtained for 2–propanol. Methanol has higher vapor pressure (13.2 kPa) than 2–propanol (5.2 kPa) at the bulk liquid temperature of 25°C (298 K). As a result, methanol is expected to cause greater quenching of the transient cavitation due to evaporation into the bubble to greater extent leading to larger reduction in radical production and decolorization. In contrast to this conjecture, 2–propanol is seen to reduce decolorization to higher extent. We explain this result on the basis of hypothesis of Ashokkumar et al. (1997) mentioned in previous section (Section 3). Due to higher molecular weight, 2–propanol (mw 60.1 g/mol) molecules adsorb onto the bubble/liquid interface to higher extent than methanol (mw 32.04 g/mol). At the final moments of collapse, some fraction of the adsorbed 2–propanol molecules gets “squeezed” into the bubble and quenches the transient collapse. Another factor that contributes to effective scavenging of $^{\bullet}OH$ radicals by 2–propanol is the intrinsic reactivity of alcohol molecules with $^{\bullet}OH$ radicals. The specific kinetic constant of reaction of $^{\bullet}OH$ radicals with 2–propanol is 2×10^9 $dm^3/mol{\cdot}s$, while the same for methanol 9

$\times 10^8$ dm^3/mol·s (Janata, 2002).

Table 4.4: Summary of decolorization of ARB at optimum condition under sono–photo–ferrioxalate system with various operating conditions

Experimental category		Decolorization of ARB (η%)		k (s^{-1})	R^2
		5 min	60 min		
10A	US + Fenton like+ FeOX + UVA + N_2 sparging	64.11 ± 0.8	90.75 ± 0.6	2.04 E–03	0.86
10B	US + Fenton like+ FeOX + UVA + O_2 sparging	66.47 ± 1.0	93.55 ± 1.3	2.55 E–03	0.90
10C	US + Fenton like+ FeOX + UVA + Ar sparging	69.52 ± 0.1	96.42 ± 0.8	2.97 E–03	0.93
11A	US + Fenton like+ FeOX + UVA + 2–propanol (25 mM)	47.84 ± 0.7	61.45 ± 1.1	1.49 E–03	0.86
11B	US + Fenton like+ FeOX + UVA + 2–propanol (50 mM)	44.93 ± 1.5	57.11 ± 0.2	1.32 E–03	0.83
11C	US + Fenton like+ FeOX + UVA + Methanol (25 mM)	51.24 ± 1.4	67.29 ± 3.8	1.63 E–03	0.85
11D	US + Fenton like+ FeOX + UVA + Methanol (50 mM)	45.73 ± 0.1	60.27 ± 2.1	1.44 E–03	0.88

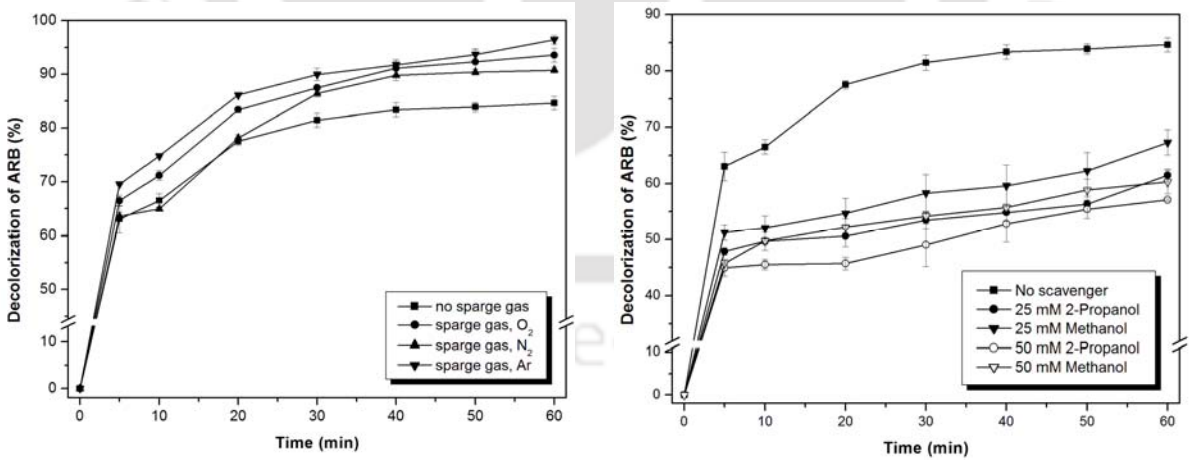

(A) (B)

Figure 4.6: Time profiles of ARB dye decolorization in different experimental categories: (A) Decolorization profile in presence and absence of sparge gas, (B) Decolorization profile with and without addition of 2–propanol and methanol as •OH radical scavengers.

Table 4.5: Summary of the simulation results of cavitation bubble dynamics

Species	Bulk liquid medium: Water			
	Argon (10 μm)	**Oxygen (10 μm)**	**Nitrogen (10 μm)**	**Air (10 μm)**
	T_{max} = 4932 K P_{max} = 1191 bar V_{turb} = 0.017 m/s P_{AW} = 3.471 bar	T_{max} = 2694 K P_{max} = 2529 bar V_{turb} = 0.015 m/s P_{AW} = 6.972 bar	T_{max} = 2817 K P_{max} = 2384 bar V_{turb} = 0.0155 m/s P_{AW} = 6.149 bar	T_{max} = 2827 K P_{max} = 1905 bar V_{turb} = 0.0156 m/s P_{AW} = 4.65 bar
	x_{N2} = 0.0 x_{O2} = 0.0 x_W = 1.0	x_{N2} = 0.0 x_{O2} = 0.875 x_W = 0.125	x_{N2} = 0.874 x_{O2} = 0.00 x_W = 0.126	x_{N2} = 0.715 x_{O2} = 0.19 x_W = 0.095
Equilibrium mole fraction at first collapse				
H_2O	2.81E–01	1.08E–01	1.05E–01	9.21E–02
O_2	4.86E–02	8.85E–01	3.25E–04	1.70E–01
N_2	–	–	8.89E–01	6.97E–01
OH	1.99E–01	5.44E–03	1.03E–03	5.01E–03
HOO	1.03E–03	7.97E–04	2.62E–06	2.59E–04
O	9.22E–02	6.59E–04	2.14E–05	5.71E–04
H	1.75E–01	6.34E–06	9.42E–05	2.30E–05
H_2O_2	7.11E–05	5.13E–05	1.14E–06	2.07E–05
H_2	2.03E–01	3.29E–05	2.80E–03	1.25E–04
O_3	–	2.07E–05	–	2.07E–06
NO	–	–	1.64E–03	3.38E–02
NO_2	–	–	1.87E–06	7.79E–04
HNO	–	–	1.92E–06	7.45E–06
N_2O	–	–	4.28E–06	6.96E–05
NH_3	–	–	2.70E–06	–
HNO_2	–	–	–	9.94E–05

Note: 2.70E–06 should read as 2.7×10^6, R_o – initial radius of the cavitation bubble; T_{max} – temperature peak reached in the bubble at the time of first collapse; P_{max} – pressure peak reached in the bubble at the time of first collapse, V_{turb} – average velocity of the micro–turbulence generated by cavitation bubble (estimated at 1 mm distance from bubble center); P_{AW} – pressure amplitude of the acoustic wave generated by the cavitation bubble; x_W – mole fraction of water vapor in the bubble; x_{N2} – mole fraction of nitrogen in the bubble; x_{O2} – mole fraction of oxygen in the bubble

4.6.2 Synergy of the hybrid AOPs

A useful tool to assess interactions among individual chemical pathways of different AOPs in a hybrid system on a gross level is to determine the synergy among the individual AOPs. The synergy could be defined on the basis of kinetic constants of decolorization, or on the basis of total decolorization achieved in hybrid system as compared to the individual systems. In the present case, we have used the former approach, and have defined synergy as:

$$\text{Synergy} = \frac{\text{kinetic constant in hybrid AOP} - \sum \text{kinetic constant of individual AOP}}{\sum \text{kinetic constant of individual AOP}}$$

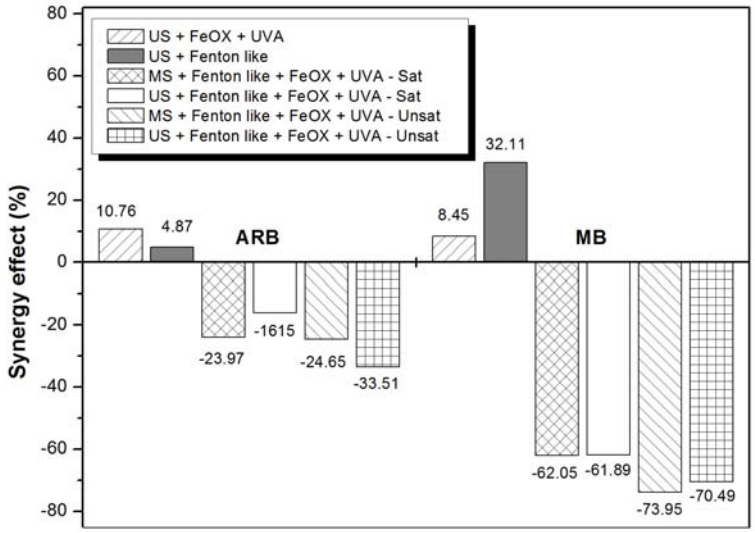

Figure 4.7: Synergism effect in hybrid advanced oxidation processes (HAOPs) for decolorization of Acid Red B (azo dye) and Methylene Blue (non–azo dye). Note: FeOX – ferrioxalate (Fe^{3+} + $C_2O_4^{2-}$)

The synergies in different hybrid AOPs, as determined by above formula, for both ARB and MB dyes are shown in Fig. 4.7. It could be seen that for binary AOPs of (sonolysis + Fenton–like) or (sonolysis + photo–ferrioxalate), the synergy is positive. On the other hand, for the ternary hybrid AOP of sonolysis + Fenton–like + photo–ferrioxalate the synergy is negative. Explanation for these trends can be given along the discussion presented in previous sections: For the binary AOPs, the physical effect of ultrasound and cavitation (i.e. generation of micro–turbulence in the medium) assists and boosts the chemical effect of Fenton–like and photo–ferrioxalate system. As noted earlier, the production of radicals through Fenton–like system or photo–ferrioxalate system is higher and volumetrically more uniform. The micro–convection generated by ultrasound and cavitation helps in effective utilization of these radicals by enhancing radical – dye molecule interaction. On the other hand, in ternary AOP

of sonolysis + Fenton–like + photo–ferrioxalate, the individual pathways of Fenton–like and photo–ferrioxalate systems hinder each other by competitive consumption of Fe^{3+}. This results in negative synergy. With unsaturation of the medium, the pathway of photo–ferrioxalate is further hindered due to scarcity of dissolved oxygen that reacts with oxalate radicals. This augments the negative synergy of ternary hybrid AOPs further. The numerical values of synergies in hybrid AOPs are different for the two dyes. However, the trends in synergy are same (i.e. positive synergy for binary AOP and negative synergy for ternary AOP), which indicates close resemblance in the physical mechanism of degradation of the two dyes.

4.7 CONCLUSION

In the present study, an attempt is made to gain insight into physical mechanism of binary and ternary hybrid AOPs with combination of sonolysis, Fenton–like system and photo–ferrioxalate system. The decolorization profiles of the two model dyes, viz. Acid Red B (azo dye) and Methylene Blue (no–azo dye), essentially reveal same trends in all experimental categories. This result points at similarities in the physical mechanism of decolorization/ degradation of the two dyes despite significant dissimilarity in the chemical structure. Among the individual AOPs, sonolysis is revealed to have least decolorization efficiency, which is attributed to highly sporadic nature of transient cavitation events and low probability of interception of the radicals generated from transient cavitation with dye molecules. Even for an unsaturated medium, in which the cavitation bubble undergoes more intense collapse, contribution of sonolysis to decolorization is interior compared to other two systems. The contribution of ultrasound and cavitation in hybrid AOP is, thus, mostly of physical nature. Coupling of sonolysis with either Fenton – like system or photo–ferrioxalate system gives enhanced decolorization due to positive energy.

However, coupling of all three AOPs gives a negative synergy due to interaction of the chemical mechanisms of Fenton–like and photo–ferrioxalate system. Dissolved oxygen in the reaction system is also revealed to have a crucial role. For unsaturated reaction systems with depleted dissolved oxygen, the pathway of photo–ferrioxalate is further hindered resulting in reduced in decolorization efficiency.

REFERENCES

Ashokkumar M, Hall R, Mulvaney P, Grieser F, Sonoluminescence from aqueous alcohol and surfactant solutions, J. Phys. Chem. B 1997, 101, 10845 – 10850.

Bhasarkar JB, Chakma S, Moholkar VS, Mechanistic features of oxidative desulfurization using sono-Fenton–peracetic acid (ultrasound/Fe^{2+}–CH_3COOH–H_2O_2) system, Ind. Eng. Chem. Res. 52 (2013) 9038-9047.

Brenner M, Hilgenfeldt S, Lohse D, Single-bubble sonoluminescence. Rev. Mod. Phys. 74 (2002) 425–484.

Chakma S, Moholkar VS, Investigations in synergism of hybrid advanced oxidation processes with combinations of sonolysis + Fenton process + UV for degradation of Bisphenol–A, Ind. Eng. Chem. Res. 53 (2014) 6855–6865.

Chakma S, Moholkar VS, Physical mechanism of sono-Fenton process, AIChE J. 59 (2013) 4303 – 4313.

Condon EU, Odishaw H, *Handbook of physics*, New York: McGraw Hill, 1958.

Daud NK, Akpan UG, Hameed BH, Decolorization of Sunzol Black DN conc. in aqueous solution by Fenton oxidation process: effect of system parameters and kinetic study, Desalin. Water Treat. 37 (2012) 1–7.

FACTSAGE, Access on March 2015, http://www.factsage.com/

Gao M, Zeng Z, Sun B, Zou H, Chen J, Shao L. Ozonation of azo dye Acid Red 14 in a

microporous tube–in–tube microchannel reactor: Decolorization and mechanism. Chemosphere 2012; 89:190–197.

Gogate PR, Tatake PA, Kanthale PM, Pandit AB, Mapping of sonochemical reactors: review, analysis, and experimental verification, AIChE J. 48 (2002) 1542–1560.

Grossmann S, Hilgenfeldt S, Zomack M, Lohse D, Sound radiation of 3 MHz driven gas bubbles, J Acoust Soc Am. 102 (1997) 1223–1227.

Hart EJ, Henglein A, Free radical and free atom reactions in the sonolysis of aqueous iodide and formate solutions, J. Phys. Chem. 89 (1985) 4342–4347.

Hart EJ, Henglein A, Sonochemistry of aqueous solutions: hydrogen-oxygen combustion in cavitation bubbles, J Phys Chem. 91 (1987) 3654–3656.

Hirschfelder JO, Curtiss CF, Bird RB, *Molecular theory of gases and liquids*, New York: Wiley, 1954.

Houas A, Lachheb H, Ksibi M, Elaloui E, Guillard C, Herrmann J-M, Photocatalytic degradation pathway of methylene blue in water, Appl. Catal. B Environ. 31 (2001) 145–157.

Janata E, Direct optical observation of the formation of some aliphatic alcohols, A pulse radiolysis study, Proc. Indian Acad. Sci. (Chem. Sci.) 114 (2002) 731–737.

Jeong J, Yoon J, Dual roles of $CO_2^{\bullet-}$ for degrading synthetic organic chemicals in the photo/ferrioxalate system, Water Res. 38 (2004) 3531–3540.

Leighton TG, The acoustic bubble, San Diego: Academic Press, 1994.

Lucas MS, Peres JA, Degradation of reactive black 5 by Fenton/UV-C and ferrioxalate/ H_2O_2/ solar light processes, Dyes and Pigments 74 (2007) 622-629.

Mettin R, Akhatov I, Parlitz U, Ohl CD, Lauterborn L, Bjerknes forces between small cavitation bubbles in a strong acoustic field, Phys. Rev. E 56 (1997) 2924-2931

Moholkar VS, Sable SP, Pandit AB, Mapping the cavitation intensity in an ultrasonic bath

using the acoustic emission. AIChE J. 46 (2004) 684–694.

Moholkar VS, Warmoeskerken MMCG, Integrated approach to optimization of an ultrasonic processor, AIChE J. 49 (2003) 2918-2932.

Monteagudo JM, Durán A, Culebradas R, San Martín I, Carnicer A, Optimization of pharmaceutical wastewater treatment by solar/ferrioxalate photo-catalysis, J. Environ. Manag. 128 (2013) 210 - 219.

Monteagudo JM, Durán A, López-Almodóvar C, Homogeneus ferrioxalate-assisted solar photo-Fenton degradation of Orange II aqueous solutions, App. Catal. B: Environ. 83 (2008) 46–55.

Press WH, Teukolsky SA, Flannery BP, Vetterling WT, *Numerical recipes*, New York: Cambridge University Press, 1992

Reid RC, Prausnitz JM, Poling BE, *Properties of gases and liquids*, New York: McGraw Hill, 1987.

Saharan VK, Pandit AB, Satishkumar PS, Anandan S, Hydrodynamic cavitation as an advanced oxidation technique for the degradation of Acid Red 88 dye, Ind. Eng. Chem. Res. 51 (2012) 1981–1989.

Storey BD, Szeri AJ, Water vapor, sonoluminescence and sonochemistry, Proc R Soc Lond Ser A 456 (2000) 1685-1709.

Stylidi M, Kondaride DI, Verykios XE, Visible light–induced photocatalytic degradation of Acid Orange 7 in aqueous TiO_2 suspension, Appl. Catal. B Environ. 47 (2004) 189–201.

Thiam A, Sirés I, Garrido JA, Rodríguez RM, Brillas E, Effect of anions on electrochemical degradation of azo dye Carmoisine (Acid Red 14) using a BDD anode and air-diffusion cathode, Separation and Purification Technology 140 (2015) 43–52.

Toegel R, Gompf B, Pecha R, Lohse D, Does water vapor prevent upscaling sonoluminescence? Phys Rev Lett. 85 (2000) 3165–3168.

Vedrenne M, Vasquez-Medrano R, Prato-Garcia D, Frontana-Uribe BA, Hernandez-Esparzaa M, de Andrés JM, A ferrous oxalate mediated photo-Fenton system: Toward an increased biodegradability of indigo dyed wastewaters, J. Hazard. Mater. 243 (2012) 292–301.

Wang X, Mei L, Xing X, Liao L, Lv G, Li Z, Wu L, Mechanism and process of methylene blue degradation by manganese oxides under microwave irradiation, Appl. Catal. B Environ. 160–161 (2014) 211–216.

Xia S-J, Zhou X-B, Shi W, Pan G-X, Ni Z-M, Photocatalytic property and mechanism studies on acid red 14 by M_xO_y/ ZnTi–layered double hydroxides (M = Fe, Sn, Ce), J. Mol. Catal. A Chem. 392 (2014) 270–277.

Yu Z, Chuang SSC, The effect of Pt on the photocatalytic degradation pathway of methylene blue over TiO2 under ambient conditions, Appl. Catal. B Environ. 83 (2008) 277–285.

Zhou D, Wu F, Deng N, Xiang W, Photooxidation of bisphenol A (BPA) in water in the presence of ferric and carboxylate salts, Water Res. 38 (2004) 4107–4116.

5

MECHANISTIC ANALYSIS OF SONO–PHOTOLYSIS PROCESS

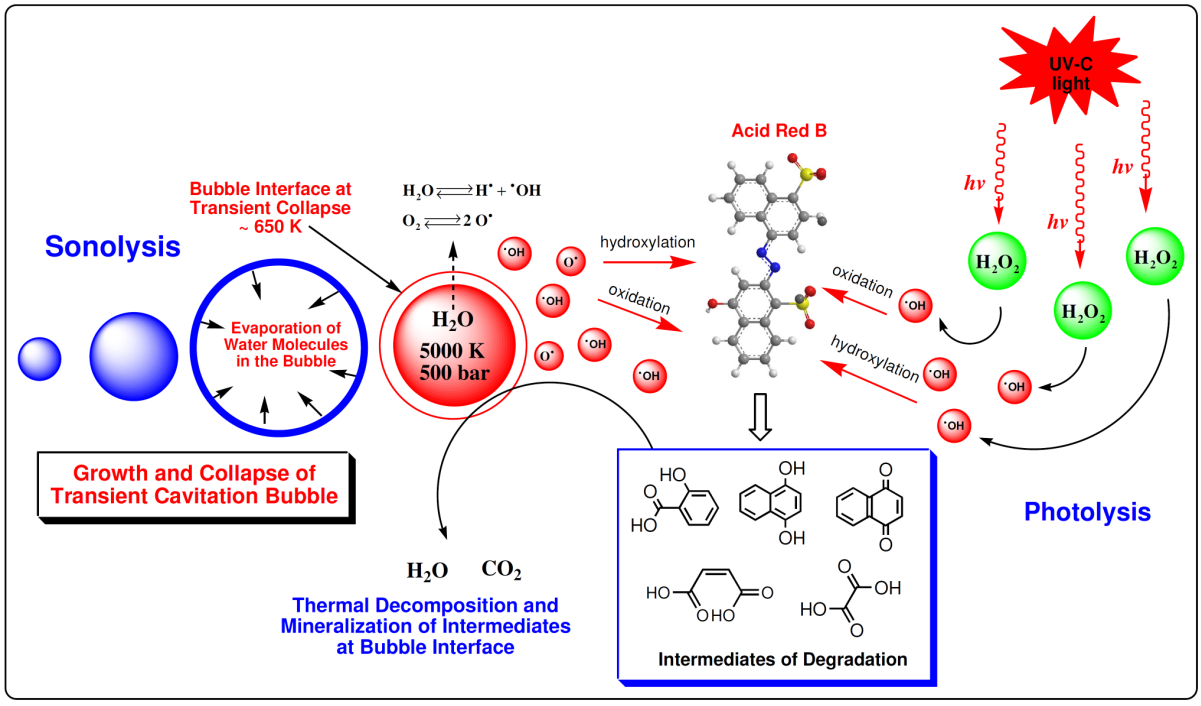

Mechanistic interactions between sonolysis and photolysis

CHAPTER 5

MECHANISTIC ANALYSIS OF SONO–PHOTOLYSIS PROCESS

5.1 INTRODUCTION

Previous three chapters dealt with hybrid AOP involving iron (sono-Fenton, sono-photo-Fenton and sono-photo-Ferrioxalate). Although these hybrid AOPs have demonstrated their efficacy in degradation of highly recalcitrant pollutants like azo, non-azo dyes and plastic intermediate of Bisphenol-A, the major limitation of these hybrid AOPs is the use of iron salt, and also use of acidic conditions for regeneration of Fe^{2+} in Fenton or Fenton-like processes. An alternate hybrid AOP is sono-photolysis, in which the conventional system of H_2O_2/UV-C is combined with sonolysis. This chapter deals with mechanistic investigations in this hybrid AOP.

The model system in our study is decolorization of the azo dye. We have used the methodology of coupling of experimental results on dye decolorization/ mineralization, and kinetic analysis of the decolorization profile using Arrhenius model with simulations of cavitation bubble dynamics. In addition, we have also studied intensification of sono–photolysis process, in terms of faster decolorization and higher mineralization of the ARB dye, with addition of sodium salts (chloride, sulphate and nitrate) to the reaction mixture.

5.2 MATERIALS AND METHODS

5.2.1 Materials

Hydrogen peroxide (H_2O_2, 30% v/v), NaOH (pellet form), H_2SO_4, NaCl, $NaNO_3$, and Na_2SO_4 were purchased from Merck India Ltd. The azo dye Acid Red B or Acid Red 14 (hereafter abbreviated as ARB) was procured from a local vendor a.b. Chemicals and Instruments, Guwahati, India. All chemicals were used as received without any pretreatment. The dye solutions for experiments were prepared using ultrapure water (≥18 ΩM·cm resistivity at 25^{o}C).

5.2.2 Experimental setup and procedure

Experiments were conducted in 6 categories as listed in Table 5.1 by permutation/combination of following techniques: (1) sonolysis, (2) mechanical stirring, (3) addition of H_2O_2, and (4) irradiation of UV–C light.

Experiments involving sonication were conducted in a dual frequency (37/80 kHz) ultrasonic bath (Model: P–30H, Elmasonic, Germany, capacity 2.75 L, Power: 130 W). The picture of the experimental setup is given in Fig. 5.1. This bath has the facility of automatic frequency tuning and amplitude compensation, which ensured constant power delivery to the reaction system during the sonication, despite changes occurring in reaction medium. The actual acoustic power input to the bath and pressure amplitude of the ultrasound waves generated thereby in the bath were determined using calorimetric technique (Chakma and Moholkar, 2014). The pressure amplitude of the ultrasound wave was calculated as 160 kPa. In each experiment, the ultrasonic bath was filled with 1.5 L of 0.04 mM (20 ppm) dye solution. The temperature of the dye solution during treatment was maintained constant at desired value by circulating water through a copper coil immersed in dye solution from a temperature–controlled water bath (Model: WB2000, Amkette Analytics). Experiments in

categories 2, 3 and 4 (refer to Table 5.1) were conducted at 298 K. Experiments in categories 1, 5 and 6 (viz. sonolysis, photolysis and sono–photolysis) were conducted at three temperatures, viz. 283, 298 and 313 K, for Arrhenius analysis (determination of activation energy and frequency factor).

For experiments with UV–C irradiation, an ultraviolet lamp with maximum peak emission wavelength of 254 nm was fixed above the ultrasonic bath, centrally over the surface of the dye solution in the bath. For safety measure, the whole setup was placed in a wooden black box to prevent the UV–C emission to surroundings. In all experiments involving UV, the UV lamp was kept switched on for 10 min prior to experiments for achieving uniform emission intensity of UV light.

For experiments with mechanical stirring, the experiments were conducted in the ultrasonic bath itself. However, bath was kept switched off and no sonication was applied. Mechanical agitation to the dye solution in the ultrasonic bath was provided using an agitator (4 blade propeller, rotation speed 300 rpm) operated by motor with digital speed control (please refer to the picture of experimental setup provided in supplementary material).

In a typical experiment, the pH of the solution was adjusted as 7 by addition of either NaOH or H_2SO_4 to desired value. In experimental categories 2, 5 and 6 desired amount of H_2O_2 (1 mM) was added to the dye solution prior to treatment. 2 mL aliquots of reaction mixture were withdrawn at regular time interval to monitor the kinetics of decolorization. The residual dye concentration in the aliquots drawn from reaction mixture was determined using UV–Vis spectrophotometer (Model: Lambda 35, Perkin Elmer, absorbance wavelength 512 nm). The total treatment period in all experimental categories was 60 min. All experiments were conducted in triplicate runs to ensure reproducibility of results.

At the end of each treatment, the solution in the bath was analyzed for complete mineralization of the original dye. The total organic carbon (TOC) removal from original dye

solution was assessed using a TOC analyzer (Aurora O–I–Analytical, Model: 1030).

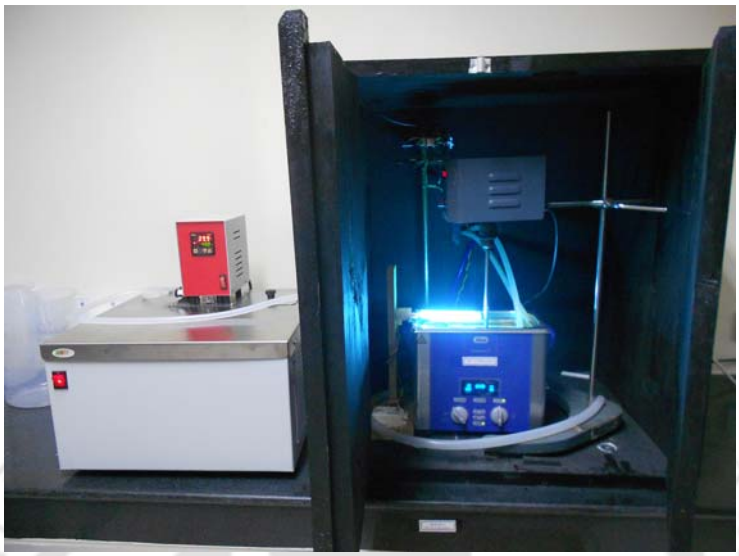

Figure 5.1: Experimental setup for sono–hybrid photolysis process for decolorization

5.2.3 Intensification of AOPs and HAOP with salt addition

Decolorization/ mineralization of ARB dye with individual AOP of sonolysis and photolysis and HAOP of sono–photolysis was intensified by addition of salt (or electrolyte) to the dye solution. Three sodium salts, viz. NaCl or $NaNO_3$ or Na_2SO_4, were used. In a typical experiment, 4 mM of NaCl or $NaNO_3$ or Na_2SO_4 was added to the solution prior to the commencement of reaction. The temperature of the dye solution was maintained at 298 K. Rest of the procedure was same as described earlier. The rationale underlying salt addition will be explained in subsequent section.

5.2.4 Kinetic (Arrhenius) analysis

The chemical pathway of the decolorization/ degradation of the ARB dye has been established by Gao et al. (2012) and Xia et al. (2014) with identification of the intermediates generated during the process. The decolorization/ degradation of the dye proceeds through three main reactions, viz. breakage of the chromophoric azo (–N=N–) bond, hydroxylation

and oxidation. A large number of reaction intermediates have been identified such as 1,4–dihydroxynaphthalene, 1,2– and 1,4– naphthoquinone, 1–naphthol, 2–hydroxybenzoic acid, benzoic acid, carboxylic acids such as maleic acid, oxalic acid, lactic acid, acetic acid and formic acid, ketones and aldehydes. A detailed kinetic model of decolorization of the dye involving all intermediates is not available. Despite this difficulty, Gao et al. (2012) and Thiam et al. (2015) have reported that the time profiles of the decolorization of ARB dye are well fitted with pseudo 1st order kinetic model with respect to dye concentration. In view of this result, the time profiles of dye decolorization in the present study have been analyzed with pseudo 1st order kinetic model. Moreover, since the principal emphasis of this study is on investigation of physical mechanism of sono–photolysis process (and decolorization of ARB dye is being used only as a model system for this investigation), we have not identified the intermediates of degradation of the ARB dye. The time profiles of decolorization have been non–uniform in time in all experimental categories. Significant (> 60%) decolorization is achieved in first 10 min of treatment. Hence, the pseudo 1st order kinetic constant for decolorization was calculated using the kinetic data for first 10 min of treatment. Using the pseudo 1st order kinetic constants, activation energies for degradation with individual AOPs of sonolysis and photolysis and with the hybrid AOP of sono–photolysis was calculated applying Arrhenius equation: $k = A\exp(-E_a / RT)$. Various notations are as follows: k – kinetic constant, A – frequency factor or pre–exponential factor, E_a – activation energy for the reaction, R – universal gas constant, T – temperature.

5.2.5 Calculation of synergy

The mechanistic interactions among the individual AOPs were determined on the basis of a synergy index. The synergy index was calculated using the pseudo 1st order kinetic constants for HAOP of sono–photolysis and individual AOPs of sonolysis and photolysis.

The formula for calculation of synergy index is as follows:

$$\text{Synergy Index} = \frac{k_{(US + H_2O_2 + UVC)}}{\left(k_{US} + k_{(MS + H_2O_2 + UVC)}\right)}$$

5.3 BUBBLE DYNAMICS MODEL

Both ultrasound and cavitation (the secondary effect of ultrasound) have physical and chemical effects on dye decolorization system (Chakma and Moholkar, 2013, 2015a). Cavitation is essentially the nucleation, growth and implosive collapse of gas or vapor bubbles, or in general sense, volume oscillations of the bubble. Occurrence of cavitation in the system requires presence of nuclei, which could be gas pockets trapped in the crevices of the solid boundaries of the reaction system such as reactor wall or sonicator surface, or these could be small, free–floating bubbles already present in the reaction mixture. The volume oscillations of cavitation bubbles are induced by variation in bulk pressure of the medium due to passage of ultrasound wave in the form of compression/ rarefaction cycles. If the pressure amplitude of the ultrasound wave is sufficiently higher than the static pressure in the medium, the cavitation bubble undergoes a transient collapse. The transient collapse of the cavitation bubble is extremely fast (occurring in few tens of nanoseconds) and adiabatic, and bubble can get compressed to extremely small size (typically $1/10^{th}$ to $1/100^{th}$ of original size). At this stage, the temperature and pressure in the bubble can reach extreme (~ 5000 K, ~ 500 bar), creating intense energy concentration on extremely small spatial and temporal scale. At transient collapse, the bubble content (which is a mixture of gas and vapor of bulk liquid medium) is subjected to extreme conditions of temperature and pressure generated in the bubble (Suslick, 1990). The gas and solvent vapor molecules present in the bubble undergo thermal dissociation to form various species, some of which are radical species. In most cases, water is employed as the bulk liquid medium for cavitation assisted processes. The

species arising out of dissociation of water vapor molecules are radical species such as $H^{\bullet}$, $O^{\bullet}$ and $^{\bullet}OH$. The oxidizing radicals, such as $^{\bullet}O$, $^{\bullet}OH$ and $HO_2^{\bullet}$, generated inside the bubble at transient collapse can either diffuse out of the bubble at the point of maximum compression of the bubble, or get released into the liquid medium if the bubble undergoes fragmentation during collapse. These radicals can induce and accelerate numerous reactions leading to oxidation/ degradation of pollutants. Cavitation also has physical effects on the reaction system (Chakma and Moholkar, 2015b). The principal physical effect of cavitation is generation of strong micro–convection in the medium through two mechanisms, viz. micro–turbulence, which is oscillatory motion of liquid in vicinity of the bubble induced by volume oscillations of the bubbles, and shock waves (or acoustic waves) which are generated due to reflection of the fluid elements from the bubble interface, when the bubble comes to a sudden halt during compression phase radial motion. Both micro–turbulence and shock waves leads to intense micro–mixing in the reaction medium. The magnitudes of the physical and chemical effects of cavitation can be estimated using simulations of cavitation bubble dynamics. Passage of ultrasound wave in the form of alternate compression / rarefaction cycles also induces high velocity oscillatory motion of the fluid elements, called micro–streaming.

In the present study, the diffusion limited ordinary differential equation (ODE) model proposed by Toegel et al. (2000) using boundary layer approximation has been used for estimation of physical and chemical effects of cavitation bubbles. This model is based on the comprehensive PDE model of Storey and Szeri (2000), which demonstrated that vapor transport and entrapment in the cavitation bubble, leading to formation of radicals, is essentially a diffusion limited process. A brief description of this hypothesis is as follows: Large amount of solvent evaporation occurs at the bubble interface during the expansion of cavitation bubble, and solvent vapor molecules enter and diffuse towards the bubble core. In

the subsequent compression phase, vapor molecules diffuse back to bubble interface and undergo phase change or condensation. However, in the final moments of transient bubble collapse, velocity of the bubble interface (or bubble wall) becomes extremely fast. At this stage, the time scale of bubble motion becomes smaller than the time scale of diffusion of vapor molecules, and time scale of their condensation at the bubble wall. As a result, not all of the vapor molecules that enter the bubble during expansion can condense during compression. This causes "entrapment" of some vapor molecules inside the bubble. These "entrapped" vapor molecules are subjected to conditions of extreme pressure and temperatures generated in the bubble at transient collapse, and undergo dissociation to generate radicals. Greater details on this model are given in our previous studies (Sivasankar and Moholkar, 2008; Chakma and Moholkar, 2013a, 2013b). For convenience of the reader, only the main components of the model and relevant data / boundary conditions have been reproduced below:

The essential equations and thermodynamic data of this model have been summarized in Tables 2.1A and B (in Chapter 2). The model comprises of 4 ordinary differential equations as follows:

(1) Keller–Miksis equation for the radial motion of the bubble.

(2) Equation for the diffusive flux of solvent vapor through bubble interface.

(3) Equation for the heat conduction through bubble interface.

(4) Overall energy balance treating the cavitation bubble as an open system.

The transport parameters, viz. thermal conductivity and diffusion coefficient, in the model have been determined using Chapman–Enskog theory using Lennard–Jones 12–6 potential at the bulk temperature of the liquid medium. Thermal and diffusive penetration depths are determined using dimensional analysis. This model does not take into account diffusion of gas across bubble interface as the time scale for the diffusion of gases (of the order of

milliseconds) is much higher than the time scale for the radial motion of bubble, which is of the order of microseconds. Numerical solution of four ODEs described in Table 2.1 (in Chapter 2) can be obtained using Runge–Kutta adaptive step size method (Press et al., 1994). We have considered an air bubble as the cavitation nuclei for simulations of cavitation bubble dynamics in the dye solution. The thermodynamic parameters for water, nitrogen and oxygen were taken from Hirschfelder et al. (1954), Condon and Odishaw (1958), Reid et al. (1987). Other parameters used in the simulation of bubble dynamics equation and their numerical values are as follows: Ultrasound frequency (f) = 37 kHz; Ultrasound pressure amplitude (P_{AW}) = 160 kPa (1.6 bar); Equilibrium bubble radius (R_o) = 10 μm. Vapor pressure of liquid medium (water) at different temperatures of treatment (viz. 283, 298, and 313 K) was calculated using Antoine type correlation. Various physical properties of water are as follows: density (ρ_L) = 1000 kg/m^3, kinematic viscosity (ν) = 10^{-6} Pa–s, surface tension (σ) = 0.072 N/m and velocity of sound (c) = 1481 m/s.

5.3.1 Estimation of physical and chemical effects of transient cavitation

***Radical generation by cavitation bubbles*:** Numerical solution of bubble dynamics model gives the number of solvent (or water) vapor molecules present in the bubble at the moment of transient collapse. These vapor molecules along with the gas (or air) molecules comprising the bubble undergo thermal dissociation at the extreme conditions of temperature and pressure reached in the bubble at transient collapse. Due to very small bubble volume at the instance of maximum compression (or minimum radius) during radial motion, the concentrations of various species in the bubble are very high. Moreover, the temperature inside the bubble at transient collapse is extremely high. As a result of these two features, the rates of various reactions occurring inside the bubble are expected to be extremely fast. The bubble contents are, thus, expected to be always at thermal equilibrium (Brenner et al., 2003).

The equilibrium mole fraction of the various species in the bubble generated from thermal dissociation of vapor and gas molecules at the conditions of temperature and pressure peak reached inside the bubble can be calculated using free–energy minimization technique (www.factsage.com; Eriksson, 1975; Bale et al., 2002).

***Sonophysical effect of cavitation*:** As stated earlier, volume oscillations of the cavitation bubble induce oscillatory motion of surrounding liquid. This is called micro–turbulence. The pulsating bubble can also emit acoustic (or shock) wave due to reflection of fluid from surface of the bubble, as the bubble comes to sudden halt during radial motion. The magnitudes of micro–turbulence velocity and pressure amplitude of the shock or acoustic wave, at a distance r from the center of the bubble, can be calculated from numerical result of bubble dynamics model using following formulae (Leighton, 1994; Grossmann et al., 1997; Moholkar and Warmoeskerken, 2003):

Micro–convection: $$V_{turb}(r,t) = \frac{R^2}{r^2}\left(\frac{dR}{dt}\right)$$

Shock Waves (or Acoustic Waves): $$P_{AW}(r,t) = \frac{\rho}{4\pi r}\frac{d^2V_b}{dt^2} = \rho\frac{R}{r}\left[2\left(\frac{dR}{dt}\right)^2 + R\frac{d^2R}{dt^2}\right]$$

where V_b is the volume of the bubble. A representative value of r is taken as 1 mm.

5.4 RESULTS AND DISCUSSION

5.4.1 Decolorization profiles and TOC removal in different experimental categories

Fig. 5.2 depicts the time evolution of the UV–vis spectra of samples of the dye solution withdrawn from reaction mixtures at different time intervals for the individual AOP of photolysis (MS + H_2O_2 + UV). Diminishing absorbance at wavelength of 512 nm with time of treatment is indicative of the decolorization of the dye. The time profiles of dye

decolorization in different experimental categories are shown in Fig. 5.3A, while the reduction in TOC in the dye solution in these categories is depicted in Fig. 5.3B. The summary of experimental results in all 6 categories along with the pseudo 1st order kinetic constant for decolorization is given in Table 5.1A. It could be seen from Fig. 5.2 that after 60 min of treatment the absorbance at 512 nm is almost negligible, indicating complete decolorization of the dye. However, the TOC removal in this period, as seen from Fig. 5.3B, is mere 37%. This essentially means that the kinetics of mineralization is not as fast as decolorization. This trend is seen for all 6 experimental categories listed in Table 5.1A. The peculiar trends in decolorization and TO removal in different experimental categories and explanations for the same can be given as follows:

(1) Among the individual AOPs, the least decolorization is seen for category 3 in which the UV–C light is applied with mechanical stirring. In this case, the UV–C light is expected to cause photo–tendering effect on dye molecules due to breakage of chromophores. However, this process is not very efficient due to low concentration of dye molecules in solution, which results in least decolorization.

(2) Sonolysis alone gives moderate decolorization of ~ 33%. In this case, the oxidation radicals generated from transient cavitation induce degradation reactions. Nonetheless, due to high instability of the radicals and also dilute concentration of dye in the solution (which restricts the probability of dye–radical interaction), the net utility of these radicals towards hydroxylation/ oxidation reactions leading to degradation of dye is limited, which results in moderate decolorization.

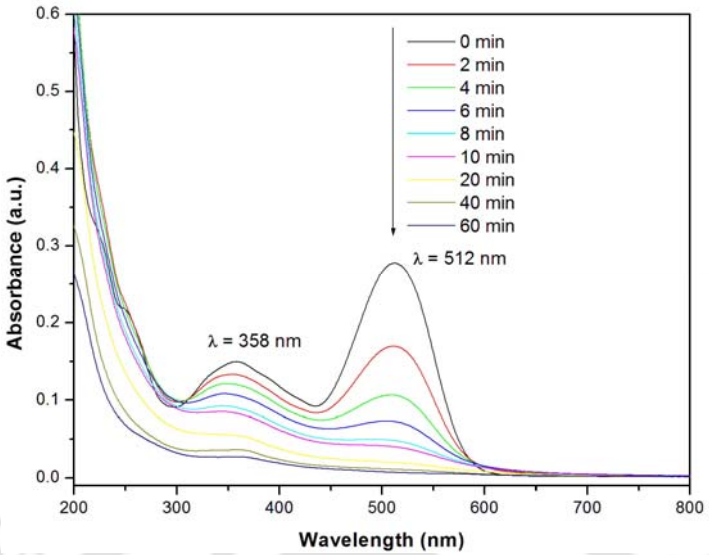

Figure 5.2: Evolution of UV–visible spectra of reaction mixture with time for individual AOP of photolysis (MS + H_2O_2 + UVC)

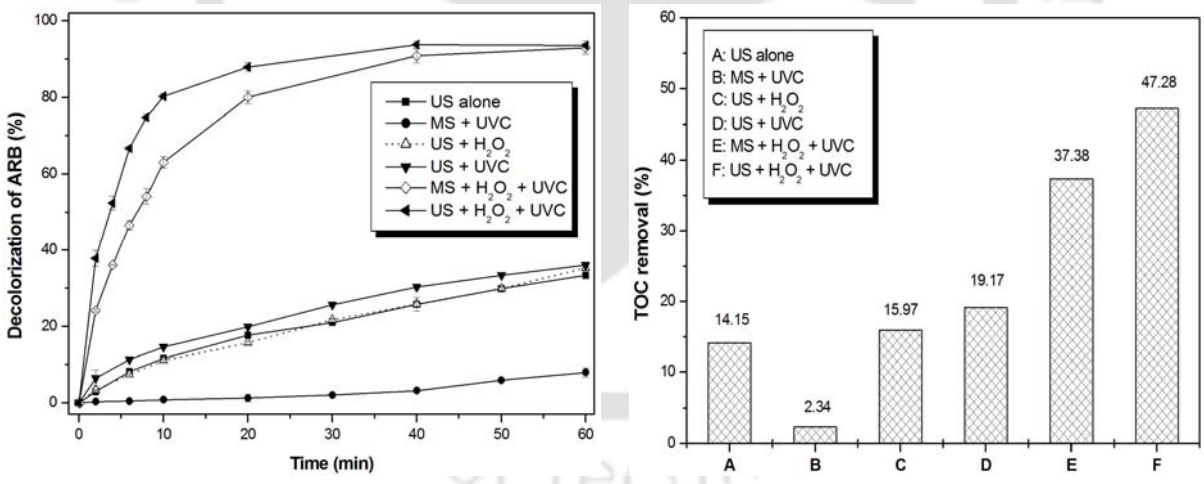

(A) (B)

Figure 5.3: (A) Time history of decolorization of ARB dye, and (B) TOC removal in different experimental protocols.

Table 5.1: Summary of experimental results

(A) Total decolorization and pseudo 1st order kinetic constant of decolorization in different protocols

Experimental category	Decolorization (%)	k (s^{-1})	R^2
1. US alone	33.29 ± 0.20	1.20×10^{-4}	0.95
2. US + H_2O_2	35.30 ± 0.77	1.30×10^{-4}	0.97
3. MS + UVC	7.95 ± 1.21	1.87×10^{-5}	0.90
4. US + UVC	36.01 ± 0.79	1.50×10^{-4}	0.88
5. MS + H_2O_2 + UVC	92.99 ± 1.72	1.65×10^{-3}	0.98
6. US + H_2O_2 + UVC	93.52 ± 0.58	3.01×10^{-3}	0.97

(B) Effect of temperature on decolorization in individual and hybrid AOP

Experimental category	Temperature (K)	Decolorization (%)	k (s^{-1})	R^2
1. Sonolysis	283	34.96 ± 0.39	1.50×10^{-4}	0.85
(US only)	298	33.29 ± 0.20	1.20×10^{-4}	0.95
	313	31.61 ± 1.84	1.10×10^{-4}	0.99
2. Photolysis	283	91.29 ± 1.24	1.42×10^{-3}	0.98
(MS+ UVC + H_2O_2)	298	92.99 ± 1.72	1.65×10^{-3}	0.98
	313	94.59 ± 2.02	3.14×10^{-3}	0.98
3. Sono–Photolysis	283	90.68 ± 1.60	2.49×10^{-3}	0.93
(US + UVC + H_2O_2)	298	93.52 ± 0.58	3.01×10^{-3}	0.97
	313	94.22 ± 1.74	4.10×10^{-3}	0.95

(C) Effect of salt addition to reaction mixture on decolorization process in HAOP of sono–photolysis

Experimental category	Decolorization (%)		k (s^{-1})	R^2
	10 min	60 min		
1. Sono–Photolysis + NaCl	84.0 ± 2.03	94.22 ± 2.60	4.76×10^{-3}	0.91
2. Sono–Photolysis + $NaNO_3$	75.24 ± 1.92	91.42 ± 2.55	3.18×10^{-3}	0.87
3. Sono–Photolysis + Na_2SO_4	83.13 ± 1.89	92.78 ± 2.55	5.27×10^{-3}	0.86

(3) The decolorization/ degradation achieved in category 2 (ultrasound + H_2O_2) is only slightly higher than in category 1, where ultrasound alone has been applied. With addition of H_2O_2 to dye solution, the reaction system is expected to generate more $^{\bullet}OH$ radicals by two possible mechanisms: (i) evaporation and thermal dissociation of H_2O_2 inside the cavitation bubble, or (ii) photolytic dissociation of H_2O_2 induced by the sonoluminescence light emitted by transient cavitation bubbles. However, almost similar decolorization in experimental category 1 & 2 indicates that neither of the two mechanisms of H_2O_2 dissociation is prevalent, which could give marked enhancement to decolorization. Evaporation of H_2O_2 in cavitation bubble is not significant due to low vapor pressure. The sonoluminescence light emitted during transient collapse is also too weak to activate photolysis, as reported by Balaji et al. (2012).

(4) In category 4, where ultrasound and UV–C light is applied simultaneously, the expected synergy among the two techniques is photolytic dissociation of the H_2O_2 – either produced during transient collapse of cavitation bubbles or in–situ generated H_2O_2 due to recombination of •OH radicals produced by the transient cavitation. However, in this category as well, the extent of decolorization is only slightly higher than sonolysis alone. This result could be explained on the basis of results of simulations of cavitation bubble dynamics given in Table 5.1. As seen from the equilibrium mole fractions of species, H_2O_2 is produced in negligible amount (i.e. mole fraction ~ 10^{-5}) at transient bubble collapse. Similarly, in–situ H_2O_2 generation through recombination of $^{\bullet}OH$ radicals is also expected to be small, and hence, the above mentioned synergy between ultrasound and UV–C irradiation is not prevalent to yield enhanced decolorization. The TOC removal with this technique, however, is approximately 15% higher than sonolysis. This effect is possibly a consequence of complete mineralization of the degradation intermediates produced by ultrasound and transient cavitation by the UV–C light through photo–tendering effect, as noted earlier.

Table 5.2: Results of simulations of cavitation bubble dynamics

Species	Bulk liquid medium: Water		
	T= 283 K	**T = 298 K**	**T = 313 K**
	T_{max} = 4070 K P_{max} = 5308 bar V_{turb} = 0.014 m/s P_{AW} = 19.48 bar	T_{max} = 3871 K P_{max} = 4704 bar V_{turb} = 0.014 m/s P_{AW} = 16.33 bar	T_{max} = 3343 K P_{max} = 3047 bar V_{turb} = 0.014 m/s P_{AW} = 9.214 bar
	x_{N2} = 0.762 x_{O2} = 0.203 x_W = 0.036	x_{N2} = 0.720 x_{O2} = 0.191 x_W = 0. 089	x_{N2} = 0.632 x_{O2} = 0. 168 x_W = 0.200
Equilibrium mole fraction at the moment of transient collapse			
N_2	0.710	0.714	0.708
O_2	0.143	0.148	0.161
NO	9.98×10^{-2}	8.91×10^{-2}	5.97×10^{-2}
H_2O	2.03×10^{-2}	2.58×10^{-2}	5.63×10^{-2}
OH	1.41×10^{-2}	1.30×10^{-2}	9.93×10^{-3}
O	8.83×10^{-3}	6.47×10^{-3}	2.37×10^{-3}
O_3	1.76×10^{-5}	1.41×10^{-5}	6.29×10^{-6}
NO_2	1.68×10^{-3}	1.57×10^{-3}	1.17×10^{-3}
HOO	7.02×10^{-4}	6.54×10^{-4}	4.97×10^{-4}
H_2	4.84×10^{-4}	4.37×10^{-4}	3.27×10^{-4}
H	5.43×10^{-4}	3.86×10^{-4}	1.33×10^{-4}
H_2O_2	2.61×10^{-5}	2.76×10^{-5}	3.09×10^{-5}
HNO	7.94×10^{-5}	6.27×10^{-5}	2.82×10^{-5}
HNO_2	1.84×10^{-4}	1.79×10^{-4}	1.54×10^{-4}
N	2.64×10^{-5}	1.34×10^{-5}	1.55×10^{-6}
N_2O	3.71×10^{-4}	3.09×10^{-4}	1.61×10^{-4}
NH	3.06×10^{-6}	1.64×10^{-6}	–

Note: T_{max} – temperature peak reached in the bubble at the time of first collapse; P_{max} – pressure peak reached in the bubble at the time of first collapse, V_{turb} – average velocity of the micro–turbulence generated by cavitation bubble (estimated at 1 mm distance from bubble center); P_{AW} – pressure amplitude of the acoustic wave generated by the cavitation bubble; x_W – mole fraction of water vapor in the bubble; x_{N2} – mole fraction of nitrogen in the bubble; x_{O2} – mole fraction of oxygen in the bubble

(5) Categories 5 and 6, i.e. photolysis and sono–photolysis, result in almost complete decolorization in 60 min of treatment. This is a consequence of effective production of $^{\bullet}OH$ radicals through dissociation of the H_2O_2 added to the reaction mixture. However, comparing the total decolorization in categories 5 and 6, only a slight increase is seen with application of ultrasound in category 6. This essentially means that dissociation of H_2O_2 to produce OH radicals that induce reactions leading to decolorization (viz. breakage of –N=N– bond,

oxidation and hydroxylation) mainly occurs via UV–C light and not through ultrasound and transient cavitation. Inefficiency of ultrasound and transient cavitation for effective dissociation of H_2O_2 is also evident from results of experimental category 2, as discussed earlier. Ultrasound and cavitation also have physical effects on the reaction system in term of generation of intense micro–convection in the medium due to shock waves and micro–turbulence induced by transient collapse of the cavitation bubble. These physical effects influence the hydroxylation/ oxidation reactions leading to degradation of the dye molecules. Random micro–turbulence generated by ultrasound and cavitation reduces the fruitful interactions between the oxidizing radicals and the dye molecules. This hypothesis is also corroborated by the law of frequency factor for sono–photolysis determined from Arrhenius analysis (discussed in greater detail in next section). Intermediate species of dye decolorization (generated mainly through photolysis induced reactions) can undergo further degradation and mineralization either via reactions with radicals generated from cavitation bubbles or thermal decomposition / degradation in the interfacial region of cavitation bubble that can get heated to high temperature (or even reach supercritical conditions) during transient collapse of the bubble (Kotranarou et al., 1991; Hua et al., 1995). This supportive (yet subordinate) role of ultrasound and cavitation in the hybrid AOP of sono–photolysis is manifested in terms of approximately 2–fold higher kinetic constant of decolorization and 35% higher TOC removal, as compared to photolysis alone.

The above discussion essentially points at physical role played by ultrasound and cavitation in the hybrid AOP of sono–photolysis.

5.4.2 Results of kinetic (or Arrhenius) analysis

As noted earlier, experiments were conducted in three temperatures (viz. 283, 298 and 313 K) of reaction mixture, for estimation of Arrhenius parameters (viz. frequency factor and

activation energy) for the individual and hybrid AOPs. The results of these experiments are given in Table 5.1B. The time profiles of decolorization and TOC removal at different temperatures with individual and hybrid AOPs are depicted in Fig. 5.4.

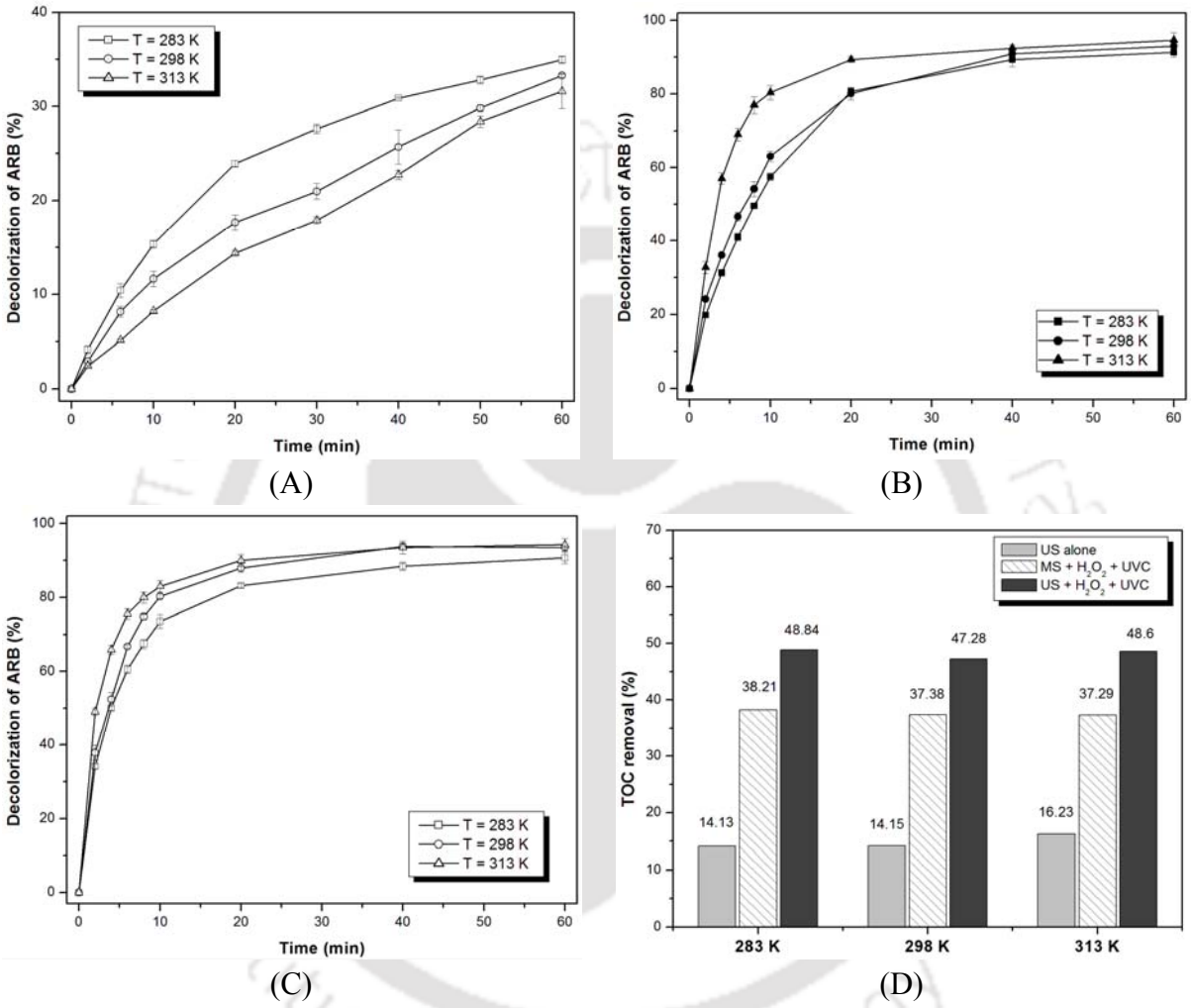

Figure 5.4: Time profiles of ARB dye decolorization at different temperatures for individual and hybrid AOP: (A) Sonolysis, (B) Photolysis, (C) Sono–photolysis. (D) TOC removal at different temperatures for individual and hybrid AOP

Table 5.3: Results of kinetic (Arrhenius) analysis for individual and hybrid AOP

Experimental Category	E_a **(kJ mol^{-1})**	A **(mol L^{-1} s^{-1})**
1. Sonolysis (US alone)	–7.38	6.46×10^{-6}
2. Photolysis (MS + H_2O_2 + UVC)	19.19	4.56
3. Sono–Photolysis (US + H_2O_2 + UVC)	12.18	0.432

The Arrhenius plots and the parameters for the individual and hybrid AOPs are given Fig. 5.5 and Table 5.3. Analysis of these parameters vis–à–vis the results of simulations of cavitation bubble dynamics highlights some important aspects of physical mechanism of the individual and hybrid AOPs as outlined below:

(1) The activation energy for sonolysis is negative (–7.38 kJ/mol) and the frequency factor is also extremely small (6.46×10^{-6} mol/L·s). An explanation for these results can be given on the basis of simulations of cavitation bubble dynamics given in Table 5.2. The temperature and pressure peak reached in the bubble at transient collapse reduces with bulk liquid temperature. This is a consequence of higher evaporation and entrapment of water vapor inside the bubble with increasing temperature of bulk liquid at the moment of transient collapse. The evaporation of the water vapor inside the bubble is proportional to the vapor pressure of the liquid at bubble interface, which increases with bulk liquid temperature. The intensity of bubble collapse reduces with increasing temperature that results in reduction in formation of oxidizing radicals such as $^{\bullet}OH$ and $^{\bullet}O$; and hence, reduction in extent of decolorization. The kinetic constant of decolorization reduces proportionally with temperature (against the Arrhenius hypothesis of rise in kinetic constant with temperature), which results in negative activation energy.

The low frequency factor for sonolysis is attributed to sporadic nature of transient cavitation phenomena and high instability of the radicals generated from cavitation bubbles.

These radicals are released into the bulk liquid medium at the spot of bubble collapse. Due to high instability, these radicals do not diffuse into the medium. Thus, these radicals are intercepted by only the dye molecules present at the interface of the bubble. The occurrence of transient cavitation phenomena is also highly non–uniform in the reaction medium. This factor puts severe limitation on the interactions (or fruitful collisions) between dye molecules and the oxidizing radicals, which is manifested in terms of low frequency factor.

(2) The activation energy for photolysis (which essentially is photon–induced cleavage of bonds) is positive, i.e. 19.19 kJ/mol. Mechanical stirring of the dye solution ensures uniform concentration of H_2O_2 in the reaction mixture, due to which the radical production is also uniform. Moreover, mechanical stirring produces even and orderly convection in the medium, which assists in enhancing interaction of $^{\bullet}OH$ radicals with dye molecules leading to effective degradation of the latter. All of these of these factor lead to high frequency factor for the process of photolysis.

(3) In case of sono–photolysis, both mechanisms described in previous points are present in the reaction medium. However, the decolorization reactions are mostly contributed by the radicals generated through photolysis of H_2O_2, due to more uniform production of these radicals in reaction volume. The contribution of radicals produced from transient cavitation is relatively lower, due to sporadic nature of transient cavitation events. As a result, the net activation energy of the decolorization process is positive. As in sonolysis, the random micro–convection generated by transient cavitation causes random motion of dye molecules and adversely affects their interactions with radicals. This is manifested in terms of reduction in frequency factor, as compared to photolysis alone.

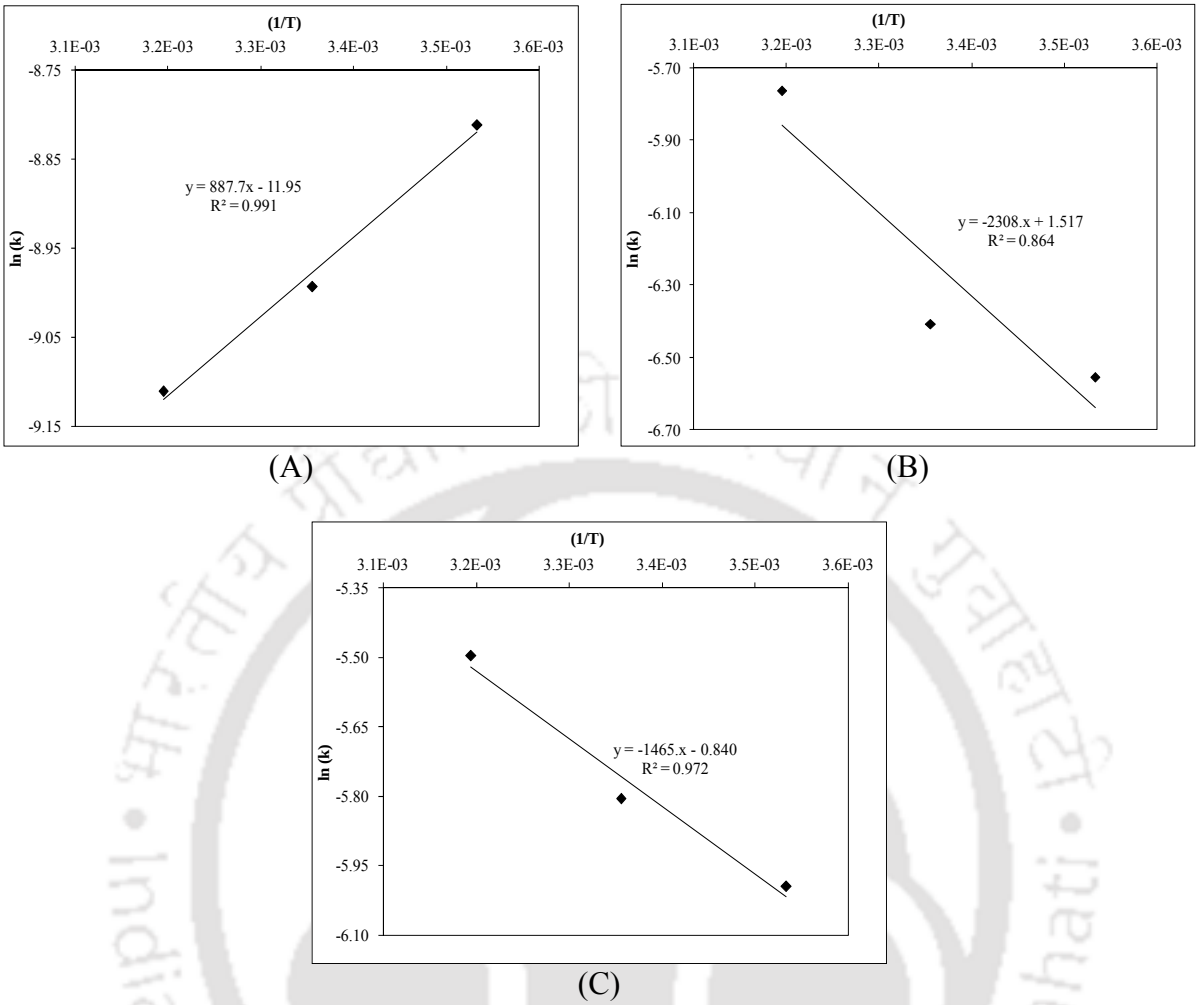

Figure 5.5: Arrhenius plots (ln *k vs.* 1/*T*) for ARB dye decolorization at different temperatures for individual and hybrid AOP. (A) Sonolysis, (B) Photolysis, (C) Sono–photolysis

5.4.3 Effect of salt addition

The results of decolorization experiments employing hybrid AOP of sono–photolysis with different salt addition are depicted in Table 5.1C. The time profiles of decolorization and the extent of TOC removal with addition of three sodium salts, viz. NaCl, $NaNO_3$ and Na_2SO_4, are shown in Fig. 5.6. Although the total decolorization obtained with all three sodium salts in 60 min of treatment is almost similar, the kinetic constants of decolorization vary significantly. The pseudo 1st order kinetic constants for decolorization for the three salts are in the order: Na_2SO_4 > NaCl > $NaNO_3$. An explanation for the same can be given as

follows: There are essentially two mechanisms through which the salt addition can enhance decolorization in sono–photolysis system:

(1) Addition of salt enhances the ionic strength of the medium. This phenomenon augments the hydrophobic repulsive interactions between dye and water molecules. As a result, the dye molecules are "pushed" towards the bubble interface, which also has hydrophobic character (Seymour and Gupta, 1997; Sivasankar and Moholkar, 2009) [43,44]. This phenomenon causes increased concentration of the dye molecules at bubble interface, which boosts the probability of radical–dye molecule interaction resulting in faster and greater decolorization/ degradation.

(2) In the second mechanism, the dissociation of the salt can generate ions, which can react with •OH and $HO_2^{\bullet}$ radicals to form other radical species that can also contribute to decolorization/ degradation of the dye. This "conservation" of radicals also prevents the radicals generated through sonolysis and photolysis from recombining, which is a loss of oxidation potential.

Evaluation of decolorization results with salt addition against these hypotheses reveals following mechanistic features of this technique: The ionic strengths of the three salts used in this study are as follows: Na_2SO_4 – 0.01 mM, NaCl and $NaNO_3$ – 0.004 mM. The highest effect on decolorization is that of ionic strength as seen from the highest kinetic constant for Na_2SO_4. NaCl and $NaNO_3$ have similar ionic strengths; however, the kinetic constant of decolorization for NaCl is 50% higher than that of $NaNO_3$. Cl^- ions produced through dissociation of NaCl in the reaction mixture can react with $^{\bullet}OH$ and $HO_2^{\bullet}$ radicals to generate additional oxidation species such as $Cl^{\bullet}$ and $Cl_2^{\bullet-}$. Various reactions reported in literature that can possibly occur between $^{\bullet}OH$ radicals and Cl^- ions are given below (Tan et al., 2013):

$$^{\bullet}OH + Cl^- \longrightarrow ClOH^{\bullet-} \qquad (5.1)$$

$$ClOH^{\bullet -} + H^{+} \longrightarrow Cl^{\bullet} + H_2O \qquad (5.2)$$

$$Cl^{\bullet} + Cl^{-} \rightleftharpoons Cl_2^{\bullet -} \qquad (5.3)$$

Conservation of $^{\bullet}OH$ radicals is manifested terms of faster decolorization of dye with NaCl addition.

In case of $NaNO_3$, however, no reactions between the anions NO_3^- and $^{\bullet}OH$ radicals have been reported in literature. Thus, there is no conservation of oxidizing radicals produced from cavitation bubbles, as seen for NaCl. The only mechanism that exists for enhancement of decolorization with $NaNO_3$ addition is that of higher partitioning of dye molecules near bubble interface, which results in greater interception of the $^{\bullet}OH$ radicals produced from cavitation bubble by dye molecules. Due to moderate ionic strength, this effect is not as marked as Na_2SO_4, which is manifested in terms of lowest kinetic constant for decolorization among the three salts.

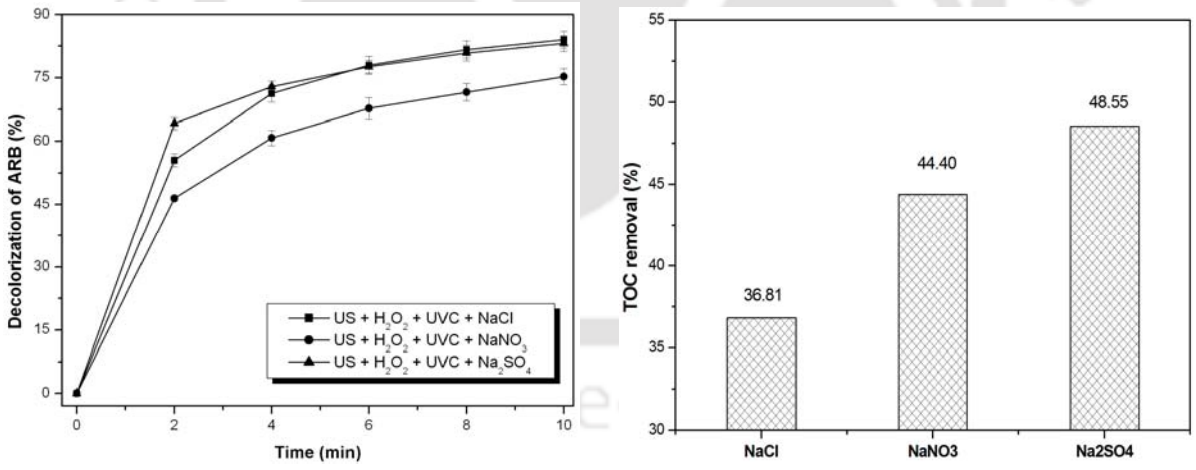

(A) (B)

Figure 5.6: (A) Time history of ARB dye decolorization, and (B) TOC removal with salt addition in the hybrid AOP of sono–photolysis

An interesting result as observed through Table 5.1C and Fig. 5.6 is slower decolorization rate (indicated by lower kinetic constant) yet higher TOC removal for $NaNO_3$ as compared to NaCl. An explanation for the same can be offered as follows: For $NaNO_3$, the reactions occurs mainly through attack of $^{\bullet}OH$ radicals, which are strong oxidants (oxidation potential of 2.8 eV) that give not only decolorization (by breakage of –N=N– chromophores) but also complete mineralization. On the other hand, $Cl^{\bullet}$ and $Cl_2^{\bullet-}$ radicals generated by reactions of Cl^- with $^{\bullet}OH$ radicals are efficient in breakage of chromophoric –N=N– linkages. However, the oxidation potentials of these radicals, viz. 2.4 and 1.36 eV for $Cl^{\bullet}$ and $Cl_2^{\bullet-}$, respectively (Tan et al., 2013), are lesser than that of OH radical. Therefore, these radicals are not as effective as $^{\bullet}OH$ radicals for complete mineralization of dye. This is reflected in relatively lesser mineralization of the ARB dye with NaCl, as compared to other two salts.

Finally the synergy index was calculated for ultrasound-assisted hybrid process and presented in Fig. 5.7.

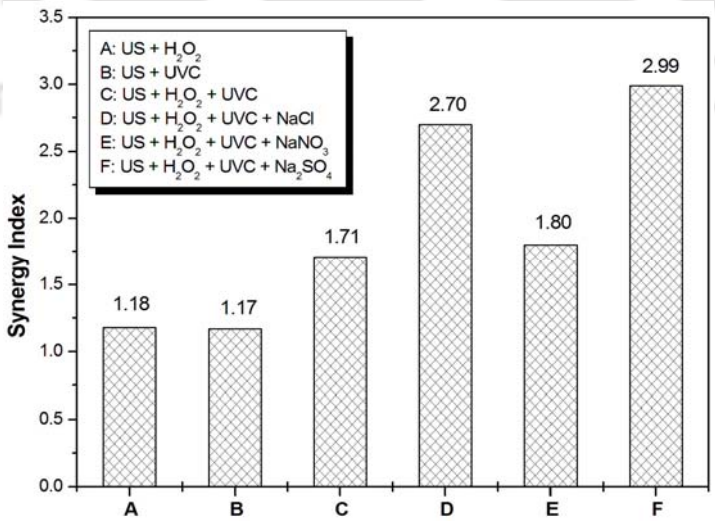

Figure 5.7: Synergy indices for hybrid advanced oxidation process (HAOP) without and with salt addition

5.5 CONCLUSION

The present study has reported mechanistic investigation of the hybrid AOP of sono–photolysis. Concurrent analysis of experimental results with simulations of cavitation bubble dynamics has brought forth some interesting links and interactions between mechanisms of individual AOPs of sonolysis and photolysis – when applied together in sono–photolysis. The major findings of this study are summarized as follows:

(1) In the hybrid AOP of sono–photolysis, $^{\bullet}OH$ radicals generated through photolytic dissociation of H_2O_2 contribute mostly to the decolorization reactions comprising breakage of –N=N– chromophoric linkages, hydroxylation and oxidation.

(2) Role of ultrasound and cavitation in the hybrid AOP is rather subordinate. The total decolorization obtained with photolysis shows negligible change with simultaneous application of ultrasound. This result is attributed to highly sporadic nature of transient cavitation events. However, ultrasound causes enhancement in the kinetics of decolorization as well as extent of mineralization, as compared to photolysis. Intermediates of dye degradation generated through photolysis possibly undergo mineralization via either thermal decomposition at the interfacial region of transient cavitation bubbles or hydroxylation/oxidation induced by radicals produced from transient collapse of cavitation bubbles.

(3) The physical effect of intense and random micro–convection induced by transient cavitation has adverse effect on the decolorization reactions induced by photolysis, as the random movement of dye molecules induced by shock waves emitted by transient cavitation bubbles reduce the number of fruitful collision (or interactions) of dye molecules with the $^{\bullet}OH$ radicals generated by photolysis.

(4) Both kinetics of decolorization and extent of TOC removal (or mineralization) in sono–photolysis can be enhanced by addition of salt to the reaction medium. The ionic strength of

the electrolyte makes major impact on this enhancement, as it increases the hydrophobic interactions between dye molecules (and also degradation intermediates) and water that results in greater partitioning of these species at the bubble interface. These species can undergo further degradation at bubble interface either through hydroxylation/ oxidation or thermal decomposition.

The mechanistic insight gained in the hybrid AOP of sono–photolysis in this study could form useful inputs for further investigations in degradation of bio–recalcitrant pollutants using sono–photolysis.

REFERENCES

Balaji C, Moholkar VS, Pandit AB, Ashokkumar M, Mechanistic investigations on sonophotocatalytic degradation of textile dyes with surface active solutes, Ind. Eng. Chem. Res. 50 (2011) 11485–11494.

Bale CW, Chartrand P, Degterov SA, Eriksson G, Hack K, Mahfoud RB, Melancon J, Pelton AD, Petersen S, Factsage thermochemical software and databases, Calphad 26 (2002) 189–228.

Brenner M, Hilgenfeldt S, Lohse D, Single–bubble sonoluminescence, Rev. Mod. Phys. 74 (2002) 425–484.

Chakma S, Moholkar VS, Intensification of wastewater treatment using sono–hybrid processes: An overview of mechanistic synergism, Indian Chem. Eng. (2015a). DOI: 10.1080/00194506.2015.1026948

Chakma S, Moholkar VS, Investigation in mechanistic issues of sonocatalysis and sonophotocatalysis using pure and doped photocatalysts, Ultrason. Sonochem. 22 (2015b) 287–299.

Chakma S, Moholkar VS, Investigations in synergism of hybrid advanced oxidation

processes with combinations of sonolysis + Fenton Process + UV for degradation of Bisphenol–A, Ind. Eng. Chem. Res. 53 (2014) 6855–6865.

Chakma S, Moholkar VS, Numerical simulation and investigation of system parameters of sonochemical process, Chinese J. Eng. 2013 (2013b) 1–14.

Chakma S, Moholkar VS, Physical mechanism of sono–fenton process, AIChE J. 59 (2013a) 4303 – 4313.

Condon EU, Odishaw H, Handbook of physics, New York: McGraw Hill, 1958.

Eriksson G, Thermodynamic studies of high temperature equilibria—XII: SOLGAMIX, a computer program for calculation of equilibrium composition in multiphase systems, Chem. Scr. 8 (1975) 100–103.

FACTSAGE, access on 30th March, 2015, www.factsage.com

Gao M, Zeng Z, Sun B, Zou H, Chen J, Shao L. Ozonation of azo dye Acid Red 14 in a microporous tube–in–tube microchannel reactor: Decolorization and mechanism. Chemosphere 2012; 89:190–197.

Grossmann S, Hilgenfeldt S, Zomack M, Lohse D, Sound radiation of 3 MHz driven gas bubbles, J. Acoust. Soc. Am. 102 (1997) 1223–1227.

Hirschfelder JO, Curtiss CF, Bird RB, Molecular theory of gases and liquids, New York: Wiley, 1954.

Hua I, Hochemer RH, Hoffmann MR, Sonochemical degradation of p–nitrophenol in a parallel plate near field acoustic processor, Environ. Sci. Technol. 29 (1995) 2790–2796.

Kotronarou A, Mills G, Hoffmann MR, Ultrasonic irradiation of p–nitrophenol in aqueous solution, J. Phys. Chem. 95 (1991) 3630–3638.

Leighton TG, The acoustic bubble, San Diego: Academic Press, 1994.

Moholkar VS, Warmoeskerken MMCG, Integrated approach to optimization of an ultrasonic processor, AIChE J. 49 (2003) 2918–2932.

Press WH, Teukolsky SA, Flannery BP, Vetterling WT, Numerical recipes, New York: Cambridge University Press, 1992.

Reid RC, Prausnitz JM, Poling BE, Properties of gases and liquids, New York: McGraw Hill, 1987.

Seymour J, Gupta RB, Oxidation of aqueous pollutants using ultrasound: salt induced enhancement, Ind. Eng. Chem. Res. 36 (1997) 3453–3457.

Sivasankar T, Moholkar VS, Mechanistic features of the sonochemical degradation of organic pollutants, AIChE J. 54 (2008) 2206–2219.

Sivasankar T, Moholkar VS, Physical insights into the sonochemical degradation of recalcitrant organic pollutants with cavitation bubble dynamics, Ultrason. Sonochem. 16 (2009) 769–781.

Storey BD, Szeri AJ, Water vapor, sonoluminescence and sonochemistry, Proc. R. Soc. Lond. Ser. A 456 (2000) 1685–1709.

Suslick KS, Sonochemistry, Science 247 (1990) 1439–1445.

Tan C, Gao N, Deng Y, Zhang Y, Sui M, Deng J, Zhou S, Degradation of antipyrine by UV, UV/H_2O_2 and UV/PS, J. Hazard. Mater. 260 (2013) 1008– 1016.

Thiam A, Sirés I, Garrido JA, Rodríguez RM, Brillas E, Effect of anions on electrochemical degradation of azo dye Carmoisine (Acid Red 14) using a BDD anode and air–diffusion cathode, Sep. Purif. Technol. 140 (2015) 43–52.

Toegel R, Gompf B, Pecha R, Lohse D, Does water vapor prevent upscaling sonoluminescence? Phys Rev Lett. 85 (2000) 3165–3168.

Xia S–J, Zhou X–B, Shi W, Pan G–X, Ni Z–M, Photocatalytic property and mechanism studies on acid red 14 by MxOy/ ZnTi–layered double hydroxides (M = Fe, Sn, Ce), J. Mol. Catal. A Chem. 392 (2014) 270–277.

भारतीय प्रौद्योगिकी संस्थान गुवाहाटी
Indian Institute of Technology Guwahati

6

MECHANISTIC INVESTIGATIONS IN SONO-PERSULFATE OXIDATION PROCESS

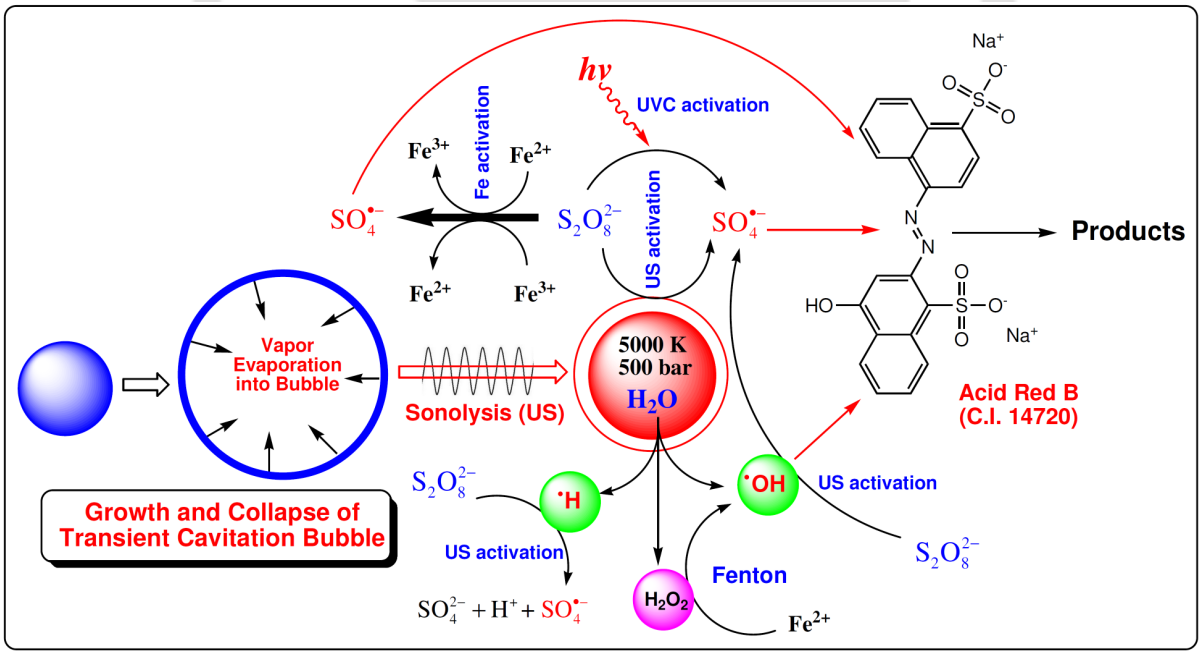

Mechanistic synergies in ultrasound-assisted persulfate based decolorization

CHAPTER 6

MECHANISTIC INVESTIGATIONS IN SONO-PERSULFATE OXIDATION PROCESS

6.1 INTRODUCTION

The previous chapters presented mechanistic investigations in hybrid AOPs which were based on production of $^{\bullet}OH$ radicals and their utilization for oxidation/ degradation reactions. Although results presented in last four chapters are encouraging as $^{\bullet}OH$ radical based hybrid AOPs have been proven to be very effective in decolorization / degradation of different recalcitrant pollutants, the practical applicability of these processes on large scale is limited due to less stability of the reagent involved in process, and the restricted range of operating conditions (specially the pH) (Watts and Teel, 2006; Huling and Pivetz, 2006; Zou et al., 2014). An alternate route for generation of oxidizing radicals is the persulfate system. Metal persulfates (sodium / potassium / ammonium salts) have been a known source of generating radicals in the reaction system. In fact, persulfate have been conventionally used as initiators of polymerization reaction (Price and Clifton 1996). However, more recently persulfate based degradation of recalcitrant pollutants as well as in-situ chemical oxidation of organic contaminants in soil and ground water has been extensively investigated. An important advantage of persulfate oxidant over hydroxyl radical is greater stability in presence of impurities (Xie et al., 2012). Moreover, persulfate is also able to maintain non-

selective reactivity over longer period for large variety of pollutants, especially for decontamination of ground water. Persulfate can be activated in the form of strong and non-reactive sulfate radical ($SO_4^{\bullet-}$) with oxidation potential of 2.6 eV (Zou et al., 2014). The activation of persulfate can be done by heat or UV or transition metal (TM) ions. The relevant reactions (Eqs. 6.1-6.7) in persulfate system have been described in Chapter 1; however, for convenience of readers, we reproduce herewith again (Wang et al., 2015; Kusic et al., 2011; Roshani and vel Leitner, 2011):

$$S_2O_8^{2-} + \text{heat} \longrightarrow 2\ SO_4^{\bullet-} \quad (6.1)$$

$$S_2O_8^{2-} \xrightarrow[ultrasound]{)))))} 2\ SO_4^{\bullet-} \quad (6.2)$$

$$S_2O_8^{2-} + h\nu \longrightarrow 2\ SO_4^{\bullet-} \quad (6.3)$$

$$S_2O_8^{2-} + Fe^{2+} \longrightarrow Fe^{3+} + SO_4^{2-} + SO_4^{\bullet-} \quad (6.4)$$

$$Fe^{3+} + S_2O_8^{2-} \longrightarrow 2\ SO_4^{\bullet-} + Fe^{2+} \quad (6.5)$$

$$S_2O_8^{2-} + {}^{\bullet}OH \longrightarrow OH^- + S_2O_8^{\bullet-} \quad (6.6)$$

$$S_2O_8^{2-} + SO_4^{\bullet-} \longrightarrow SO_4^{2-} + S_2O_8^{\bullet-} \quad (6.7)$$

A few authors have recently combined the persulfate system with ultrasound (Zou et al., 2014; Wang et al., 2015). Ultrasound can cause activation of persulfate leading to generation of sulfate radicals by two mechanisms. The first mechanism is thermal and related to transient cavitation. At the moment of transient collapse, the temperature and pressure inside the bubble reach extreme (~ 5000 K, ~ 500 bar) (Suslick, 1990). Although the collapse of bubble is extremely fast and adiabatic and extreme conditions inside the bubble also last for very short period (of the order of few tens of nano-seconds), some heat transfer does occur across the bubble wall (Yasui, 1997). A thin liquid layer in immediate vicinity of bubble interface gets heated to moderate temperature of ~ 300 – 500^{o}C (Kotronarou et al., 1991). This temperature is sufficient to causes thermal decomposition of the persulfate into sulfate

radicals. In addition, the transient collapse of cavitation bubble also generates $^{\bullet}H$ and $^{\bullet}OH$ radicals through dissociation of water molecules (Chakma and Moholkar, 2013a, 2013b). These radicals can also activate persulfate ion into sulfate radical via following reactions (Kusic et al., 2011; Roshani and vel Leitner, 2011).

$$S_2O_8^{2-} + {}^{\bullet}OH \longrightarrow SO_4^{\bullet-} + HSO_4^- + \frac{1}{2} O_2 \qquad (6.8)$$

$$S_2O_8^{2-} + {}^{\bullet}H \longrightarrow SO_4^{\bullet-} + H^+ + SO_4^{2-} \qquad (6.9)$$

Literature in the area of hybrid sono-persulfate process for degradation of recalcitrant pollutants is limited (for example: Zou et al., 2014; Wang et al., 2015; Chen and Huang, 2015; Deng et al., 2015; Wang et al., 2014; Hao et al., 2014; Nachiappan and Muthukumar, 2013; Hori et al., 2012). The focus of this literature is mostly on results and not on rationale. Although all authors have reported augmentation in degradation of pollutants through the hybrid process as compared to either sonolysis or persulfate treatment. The exact mechanism of synergy between these two processes is not fully explored. Discernment of the physical mechanism of sono-persulfate process would essential mean identification of links between physics of cavitation and ultrasound and chemistry of persulfate treatment. In the present study, we have addressed this fundamental issue. By application of the three techniques (*viz.* sonolysis, UV-C and transition metal (Fe^{2+})) for activation of persulfate anion into sulfate radical either individually or in combination. We have experimentally deduced the variation in extent of decolorization. The trends in extent of decolorization in different experimental categories (employing either individual or combined activation technique) reveal the individual contribution of each technique and also help in discrimination between the different mechanisms, as explained in the sections below.

6.2 MATERIALS AND METHODS

6.2.1 Materials

Sodium persulfate ($Na_2S_2O_8$, 99%) and ferrous heptahydrate sulfate ($FeSO_4 \cdot 7H_2O$, 99.5%) were procured from HiMedia Laboratories Pvt. Ltd. Sodium hydroxide pellet (NaOH) and sulfuric acid (H_2SO_4, 98%) were procured from Merck India Ltd. All of these chemicals were analytical reagent grade. Acid Red B dye ($C_{20}H_{12}N_2Na_2O_7S_2$ or disodium 4–hydroxy–2–[(*E*)–(4–sulfonato–1–naphthyl)diazenyl] naphthalene–1–sulfonate) was procured from a local vendor a.b. Chemicals and Instrumentations Pvt. Ltd., Guwahati, India. All chemicals were used as received from the suppliers without any pretreatment. The experiments were carried out using ultrapure Milli–Q water (≥18 MΩ·cm resistivity at 25°C) from Milli–Q synthesis unit (Millipore®, USA).

6.2.2 Experimental setup and procedure

Experiments were conducted in 3 categories with either individual or binary or ternary activation techniques (with combinations of ultrasound, Fe^{2+} and UV-C) for activation of persulfate. As base case for comparison of decolorization results, experiments were also conducted with individual technique of sonolysis, UV-C treatment with mechanical stirring and persulfate treatment with mechanical stirring.

All decolorization reactions were carried out in 250 mL beaker of borosilicate glass. Experiments with mechanical stirring were conducted using a magnetic plate at 300 rpm. An ultrasound bath (Jeio Tech, South Korea, Capacity: 10 L, Model: UC–10, frequency: 40 kHz, power rating: 200 W) was used for sonication in experiments with ultrasound irradiation. The acoustic power dissipation in the ultrasound bath was calibrated using calorimetric technique (Bhasarkar et al., 2013; Chakma and Moholkar, 2014). The acoustic intensity of the bath was determined as 1.2 W/cm^2 with a volumetric energy dissipation of 8.71 W/L. On the basis of

the acoustic intensity, the pressure amplitude of the ultrasound waves was calculated as 1.9 bar. The beaker with reaction mixture was placed at the center of the ultrasound bath. The position of the reaction beaker in the bath was maintained carefully the same in all experiments to avoid artifacts arising due to spatial variation of the acoustic intensity in the bath (Gogate et al., 2002).

For experiments with UV irradiation, UV-C tube (Philips, TUV 11W) with maximum peak emission wavelength at 254 nm was used as UV source. The UV source was placed exactly above the mouth of the reaction beaker. The distance of the UV lamp from the surface of the reaction mixture was 14 cm.

In a typical decolorization experiment, 50 mL of dye solution with an initial concentration of 20 mg/L (corresponding concentration 0.04 mM) was taken in the reaction beaker. Prior to commencement of the treatment, persulfate (4 mM) and Fe^{2+} (4 mM) were added to the solution and the pH of the solution was adjusted to desired value using NaOH or H_2SO_4. For UVC-activated persulfate treatment for decolorization, the pH of the reaction mixture was set at optimum value of 6.5, as reported by Gao et al. (2012). For Fe^{2+} activated persulfate treatment, the pH of the reaction mixture was set at 3.5, which is the optimum value of pH reported by Xu and Li (2010). Aliquots of the reaction mixture were withdrawn at regular time intervals for monitoring the progress of decolorization. After withdrawal of the aliquot, the decolorization reactions were immediately quenched by adding 1 mL of methanol. The residual concentration of dye in the aliquot was measured with a UV–Vis spectrophotometer (Perkin Elmer, Model: Lambda 35) by monitoring absorbance at 512 nm. In addition, the mineralization in term of total organic carbon (TOC) removal from the dye solution was analyzed using a TOC analyzer (O–I–Analytical, Model: Aurora 1030).

6.2.3 Kinetics of decolorization

Rodriguez et al. (2014) have reported the chemical pathway for oxidation of azo dye Orange G by Fe^{2+} and Fe^{3+} activated persulfate. The degradation commences with breakage of the azo bond; that results in formation of aniline and substituted naphthalene disulfonic acid. Aniline is further oxidized to phenol, benzoquinone and straight chain organic acid (after ring opening) such as oxalic, fumeric and maleic acids. The naphthalene disulfonic acid is degraded into naphthalene derivatives and further converted into phthalic acid and benzene derivatives such as catechol, hydroquinone, naphthoquinone and other organic acids. A similar mechanism is also observed for degradation of azo dye of ARB used in the present study (detail degradation mechanism is given in corrigendum). Formulation of a detailed kinetic model that takes into account all intermediates of degradation mentioned above would be a formidable task. In view of this difficulty, we have adopted a simple yet physically realistic approach of fitting the decolorization profile to pseudo first order kinetic model. As revealed in the analysis of experimental results, the pseudo 1^{st} order model fits well to the decolorization profile, as indicated by the regression coefficient of > 0.8.

6.2.4 Synergy calculation

Synergies between the three techniques of persulfate activation (sonolysis, TM ions and UV-C) applied simultaneously were determined on the basis of the decolorization obtained with individual techniques. The following formula was used for the synergy calculation:

$$\text{Synergy effect} = \frac{\left(\text{Decolorization in Hybrid Process}\right) - \sum \text{Decolorization in Individual Process}}{\sum \text{Decolorization in Individual Process}}$$

A positive value of synergy would mean that individual mechanisms of the two or three techniques reinforce each other's effect resulting in greater activation of persulfate anion that would result in higher sulfate radical generation leading to enhanced decolorization as compared to the sum total of decolorization obtained with the two individual techniques of persulfate activation.

6.3 RESULTS AND DISCUSSION

The decolorization experiments were performed in three categories, *viz*. (1) individual techniques of sonolysis, UV-C and persulfate, (2) per sulfate oxidation induced by a single activation technique, and (3) persulfate oxidation induced by binary or ternary activation techniques. The experimental results and the time profiles of decolorization in these three experimental categories are given Table 6.1 and Fig. 6.1. It could be seen that decolorization profiles are rather non-uniform in time in that significant decolorization occurs within first 10 min of treatment. The summary of results of decolorization experiments depicting total percentage decolorization achieved in 1 h of treatment, the decolorization achieved in the first 10 min of treatment and the pseudo 1st order kinetic constant calculated on that basis.

The salient features of experimental results and the explanation for the same can be given as follows:

(1) The individual techniques are not effective in decolorization of the dye, as seen for low percentage decolorization values for category 1 experiments. Among the three individual techniques, persulfate ($S_2O_8^{2-}$) induced oxidation gives the highest decolorization of ~ 13%. The decolorization due to UV-C could be due to radicals produced through direct photolysis of water or photo-tendering of dye pigments.

Table 6.1: Summary of decolorization of Acid Red B in different experimental categories employing either individual or combined techniques for persulfate activation

Experimental protocols		Percentage Decolorization of Acid Red B			
		10 min	60 min	k (s^{-1})	R^2
Category 1: Individual decolorization techniques					
1A	US	3.96 ± 1.73	9.82 ± 0.54	7.58E–05	0.88
1B	MS + UVC	3.27 ± 0.45	5.67 ± 0.41	4.95E–05	0.93
1C	MS + PS (without activator)	7.91 ± 0.17	12.63 ± 1.95	1.56E–04	0.86
Category 2: Decolorization by persulfate oxidation activated by single technique					
2A	US + PS	15.36 ± 3.14	33.69 ± 0.86	3.26E–04	0.82
2B	MS + PS + Fe^{2+}	69.09 ± 0.35	70.33 ± 0.60	4.50E–03	0.91
2C	MS + PS + UVC	82.45 ± 0.70	84.99 ± 0.66	5.38E–03	0.94
Category 3: Decolorization by persulfate oxidation activated by binary or ternary techniques					
3A	US + PS + Fe^{2+}	64.28 ± 305	66.54 ± 2.05	3.85E–03	0.90
3B	US + PS + UVC	91.68 ± 1.95	94.09 ± 0.25	8.77E–03	0.99
3C	MS + PS + Fe^{2+} + UVC	74.69 ± 1.15	79.96 ± 0.60	4.85E–03	0.83
3D	US + PS + Fe^{2+} + UVC	68.56 ± 3.20	81.20 ± 3.76	4.44E–03	0.90

Notation: US – ultrasound (or sonolysis), MS – mechanical stirring, PS – persulfate

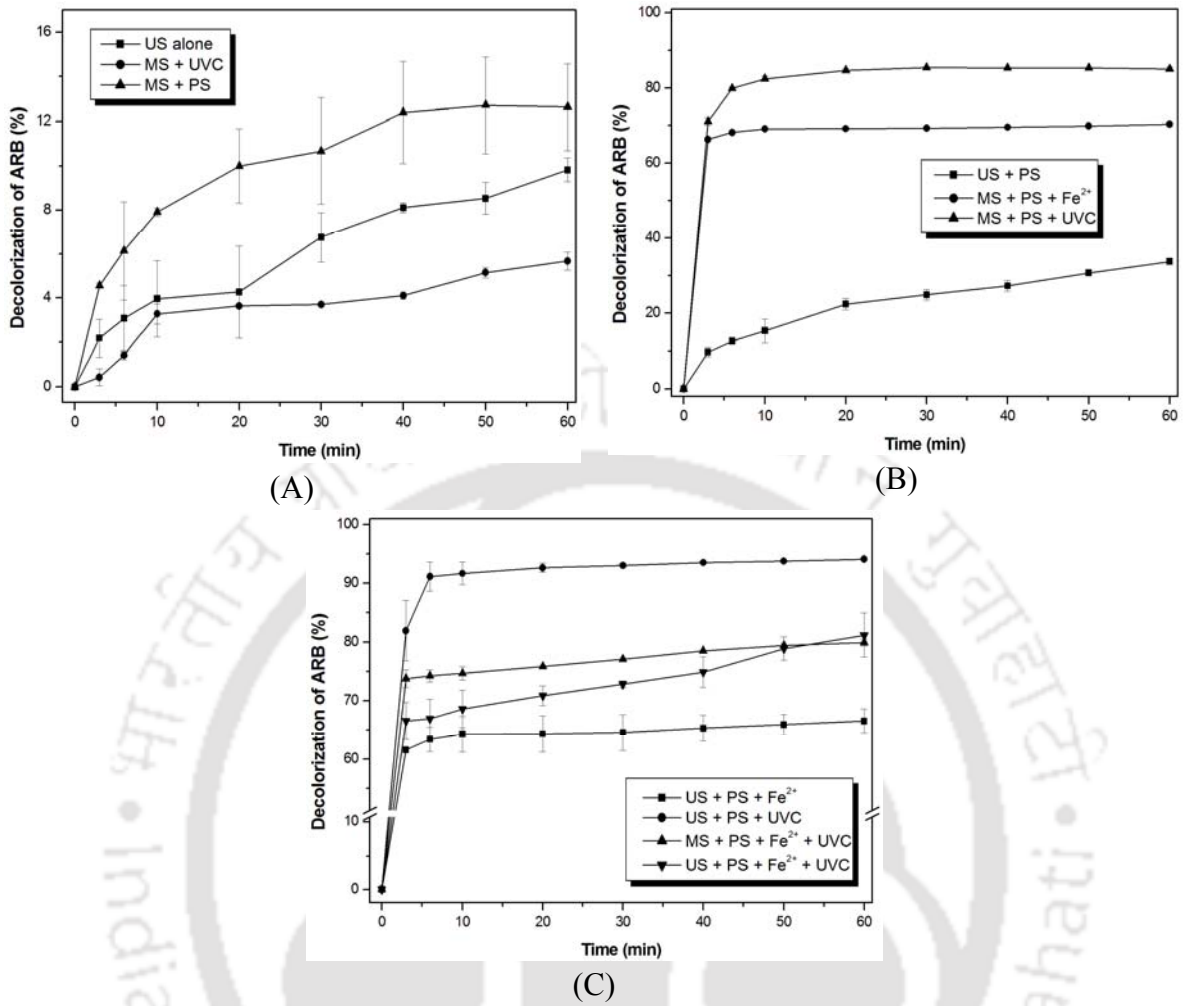

Figure 6.1: Time profiles of ARB dye decolorization in different experimental categories employing either single or combined techniques for persulfate activation. (A) Category 1 experiments: individual techniques of sonolysis, UVC (with mechanical stirring) and persulfate (without activator but with mechanical stirring). (B) Category 2 experiments: persulfate oxidation activated by individual techniques of sonolysis, Fe^{2+} ions (with mechanical stirring) and UV-C (with mechanical stirring), (C) Category 3 experiments: persulfate oxidation activated by binary (sonolysis + Fe^{2+}, sonolysis + UV-C, and Fe^{2+} + UV-C) and ternary (sonolysis + Fe^{2+} + UV-C) techniques.

(2) In category 2, the least decolorization is obtained for persulfate activated by sonolysis. This result is attributed to highly sporadic nature of transient cavitation events, both in space and time. Thus, the thermal activation of $S_2O_8^{2-}$ in the interfacial region of the bubble is not uniform throughout the reaction volume. Moreover, the $^{\bullet}OH$ radicals produced by transient

cavitation also scavenge the $SO_4^{\bullet-}$ radicals generated from persulfate activation. As a consequence, the activation of persulfate anions and the $SO_4^{\bullet-}$ radical generation in the reaction mixture is non-uniform, resulting in least decolorization. The Fe^{2+}-activation of persulfate with mechanical stirring in category 2B gives much higher decolorization than sonolysis due to volumetrically uniform activation of $S_2O_8^{2-}$ and generation of $SO_4^{\bullet-}$ radicals. Nonetheless, some scavenging of $SO_4^{\bullet-}$ radicals by Fe^{2+} is also feasible through reaction (Kusic et al., 2011): $Fe^{2+} + SO_4^{\bullet-} \longrightarrow Fe^{3+} + SO_4^{2-}$. The highest decolorization is obtained for the UV-C activation of persulfate with mechanical stirring, which indicates that this technique is most effective for persulfate oxidation of the dye.

(3) Category 3 experiments, in which binary or ternary persulfate activation techniques were applied, reveal interesting trends in decolorization. The highest decolorization is obtained in category 3B for the binary activation technique of (US + PS + UVC). The ternary technique in category 3D (US + PS + UVC + Fe^{2+}) gives 81.2% decolorization, while the other two binary techniques, *viz.* category 3A (US + PS + Fe^{2+}) and category 3C (MS + PS + Fe^{2+} + UVC) give 66.5% and 79.96% decolorization, respectively. Quite interestingly, the decolorization in categories 3A, 3C and 3D is lesser than the category 2C, in which single activation technique of UV-C was applied.

An explanation for these results can be given as follows: The UV-C induced activation of persulfate is hindered or slowed down by Fe^{2+}. This is due to scavenging of the $SO_4^{\bullet-}$ radicals generated by UV-C activation by Fe^{2+} ions, which get oxidized to Fe^{3+}. The UV-C activation of persulfate is expected to be very fast; and thus, the concentration of $SO_4^{\bullet-}$ radicals in the reaction mixture increases very rapidly. This triggers the oxidation of Fe^{2+} in the reaction mixture, for the binary system of (Fe^{2+} + UVC) in category 3C, rather than activation of persulfate by Fe^{2+}. This phenomenon reduces the utility of the $SO_4^{\bullet-}$ radicals for

decolorization of the dye. On the other hand, application of UV-C to the Fe^{2+} activated persulfate oxidation system increases the generation of $SO_4^{\bullet-}$ radicals due to faster and more efficient activation of $S_2O_8^{2-}$ by UV-C. Relatively low decolorization in categories 3A and 3D is also contributed by the scavenging of $SO_4^{\bullet-}$ radicals by $^{\bullet}OH$ radicals generated by transient cavitation.

As a consequence of these mechanistic interactions among the three techniques of persulfate activation, the extent of decolorization in categories 3C and 3D is lesser as compared to category 2C, in which single activation of persulfate with UV-C has been applied. On the other hand, the extent of decolorization in categories 3C and 3D is higher than categories 3A and 2B (single activation with Fe^{2+}).

These trends in decolorization of azo dye in the three experimental categories clearly point that UV-C based activation system is most efficient for effective for persulfate oxidation. The mechanistic interactions among the three techniques of persulfate activation also get reflected in the synergy values of binary and ternary activation systems in category 3, as well as in trends in reduction of total organic carbon (TOC) in the system, as discussed in the next sections.

6.4 ANALYSIS OF MINERALIZATION (TOC REMOVAL)

The results of total organic carbon (TOC) removal in different experimental categories are depicted in Fig. 6.2. Comparing the values of TOC removal with those of percentage decolorization, it could be perceived that the rate of mineralization is not as fast as that of decolorization. In all categories, the TOC removal values are almost 20-30% smaller than those for decolorization. Typical trends in TOC with different experimental techniques and explanations for the same are follows:

(1) All individual techniques of sonolysis, UV-C and persulfate are not efficient in TOC

removal, as evident from results of category 1 experiments. This result is attributed to very small extent of radical production by these techniques.

(2) In category 2, in which single activation technique of persulfate is applied, the trend in TOC removal is UV-C > Fe^{2+} > sonolysis. The least TOC removal for ultrasound is attributed to highly sporadic nature of transient cavitation events, in both space and time. This results in non-uniform activation of persulfate anions and radical production in reaction volume. Moreover, the $^{\bullet}OH$ radicals produced from transient cavitation can scavenge sulfate radicals ($SO_4^{\bullet-}$), and adversely affect their utility for TOC removal. The TOC removal with Fe^{2+} activation is limited by the reversible nature of Fe^{2+} activation. As the concentration of $SO_4^{\bullet-}$ radicals builds up in reaction volume, oxidation of Fe^{2+} to Fe^{3+} may occur with scavenging of some $SO_4^{\bullet-}$ radicals. UV-C activation, with the fast kinetics and irreversible nature, results in the highest radical production; and hence, TOC removal.

(3) For binary and ternary persulfate activation system applied in category 3, the TOC removal can be compared against the TOC obtained with individual techniques.

(i) For category 3A (US + PS + Fe^{2+}), the TOC removal (35.24%) is less than the sum total for categories 2A & 2B (19.05 + 31.98 = 51.03%). This essentially means that the extent of radical production in category 3A is reduced, when the two activation techniques are applied together. This result is attributed to scavenging of the $SO_4^{\bullet-}$ radicals (produced through transient cavitation) by Fe^{2+}.

(ii) For category 3B (US + PS + UVC), the TOC removal (66.35%) is almost equal to the TOC removal in categories 2A (19.05%) and 2C (46.01%). This essentially means that the techniques of sonolysis and UV-C for persulfate activation act almost independently without influencing each other.

(iii) For category 3C (MS + PS + Fe^{2+} + UVC), the TOC removal is lesser than for 2B and

2C. This effect is again attributed to scavenging of $SO_4^{\bullet-}$ radicals (generated by UV-C) by Fe^{2+}, which reduces their utility towards dye degradation.

(iv) For category 3D, in which the ternary system of (US + Fe^{2+} + UVC) was applied for persulfate activation, the TOC removal of 59.18% is much smaller than the total TOC removal of 97.04% for the three activation techniques applied individually. We attribute this effect to scavenging of these sulfate radicals ($SO_4^{\bullet-}$) by Fe^{2+}. Nonetheless, comparison the TOC removal for category 3D with 3C, gives indication of the beneficial effect of ultrasound, when replace with mechanical stirring. An augmentation of ~ 36% is seen in category 3D as against category 3C. This effect is attributed to additional radical production by ultrasound through transient cavitation. Strong micro-mixing provided by ultrasound also assists effective utilization of UV-C radiations in the system. Similar explanation can also be given for augmentation of ~ 49% in TOC removal in category 3B as compared to category 2C.

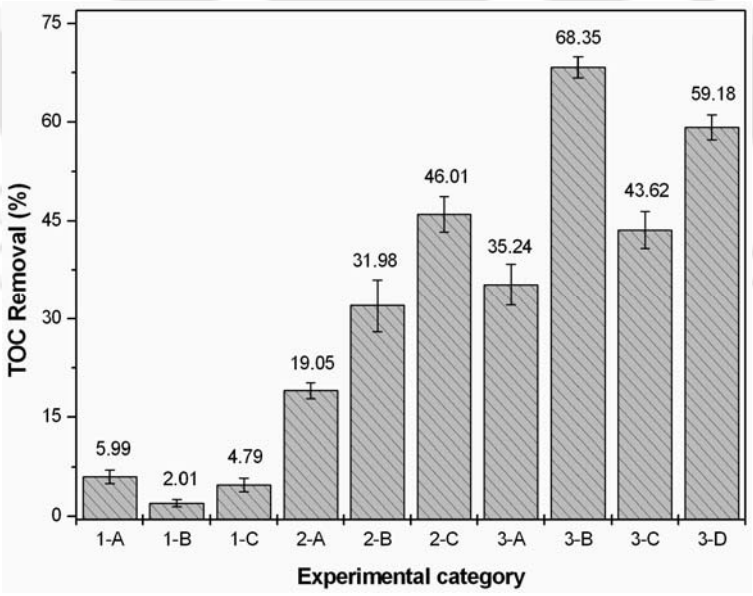

Figure 6.2: Removal of TOC (or extent of complete mineralization) of the ARB dye solution under various operating conditions assisted with mechanical stirring and ultrasound. US – ultrasound, MS – mechanical stirring, 1A: US alone (or sonolysis), 1B: (MS + UVC), 1C: (MS + PS), 2A: (US + PS), 2B: (MS + PS + Fe^{2+}), 2C: (MS +PS + UVC), 3A: (US + PS + Fe^{2+}), 3B: (US + PS + UVC), 3C: (MS + PS + Fe^{2+} + UVC), 3D: (US + PS + Fe^{2+} + UVC)

6.5 MECHANISTIC SYNERGIES IN BINARY/ TERNARY ACTIVATION TECHNIQUES

The synergies between different activation techniques for category 3 experiments are shown in Fig. 6.3. The synergy is found to be negative in all 4 subcategories. In categories 3A, C & D; in which Fe^{2+} activation is applied concurrently with either sonolysis or UV-C or both, the synergy values are rather close (± 5%). The synergy value for category 3B, in which binary activation of sonolysis and UV-C is applied, is significantly smaller, *i.e.* -0.76%. An explanation for these results can be given as follows:

As the results of decolorization experiments imply, the relative kinetics of persulfate activation by individual techniques is in the order: UV-C > Fe^{2+} > sonolysis. The technique of UV-C is irreversible in that it does not scavenge the $SO_4^{\bullet-}$ radicals once generated. However, the Fe^{2+} activation technique is reversible. Essentially, in presence of high concentration of $SO_4^{\bullet-}$ radicals (generated through activation techniques of either UV-C or US or both), Fe^{2+} itself undergoes oxidation to Fe^{3+}. This results in scavenging of radicals, and thereby, negative synergy.

The synergy effect for binary activation techniques of (US + UVC + PS) is also negative, however, the synergy value (-0.76%) is much smaller than other categories. This is attributed to scavenging of $SO_4^{\bullet-}$ radicals by $^{\bullet}OH$ radicals generated from transient cavitation bubble through following reaction (Kusic et al. 2011):

$$^{\bullet}OH + SO_4^{\bullet-} \longrightarrow HSO_4^- + \frac{1}{2}O_2 \qquad (6.10)$$

Nonetheless, the extent of $^{\bullet}OH$ radical production through cavitation bubble is rather small (as indicated by small value of decolorization in category 1A), and hence, the scavenging effect, and the negative synergy induced thereby is trivial. The schematic showing the mechanistic synergies between the three activation techniques as described above is given in

Fig. 6.4.

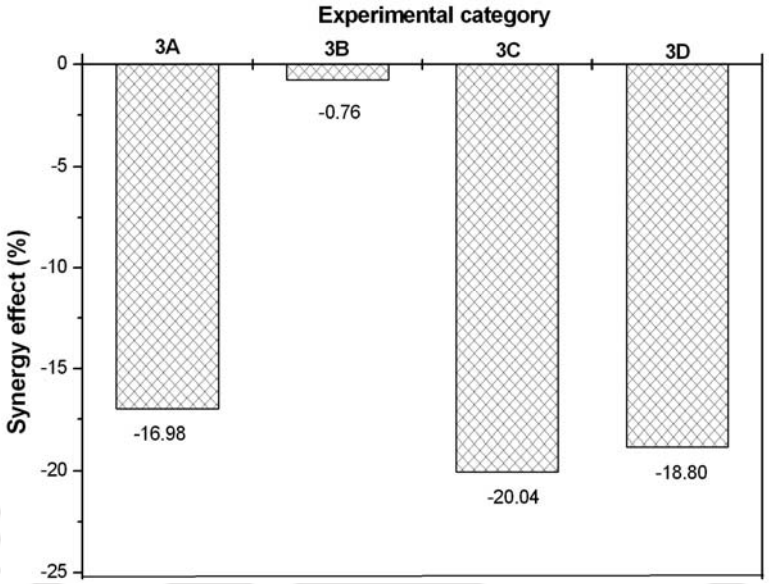

Figure 6.3: Synergy effect in experimental categories with binary or ternary activation of persulfate for decolorization of azo dye.

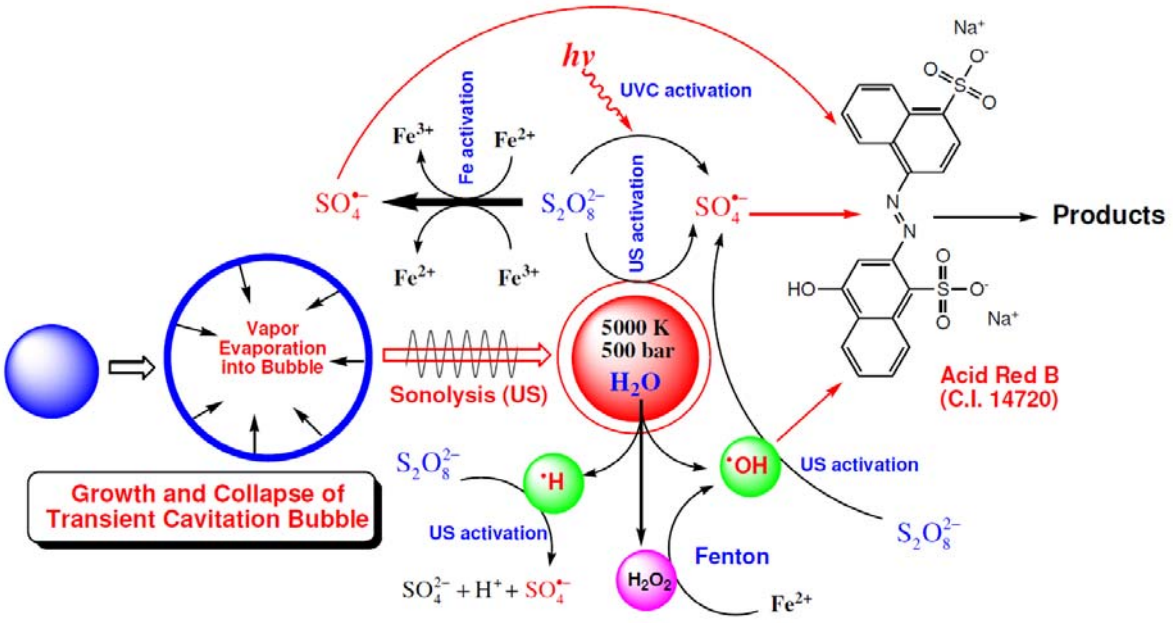

Figure 6.4: Mechanistic synergies in ultrasound-assisted persulfate based decolorization of ARB dye

6.6 CONCLUSION

In the present study, an attempt is made to identify the physical mechanism of persulfate-based decolorization of azo dyes using different activators for generation of sulfate radicals. Three techniques, *viz*. transition metal ion (Fe^{2+} ions), sonolysis and UV-C light, have been applied, either individually or in binary or ternary combinations, for activation of persulfate ions. Analysis of trends in decolorization with single/ binary/ ternary activation techniques shed important light on mechanistic interactions between the activation techniques. UV-C is revealed to be the most efficient technique for activation. Among the other two techniques, *viz*. sonolysis and Fe^{2+} ions, the former is found to have almost independent mechanism (thermal decomposition of persulfate in bubble-bulk interfacial region) than UV-C. Thus, decolorization as well as mineralization obtained with simultaneous application of sonolysis and UV-C is almost addition of individual effects. Fe^{2+} ions have been revealed to have adverse impact on the UV-C based activation, due to scavenging of $SO_4^{\bullet-}$ radicals. Among all techniques (single/binary/ternary) attempted for activation of persulfate and decolorization, the binary technique of (US + PS + UVC) is found to yield maximum decolorization as well as mineralization. The results of this study could form useful guidelines for optimization of the persulfate-based oxidation of textile dyes. Moreover, the methodology presented in this study can form general framework, which could be extended for mechanistic investigation in persulfate-based oxidation of any other recalcitrant pollutant.

REFERENCES

Bhasarkar JB, Chakma S, Moholkar VS, Mechanistic features of oxidative desulfurization using sono–Fenton–peracetic acid (ultrasound/Fe^{2+}–CH_3COOH–H_2O_2) system, Ind. Eng. Chem. Res. 52 (2013) 9038–9047

Chakma S, Moholkar VS, Investigations in synergism of hybrid advanced oxidation processes with combinations of sonolysis + Fenton process + UV for degradation of Bisphenol–A, Ind. Eng. Chem. Res. 53 (2014) 6855–6865.

Chakma S, Moholkar VS, Numerical simulation and investigation of system parameters of sonochemical process, Chinese J. Eng. 2013 (2013b) 1-14.

Chakma S, Moholkar VS, Physical mechanism of sono-Fenton process, AIChE J. 59 (2013a) 4303 – 4313.

Chen W-S, Huang C-P, Mineralization of aniline in aqueous solution by electro-activated persulfate oxidation enhanced with ultrasound, Chem. Eng. J. 266 (2015) 279–288.

Deng D, Lin X, Ou J, Wang Z, Li S, Deng M, Shu Y, Efficient chemical oxidation of high levels of soil-sorbed phenanthrene by ultrasound induced, thermally activated persulfate, Chem. Eng. J. 265 (2015) 176–183.

Gao Y, Gao N, Deng Y, Yang Y, Ma Y, Ultraviolet (UV) light-activated persulfate oxidation of sulfamethazine in water, Chem. Eng. J. 195–196 (2012) 248–253.

Gogate PR, Tatake PA, Kanthale PM, Pandit AB, Mapping of sonochemical reactors: review, analysis, and experimental verification, AIChE J. 48 (2002) 1542–1560.

Hao F, Guo W, Wang A, Leng Y, Li H, Intensification of sonochemical degradation of ammonium perfluorooctanoate by persulfate oxidant, Ultrason. Sonochem. 21 (2014) 554–558.

Hori H, Nagano Y, Murayama M, Koike K, Kutsuna S, Efficient decomposition of perfluoroether carboxylic acids in water with a combination of persulfate oxidant and ultrasonic irradiation, J. Fluorine Chem. 141 (2012) 5–10.

Huling SG, Pivetz BE, In situ chemical oxidation (EPA/600/R-06/072), Office of Research and Development, National Risk Management Research Laboratory, U. S. EPA, 2006.

Kotronarou A, Mills G, Hoffmann MR, Ultrasonic irradiation of p-nitrophenol in aqueous

solution J. Phys. Chem. 95 (1991) 3630–3638.

Kusic H, Peternel I, Ukic S, Koprivanac N, Bolanca T, Papic S, Bozic AL, Modeling of iron activated persulfate oxidation treating reactive azo dye in water matrix, Chem. Eng. J. 172 (2011) 109–121.

Nachiappan S, Muthukumar K, Treatment of pharmaceutical effluent by ultrasound coupled with dual oxidant system, Environ. Technol. 34 (2013) 209–217.

Price GJ, Clifton AA, Sonochemical acceleration of persulfate decomposition, Polymer 37 (1996) 3971-3973

Rodriguez S, Vasquez L, Costa D, Romero A, Santos A, Oxidation of Orange G by persulfate activated by Fe(II), Fe(III) and zero valent iron (ZVI), Chemosphere 101 (2014) 86–92.

Roshani B, vel Leitner NK, The influence of persulfate addition for the degradation of micropollutants by ionizing radiation, Chem. Eng. J. 168 (2011) 784–789.

Suslick KS, Sonochemistry, Science 247 (1990) 1439–1445.

Wang S, Zhou N, Wu S, Zhang Q, Yang Z, Modeling the oxidation kinetics of sono-activated persulfate's process on the degradation of humic acid, Ultrason. Sonochem. 23 (2015) 128–134.

Wang X, Wang L, Li J, Qiu J, Cai C, Zhang H, Degradation of Acid Orange 7 by persulfate activated with zero valent iron in the presence of ultrasonic irradiation, Sep. Purif. Technol. 122 (2014) 41–46.

Watts RJ, Teel AL, Treatment of contaminated soils and groundwater using ISCO, J. Hazard. Toxic Radioact. Waste 10 (2006) 2–9.

Xie X, Zhang Y, Huang W, Huang S, Degradation kinetics and mechanism of aniline by heat-assisted persulfate oxidation, J. Environ. Sci. 24 (2012) 821–826]

Xu X-R, Li X-Z, Degradation of azo dye Orange G in aqueous solutions by persulfate with ferrous ion, Sep. Purif. Technol. 72 (2010) 105–111.

Yasui K, Alternative model for single-bubble sonoluminescence, Phys. Rev. E 56 (1997) 6750.

Zou X, Zhou T, Mao J, Wu X, Synergistic degradation of antibiotic sulfadiazine in a heterogeneous ultrasound-enhanced Fe0/persulfate Fenton-like system, Chem. Eng. J. 257 (2014) 36–44.

भारतीय प्रौद्योगिकी संस्थान गुवाहाटी
Indian Institute of Technology Guwahati

7

INVESTIGATIONS IN SONO–ENZYMATIC DEGRADATION OF IBUPROFEN

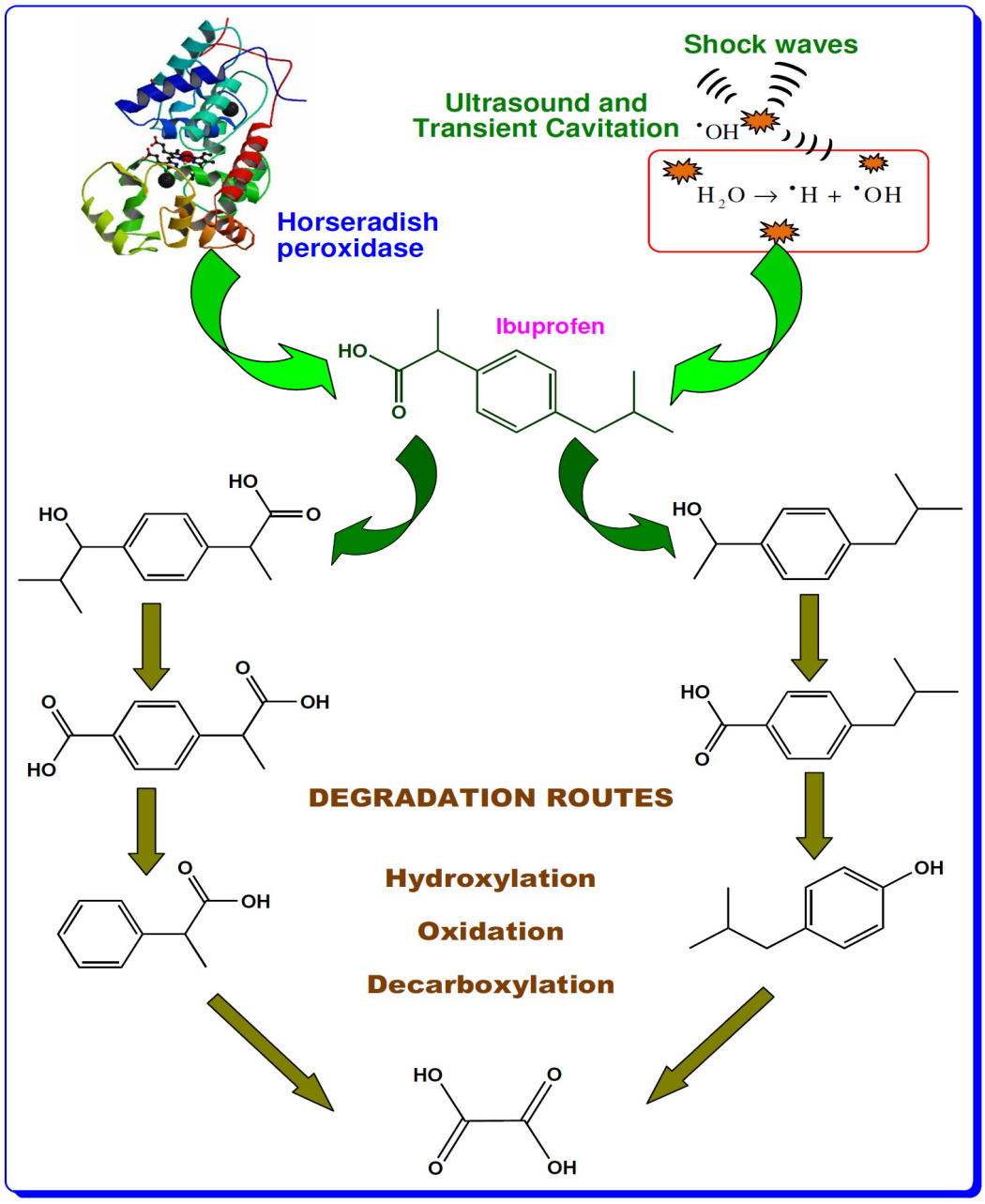

CHAPTER 7

INVESTIGATIONS IN SONO–ENZYMATIC DEGRADATION OF IBUPROFEN

7.1 INTRODUCTION

The hybrid AOPs of sono-Fenton, sono-photo-Fenton, sono-Ferrioxalate, sono-photolysis or sono-persulfate described in previous chapters are radical based processes. The radicals are essentially non-specific and non-selective oxidant species. An alternate sono–hybrid technique for degradation of bio–recalcitrant organic pollutants is sono–enzymatic treatment (Entezari and Petrier, 2003; Sangave and Pandit, 2006; Sun et al., 2011), in which sonolysis is combined with enzymatic treatment. This technique has especially been applied for degradation/ decolorization of dyestuffs in wastewater from textile industries. Peroxidase enzymes (such as lignin peroxidase, manganese peroxidase, laccase and horseradish peroxidase) that utilize H_2O_2 as electron acceptor have been used in sono–enzymatic technique. In this chapter, we have presented studies in mechanistic investigation of this process using a drug appearing in wastewater of pharmaceutical industry as model pollutant.

Wastewater discharge from pharmaceutical industries is of special concern, due to presence of numerous drugs in it, which are potentially harmful to ecosystem. A common drug that appears in wastewater discharge from pharmaceutical industries is ibuprofen (IBP) or 2–(4–isobutyl phenyl) propanoic acid ($C_{13}H_{18}O_2$). This is a non–steroidal, anti–

inflammatory, antipyretic drug, which is widely used for treatment of inflammatory disorders. This drug has several adverse impacts on the ecosystem (Richardson and Bowron, 1985; Ternes et al., 2004; Matamoros et al., 2005). Advanced oxidation techniques (AOTs) such as Fenton, photo–Fenton, photocatalysis, ozonation are required for complete mineralization of pharmaceutical wastewater containing IBP (Méndez–Arriaga et al., 2010; Sabri et al., 2012; Esplugas et al., 2007; Choina et al., 2013). More recently, sonolysis (Méndez–Arriaga et al., 2008) and sono–hybrid techniques, in which sonication is coupled with AOTs like photocatalysis and Fenton process (Vinu and Madras, 2009; Madhavan et al., 2010; Chakma et al., 2013; Chakma and Moholkar, 2015; Bagal and Gogate, 2014; Michael et al., 2014), have been employed for degradation of IBP. Sonolysis (or ultrasound irradiation) alone is not effective in degradation as well as complete mineralization of organic pollutants. This is attributed to formation of hydrophilic intermediates during degradation. These intermediates form by hydroxylation/oxidation reactions induced by radicals formed during transient cavitation. Hence, sono–hybrid techniques have been applied for degradation/ mineralization of the IBP.

In this chapter, our mechanistic investigation is based on Arrhenius and thermodynamic analysis of the experimental data, as reported in one of our earlier study (Malani et al., 2014). Moreover, identification of the intermediates of degradation also gives an insight into the chemical mechanism of degradation.

7.2 MATERIALS AND METHODS

7.2.1 Materials

Ibuprofen, horseradish peroxidase (EC 1.11.1.7, 140 U/mg) enzyme and pyrogallol ($C_6H_6O_3$) were procured from Sigma–Aldrich India Ltd. Mono–potassium phosphate (KH_2PO_4), di–potassium phosphate (K_2HPO_4) and hydrogen peroxide (H_2O_2, 30% v/v) were

procured from Merck India Ltd. All solutions were prepared in ultrapure Milli–Q water (resistivity ≥18 MΩ·cm at 298 K).

7.2.2 Activity and Bradford Assay for HRP enzyme

Activity of HRP enzyme was determined as per standard protocol (Sigma–Aldrich, EC 1.11.1.7) (Enzymatic assay of peroxidase, EC 1.11.1.7) with pyrogallol as substrate. The following reaction determines the activity of HRP enzyme:

$$\text{Pyrogallol (donor)} + H_2O_2 \xrightarrow{\text{HRP}} 2H_2O + \text{Purpurogallin (oxidized donor)}$$

The assay composition was as follows: ultrapure water 2.1 mL, phosphate buffer (pH 7, 100 mM) 0.32 mL, hydrogen peroxide solution (diluted to 60:1) 0.16 mL, pyrogallol solution 0.32 mL, enzyme (HRP) 0.1 mL. After mixing of above solutions, the final concentrations in 3 mL mixture were: 14 mM of phosphate buffer, 0.027% (w/w) H_2O_2, 0.5% (w/v) pyrogallol. These concentrations were maintained same in all experiments of IBP degradation. The absorbance of purpurogallin was recorded every 20s at 420 nm using UV–Vis spectrophotometer (ThermoFischer, Model: UV–2300). The activity of the enzyme was calculated using the following formula:

$$\text{Unit/mL Enzyme} = \frac{\left(\Delta A_{420}/20\ \text{s}\right)\times V_t \times D_f}{\varepsilon \times v_S}$$

Notation: V_t – total volume of reaction mixture (3 mL), D_f – dilution factor, ε – extinction coefficient (12 for purpurogallin at 420 nm), v_s– volume of sample (0.1 mL).

The protein content of the HRP enzyme was also determined by Bradford assay. Bovine serum albumin (BSA) was used as the standard protein. 3 ml of Bradford reagent and 0.1 ml HRP enzyme were mixed to form Bradford assay mixture. The mixture was kept in incubation for 15 min and the absorbance in mixture was measured at 595 nm. With this procedure, the protein content of HRP was determined as 0.0228 mg/mL.

7.2.3 Experimental setup and procedure

Purely enzymatic reactions were carried out under well stirred conditions using mechanical stirring with a small magnetic bar (length = 1 cm, diameter = 0.5 cm) at 150 rpm. A schematic of the experimental setup is given in Fig. 7.1. Experiments were carried out in a custom built (20 mL) test tube made of borosilicate glass. The experiments with sonication were conducted in an ultrasound bath (Elmasonic, Germany, Model: P−30H). The ultrasound bath could operate at two frequencies, viz. 37 kHz (130 W) and 80 kHz (100 W). Approximately 2/3rd volume of the bath was filled with water that acted as medium for transmission of ultrasound waves. The test tube with reaction mixture was placed exactly at the center of the ultrasound bath and it was immersed to approx. 75% of its height. This ensured that entire reaction mixture in the test tube was exposed to ultrasound waves. The position of test tube in the bath was maintained carefully same in all experiments to avoid the artifacts in experimental results due to spatial variation of acoustic intensity (Moholkar et al., 2000; Gogate et al., 2002). The actual power input to the ultrasound bath and to the reaction mixture inside the test tube was determined using calorimetric technique (Bhasarkar et al., 2013; Chakma and Moholkar, 2014). On this basis, the pressure amplitudes of ultrasound waves in the bath for frequencies of 80 and 37 kHz were calculated as 170 kPa and 200 kPa, respectively. Moreover, the pressure amplitudes of ultrasound waves in the bath and the reaction mixture inside the reaction tube was found to be same, which indicated negligible attenuation of ultrasound waves through the wall of reaction test tube. Due viscous dissipation of energy of ultrasound waves during propagation, the temperature of the water in the bath rises. This rise was controlled by circulation of water from a temperature controlled cooling water circulating bath (Amkette Analytics, Model: WB2000). The temperature of the reaction mixture in the test tube was same as that of the water in the bath.

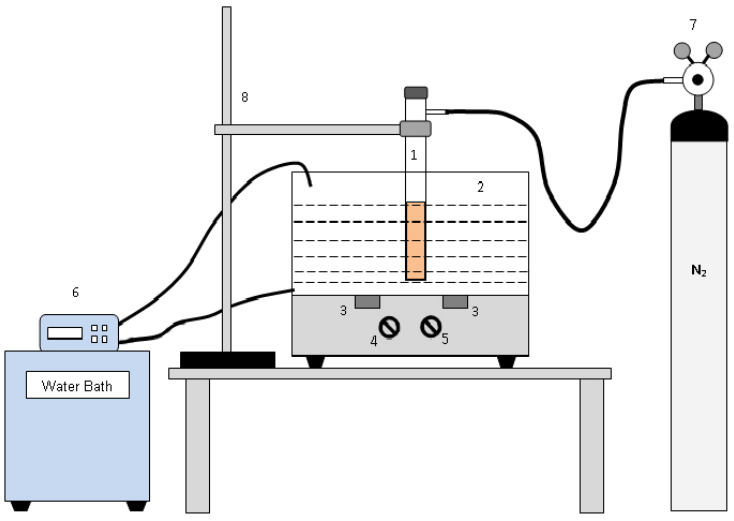

Figure 7.1: Schematic diagram for sono-enzymatic experiment. (1) Reaction solution, (2) ultrasound bath, (3) transducers, (4) timer, (5) temperature controller, (6) cooling water bath, (7) nitrogen gas cylinder, and (8) burette stand

The IBP degradation experiments were conducted in four categories, viz. (1) enzymatic treatment with mechanical stirring, (2) sonolysis, (3) sono-enzymatic treatment at atmospheric static pressure, and (4) sono-enzymatic treatment at elevated static pressure of 200 kPa. In categories 2, 3 and 4 involving sonolysis, experiments were conducted at two frequencies (either 37 or 80 kHz). In category 4 experiments, the test tube containing reaction mixture was connected to a nitrogen cylinder through a side nozzle. The mouth of the test tube was sealed with threaded cap as shown in Fig. 7.1. During withdrawal of aliquots of reaction mixture, the pressure in reaction test tube was released. The static pressure was restored to original level, as the sonication was resumed. The rationale underlying the technique of elevating static pressure of reaction mixture will be explained subsequently. The actual pressure amplitude of ultrasound waves reaching the reaction mixture is a strong function of wall thickness of the test tube holding reaction mixture. In order to keep this important parameter constant, same test tube has been used in all experiments.

The total reaction volume in a typical experiment was 15 mL. In this volume, concentrations of different components were as follows: IBP = 10 ppm (or 4.76×10^{-2} mM), H_2O_2 = 8.55 mM, HRP = 0.08 U/mL, phosphate buffer (pH 7) = 14 mM. The pH of the reaction mixture was maintained at 7 in all experiments. This pH was optimum for the highest activity of enzyme (results are shown in Fig. 7.2). To monitor the time profile of IBP degradation, aliquots of reaction mixture (200 μL) were withdrawn at regular intervals and were analyzed for the residual IBP. After completion of the treatment, aliquotes of reaction mixture were analyzed for identification of intermediates of IBP degradation.

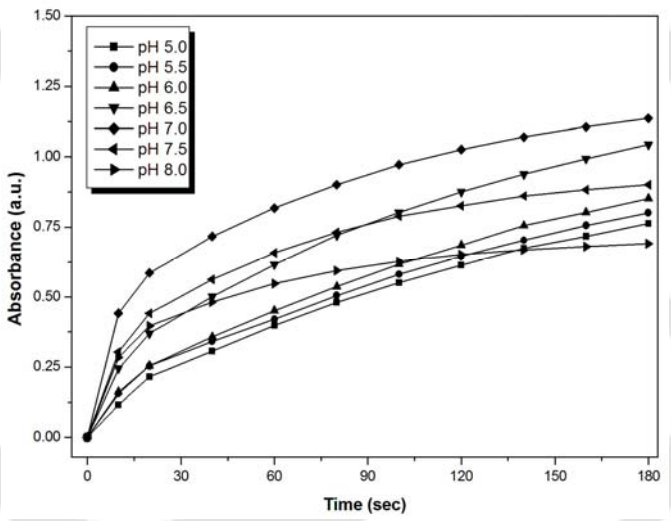

Figure 7.2: Time scan for enzyme activity at different pH

7.2.4 Analytical methods

The concentration of IBP in the aliquot of the reaction mixture was analyzed using High Performance Liquid Chromatography (Shimadzu, Model: SPD–20A) equipped with C–18 reverse phase column (250 mm × 4.6 mm, 5 μm) and UV detector at 220 nm. The mobile phase was a mixture of acetonitrile and aqueous acetic acid 0.1% (60/40, v/v) with an isocratic flow of 1.5 mL/min. In order to determine the mineralization, the total organic carbon (TOC) in the IBP reaction solution was measured with Aurora TOC analyzer (O–I–

Analytical, Model: 1030). The intermediates formed during sono–enzymatic degradation of IBP were identified using GC–MS (Varian 240–GC) after liquid–liquid extraction with dichloromethane. 1 μL of extracted sample was injected with a split ratio of 10:1. Helium gas was used as a carrier and the mass detector worked in scan mode with m/z range of 50 – 600. The GC–MS spectrums are given in Annexure-I (Figs. 7.S1 – 7.S5).

7.2.5 Experimental data analysis

The kinetic constants of IBP degradation were determined by fitting pseudo 1st order model to the kinetic data of IBP degradation. Using these kinetic constants, activation energy for IBP degradation was calculated applying Arrhenius equation: $k = A\exp(-E_a / RT)$. Various notations are as follows: k – kinetic constant, A – frequency factor or pre–exponential factor, E_a – activation energy for the reaction, R – universal gas constant, T – temperature. The thermodynamic parameters for IBP degradation were determined using Eyring equation as follows (Malani et al., 2014):

$$\ln\left(\frac{k}{T}\right) = -\left(\frac{\Delta H}{R}\right)\left(\frac{1}{T}\right) + \ln\left(\frac{k_b}{h}\right) + \frac{\Delta S}{R}$$

$$\Delta H = E_a - R \cdot T$$

$$\Delta G = \Delta H - T \cdot \Delta S$$

Notations: k_b – Boltzmann constant (1.381×10^{-23} J K^{-1}), h – Planck's constant (6.626×10^{-34} J·s). The values of k and E_a obtained from Arrhenius analysis can be substituted in above set of equations to yield thermodynamic parameters, *viz*. ΔH (enthalpy change), ΔS (entropy change) and ΔG (Gibbs free energy change), associated with IBP degradation. Finally, the synergy effect in hybrid sono–enzymatic processes was determined as follows:

$$\text{Synergy effect} = \frac{\left(\begin{matrix}\text{IBP Degradation in}\\ \text{sono-enzymatic treatment}\end{matrix}\right) - \left\{\left(\begin{matrix}\text{IBP Degradation in}\\ \text{enzymatic treatment}\end{matrix}\right) + \left(\begin{matrix}\text{IBP Degradation}\\ \text{in sonolysis}\end{matrix}\right)\right\}}{\left(\begin{matrix}\text{IBP Degradation in}\\ \text{enzymatic treatment}\end{matrix}\right) + \left(\begin{matrix}\text{IBP Degradation}\\ \text{in sonolysis}\end{matrix}\right)}$$

7.3 RESULTS AND DISCUSSION

7.3.1 Results of sono-enzymatic degradation

The results of IBP degradation are given in Tables 7.1 – 7. 4 and Figs. 7.3 – 7.6. Table 7.1 gives the summary of IBP degradation in different experimental protocols employing either individual or hybrid technique. The time profiles of IBP degradation are depicted in Figs. 7.3 & 7.4. The following features of IBP degradation can be identified from the results shown in Table 7.1 and Figs. 7.3 & 7.4.

(1) Among individual processes of sonolysis and enzymatic treatment, the latter gives faster as well as higher IBP degradation.

(2) Hybrid sono–enzymatic treatment gives higher degradation than either sonolysis or enzymatic treatment alone, indicating positive synergy. Among the three temperatures used for degradation, 308 K gives the highest degradation. The synergy is more pronounced at lower frequency of 37 kHz.

(3) Elevated static pressure on reaction mixture, which eliminates the transient cavitation (Chakma and Moholkar, 2013a; 2013b), reduces IBP degradation. This effect is consistent for both ultrasound frequencies and all three temperatures.

These trends in IBP degradation can be explained as follows:

(1) The extent of IBP degradation depends on the interaction between the enzyme and IBP molecules in case of enzymatic treatment. On the other hand, in sonolysis, the degradation is a function of interaction between radicals generated by transient cavitation and IBP molecules. In a well stirred reaction mixture, the enzyme concentration is uniform

throughout the volume. However, occurrence of transient cavitation events in the reaction volume is completely random. The radicals generated inside the transient cavitation bubble (due to thermal dissociation of vapor entrapped in the bubble) are released at the site of transient bubble collapse. Due to extreme instability, these radicals do not diffuse into the medium from the site of bubble collapse. Hence, IBP molecules present in close vicinity of the site of bubble collapse (or the interfacial region of the bubble) are likely to intercept these radicals. This feature puts limitation on the interaction probability of radicals and IBP molecules. As a consequence, the extent of IBP degradation through sonolysis route is low.

(2) Lesser IBP degradation at elevated static pressure is a consequence of elimination of transient cavitation. Due to this, production of hydroxyl radicals ($^{\bullet}$OH) in the reaction mixture is also eliminated. In sono–enzymatic treatment, the degradation of IBP is likely to commence with hydroxylation induced by $^{\bullet}$OH radicals to give hydrophilic intermediates (greater details on this are given in GC–MS analysis section) (Méndez–Arriaga et al., 2008). These intermediates are subsequently degraded by enzyme through oxidation and decarboxylation. At elevated static pressure, this pathway of degradation is adversely affected because of elimination of $^{\bullet}$OH radical production.

(3) At higher frequency of ultrasound (80 kHz), IBP degradation was reduced. A similar result is also reported by Chiha et al. (2011) for degradation of 4–cumylphenol. Possible causes underlying this effect are as follows: (a) lower pressure amplitude of ultrasound waves, and (b) higher transient cavitation threshold (i.e. minimum acoustic pressure amplitude required for occurrence of transient cavitation). This is further explained as follows:

Table 7.1: Summary of experimental results on IBP degradation in different experimental protocols

Temperature	**288 K**			**298 K**			**308 K**		
Experimental Protocols	**η%**	***k*** **(s^{-1})**	***R*²**	**η%**	***k*** **(s^{-1})**	***R*²**	**η%**	***k*** **(s^{-1})**	***R*²**
1. Enzyme treatment	29.28 ± 1.59	1.06×10^{-4}	0.97	31.02 ± 0.59	1.65×10^{-4}	0.85	33.96 ± 1.20	1.85×10^{-4}	0.75
	***frequency* = 37 kHz**								
2. Sonolysis	19.96 ± 1.92	6.57×10^{-5}	0.95	16.46 ± 0.06	6.04×10^{-5}	0.77	13.11 ± 0.61	4.03×10^{-5}	0.96
3. Sono–enzymatic treatment P_o = 101.3 kPa	59.34 ± 1.88	2.78×10^{-4}	0.90	61.93 ± 0.85	3.10×10^{-4}	0.89	71.54 ± 0.71	3.61×10^{-4}	0.96
4. Sono–enzymatic treatment P_o = 200 kPa	44.80 ± 1.44	1.82×10^{-4}	0.90	50.18 ± 2.78	2.27×10^{-4}	0.85	48.02 ± 1.59	2.4×10^{-4}	0.85
	***frequency* = 80 kHz**								
5. Sonolysis	7.53 ± 0.22	2.27×10^{-5}	0.97	8.21 ± 0.18	2.44×10^{-5}	0.97	8.44 ± 0.40	2.50×10^{-5}	0.95
6. Sono–enzymatic treatment P_o = 101.3 kPa	34.12 ± 1.95	2.37×10^{-4}	0.82	34.72 ± 1.57	2.57×10^{-4}	0.82	40.44 ± 0.87	3.19×10^{-4}	0.82
7. Sono–enzymatic treatment P_o = 200 kPa	31.30 ± 0.34	1.69×10^{-4}	0.93	30.48 ± 0.28	2.40×10^{-4}	0.79	33.07 ± 0.83	2.52×10^{-4}	0.82

Note: η – percentage degradation of IBP, *k* – pseudo 1st order kinetic constant (s^{-1}), R^2 – regression coefficient

Table 7.2: Arrhenius parameters for different protocols of IBP degradation

Experimental Protocols	Activation energy E_a (kJ mol^{-1})	Frequency factor A (mol L^{-1} s^{-1})
1. Enzyme treatment	20.71	0.64
	Frequency = 37 kHz	
2. Sonolysis	–17.91	3.94×10^{-8}
3. Sono–enzymatic treatment, P_o = 101.3 kPa	9.63	1.54×10^{-2}
4. Sono–enzymatic treatment, P_o = 200 kPa	10.26	1.36×10^{-2}
	Frequency = 80 kHz	
5. Sonolysis	3.44	9.63×10^{-5}
6. Sono–enzymatic treatment, P_o = 101.3 kPa	10.89	2.19×10^{-2}
7. Sono–enzymatic treatment, P_o = 200 kPa	14.95	9.13×10^{-2}

Increase in transient cavitation threshold with ultrasound frequency is essentially a consequence of reduction in duration of the rarefaction half cycle of ultrasound wave. As a consequence, expansion of the bubble during radial motion (at a given acoustic pressure amplitude) is also reduced. For the present case, acoustic pressure amplitudes generated at 80 and 37 kHz frequencies are 170 and 200 kPa, respectively. Ahmadi et al. (2012) have reported the following correlation for the estimation of transient cavitation threshold (P_t in MPa) as a function of frequency (f in MHz) for water as the medium: $P_t = 0.1 + 0.216\, f^{0.6}$. According to this correlation, transient cavitation thresholds for the two frequencies are: 130 kPa (for 37 kHz) and 147 kPa (for 80 kHz). The intensity of transient cavitation is proportional to the expansion of the bubble during rarefaction cycle (Flynn, 1975). This expansion, in turn, depends on the difference between pressure amplitude of ultrasound wave driving radial bubble motion and the static pressure in the medium. This difference, and hence, the intensity of transient cavitation is lower for higher frequency. Thus, the extent of IBP degradation obtained at 80 kHz is lesser than the degradation at 37 kHz.

Table 7.3: Thermodynamic parameters for different protocols of IBP degradation

Experimental Protocols	ΔH (kJ mol^{-1})			ΔS (kJ mol^{-1} K^{-1})			ΔG (kJ mol^{-1})		
	288 K	**298 K**	**308 K**	**288 K**	**298 K**	**308 K**	**288 K**	**298 K**	**308 K**
1. Enzyme treatment	18.32	18.23	18.15	–0.26	–0.26	–0.26	92.37	94.56	97.53
	***frequency* = 37 kHz**								
2. Sonolysis	–20.3	–20.39	–20.47	–0.39	–0.39	–0.4	93.51	97.05	101.43
3. Sono–enzymatic treatment P_o = 101.3 kPa	7.23	7.15	7.07	–0.29	–0.29	–0.29	90.06	93.	95.81
4. Sono–enzymatic treatment P_o = 200 kPa	7.87	7.78	7.69	–0.29	–0.29	–0.29	91.07	93.77	96.86
	***frequency* = 80 kHz**								
5. Sonolysis	1.04	0.96	0.88	–0.33	–0.33	–0.33	96.05	99.3	102.66
6. Sono–enzymatic treatment P_o = 101.3 kPa	8.5	8.41	0.83	–0.28	–0.29	–0.29	90.44	93.46	96.13
7. Sono–enzymatic treatment P_o = 200 kPa	12.55	12.47	12.39	–0.27	–0.27	–0.27	91.25	93.63	96.73

Note: As per the norms of chemical thermodynamics, the relative values of ΔH and ΔS indicate the following: (1) positive ΔS and negative $\Delta H \Rightarrow$ spontaneous reaction; (2) positive ΔS and positive $\Delta H \Rightarrow$ spontaneous reaction at high temperature; (3) negative ΔS and negative $\Delta H \Rightarrow$ spontaneous reaction at low temperature; (4) negative Δ_S and positive $\Delta H \Rightarrow$ non–spontaneous reaction at any temperature but spontaneous reversible reaction, if applicable.

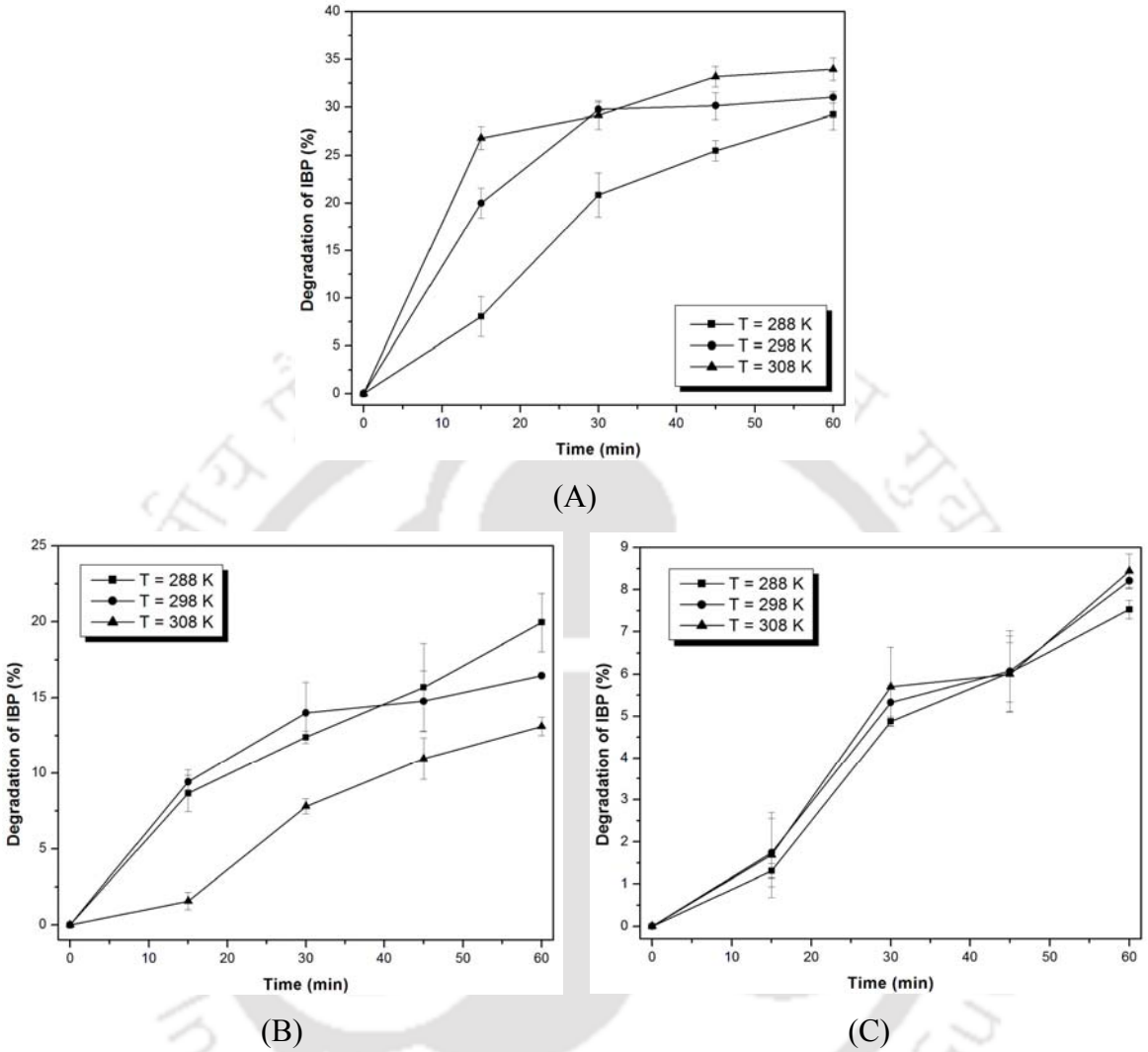

Figure 7.3: Time profiles of IBP degradation in different individual processes. (A) Enzymatic treatment at 150 rpm, (B) sonolysis (37 kHz), and (C) sonolysis (80 kHz)

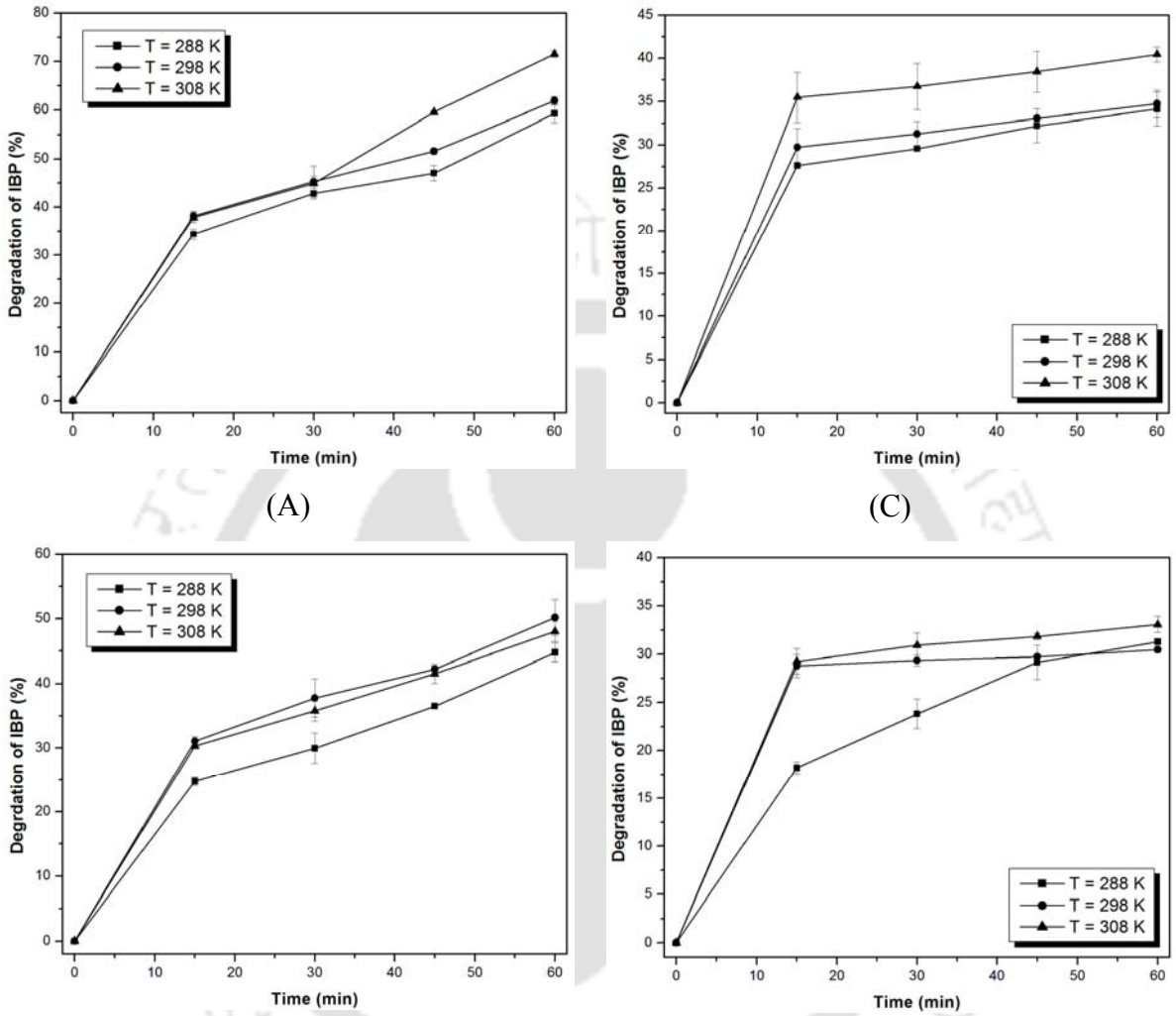

Figure 7.4: Time profiles of IBP degradation in different sono–enzymatic processes: (A) frequency = 37 kHz, static pressure = 101.3 kPa; (B) frequency = 37 kHz, static pressure = 200 kPa; (C) frequency = 80 kHz, static pressure = 101.3 kPa; and (D) frequency = 80 kHz, static pressure = 200 kPa

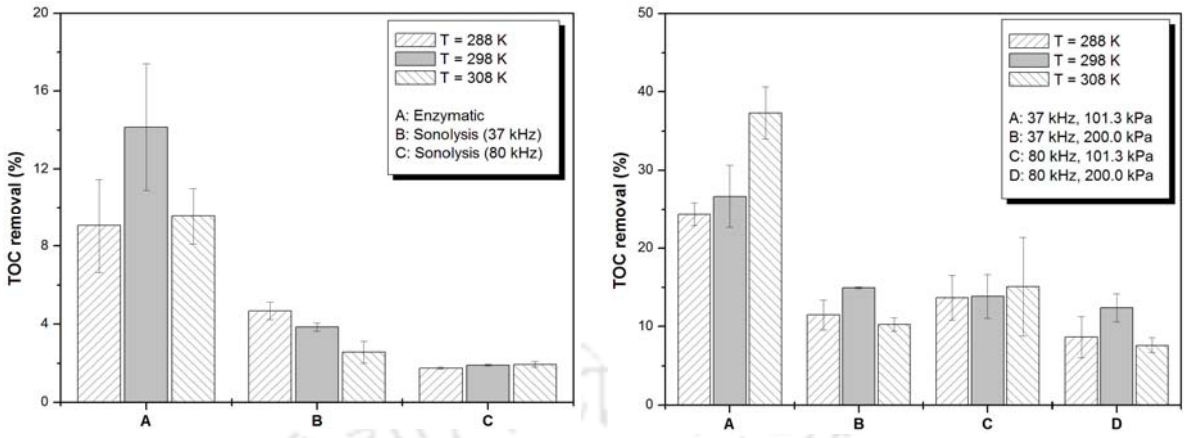

Figure 7.5: TOC removal in different individual and hybrid processes. (I) Individual processes, (II) sono–enzymatic process (under atmospheric, P_o = 101.3 kPa) and elevated static pressure (P_o = 200 kPa)

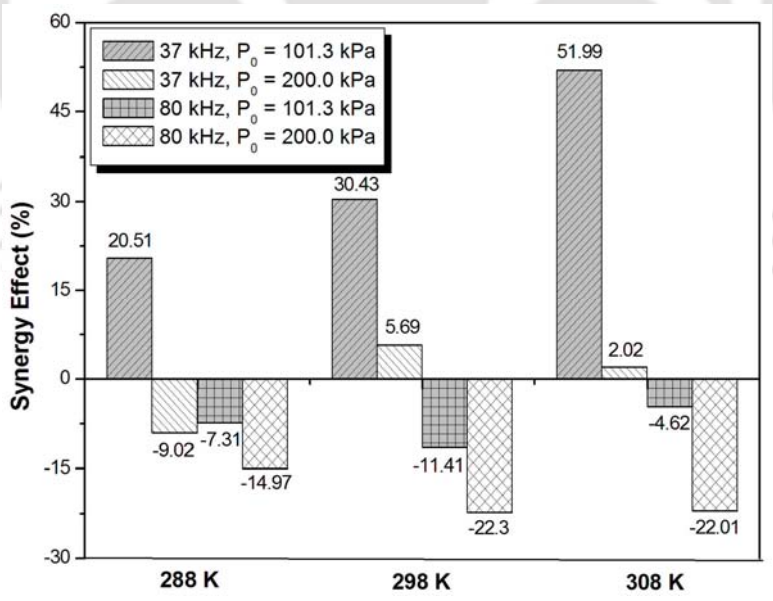

Figure 7.6: Synergy effect in hybrid processes for degradation of IBP

7.3.2 Results of Arrhenius and thermodynamic analysis

The results of Arrhenius analysis of IBP degradation (i.e. the values of activation energy and frequency factor for different experimental protocols) are given in Table 2. The corresponding Arrhenius plots are given in Figs. 7.7 & 7.8. Peculiar trends in Arrhenius parameters that could be identified from data presented in Table 7.2 are:

(1) The individual processes of sonolysis and enzymatic treatments show highly contrasting values of activation energy (E_a) and frequency factor (A). Sonolysis is characterized by negative activation energy that indicates spontaneous reaction. However, the frequency factor for sonolysis is extremely small (3.9×10^{-8} mol L^{-1} s^{-1}), which indicates very small number of fruitful collisions (per unit volume) between IBP molecules and $^{\bullet}OH$ radicals generated by transient cavitation bubble. On the other hand, positive activation energy for enzymatic treatment is an indication of requirement of external energy input for inducing the reaction. Nonetheless, a higher frequency factor for enzymatic treatment indicates large number of fruitful collisions per unit volume between enzyme and IBP molecules.

The values of Arrhenius parameters for sonolysis are essentially an indication of extreme intrinsic reactivity as well as instability of the $^{\bullet}OH$ radicals generated through transient cavitation that leads to volumetrically non–uniform reaction. On the contrary, Arrhenius parameters for enzyme treatment are indication of relatively lower intrinsic reactivity yet more volumetrically uniform reaction.

(2) Arrhenius parameters for hybrid sono–enzymatic treatments show characteristics of both sonolysis and enzymatic treatments, as noted earlier. The activation energy is positive, yet smaller than that for enzymatic treatment alone. The frequency factor is an order of magnitude higher than that for sonolysis, yet smaller than that for enzymatic treatment alone. These values of parameters essentially indicate contribution of individual mechanisms of

sonolysis as well as enzymatic treatment to the IBP degradation in hybrid technique. However, values of Arrhenius parameters for hybrid process show greater proximity with the values for enzymatic treatment. This essentially indicates greater contribution of the enzymatic mechanism (or pathway) to the overall IBP degradation.

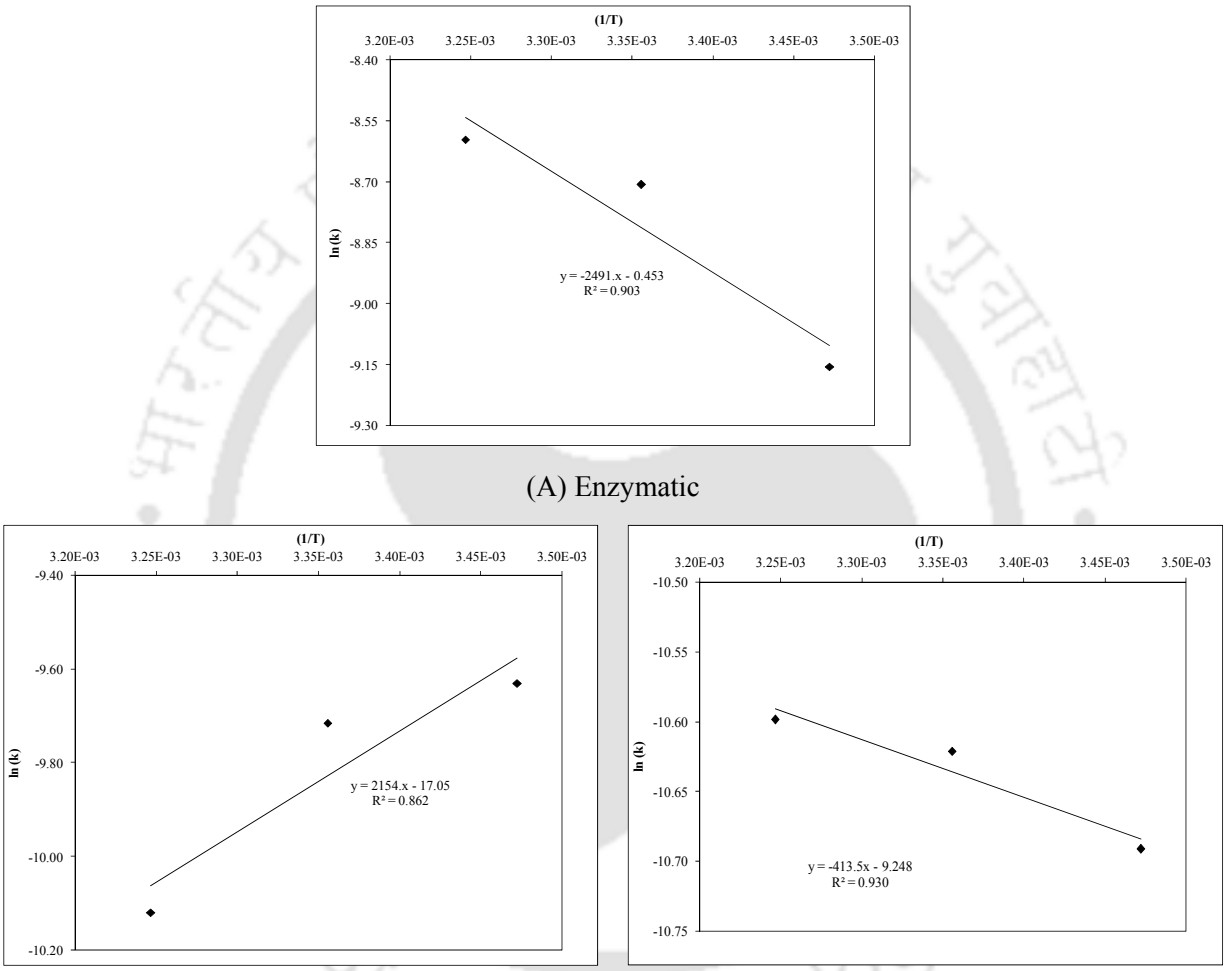

(A) Enzymatic

(B) Sonolysis with f = 37 kHz

(C) Sonolysis with f = 80 kHz

Figure 7.7: Arrhenius plot ln(k) vs. (1/T) for (A) enzymatic reaction, (B) sonochemical reaction at 37 kHz and (C) sonochemical reaction at 80 kHz

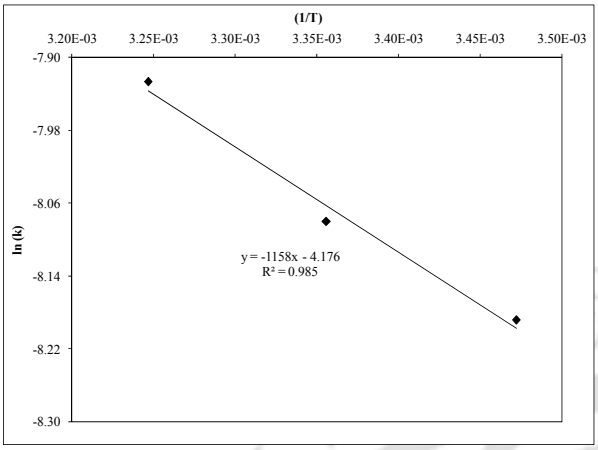

(A) f = 37 kHz, P_o = 101.3 kPa

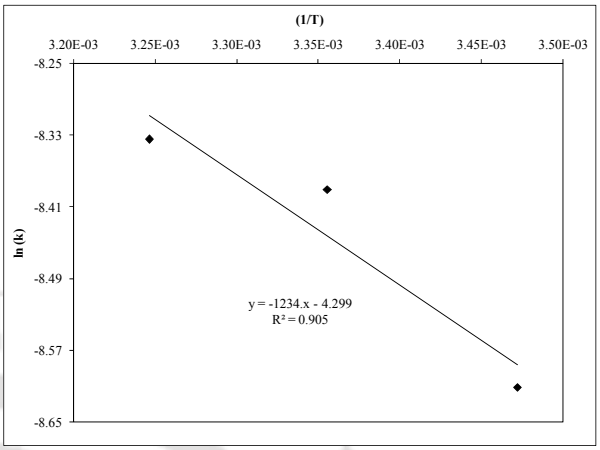

(B) f = 37 kHz, P_o = 200 kPa

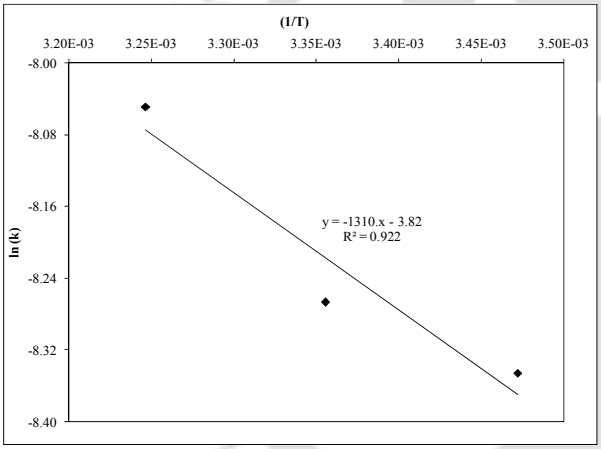

(C) f = 80 kHz, P_o = 101.3 kPa

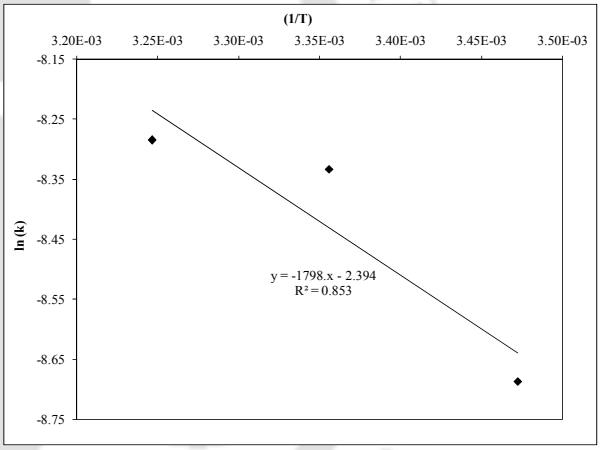

(D) f = 80 kHz, P_o = 200 kPa

Figure 7.8: Arrhenius plot ln(k) vs. (1/T) for sono–enzymatic reaction at atmospheric and elevated static pressure with ultrasonic frequencies of 37 kHz and 80 kHz.

(3) As noted earlier, elevated static pressure eliminates transient cavitation in the medium. Thus, the contribution of enzymatic pathway to overall IBP degradation is greater at elevated static pressure. This is indicated by increase in the values of both activation energy and frequency factor at elevated static pressure for the hybrid sono–enzymatic treatment.

Trends in thermodynamic parameters for different techniques for IBP degradation also provide mechanistic insight into the process as follows:

(i) Negative ΔH value for sonolysis at 37 kHz indicates spontaneous reaction induced by radicals, while positive ΔH value for enzymatic treatment indicates molecular reaction that require external energy input.

Positive ΔH value for sono–enzymatic process at 37 kHz is an indication of greater contribution of enzymatic pathway to overall IBP degradation. ΔH value increases for all reaction temperatures (viz. 288, 298 and 308 K) at elevated static pressure of the medium. This is a consequence of elimination of $^{\bullet}$OH radical induced IBP degradation at elevated static pressure, which results in greater contribution to IBP degradation through enzymatic route.

ΔH value for sonolysis at 80 kHz is positive; which indicates reduced spontaneity of degradation reactions. We attribute this result to reduction in cavitation intensity and $^{\bullet}$OH radical production at higher frequency, as explained earlier. Moreover, for sono–enzymatic treatment at 80 kHz (for both atmospheric and elevated static pressure), ΔH values are higher than the corresponding values for 37 kHz. This result is again attributed to reduction in cavitation intensity in the medium at higher frequency.

(ii) Entropy change ($-\Delta S$) values for IBP degradation show following trend: sonolysis > sono–enzymatic treatment > enzymatic treatment. These trends are consistent for both frequencies and all three temperatures. More negative ΔS value for sonolysis is an indication of fragmentation or degradation of IBP molecules into smaller species. This is possible for

radical induced reactions in sonolysis. Degradation of IBP molecule also occurs in enzymatic treatment; however, the mechanism is quite different. In this case, the process is relatively slower and requires binding of active sites of the enzyme to IBP molecules. As noted earlier, the enzymatic reactions occur far more uniformly in the reaction volume. Hence, the overall degradation is higher as compared to sono–enzymatic treatment. However, the spontaneity of this degradation is much lesser than sonication, which is reflected in greater ($-\Delta S$) values. The ($-\Delta S$) values for sono–enzymatic treatments are intermediate between sonolysis and enzyme treatments, as these are essentially manifestation of both radical as well as enzyme induced reactions.

(iii) ΔG values for all treatments (individual or hybrid) at 3 temperatures and elevated/atmospheric static pressures are similar. This result indicates that both sonolysis and enzyme treatments synergize (and compliment) each other's effect. This observation is concurrent with the results of Kadkhodaee and Povey (2008) for deactivation of α–amylase using sono–thermal treatment.

7.3.3 IBP degradation intermediates and mineralization

The major problem with IBP degradation reported in literature is greater toxicity of the intermediates than IBP itself (Méndez–Arriaga et al., 2009). Hence, the TOC content of the reaction mixture has been analyzed after each treatment. Moreover, the by–products and intermediates of IBP degradation have also been identified by means of GC–MS analysis. The results of GC–MS analysis are given in Table 4 (for reaction mixture treated at 37 kHz, 298 K, 101.3 kPa).

Table 7.4: Degradation products of ibuprofen (IBP) with sono–enzymatic process

Mol. Wt.	Structure	Names	References
206	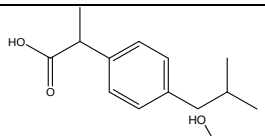	2–(4–Isobutylphenyl) propanoic acid or Ibuprofen	–
222	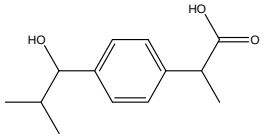	2–[4–(1–hydroxyisobutyl) phenyl]propionic acid	Madhavan et al. (2010); Caviglioli et al. (2002)
238	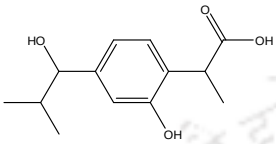	2–[2–hydroxy–4–(1–hydroxy– 2–methylpropyl) phenyl]propanoic acid	Madhavan et al. (2010)
194	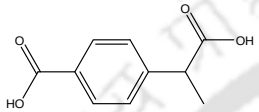	4–(1–Carboxyethyl) benzoic acid	Madhavan et al. (2010); Caviglioli et al. (2002)
178	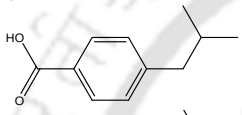	4–Isobutylbenzoic acid	Caviglioli et al. (2002)
178	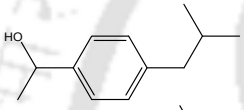	1–(4–Isobutylphenyl)–1–ethanol or 1–(1–hydroxyethyl)–4–isobutyl–benzene	Szabó et al. (2011); Caviglioli et al. (2002)
176	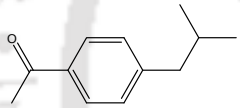	4–(2–methylpropyl) acetophenone	Sabri et al. (2012); Madhavan et al. (2010); Szabó et al. (2011)
162	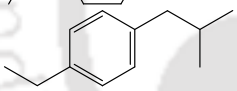	1–ethyl–4–(2–methylpropyl)–benzene	Szabó et al. (2011)
150	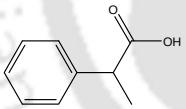	Hydratropic acid	Caviglioli et al. (2002)
150	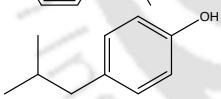	4–Isobutylphenol	Caviglioli et al. (2002) [35]
134	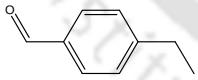	4–ethylbenzaldehyde	Madhavan et al. (2010); Caviglioli et al. (2002)
122	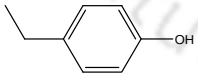	4–ethylphenol	Madhavan et al. (2010)
90	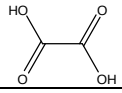	oxalic acid	Sabri et al. (2012)

The GC–MS spectra are provided in the Annexure-I (Figs. 7.S1–7.S5). The degradation products mainly comprise substituted phenols and aromatic carboxylic acids. Hydroxylation induced by $^{\bullet}OH$ radicals on propanoic acid and isobutyl substituents of the IBP structure results in formation of 4(1–carboxyethyl) benzoic acid, 4–isobutyl benzoic acid, 4–(2–

methylpropyl) acetophenone, 4–isobutyl phenol, 4–ethylphenol, hydratropic acid. The intermediates and by–products observed in the present study were matched with those reported in literature. Formation of 2–[4–(1–hydroxyisobutyl) phenyl] propionic acid (m/z 222) and 2–[2–hydroxy–4–(1–hydroxy–2–methylpropyl) phenyl] propanoic acid (m/z 238) has been reported by Madhavan et al. (2010). The intermediate 4–ethylbenzaldehyde has also been reported by Méndez–Arriaga et al. (2008) during photo–catalytic degradation of IBP in presence of TiO_2. Méndez–Arriaga et al. (2008) have proposed that hydroxylation is the first step of degradation, which is followed by demethylation and decarboxylation leading to formation of other products with smaller m/z values. Szabó et al. (2011) have also reported formation of 4–(2–methylpropyl) acetophenone (m/z 176) and 1–(1–hydroxyethyl)–4–isobutyl–benzene (m/z 178). Caviglioli et al. (2002) have reported degradation of IBP through oxidative and thermal routes with identification of degradation products. As per the degradation pathway proposed by Caviglioli et al. (2002), hydroxylation, oxidation and decarboxylation are the principal chemical mechanisms for the degradation of IBP. Some degradation products with smaller m/z values identified in this study are: hydratropic acid (m/z 150), 4–ethylbenzaldehyde (m/z 134) and 4–isobutylphenol (m/z 150).

7.3.4 Mineralization of IBP and synergy between the individual treatments

The results of total mineralization or TOC removal are shown in Fig. 7.5 and the effect of synergy in hybrid process is shown in Fig. 7.6. From the results, it has been found that in all protocols the percentage TOC removal was lesser than IBP degradation.

Enzymatic treatment was more efficient in TOC removal than sonolysis for the reason of volumetrically more uniform reaction, as noted earlier. Another cause that contributes to this effect is the formation of hydrophilic intermediates during IBP degradation that are easily degraded further by enzymes through decarboxylation and oxidation. On the other hand, in

sonolysis alone, the degradation is mainly through hydroxylation reaction. The hydroxylated intermediate species, being hydrophilic, move away from the hydrophobic bubble interface. This drastically reduces the extent of further interception of the •OH radicals released by cavitation bubble collapse for additional degradation leading to complete mineralization and TOC removal.

In the hybrid sono–enzymatic treatment at atmospheric pressure, positive synergy between sonolysis and enzymatic treatment is seen at 37 kHz, as the total mineralization achieved is more than the additive effects of individual processes. This results is attributed to synergism in hydroxylation induced by sonolysis and further oxidation/decarboxylation induced by enzymes leading to complete mineralization of IBP. Peroxidase enzymes have a heme cofactor in their active sites or redox active cysteine. The binding site for the aromatic substrate oxidation is the exposed heme edge. Sonolysis of IBP leads to hydroxylation, and subsequent formation of carboxylated intermediates. The carboxylated intermediates are likely to have higher affinity for the active sites of HRP enzyme that leads to further decarboxylation leading to higher mineralization. Moreover, the strong micro–convection generated by ultrasound and cavitation also enhances the interaction between enzyme and IBP molecules.

On the other hand, the mineralization achieved with sono–enzymatic treatment at elevated static pressure is lesser than the sum of mineralization with individual treatments, indicating negative synergy. This is clearly attributed to elimination of transient cavitation, and hence, the hydroxylation induced by the •OH radicals generated by cavitation at elevated pressure. This also slows down the decarboxylation; and hence the further degradation by enzyme. For the higher frequency of 80 kHz, the cavitation intensity is already lesser for the reasons discussed earlier. This results in greater negative synergy between enzymatic treatment and sonolysis.

Finally, the GC–MS analysis indicates the formation of the small carboxylic acid (i.e. oxalic acid) that confirms mineralization. Oxalic acid formation has also been confirmed by Madhavan et al. (2010); and Skoumal et al. (2009) have reported oxalic acid to be the ultimate by–product of photoelectro – Fenton degradation of IBP.

7.4 CONCLUSION

In the present study, a new hybrid technique of sono–enzymatic treatment for degradation of inflammatory drug ibuprofen has been explored. This technique has been found to be an effective tool for degradation as well as mineralization of the IBP. At low ultrasound frequency and atmospheric static pressure, sono-enzymatic treatment is revealed to be more effective than the individual techniques of sonolysis and enzyme treatment. GC–MS analysis of the reaction reveals the intermediates of IBP degradation, which shed light on the chemical pathway of degradation. Arrhenius and thermodynamic analysis of the experimental data gives a physical insight into the mechanistic synergism between individual techniques of enzyme treatment and sonolysis. The positive synergy between sonolysis and enzyme treatment is a consequence of formation of hydrophilic intermediates due to hydroxylation induced by radicals generated by transient cavitation. These intermediates are rapidly degraded by the enzyme action through decarboxylation. The activation energy of sono–enzymatic treatment is lesser than enzyme treatment (due to spontaneity of reactions induced by radicals produced by transient cavitation), while the frequency factor of sono–enzymatic treatment is greater than sonolysis (due to volumetrically uniform enzymatic reactions).

ANNEXURE – I

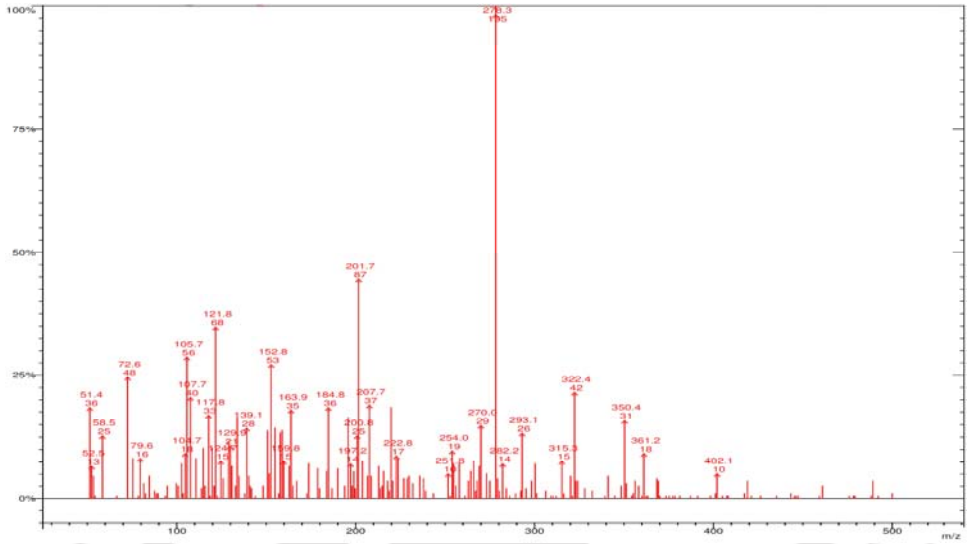

Figure 7.S1: Mass spectrum for reference of 4-ethylphenol (m/z 122) and 2-[4-(1-hydroxyisobutyl) phenyl]propionic acid (m/z 222). Experimental conditions: frequency = 37 kHz, temperature = 25°C, IBP = 4.76×10^{-2} mM, H_2O_2 = 8.55 mM, HRP = 0.08 U/mL, pH = 7.

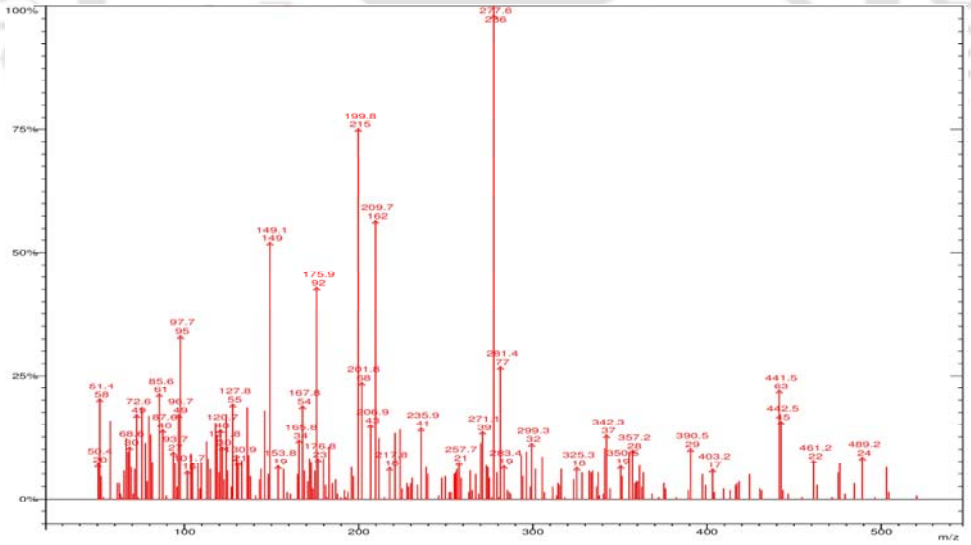

Figure 7.S2: Mass spectrum for reference of 4-Isobutylphenol (m/z 150) and 4'-(2-methylpropyl) acetophenone (m/z 176). Experimental conditions: frequency = 37 kHz, temperature = 25°C, IBP = 4.76×10^{-2} mM, H_2O_2 = 8.55 mM, HRP = 0.08 U/mL, pH = 7.

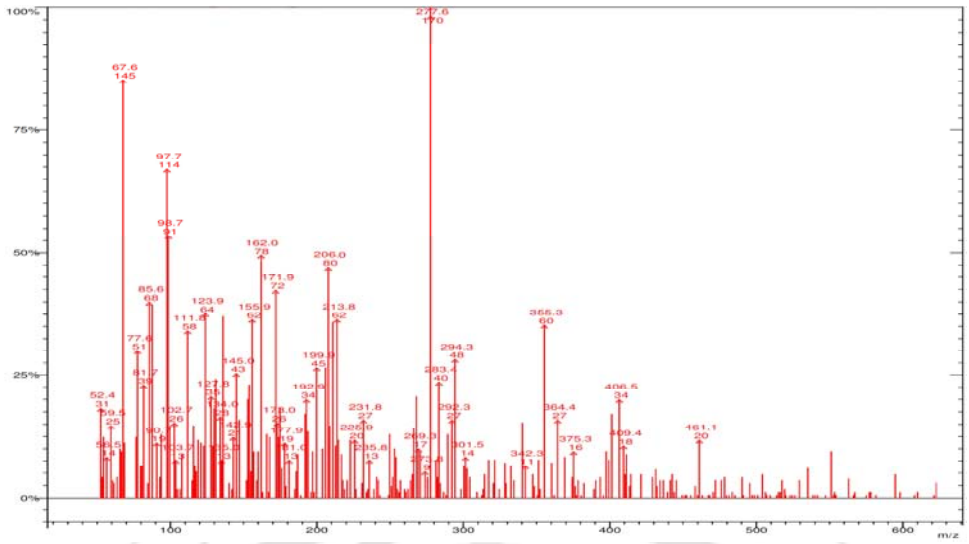

Figure 7.S3: Mass spectrum for reference of 1-ethyl-4-(2-methylpropyl)-benzene (m/z 162), 2-(4-Isobutylphenyl)propanoic acid (m/z 206) and oxalic acid (m/z 90). Experimental conditions: frequency = 37 kHz, temperature = 25°C, IBP = 4.76×10^{-2} mM, H_2O_2 = 8.55 mM, HRP = 0.08 U/mL, pH = 7.

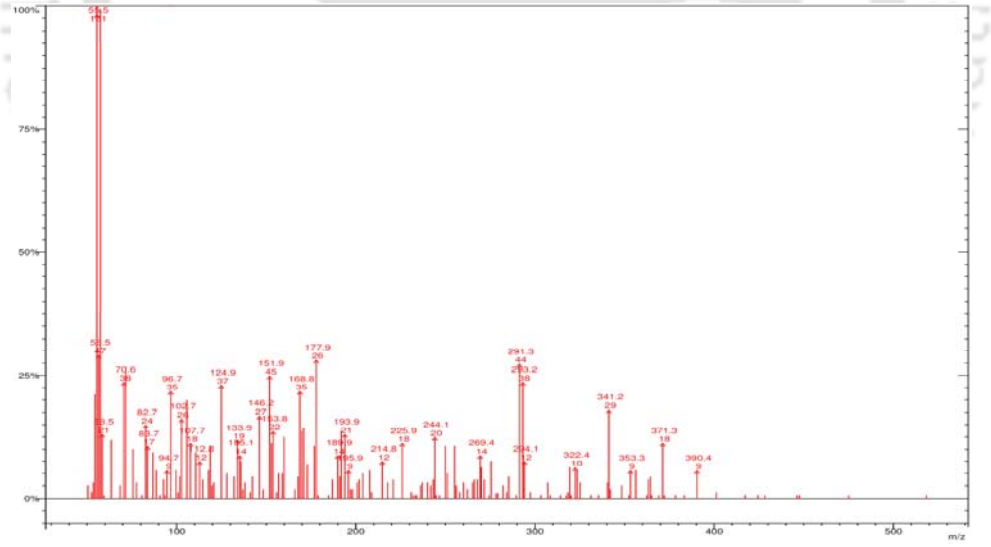

Figure 7.S4: Mass spectrum for reference of 1-(1-hydroxyethyl)-4-isobutyl-benzene (m/z 178) and 4-ethylbenzaldehyde (m/z 134). Experimental conditions: frequency = 37 kHz, temperature = 25°C, IBP = 4.76×10^{-2} mM, H_2O_2 = 8.55 mM, HRP = 0.08 U/mL, pH = 7.

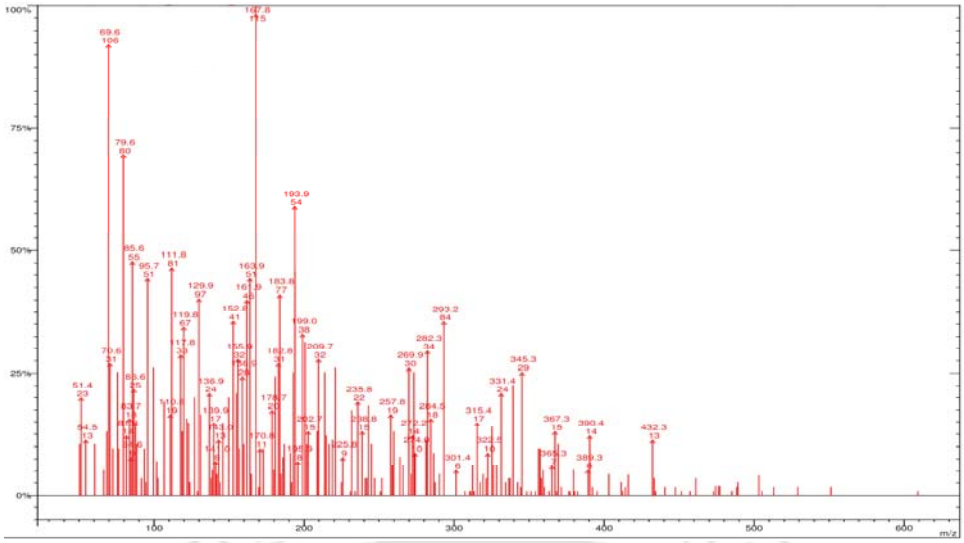

Figure 7.S5: Mass spectrum for reference of 4-(1-Carboxyethyl)benzoic acid (m/z 194) and 2-[2-hydroxy-4-(1-hydroxy-2-methylpropyl)phenyl]propanoic acid (m/z 238). Experimental conditions: frequency = 37 kHz, temperature = 25°C, IBP = 4.76×10^{-2} mM, H_2O_2 = 8.55 mM, HRP = 0.08 U/mL, pH = 7.

REFERENCES

Ahmadi F, McLoughlin IV, Chauhan S, ter–Haar G, Bio–effects and safety of low–intensity, low–frequency ultrasonic exposure, Prog. Biophys. Mol. Bio. 108 (2012) 119–138.

Bagal MV, Gogate PR, Wastewater treatment using hybrid treatment schemes based on cavitation and Fenton chemistry: A review, Ultrason. Sonochem. 21 (2014) 1–14.

Bhasarkar JB, Chakma S, Moholkar VS, Mechanistic features of oxidative desulfurization using Sono–Fenton–Peracetic acid (Ultrasound/Fe^{2+}–CH_3COOH–H_2O_2) system, Ind. Eng. Chem. Res. 52 (2013) 9038–9047.

Caviglioli G, Valeria P, Brunella P, Sergio C, Attilia A, Gaetano B, Identification of degradation products of Ibuprofen arising from oxidative and thermal treatments, J. Pharm. Biomed. Anal. 30 (2002) 499–509.

Chakma S, Bhasarkar JB, Moholkar VS, Preparation, characterization and application of sonochemically doped Fe^{3+} into ZnO nanoparticles, Int. J. Res. Eng. Technol. 2 (2013)

177–183.

Chakma S, Moholkar VS, Investigation in mechanistic issues of sonocatalysis and sonophotocatalysis using pure and doped photocatalysts, Ultrason. Sonochem. 22 (2015) 287–299.

Chakma S, Moholkar VS, Investigations in synergism of hybrid advanced oxidation processes with combinations of sonolysis + Fenton process + UV for degradation of bisphenol–A, Ind. Eng. Chem. Res. 53 (2014) 6855–6865.

Chakma S, Moholkar VS, Numerical simulation and investigation of system parameters of sonochemical process, Chinese J. Eng. 2013 (2013b) 1–14.

Chakma S, Moholkar VS, Physical mechanism of sono–Fenton process, AIChE J. 59 (2013a) 4303–4313.

Chiha M, Hamdaoui O, Baup S, Gondrexon N, Sonolytic degradation of endocrine disrupting chemical 4–cumylphenol in water, Ultrason. Sonochem. 18 (2011) 943–950.

Choina J, Kosslick H, Fischer Ch., Flechsig G–U, Frunza L, Schulz A, Photocatalytic decomposition of pharmaceutical ibuprofen pollutions in water over titania catalyst, Appl. Catal. B Environ. 129 (2013) 589–598.

Entezari MH, Pétrier C, A combination of ultrasound and oxidative enzyme: sono–biodegradation of substituted phenols, Ultrason. Sonochem. 10 (2003) 241–246.

Enzymatic assay of peroxidase (EC 1.11.1.7), http://www.sigmaaldrich.com/technical-documents/protocols/biology/enzymatic-assay-of-peroxidase.html

Esplugas S, Bila DM, Krause LGT, Dezotti M, Ozonation and advanced oxidation technologies to remove endocrine disrupting chemicals (EDCs) and pharmaceuticals and personal care products (PPCPs) in water effluents, J. Hazard. Mater. 149 (2007) 631–642.

Flynn GH, Cavitation dynamics. II. Free pulsations and models for cavitation bubbles, J. Acoust. Soc. Am. 58 (1975) 1160–1170.

Gogate PR, Tatake PA, Kanthale PM, Pandit AB, Mapping of sonochemical reactors: Review, analysis, and experimental verification, AIChE J. 48 (2002) 1542–1560.

Kadkhodaee R, Povey MJW, Ultrasonic inactivation of Bacillus α–amylase. I. Effect of gas content and emitting face of probe, Ultrason. Sonochem. 15 (2008) 133–142.

Loaiza–Ambuludi S, Panizza M, Oturan N, Özcan A, Oturan MA, Electro–Fenton degradation of anti–inflammatory drug ibuprofen in hydroorganic medium, J. Electroanal. Chem. 702 (2013) 31–36.

Madhavan J, Grieser F, Ashokkumar M, Combined advanced oxidation processes for the synergistic degradation of ibuprofen in aqueous environments, J. Hazard. Mater. 178 (2010) 202–208.

Malani RS, Khanna S, Chakma S, Moholkar VS, Mechanistic insight into sono–enzymatic degradation of organic pollutants with kinetic and thermodynamic analysis, Ultrason. Sonochem. 21 (2014) 1400–1406.

Matamoros V, Garcia J, Bayona JM, Behavior of selected pharmaceuticals in subsurface flow constructed wetlands: A pilot–scale study, Environ. Sci. Technol. 39 (2005) 5449–5454.

Méndez–Arriaga F, Esplugas S, Giménez J, Degradation of the emerging contaminant ibuprofen in water by photo–Fenton, Water Res. 44 (2010) 589–595.

Méndez–Arriaga F, Torres–Palma RA, Pétrier C, Esplugas S, Gimenez J, Pulgarin C, Ultrasonic treatment of water contaminated with ibuprofen, Water Res. 42 (2008) 4243–4248.

Méndez–Arriaga F, Torres–Palma RA, Pétrier C, Esplugas S, Gimenez J, Pulgarin C, Mineralization enhancement of a recalcitrant pharmaceutical pollutant in water by advanced oxidation hybrid processes, Water Res. 43 (2009) 3984–3991.

Michael I, Achilleos A, Lambropoulou D, Osorio Torrens V, Pérez S, Petrović M, Barceló D, Fatta–Kassinos D, Proposed transformation pathway and evolution profile of diclofenac

and ibuprofen transformation products during (sono)photocatalysis, Appl. Catal. B Environ. 147 (2014) 1015–1027.

Moholkar VS, Sable SP, Pandit AB, Mapping the cavitation intensity in an ultrasonic bath using the acoustic emission, AIChE J. 46 (2000) 684–694.

Richardson ML, Bowron JM, The fate of pharmaceutical chemicals in the aquatic environment, J. Pharm. Pharmacol. 37 (1985) 1–12.

Sabri N, Hanna K, Yargeau V, Chemical oxidation of ibuprofen in the presence of iron species at near neutral pH, Sci. Total Environ. 427–428 (2012) 382–389.

Sangave PC, Pandit AB, Ultrasound and enzyme assisted biodegradation of distillery wastewater, J. Environ. Manag. 80 (2006) 36–46.

Skoumal M, Rodríguez RM, Cabot PL, Centellas F, Garrido JA, Arias C, Brillas E, Electro–Fenton, UVA photoelectro–Fenton and solar photoelectro–Fenton degradation of the drug ibuprofen in acid aqueous medium using platinum and boron–doped diamond anodes, Electrochimica Acta 54 (2009) 2077–2085.

Sun Y, Yang H, Zhong X, Zhang L, Wang W, Ultrasonic–assisted enzymatic degradation of cholesterol in egg yolk, Innov. Food Sci. Emerg. Technol. 12 (2011) 505–508.

Szabo RK, Megyeri Cs, Illés E, Gajda–Schrantz K, Mazellier P, Dombi A, Phototransformation of ibuprofen and ketoprofen in aqueous solutions, Chemosphere 84 (2011) 1658–1663.

Ternes TA, Herrmann N, Bonerz M, Knacker T, Siegrist H, Joss A, A rapid method to measure the solid–water distribution coefficient (K_d) for pharmaceuticals and musk fragrances in sewage sludge, Water Res. 38 (2004) 4075–4084.

Thokchom B, Kim K, Park J, Khim J, Ultrasonically enhanced electrochemical oxidation of ibuprofen, Ultrason. Sonochem. 22 (2015) 429–436.

Vinu R, Madras G, Kinetics of sonophotocatalytic degradation of anionic dyes with nano–

TiO_2, Environ. Sci. Technol. 43 (2009) 473–479.

Ziylan A, Ince NH, Catalytic ozonation of ibuprofen with ultrasoundand Fe–based catalysts, Catalysis Today 240 (2015) 2–8.

भारतीय प्रौद्योगिकी संस्थान गुवाहाटी
Indian Institute of Technology Guwahati

8

MECHANISTIC INVESTIGATIONS IN HETEROGENEOUS HYBRID AOPS: SONOCATALYSIS AND SONOPHOTOCATALYSIS

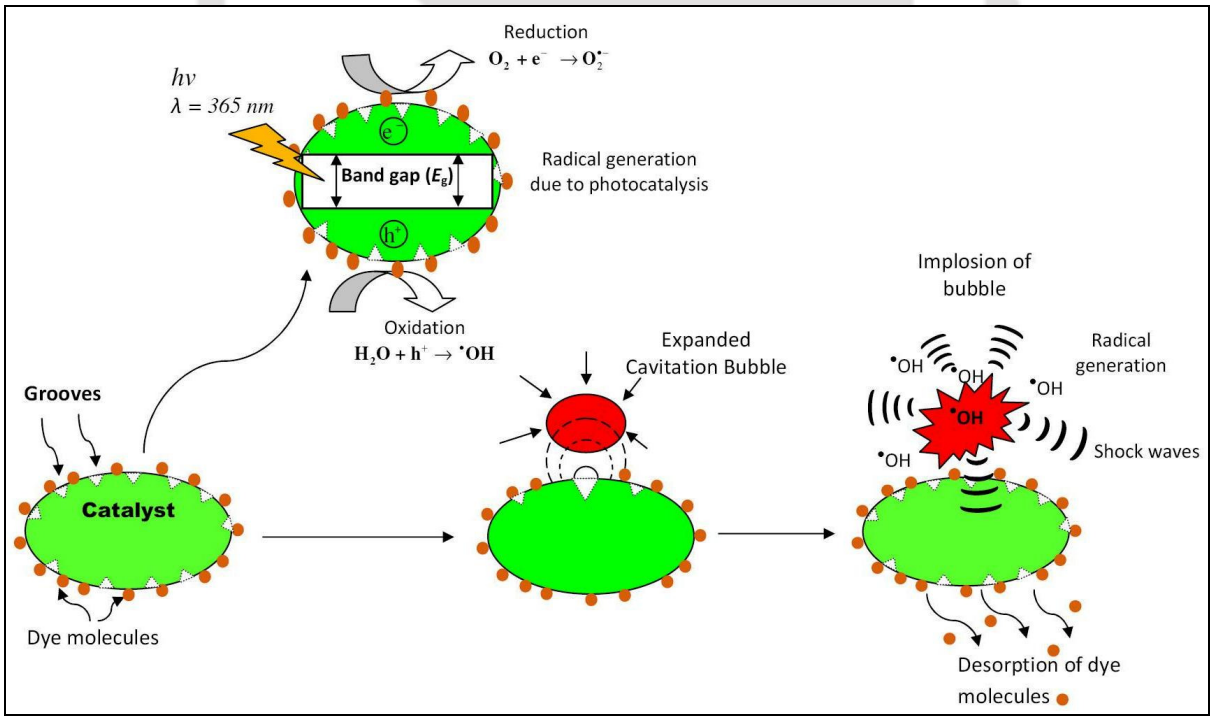

Physical mechanism between sonolysis, sonocatalysis and sonophotocatalysis

CHAPTER 8

MECHANISTIC INVESTIGATIONS IN HETEROGENEOUS HYBRID AOPS: SONOCATALYSIS AND SONOPHOTOCATALYSIS

8.1 INTRODUCTION

In previous chapters, we dealt with several advanced oxidation processes in which the reaction mixture was homogeneous. There is also class of advanced oxidation processes in which the reaction mixture has heterogeneous phase. The foremost AOP in this category is photocatalysis. The conventional semiconductor photocatalysts are transition metal oxides or semiconductors such as anatase–TiO_2 and ZnO. These materials have a band gap between the valence band and conduction band. With absorption of a photon with energy equal to or greater than the band gap, an electron in the conduction band is promoted to valence band resulting in creation of a hole. Due to the electron-hole pair generation, oxidation-reduction reactions occur at the surface of the photocatalyst. In the present context of oxidative degradation of recalcitrant pollutants, reaction of the hole with the moisture present on the surface of catalyst gives rise to hydroxyl radical, which induces the degradation reactions.

Combination of sonolysis and photocatalysis, known as sono-photocatalysis has been widely investigated by numerous researchers. In Chapter 1, a review of literature in this area has been presented. A variant of sonophotocatalysis is sonocatalysis, in which sonication is

applied to reaction mixture in presence of a photocatalyst – but without an external source of UV light. Both sonocatalysis and sonophotocatalysis have been reported to give enhanced degradation of organic pollutants in comparison to sonication alone (Chen et al., 2003; Madhavan et al., 2010; Selli et al., 2008). During transient collapse, cavitation bubbles also emit light, known as sonoluminescence (Suslick, 1990; Hilgenfeldt et al., 1996). The sonoluminescence light has wide range of wavelength from UV to visible (Ashokkumar and Grieser, 2007). In sonocatalysis, the photon emission during sonoluminescence is expected to activate the photocatalyst for additional production of $^{\bullet}OH$ radicals (Balaji et al., 2011). In a study reported by Balaji et al. (2011), a secondary role of photocatalyst in the sonocatalysis process in terms of adsorption of the dye molecules on the surface of photocatalyst has been identified. The adsorption of the dye enhances the probability of dye–radical interaction leading to higher degradation of the dye. For effective utilization of sonoluminescence light emission during transient cavitation, doped photocatalysts with higher absorption range and smaller band gaps are necessary. Despite significant research in degradation of recalcitrant pollutants by sonocatalysis or sonophotocatalysis, the exact mechanism of these hybrid AOPs remains relatively unexplored. The individual mechanisms of sonolysis and photocatalysis are different. What is the exact nature of interaction between these mechanisms (or in other words the mechanistic synergy) in the hybrid AOP is a crucial question.

In this chapter, we have addressed the issue of mechanistic investigation of sonocatalysis and sono-photocatalysis. This study has two components: (1) ultrasound–assisted synthesis and characterization of a Fe^{3+} doped ZnO nanoparticles, and (2) discernment of physical mechanism of sonocatalysis and sonophotocatalysis with pure ZnO nanoparticles as well as Fe–doped ZnO nanoparticles. Decolorization process of two textile dyes, viz. azo dye Acid Red B (ARB) and non–azo dye Methylene Blue (MB) has been used as model reaction system.

8.2 EXPERIMENTAL

Prior to describing the experimental methods, we briefly outline the rationale of using doped photocatalyst. Conventional photocatalysts such as anatase–TiO_2 and ZnO have large band gap energy, and hence, these are not much effective in visible light range. For effective utilization of the light energy for photocatalysis, it is essential that the absorption range of photocatalyst should be extended to visible range (i.e. longer wavelengths) by decreasing the band gap between conduction and valence band of the photocatalyst. For this purpose, doping of conventional photocatalysts with transition metal ions like Fe^{3+}, Co^{2+} or Ni^{2+} etc., which increase the absorption of photons, is a well–known technique (Mills and Stephen, 1997; Carp et al., 2004; Fang et al., 2009; Samadi et al., 2012; Xu and Li, 2010; Dong et al., 2011; Ba-Abbad et al., 2013; Daghrir et al., 2013; Aydin et al., 2013). As the transition metal ions are incorporated into the TiO_2 or ZnO lattice, impurity energy levels in the band gap of TiO_2 or ZnO are formed as follows (Ni et al., 2007):

$$M^{n+} + h\nu \longrightarrow M^{(n+1)+} + e^-_{cb} \qquad \text{(cb – conduction band)} \qquad (8.1)$$

$$M^{n+} + h\nu \longrightarrow M^{(n-1)+} + h^+_{vb} \qquad \text{(vb – valence band)} \qquad (8.2)$$

where, M and M^{n+} represent the metal and metal ion dopant respectively. Further, electron–hole transfer between metal ions and photocatalyst (TiO_2 or ZnO) can alter electron–hole recombination as:

$$\text{Electron trap} \quad : M^{n+} + e^-_{cb} \longrightarrow M^{(n-1)+} \qquad (8.3)$$

$$\text{Hole trap} \quad : M^{n+} + h^+_{vb} \longrightarrow M^{(n+1)+} \qquad (8.4)$$

The energy level of $M^{n+}/M^{(n-1)+}$ is less negative than that of the energy level of the conduction band (CB) of original photocatalyst, while the energy level of $M^{n+}/M^{(n+1)+}$ is less positive than that of the energy level of valence band (VB) of original photocatalyst.

8.2.1 Materials

The following chemicals were used to study the activity of Fe^{3+} doped ZnO photocatalyst: ZnO, Ferric sulfate monohydrate, Sodium dodecylsulfate (SDS), Acid red B (ARB), and Methylene blue (MB). All the chemicals were purchased from Merck India and used as received without further any pretreatment. For all experiments, ultrapure water (≥18 MΩ·cm resistivity at 25°C) from Milli–Q Synthesis unit (Millipore®, USA) was used as the aqueous medium.

8.2.2 Synthesis of doped photocatalyst

Surface modified nano–sized Fe^{3+}–doped ZnO was prepared using ultrasound assisted impregnation method (Madhavan et al., 2010). An ultrasonic probe with a frequency of 20 kHz (Model: VCX–500, 500 W) was used for sonication of the medium. The diameter of the probe is 13 mm with total active surface area of 1.33 cm^2. An aqueous solution (80 mL) of $Fe_2(SO_4)_3 \cdot H_2O$ was prepared in de–ionized water with concentration of 0.00375 mM of Fe^{3+}. To this solution, 3 g of pre–calcined (at 400°C for 5 h) ZnO particles were added. This corresponds to a weight ratio of $Fe_2(SO_4)_3 \cdot H_2O$/ZnO as 2% w/w. Another parameter used in the synthesis was addition of surfactant, sodium dodecylsulfate (SDS) to the reaction mixture. Synthesis was carried out with addition of surfactant as well as without it. Due to very low concentration of surfactant in solution (0.0026 M << CMC value of 0.0082 M), the structure or shape of the catalyst is not expected to change (Jana et al., 2007). However, surfactant helps in avoiding agglomeration of particles in the medium resulting in their even dispersion. Another effect of this is the higher interaction probability the ZnO particles with Fe^{3+} ions, which is expected to give uniform better doping. This solution was sonicated for 2 h using 5 s pulse mode (5 s on and 5 s off mode) (Bhatte et al., 2011). The system was operated at 30% amplitude with the theoretical power dissipation rate of 150 W. The actual power input to the

reaction system was determined using calorimetric measurements. During sonication, the temperature of the reaction mixture was controlled at 30^{o}C with circulation of cooling water. Finally, Fe–doped ZnO particles were filtered and kept in oven at 100^{o}C overnight, followed by calcination at 600^{o}C for 5 h.

The Fe–doped ZnO catalyst synthesized with these techniques were designated as Fe–ZnO (I) and Fe–ZnO (II), for the doping carried out in presence and absence of surfactant SDS, respectively. The original ZnO catalyst as well as two Fe–doped catalysts were characterized for size distribution, crystal structure using x–ray diffraction (XRD), surface area using Brunauer–Emmett–Teller (BET) surface area analyzer, bonding configuration using Fourier transform infrared spectroscopy (FTIR), optical properties using UV–Vis diffuse reflectance spectra, morphology using field emission scanning electron microscopy (FE–SEM), elemental composition using energy dispersive x–ray (EDX) spectroscopy and Fe oxidation states using temperature programmed reduction (TPR).

8.2.3 Decolorization experiments

The decolorization experiments with ARB dye and MB dye were conducted with four protocols, viz. (1) sonolysis, (2) photocatalysis, (3) sonocatalysis, and (4) sonophotocatalysis.

In each of the above protocols, 50 ml of dye solution with an initial concentration of 20 ppm (corresponding concentration 0.04 mM ARB and 0.063 mM MB) was used. The quantity of photocatalyst added to the solution was kept constant at 0.025 g in all experiments. It should be mentioned that addition of solid particles increases the number of cavitation bubbles in the system, as the tiny gas pockets trapped in the crevices of the solid particles act as cavitation nuclei (Tuziuti et al., 2005). Presence of solid particles in the medium contributes to attenuation of acoustic wave (Tuziuti et al., 2005), and hence, the amount of photocatalyst was kept as low as 0.05wt% to avoid these effects. The dye has

tendency to adsorb on the catalyst surface, which usually is wrongly accounted for as decolorized dye. However, the adsorbed dye is removed from the solution along with the catalyst particles as they are filtered out after treatment. In our analysis, we have accounted for both of these effects.

In sonocatalysis, photocatalysis and sonophotocatalysis protocols, the mixture of catalyst and dye solution was stirred for 1 h in dark place prior to sonication or UV–irradiation. This was done to achieve adsorption–desorption equilibrium of dye on catalyst surface. Sonication of the dye solution was carried out in a 40 kHz frequency ultrasound bath (Jeio Tech, Capacity: 10 L, 200 W), which had the facilities of automatic frequency tuning and amplitude compensation to ensure constant power delivery to the reaction system during sonication, irrespective of the changes occurring in the medium. The acoustic pressure amplitude generated by transducers attached at the bottom in the ultrasound bath was measured using calorimetric method as 1.9 bar, which corresponds to the acoustic energy intensity of 1.2 W/cm^2 with a volumetric energy dissipation of 8.71 W/L (Chakma and Moholkar, 2014). The initial temperature of the reaction mixture was 27^{o}C. To control the temperature of water in the bath, hence the reaction mixture, the water was changed in every 10 min. By this procedure, the variation in temperature was cut down to ±2^{o}C. 1 mL of sample of the dye solution was withdrawn in every 10 min and centrifuged (Remi, R–8C) for 30 min at 4500 rpm to separate the catalyst particles. The filtrate was then analyzed for the residual dye concentration using UV–Vis spectrophotometer (Perkin Elmer, Lambda 35).

In photocatalysis and sonophotocatalysis protocols, the UV irradiation of reaction mixture was provided using a blended high pressure mercury UV lamp (Starlite, 160 W). The maximum peak emission wavelength of this UV source was at 365 nm. However, it also had significant emissions in the visible range. The UV lamp was placed at the center of the bath above the reaction mixture. The whole assembly was stored in a black box to avoid light

radiation diffusion. Prior to commencement of the experiments, the UV lamp was kept on for 15 min to obtain proper emission and diffusion of ultraviolet irradiation. We have also conducted experiments with degassing/ unsaturated medium by subjecting it to vacuum. For this purpose, a vacuum pump producing a vacuum of 600 mm Hg (or 160 mm Hg pressure) was used. With this procedure, the dissolved oxygen content of water was reduced from 9 ppm to 4 ppm. All experiments were carried out twice to assess the reproducibility of the results and the mean value of decolorization achieved in the two experimental runs was considered for analysis.

8.3 RESULTS OF CATALYST CHARACTERIZATION

8.3.1 Size distribution analysis

The size distribution of original ZnO particles and Fe^{3+} doped ZnO particles was determined using Delsa^{TM} Nano C (Beckman Coulter, Model: A53878) particle size analyzer. The volume distribution of the catalyst particles, ZnO and Fe–doped ZnO, is shown in Fig. 8.1. The doped Fe–ZnO catalysts have smaller and uniform particle size, which can be attributed to sonication. The volume distribution of prepared Fe–doped catalysts was as follows:

(i) ZnO: D (10%): 444.5 nm; D (50%): 647.5 nm, D (90%): 1100.3 nm

(ii) Fe–ZnO (I): D (10%): 338 nm, D (50%): 466.6 nm, D (90%): 728 nm

(iii) Fe–ZnO (II): D (10%): 246.9 nm, D (50%): 352.1 nm, D (90%): 600.8 nm

Among the two varieties of Fe–doped catalysts, the Fe–ZnO(II) has a smaller mean particle size with narrower size distribution. We attribute this result to de–agglomeration of particles caused by adsorption of the surfactant molecules on the surface.

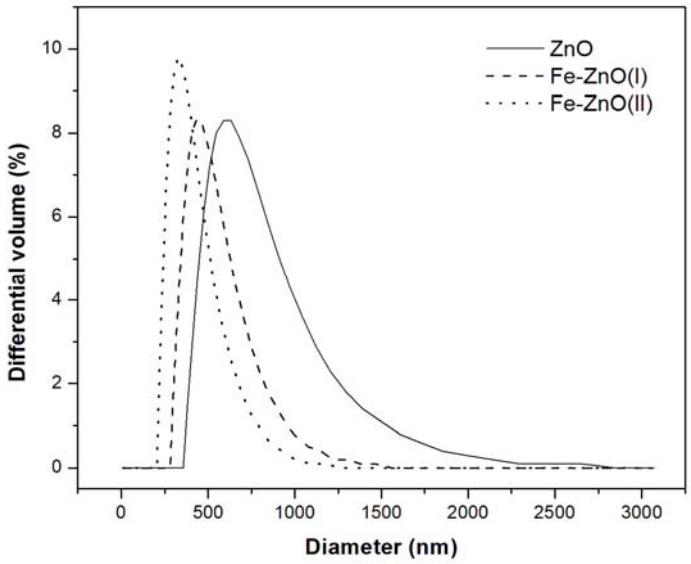

Figure 8.1: Particle size distribution for pure and Fe-doped ZnO on the basis of differential volume. Summary of distribution for ZnO: D(10%): 444.5 nm; D(50%): 647.5 nm, D(90%): 1100.3 nm; Summary of distribution for Fe–ZnO(I): D(10%): 338 nm, D(50%): 466.6 nm, D(90%): 728 nm; Summary of distribution for Fe–ZnO(II): D(10%): 246.9 nm, D(50%): 352.1 nm, D(90%): 600.80 nm.

8.3.2 Morphology of photocatalyst particles

The surface morphology of the ZnO and Fe–ZnO was assessed using Field Emission Scanning Electron Microscope or FE–SEM (Model: SIGMA VP, Make: Carl Zeiss GmbH, Germany). The FE–SEM micrographs of the photocatalyst particles are depicted in Fig. 8.2. In these micrographs, the hexagonal structure of ZnO and Fe–ZnO is clearly revealed.

8.3.3 Energy-dispersive X-ray (EDX) spectroscopy analysis

The elemental composition of Fe–doped ZnO photocatalyst was analyzed and confirmed using Energy Dispersive X–ray spectroscopy (Make: LEO, Model: 1430vp). Fig. 8.3 shows the EDX spectrum of the Fe–doped ZnO nanopowder synthesized using two protocols mentioned earlier.

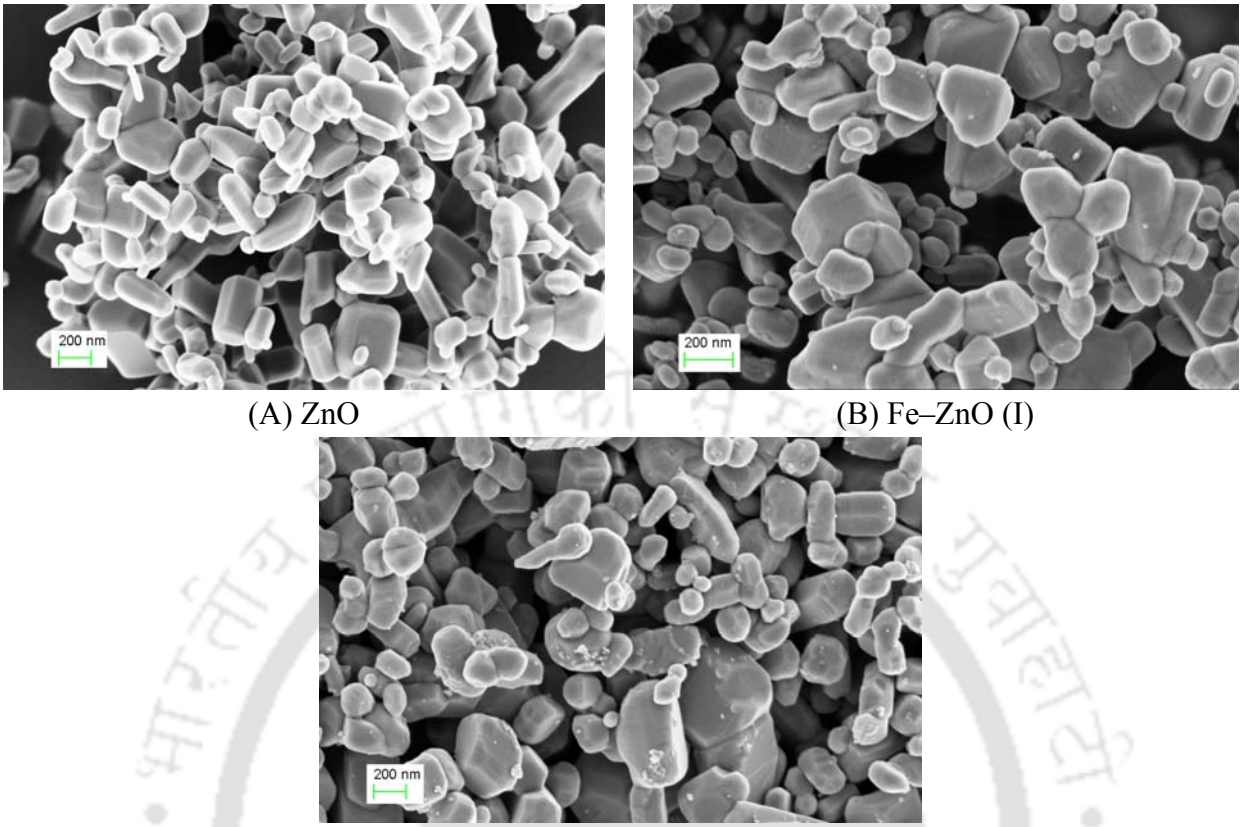

(A) ZnO (B) Fe–ZnO (I)

(C) Fe–ZnO (II)

Figure 8.2: FE-SEM images of (A) ZnO, (B) Fe–ZnO(I), and (C) Fe–ZnO(II) at 80 KX

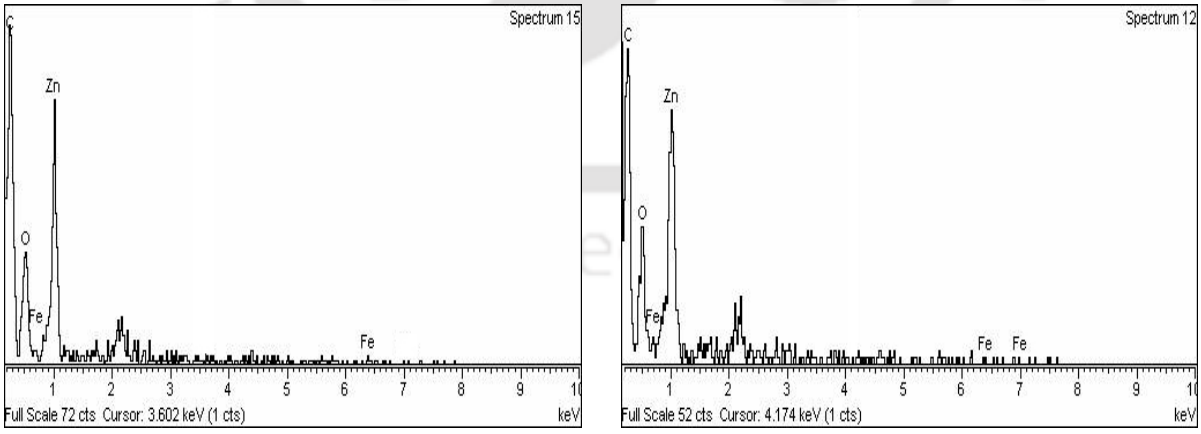

(A) (B)

Figure 8.3: Energy Dispersive X-ray spectroscopy (EDX) results for two versions of Fe-doped ZnO. (A) Fe-ZnO(I), (B) Fe-ZnO(II)

8.3.4 Powder X–ray diffraction (XRD) analysis

The influence of Fe–doping on structural properties and crystallinity of the ZnO catalyst was assessed using XRD analysis. This analysis was performed using Bruker D8 Advance X–ray powder diffractometer with monochromatic Cu–K_α (λ = 1.5406 Å) radiation, which operates at 40 kV and 40 mA. The XRD spectrum has been taken in the range 5–80 degree and is depicted in Fig. 8.4. No characteristic peaks of iron were detected in XRD pattern due to low concentration of iron (2% w/w ZnO). Similar results have been reported in previous literature (Westmoreland and Harrision, 1976).

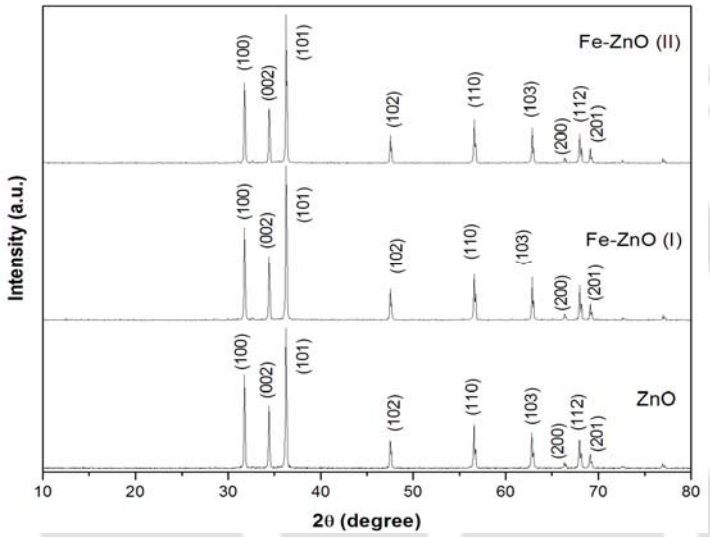

Figure 8.4: XRD spectrum of the pure and Fe-doped ZnO photocatalysts

The intensity values of different peaks increased significantly with Fe–doping for both Fe–ZnO(I) and Fe–ZnO(II) catalyst. However, the major peaks present in the spectra were same for both pure and Fe–doped ZnO. The characteristic peaks of ZnO, Fe–ZnO(I), and Fe–ZnO(II) were seen at 2θ values of 31.76 (100), 34.4 (002), 36.23 (101), 47.51 (102), 56.6 (110), 62.84 (103), 67.94 (112). The peaks located at (002) and (101) lattice plane is the indication of same hexagonal Wurtzite structure, whereas the peaks at (102) and (103) indicate the same Wurtzite crystal structure in all pure and Fe–doped ZnO (Saleh et al., 2013). Therefore, it is clear that doping does not change the properties of catalyst. As the ionic radius of the Fe^{3+} (0.64 Å) is very close to the Zn^{2+} radius (0.60 Å), it could be assumed

that Fe^{3+} can easily penetrate into the semiconductor lattice (Madhavan et al., 2010; Ahrens, 1952; Shi et al., 2008). Average particle size (D_{avg}) of the catalysts was determined as 56–60 nm from the most intense peak, corresponding to (101) reflection using Debye–Scherer formula (Goswami et al., 2013a, 2013b): $D_{avg} = 0.89\lambda/\beta\cos\theta$ (Notation: λ is the X–ray wavelength of Cu–K_α, β is the line broadening at half–height and θ is the Bragg's angle of the particles).

8.3.5 FTIR analysis

The Fourier transform infrared (FTIR) transmittance measurements were performed to investigate the bonding configuration in the catalyst particles and depicted in Fig. 8.5. The spectrum was taken in the range of 400 – 4000 cm^{-1} using a Fourier Transform Infrared Spectrometer (Shimadzu, Model: IRAffiniti–1). The peaks in the range of 400 – 700 cm^{-1} present in spectra are the characteristic peaks of ZnO stretching modes (Saleh et al., 2013). The peaks obtained in the range from 800 – 1500 cm^{-1} are attributed to the incorporation of Fe^{3+} ions into the lattice position of ZnO nanoparticles (Pandiyarajan et al., 2012).

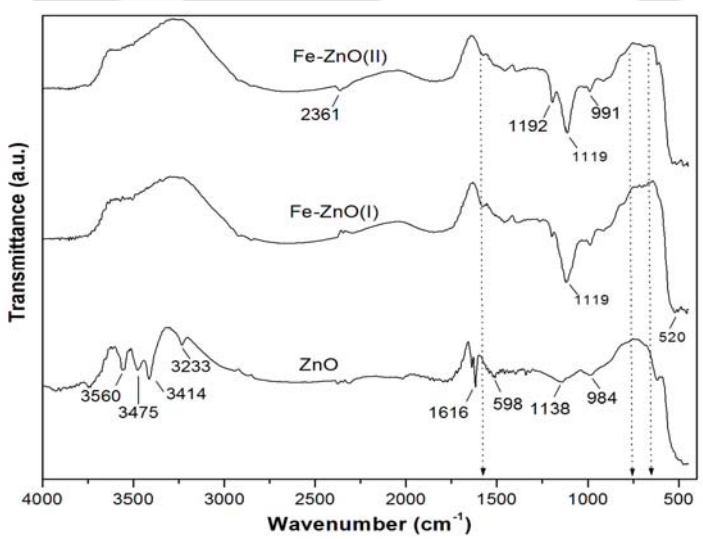

Figure 8.5: FTIR spectra of pure ZnO, Fe–ZnO(I), and Fe–ZnO(II) photocatalyst

8.3.6 BET surface area analysis

The surface area of undoped ZnO and Fe–doped ZnO was determined using BET surface area analyzer (Beckman Coulter, Model No. SA3100). The N_2 adsorption–desorption isotherms and the corresponding BJH pore size distribution curve for ZnO, Fe–ZnO (I), and Fe–ZnO (II) are given in Fig. 8.6.

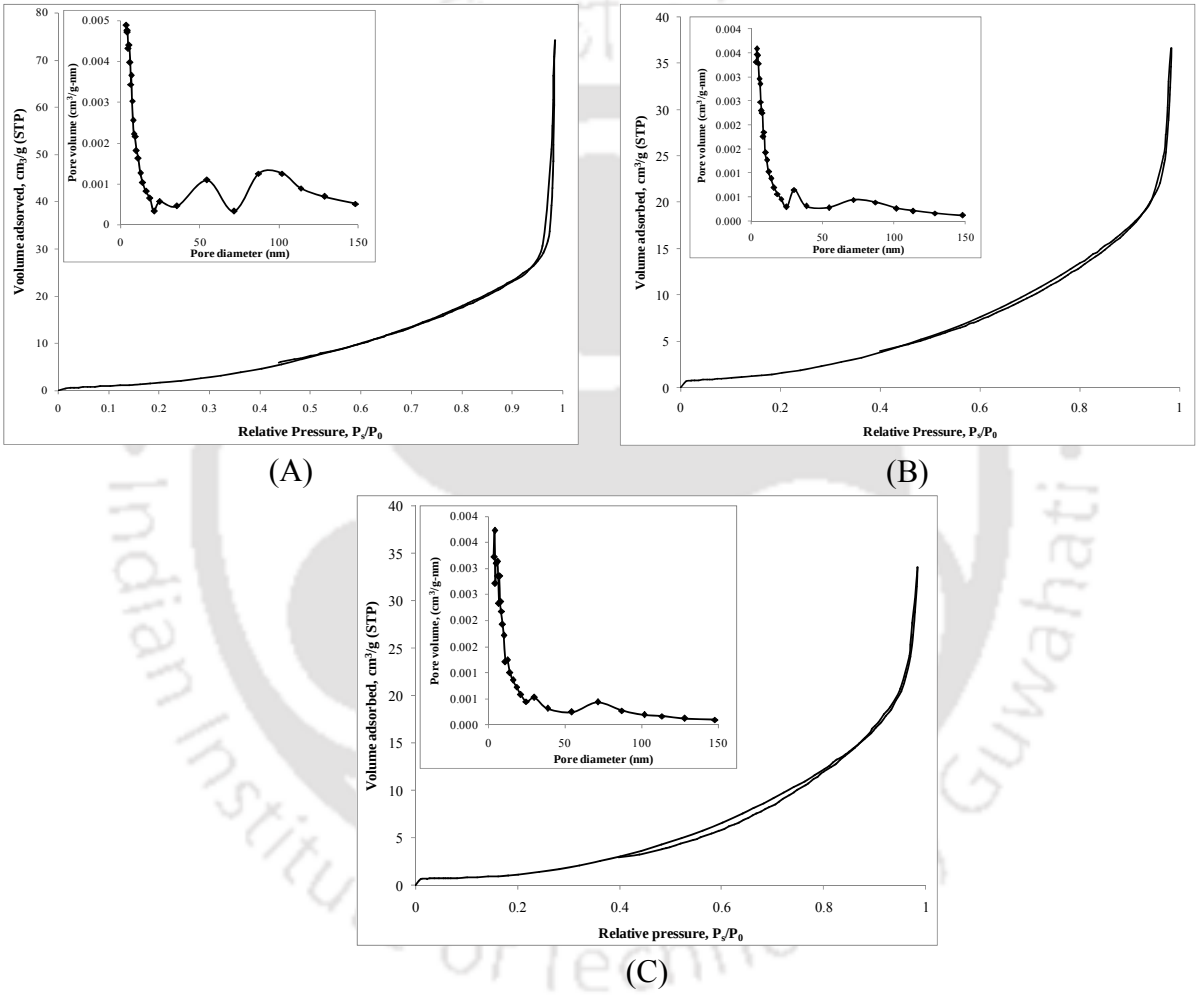

Figure 8.6: Results of BET surface area analysis. N_2 adsorption–desorption isotherms of catalysts and the corresponding BJH pore size distribution curves (inset). (A) pure ZnO, (B) Fe-ZnO(I), and (C) Fe-ZnO(II).

The N_2 gas adsorption–desorption isotherms of the catalysts display the typical type III curve. The BET surface area of ZnO and Fe–ZnO(I) and Fe–ZnO(II) were 7.36, 4.34, and

6.18 m^2/g, respectively; with corresponding total pore volume of 0.0834, 0.0497, and 0.0474 cm^3/g, respectively. The BET surface area of Fe–doped ZnO was reduced due to the doping of Fe^{3+} into the semiconductor, but in the latter case the surface area increases slightly. This effect is attributed to de–agglomeration caused due to addition of surfactant.

8.3.7 UV–Vis diffuse reflectance spectra (DRS)

Fig. 8.7A and B show the UV–Vis reflectance spectra and band gap energies of pure and Fe–doped ZnO particles. Fig. 8.7A shows the change in percentage reflectance of Fe–doped ZnO as compared to original undoped ZnO. The red–shift in the reflectance spectra for doped ZnO particles towards the visible light region is clearly evident from Fig. 8.7(A.1) and (A.2). The change in % reflectance for Fe–ZnO(I) photocatalyst was observed from 385 to 850 nm, while the Fe–ZnO(II) exhibits the maximum change in % reflectance for higher wavelength greater than 400 nm. The red–shift of modified photocatalyst for Fe–ZnO (I) is attributed to the dopant. Higher red–shift for the second case, i.e. for Fe–ZnO(II) is attributed to the doping carried out in presence of SDS surfactant, which helps for uniform doping of Fe in the ZnO lattice, as noted earlier. The band gap energy for the photocatalysts has been determined by plotting $[F(R).hv]^{0.5}$ against photon energy hv (eV), and extrapolating the linear portion of $[F(R).hv]^{0.5}$ to 0 (zero). Here, $F(R)$ is the Kubelka–Munk function and is defined as: $F(R) = (1-R)^2/2R$, where R is the reflectance (Aydin et al., 2013). With this procedure, the band gap energies are found to be 3.15, 3.09 and 3.0 eV for ZnO, Fe–ZnO (I) and Fe–ZnO (II), respectively. Doping of Fe^{3+} in ZnO nanostructure lattice replaces Zn^{2+} with Fe^{3+} resulting in formation of oxygen vacancies with additional energy level in the photocatalyst. Due to this, the average atomic distance increases that results in decrease of band gap energy. Doped–ZnO thus exhibits higher tendency to absorb photons, which excite the electrons from valence band (VB) to conduction band (CB). Many researchers have also

reported that the red–shift or narrower band gap of transition metals (TM) is due to the *sp–d* spin exchange interaction between the band edge electrons by replacing cation with localized *d*–electrons of TM ion (Zhao et al., 2007; Parra–Palomino et al., 2008). The substitution of cation has also been experimentally investigated and reported by Ando et al. (2001).

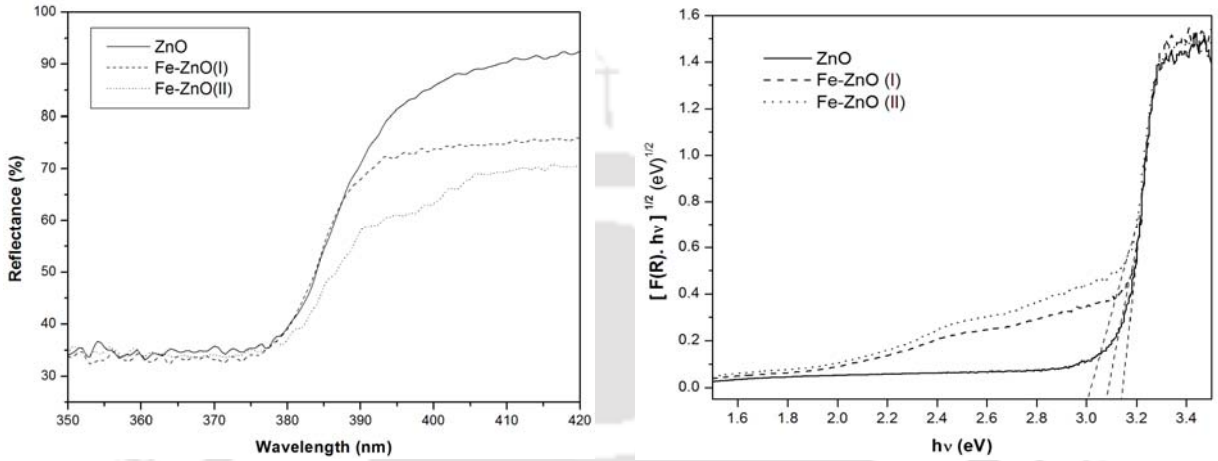

(A) (B)

Figure 8.7: Optical properties of pure and Fe-doped ZnO photocatalyst: (A) UV–visible diffuse reflectance spectra, and (B) Band gap energies of pure ZnO, Fe– ZnO.

8.3.8 Temperature–programmed reduction (TPR) analysis

Temperature–programmed reduction (TPR) (Model: ChemiSorb 2720, Micromeritics) in hydrogen gas was performed by passing hydrogen gas over the Fe–doped ZnO at a flow–rate of 10 mL/min. The temperature range was 50 to 850^{o}C at a linear heating rate of 10^{o}C/min. A two–stage reduction was observed for both Fe–ZnO (I) and Fe–ZnO (II), as seen in Fig. 8.8. The shape of TPR profile for Fe–ZnO (II) changed as compared to Fe–ZnO (I). The maximum rates of reduction for Fe–ZnO (II) shifted to higher temperatures with higher H_2 consumption. However, the H_2 consumption in the second stage was lesser for Fe–ZnO (II) as compared to Fe–ZnO (I). The increase in hydrogen consumption during TPR with shift of peaks to higher temperatures is essentially attributed to present of dopant in the ZnO

matrix. Formation of Fe–O_x phase within ZnO matrix cannot be ruled out. However, these are in very small concentration, so as to be detected during XRD analysis. Similar observations have also been made by Balaraju et al. (2012) for Cu–MgO catalyst. They have attributed the higher temperature peak to reduction of cluster or bulk CuO particles.

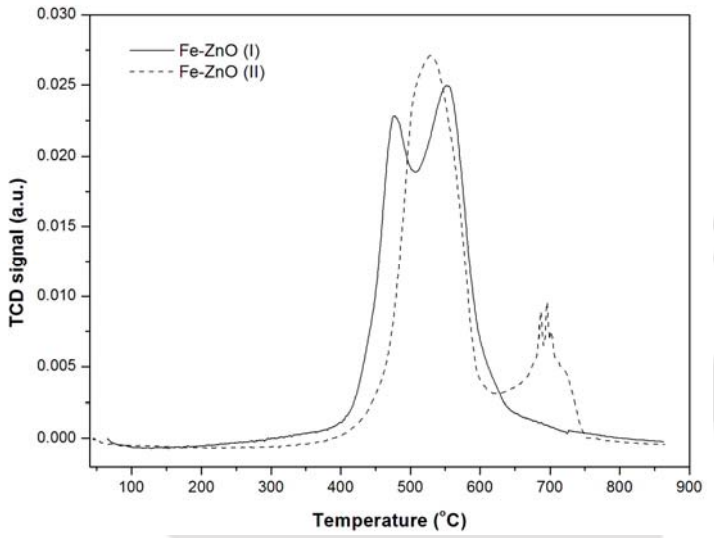

Figure 8.8: TPR profile of Fe–doped ZnO with and without SDS

8.4 RESULTS OF DECOLORIZATION/ DEGRADATION OF TEXTILE DYES

Before presentation of main results of this study and their analysis, we briefly discuss herewith the beneficial effect of Fe doping on ZnO from the viewpoint of decolorization of textile dye.

8.4.1 Fe–doping on ZnO: Reaction mechanism

For Fe–doped ZnO, absorption is enhanced to include the visible region through a red shift of the ZnO band gap. Small concentration of Fe ions (typically < 2 wt%) can be used for doping of ZnO. Excess concentration of Fe ions results in decrease of photocatalytic activity. This result is attributed to the fact that small concentration of Fe ions can function as a photo–generated hole and trap, inhibiting the recombination of hole–electron, as described by

equations below:

$$ZnO + h\nu \longrightarrow e^- + h^+ \quad \text{(charge pair generation)} \quad (8.5)$$

$$Fe^{3+} + e^-_{cb} \longrightarrow Fe^{2+} \quad \text{(electron trap)} \quad (8.6)$$

$$Fe^{2+} + O_2(ads) \longrightarrow Fe^{3+} + O_2^{\bullet -} \quad \text{(electron release)} \quad (8.7)$$

$$Fe^{3+} + h^+_{vb} \longrightarrow Fe^{4+} \quad \text{(hole trap)} \quad (8.8)$$

$$Fe^{4+} + OH^- \longrightarrow Fe^{3+} + {}^{\bullet}OH \quad \text{(hole release)} \quad (8.9)$$

Fe^{3+} ions react as electron holes and trap, which then form Fe^{2+} and Fe^{4+}, which are relatively unstable as compared to Fe^{3+} ions. These ions react with oxygen and hydroxyl ions adsorbed onto the catalytic surface to produce hydroxyl radicals and superoxide ($O_2^{\bullet -}$) radicals, which enhance the oxidation of the pollutant. This recombination rate is found to be much faster at optimum concentration of Fe^{3+} ions. At higher than optimum concentration of Fe^{3+}, the availability of the traps is reduced because the Fe^{4+} reacts with electrons: $Fe^{4+} + e^- \longrightarrow Fe^{3+}$ and Fe^{3+} acts as the recombination center $Fe^{3+} + e^- \longrightarrow Fe^{2+}$ and $Fe^{2+} + h^+_{vb} \longrightarrow Fe^{3+}$, thus reducing the activity of Fe–ZnO photocatalyst.

8.4.2 Experimental results

The results of experiments of textile dye decolorization are shown in Table 8.1 for ARB and Table 8.2 for MB dye. The time histories of decolorization are shown in Fig. 8.9 for ARB dye and Fig. 8.10 for MB dye. In all experimental categories, the rate of dye decolorization was non–uniform with time (i.e. faster decolorization was achieved in first few minutes of sonication as compared to total decolorization achieved in 60 min of sonication).

Table 8.1: Summary of experimental results on decolorization/ degradation of Acid red B

Experimental Category	**Decolorization of ARB**								
1. Sonolysis (US)	16.36 ± 1.48 (3.86 ± 0.38 after 10 min)					$k = 4.34 \times 10^{-5}$			
	ZnO			**Fe–ZnO (I)**			**Fe–ZnO (II)**		
	10 min	60 min	k (s^{-1})	10 min	60 min	k (s^{-1})	10 min	60 min	k (s^{-1})
2. MS + UV	46.3±0.99	63.45±1.91	6.28×10^{-4}	48.74±0.16	65.36±0.32	6.87×10^{-4}	53.49±0.39	74.3±1.06	8.49×10^{-4}
	(1099%)	(287.84%)	(1347%)	(5.27%)	(3.01%)	(9.4%)	(15.53%)	(17.1%)	(35.19%)
3. US + Sat	30.6±0.79	50.21±1.01	3.49×10^{-4}	35.26±1.43	51.96±0.49	4.15×10^{-4}	47.93±0.19	58.52±0.23	7.24×10^{-4}
	(693%)	(207%)	(704.15%)	(15.23%)	(3.49%)	(18.91%)	(56.63%)	(16.55%)	(107.45%)
4. US + Unsat	9.93±0.53	43.12±1.20	1.21×10^{-4}	32.69±0.95	41.46±1.22	4.45×10^{-4}	42.88±1.47	52.42±0.30	6.13×10^{-4}
	(157%)	(163.56%)	(178.8%)	(229.2%)	(317.52%)	(267.77%)	(331.82%)	(21.57%)	(447.32%)
5. US + UV + Sat	60.25±0.81	80.98±1.02	9.22×10^{-4}	65.45±2.3	79.99±1.32	1.07×10^{-3}	60.25±0.21	74.75±0.64	1.13×10^{-3}
	(1461%)	(395%)	(2024%)	(8.63%)	(~0)	(16.05%)	(0)	(~ 0)	(22.56%)
6. US + UV + Unsat	43.8±2.88	73.32±1.39	6.05×10^{-4}	50.42±3.99	70.58±2.24	7.27×10^{-4}	56.03±4.03	74.13±2.90	8.70×10^{-4}
	(1035%)	(348.17%)	(1294%)	(15.11%)	(~0)	(20.17%)	(27.92%)	(1.11%)	(43.8%)

Notations: US – ultrasound assisted, MS – assisted with mechanical stirring, η – decolorization efficiency (%), k – pseudo 1st order kinetic constant (sec^{-1}). Figures given in bracket in each column indicate percentage enhancement in extent of decolorization / rate constant for decolorization in comparison to the base case. For pure ZnO catalyst, the base case has been sonolysis alone, while for Fe-ZnO (I) and Fe-ZnO (II) catalysts, the base case has been pure ZnO catalyst, against which the comparison has been made.

Table 8.2: Summary of experimental results on decolorization/ degradation of Methylene Blue

Experimental Category	**Decolorization of MB**								
1. Sonolysis (US)	7.14 ± 0.48 (1.07 ± 0.09 after 10 min)				$k = 2.17 \times 10^{-5}$				
	ZnO			**Fe–ZnO (I)**			**Fe–ZnO (II)**		
	10 min	60 min	k (s^{-1})	10 min	60 min	k (s^{-1})	10 min	60 min	k (s^{-1})
2. MS + UV	20.18±0.74	41.15±1.05	2.48×10^{-4}	27.69±2.34	52.07±3.96	3.36×10^{-4}	28.52±1.74	69.23±2.43	4.14×10^{-4}
	(1786%)	(476%)	(1043%)	(37.21%)	(26.54%)	(35.48%)	(41.32%)	(68.23%)	(66.93%)
3. US + Sat	36.71±0.41	47.93±0.79	5.42×10^{-4}	41.71±0.41	54.63±0.38	5.97×10^{-4}	45.86±1.22	55.46±0.63	6.86×10^{-4}
	(3331%)	(571%)	(2398%)	(13.62%)	(13.97%)	(10.14%)	(24.92%)	(15.71%)	(26.56%)
4. US + Unsat	31.27±1.03	43.45±0.50	4.20×10^{-4}	35.62±0.54	42.14±1.36	4.84×10^{-4}	37.49±1.41	54.31±0.98	5.78×10^{-4}
	(2822%)	(509%)	(1836%)	(13.91%)	(~ 0)	(15.23%)	(19.89%)	(25%)	(37.6%)
5. US + UV + Sat	42.87±2.19	53.28±0.07	6.39×10^{-4}	43.16±0.04	60.10±0.87	6.33×10^{-4}	53.51±1.12	67.55±0.28	9.07×10^{-4}
	(3906%)	(646%)	(2845%)	(1%)	(12.8%)	(~0)	(24.82%)	(26.78%)	(41.94%)
6. US + UV + Unsat	20.88±0.21	53.38±3.83	3.19×10^{-4}	49.89±1.3	61.85±1.17	7.94×10^{-4}	48.57±3.84	71.50±1.65	8.13×10^{-4}
	(1851%)	(648%)	(1370%)	(139%)	(15.86%)	(149%)	(132.6%)	(33.94%)	(154.8%)

Notations: US – ultrasound assisted, MS – assisted with mechanical stirring, η – decolorization efficiency (%), k – pseudo 1st order kinetic constant (sec^{-1}). Figures given in bracket in each column indicate percentage enhancement in extent of decolorization / rate constant for decolorization in comparison to the base case. For pure ZnO catalyst, the base case has been sonolysis alone, while for Fe-ZnO (I) and Fe-ZnO (II) catalysts, the base case has been pure ZnO catalyst, against which the comparison has been made.

Hence, we have mentioned in Tables 8.1 and 8.2, the percentage decolorization achieved in first 10 min, in addition to the total decolorization obtained in 60 min of sonication. As noted earlier, the dye adsorbs on the photocatalyst, and to distinguish this effect in total decolorization, the dye solution was stirred in dark ambience for 60 min after addition of the photocatalyst – prior to sonication. Zero time for sonication was marked at completion of 60 min of stirring (in other words the negative time of 60 min in Figs. 9 & 10 indicates adsorption step with stirring).

The kinetics of decolorization in experimental categories has been quantified using a pseudo 1st order kinetic constant for decolorization. This constant has been calculated using the decolorization data for 30 min of sonication (considering that the rate of decolorization almost levels off after 30 min). The assumption of pseudo 1st order kinetics is based on results published in previous literature as well as our own experience with sonochemical degradation of recalcitrant and non–volatile pollutants (Sivasankar and Moholkar, 2009; Patidar et al., 2012; Malani et al., 2014).

We can compare the experimental data in two ways: vertical comparison in a column and horizontal comparison in a row. The vertical comparison determines the synergy between different techniques as they are applied in combination, and the horizontal comparison gives a picture of the effectiveness of Fe–doping on ZnO (either in absence or presence of surfactant).

8.4.2.1 Vertical comparison

Some interesting trends in the results of decolorization of the dyes under different conditions can be identified with vertical comparison as follows:

(1) With respect to ultrasound alone, the decolorization in all categories with ZnO increases. This indicates a clear influence of ZnO on the decolorization.

(2) Interestingly, with addition of ZnO particles but in absence of external UV irradiation, the decolorization reduces with degassing or unsaturation of medium. The cavitation intensity is known to increase with degassing – but the trend observed with ZnO is reverse.

In our earlier study (Balaji et al., 2011), it is proven that the sonoluminescence emission is not able to activate the photocatalyst. Therefore, in categories where external UV light is not used, the role of ZnO is that of mere adsorbent. In another earlier studies (Chakma and Moholkar, 2011), we have shown that the shockwaves generated from cavitation bubbles enhance desorption. The cavitation intensity increases with degassing or unsaturation, and hence, the extent of desorption is also expected to increase with unsaturation. This could be the cause leading to the effect of reduction in extent of decolorization.

Adsorption of dye creates local concentration of dye molecules in the solution. The ZnO or Fe–ZnO particle can act as local nucleation sites for cavitation events. Occurrence of transient cavitation in the close vicinity of the photocatalyst particles helps in higher dye–radical interaction that result in higher and faster decolorization. With degassing of the medium, the cavitation intensity increases. This creates intense turbulence in the medium due to generation of shockwaves. These shockwaves cause desorption of the dye from surface of photocatalyst which in turn reduces the probability of dye/radical interaction and hence the extent of decolorization.

(3) In case of experimental category sonication + photocatalyst + UV irradiation, the saturation level (or dissolved gas content) of the medium does not show much effect on decolorization. Referring to the studies by Sivasankar et al. (2007), Moholkar and Warmoeskerken (2003), and Moholkar et al. (2004), the saturation level of the medium has a critical effect on the outcome of the sono–process – both sonophysical and sonochemical process. However, in presence of ZnO is almost independent of the saturation.

The synergy between sonocatalysis and photocatalysis is even more negative for the

case of unsaturated medium in which highly intense cavitation is likely to occur. Comparing the results for the two dyes, we see that the above trend remains more–or–less the same. For methylene blue, the decolorization obtained under saturated and unsaturated medium for sono–photocatalysis is almost the same (within practical limits) for all three photocatalysts. For ARB dye, the decolorization reduces under unsaturated medium for ZnO and Fe–ZnO(I) catalysts, while no change in decolorization is seen for Fe–ZnO(II).

The values of the percentage decolorization achieved under different combination of ultrasound, photocatalyst and UV help in determining the synergy between different mechanisms. For example, for the ARB dye and ZnO catalyst, sonication alone gives a decolorization of 16% which is boosted more than 3× with addition of ZnO. This is the technique of sonocatalysis. In absence of UV, ZnO acts merely as an adsorbent that generates local concentration of dye (in a highly dilute solution). With mechanical stirring and UV – irradiation, ZnO alone gives a decolorization of 63%. This is the technique of photocatalysis. From these results, one could essentially expect that, if sonocatalysis is combined with photocatalysis, i.e. simultaneous application of ultrasound and UV – irradiation with ZnO, complete decolorization should be achieved. However, contrary to this expectation, decolorization of only 80% is seen. This result is an indication of negative synergy between sono–catalysis and photocatalysis. Interestingly, this result is consistent for all three photocatalysts used in this study, viz. ZnO, Fe–ZnO(I) and Fe–ZnO(II).

8.4.2.2 Horizontal comparison

Comparing the results in rows of Tables 8.1 and 8.2 helps identify the influence of Fe–doping on the dye decolorization. The number indicated in bracket give the percentage rise in decolorization achieved in each category against the base case. The interesting results in this case can be summarized as follows:

(1) Addition of ZnO (in either pure form or doped form) gives an enormous boost to the extent of decolorization. The boost is not only in the total decolorization achieved within 1 h of sonication, but also in the kinetics of decolorization as indicated by the results for initial 10 min of decolorization.

(2) For the saturated medium, decolorization achieved with both doped catalysts, viz. Fe–ZnO(I) & Fe–ZnO(II), is practically same as seen from results of category 3 experiments. Marginal rise is seen in the kinetics of decolorization for Fe–ZnO(II). Similar conclusion can also be drawn for category 5 experiments, in which UV light was applied simultaneously with sonication. The percentage rise in total decolorization as well as kinetics of decolorization with Fe–ZnO (II) catalyst is somewhat higher in this case.

(3) For unsaturated medium, sonication alone gives marginal rise (15–25%) in both kinetics of decolorization and total decolorization for both Fe–ZnO (I) and Fe–ZnO (II) catalysts. Comparing between Fe–ZnO (I) and Fe–ZnO (II), we find that performance of latter is better.

Total enhancement in decolorization (with respect to sonolysis alone, or in absence of external UV source) with addition of photocatalysis is attributed to adsorption of dye on the catalyst. It could be seen that for unsaturated medium, the enhancement is less. This essentially means that relatively high intensity shock waves generated by smaller bubbles in unsaturated medium are responsible for desorption of dye that leads to reduced probability of dye molecule – radical interaction, causing reduction in extent of decolorization (Chakma and Moholkar, 2011; Midathana and Moholkar, 2009). Comparing this trend among the three catalysts, one can observe that for Fe–ZnO (II), extent of decolorization for saturated as well as unsaturated medium is almost the same. This is indication of better adsorbability of doped ZnO catalyst due to which the adverse effect of shock waves is minimized.

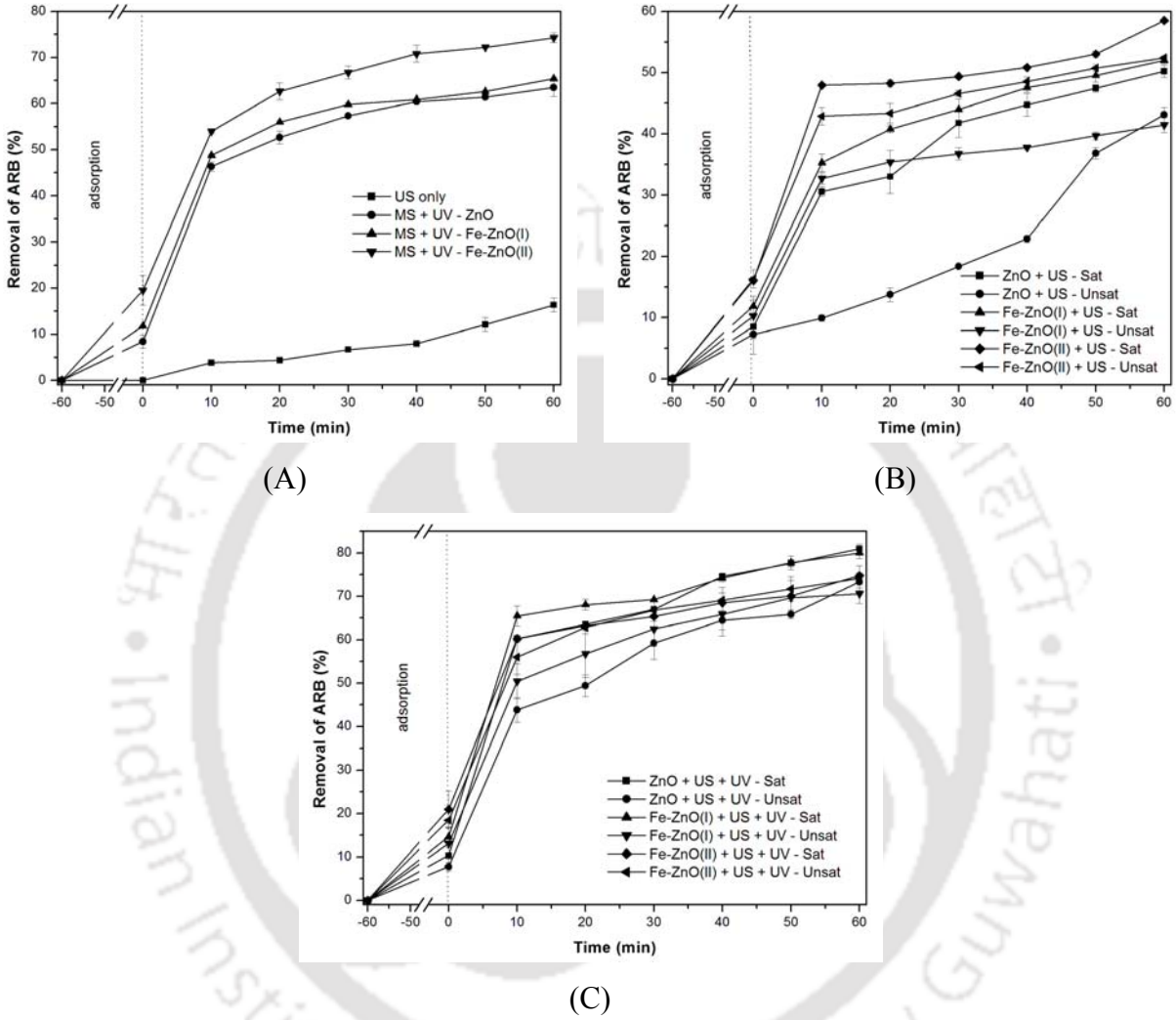

Figure 8.9: Time histories of decolorization of dye Acid Red B in various experimental categories (or protocols). (A) Individual advanced oxidation process. (B) Sonocatalysis process with pure ZnO, Fe–ZnO (I) and Fe–ZnO (II) catalyst. (C) Sonophotocatalysis process with pure ZnO, Fe–ZnO (I) and Fe–ZnO (II) catalyst. (Abbreviations: US – ultrasound, MS – mechanical stirring, Sat – Saturated reaction medium, Unsat – Unsaturated reaction medium)

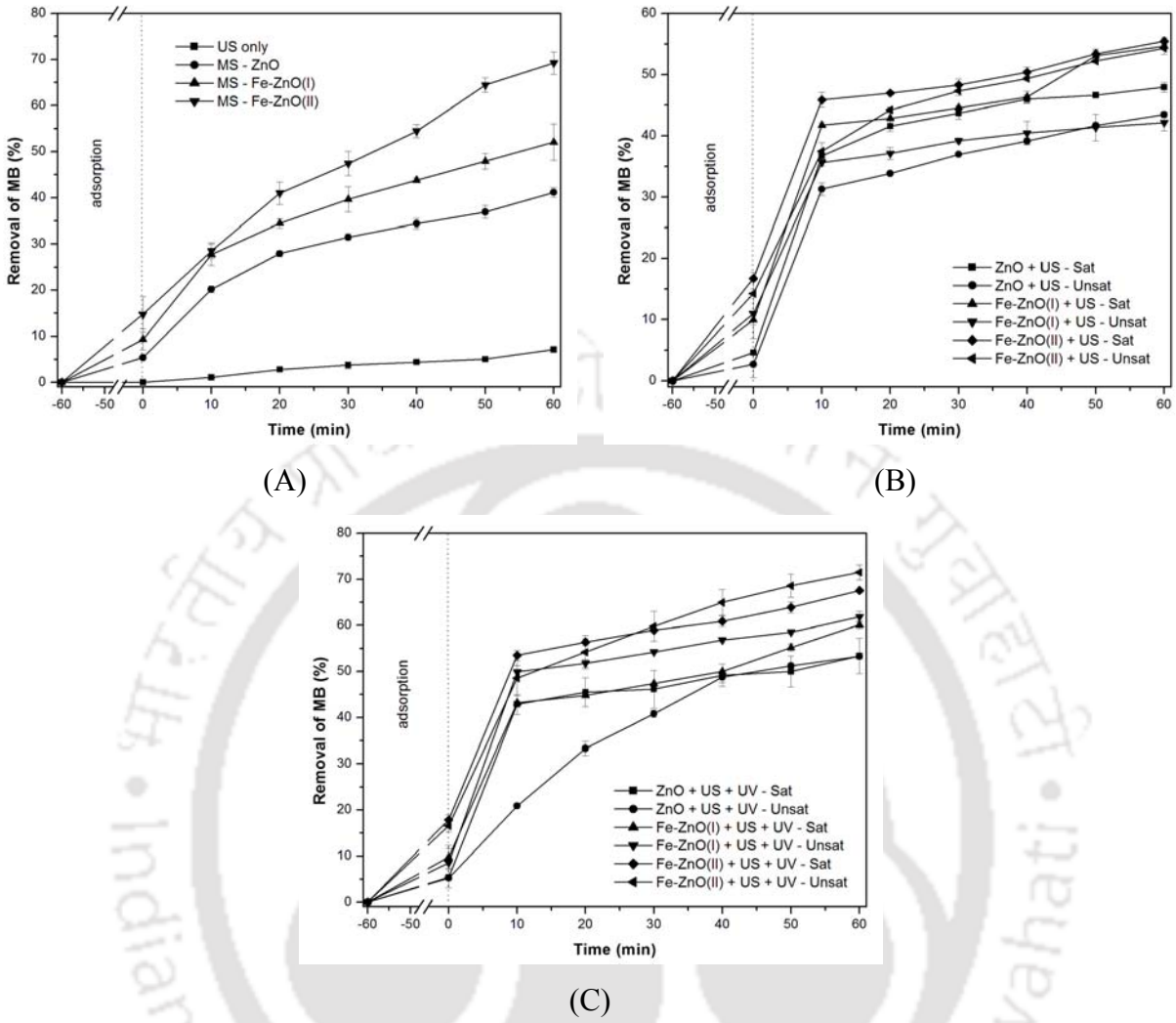

Figure 8.10: Time histories of decolorization of dye Methylene Blue in various experimental categories (or protocols). (A) Individual advanced oxidation process. (B) Sonocatalysis process with pure ZnO, Fe–ZnO (I) and Fe–ZnO (II) catalyst. (C) Sonophotocatalysis process with pure ZnO, Fe–ZnO (I) and Fe–ZnO (II) catalyst. (Abbreviations: US – ultrasound, MS – mechanical stirring, Sat – Saturated reaction medium, Unsat – Unsaturated reaction medium)

8.4.3 Identification of synergy in hybrid advanced oxidation process (HAOP)

Having described and discussed the trends in decolorization in preceding section, we now try to identify the synergy between individual AOPs of sonolysis and photocatalysis in hybrid AOPs, viz. sonocatalysis and sonophotocatalysis, using pure and Fe–doped ZnO. We define a quantitative measure of synergy as follows:

$$Synergy\ Effect = \frac{\left(\begin{matrix}\text{Decolorization obtained}\\ \text{with hybrid AOP}\end{matrix}\right) - \left[\left(\begin{matrix}\text{Decolorization with}\\ \text{sonolysis}\end{matrix}\right) + \left(\begin{matrix}\text{Decolorization with}\\ \text{photocatalysis}\end{matrix}\right)\right]}{\left[\left(\begin{matrix}\text{Decolorization with}\\ \text{sonolysis}\end{matrix}\right) + \left(\begin{matrix}\text{Decolorization with}\\ \text{photocatalysis}\end{matrix}\right)\right]}$$

Figs. 8.11A and B depict the synergy effect for the hybrid AOPs using pure ZnO and Fe–doped ZnO catalysts for ARB and MB dyes, respectively. These figures show large negative values of synergy effect for categories 3 and 4, in which no external UV source was used. In this case, we conjectured the activation of photocatalyst by the light emission during sonoluminescence. This emission is expected to increase with unsaturation, as the intensity of the transient collapse of bubbles increases.

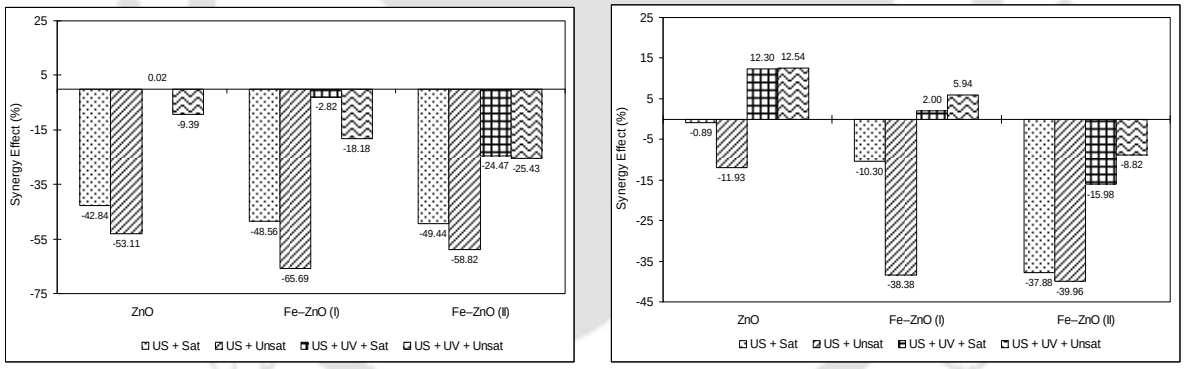

(A) (B)

Figure 8.11: Synergism of hybrid advanced oxidation processes (HAOPs): (A) Synergistic effect for decolorization of Acid Red B (azo dye) and (B) Synergistic effect on decolorization for Methylene Blue (non-azo dye). Note: While calculation of the synergies, the extent of adsorption of the dye onto the photocatalyst at time zero as shown in Figs. 9 & 10 (prior to commencement of the advanced oxidation treatment) has been accounted for.

However, contrary to this conjecture, we see negative synergy with all three photocatalysts for categories 3 and 4. This result is consistent for both dyes. Moreover, the

synergy is more negative for the unsaturated medium. This result is clear evidence that the expected activation of photocatalyst by sonoluminescence light does not occur. Moreover, higher intensity shock waves cause desorption of the dye, as noted earlier. These results are further corroboration of our results on physical mechanism of ultrasound assisted adsorption/ desorption published earlier (Balaji et al., 2011; Chakma and Moholkar, 2011; Midathana and Moholkar, 2009).

Even for categories 5 and 6, where external UV source was used for activation of photocatalyst, we see negative synergy as compared to the sum total of decolorization obtained with sonolysis and photocatalysis. This essentially means that the desorption effect caused by shock waves overwhelms the additional radical generation by the photocatalyst. These radicals are generated at the surface of the catalyst, and due to extreme instability do not penetrate deeper into the medium. Therefore, the higher the extent of dye adsorption on to the catalyst, the higher the probability of interaction between radicals generated by photocatalytic effect and the dye molecules. As noted earlier, the shock waves cause desorption of dye molecules from surface, which reduces the probability of the dye molecule – radical interaction leading to smaller degradation. It needs to be mentioned that another mechanism for cleaning of the solid surface by cavitation bubbles is the jetting due to bubbles as observed by Ohl et al. (2006). However, in the present context, the scale of size of the catalyst particle (~1 μm) and a transient cavitation bubble is similar, and hence the probability of jet formation due to asymmetric collapse of bubble is expected to be slim. Thus, shock waves remain to be the principal mechanism for desorption of the dye molecules. This trend is same for all three catalysts used in this study, viz. pure ZnO and Fe–doped ZnO. Fig. 8.12 depicts the exact synergy of the two individual AOPs of sonolysis and photocatalysis.

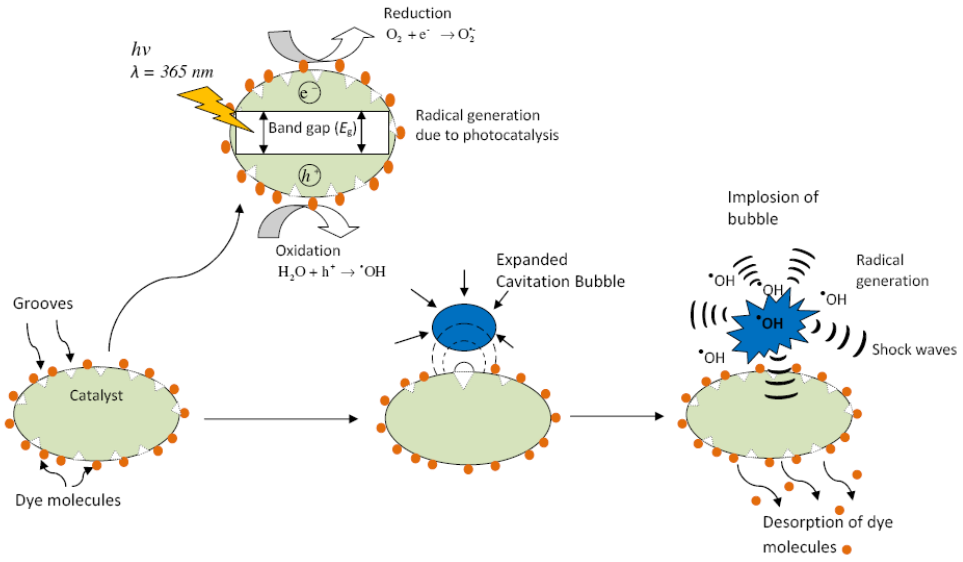

Figure 8.12: Schematic depicting the synergy of physical mechanism between sonolysis, sonocatalysis and sonophotocatalysis. Adsorption of the dye molecules onto surface of photocatalyst increases the probability of interaction between dye molecules and radicals generated through photocatalysis. The photocatalyst particles act as nucleation sites for cavitation events. However, the shock waves generated by cavitation bubbles cause desorption of dye molecules from surface and reduce the interaction probability of dye molecules with radicals generated from photocatalyst. On the other hand, the radicals generated by transient implosion of cavitation bubbles in vicinity of photocatalyst particles can cause some decolorization.

Fe–doping of ZnO catalyst increases the absolute decolorization of both dyes obtained in different categories of experiments as compared to pure ZnO. However, the nature of interaction of the mechanisms of the two processes, viz. sonolysis and photocatalysis, does not change with doping. The net synergy between these processes stays negative in case of all three catalysts.

8.5 CONCLUSION

In the present study, we have investigated the mechanistic issues of the hybrid AOPs of sonocatalysis and sonophotocatalysis. Three photocatalysts, viz. pure ZnO and Fe–doped

ZnO (synthesized with two protocols) have been used. Decolorization of two textile dyes (azo and non–azo) was used as model reaction. Characterization of doped ZnO catalyst indicated that Fe–doping increased the absorption band width in visible region, in addition to reducing the hole–electron recombination, due to which $^{\bullet}OH$ radical generation potential of the catalyst increases. However, experiments in 6 different protocols that alter the characteristics of ultrasound and cavitation events in the medium have clearly revealed a negative synergy between individual AOPs of sonolysis and photocatalysis. A major cause leading to this effect are the shock waves generated by cavitation bubbles, which desorbs the dye molecules adsorbed on the surface of photocatalyst, thus reducing the probability of radical–dye molecule interaction. The sonoluminescence light emitted during transient cavitation is also unable to activate the photocatalyst, in absence of an external UV source. These results have been found to be almost consistent for all three photocatalysts and for both dyes. The Fe–doping of ZnO could increase the extent of decolorization with respect to pure ZnO, but the synergy between two AOPs remains unaltered in the hybrid AOPs employing all three catalysts. Thus, this work has highlighted important issues of physical mechanism of hybrid advanced oxidation process of sonocatalysis and sonophotocatalysis, which could be useful for further research in this area.

REFERENCES

Ahrens LH, The use of ionization potentials: part 1. Ionic radii of the elements. Geochim. Cosmochim. Acta 2 (1952) 155–169.

Ando K, Saito H, Jin Z, Fukumra T, Kawasaki M, Matsumoto Y, Large magneto–optical effect in an oxide diluted magnetic semiconductor $Zn_{1-x}Co_xO$, Appl. Phys. Lett. 78 (2001) 2700 – 2702.

Ashokkumar M, Grieser F, The effect of surface active solutes on bubbles in an acoustic

field, Phys. Chem. Chem. Phys. 9 (2007) 5631–5643.

Aydın C, El–sadek MSA, Zheng K, Yahia IS, Yakuphanoglu F, Synthesis, diffused reflectance and electrical properties of nanocrystalline Fe–doped ZnO via sol–gel calcination technique, Optic. Laser Technol. 48 (2013) 447–452.

Ba–Abbad MM, Kadhum AAH, Mohamad AB, Takriff MS, Sopian K, Visible light photocatalytic activity of Fe^{3+}–doped ZnO nanoparticle prepared via sol–gel technique, Chemosphere 91 (2013) 1604–1611.

Balaji C, Moholkar VS, Pandit AB, Ashokkumar M, Mechanistic investigations on sonophotocatalytic degradation of textile dyes with surface active solutes, Ind. Eng. Chem. Res. 50 (2011) 11485–11494.

Balaraju M, Jagadeeswaraiah K, Sai Prasad PS, Lingaiah N, Catalytic hydrogenolysis of biodiesel derived glycerol to 1,2–propanediol over Cu–MgO catalysts, Catal. Sci. Technol. 2 (2012) 1967–1976.

Bhatte KD, Fujita S–I, Arai M, Pandit AB, Bhanage BM, Ultrasound assisted additive free synthesis of nanocrystalline zinc oxide, Ultrason. Sonochem. 18 (2011) 54–58.

Carp O, Huisman CL, Reller A, Photoinduced reactivity of titanium dioxide, Prog. Solid State Chem. 32 (2004) 33–177.

Chakma S, Moholkar VS, Investigations in synergism of hybrid advanced oxidation processes with combinations of sonolysis + Fenton process + UV for degradation of bisphenol–A, Ind. Eng. Chem. Res. 53 (2014) 6855–6865.

Chakma S, Moholkar VS, Mechanistic features of ultrasonic desorption of aromatic pollutants, Chem. Eng. J. 175 (2011) 356–367.

Chen YC, Vorontsov AV, Smirniotis PG, Enhanced photocatalytic degradation of dimethyl methylphosphonate in the presence of low frequency ultrasound, Photochem. Photobiol. Sci. 2 (2003) 694–698.

Daghrir R, Drogu P, Robert D, Modified TiO_2 for environmental photocatalytic applications: a review, Ind. Eng. Chem. Res. 52 (2013) 3581−3599.

Dong S, Xu K, Liu J, Cui H, Photocatalytic performance of ZnO:Fe array films under sun light irradiation, Physica B 406 (2011) 3609–3612.

Fang H, Venkata Subba Rao K, Madapusi S, Dharmarajan R, Ravi N, Tailored titanium dioxide photocatalysts for the degradation of organic dyes in wastewater treatment: a review, Appl. Catal. A: General 359 (2009) 25–40.

Goswami PP, Choudhury HA, Chakma S, Moholkar VS, Sonochemical synthesis and characterization of manganese ferrite nanoparticles, Ind. Eng. Chem. Res. 52 (2013a) 17848 −17855

Goswami PP, Choudhury HA, Chakma S, Moholkar VS, Sonochemical synthesis of cobalt ferrite nanoparticles, Int. J. Chem. Eng. 2013 (2013b), ID 934234.

Hilgenfeldt S, Lohse D, Brenner MP, Phase diagrams for sonoluminescing bubbles, Phys. Fluids 8 (1996) 2808–2826.

Jana S, Basu S, Pande S, Ghosh SK, Pal T, Shape–selective synthesis, magnetic properties, and catalytic activity of single crystalline β–MnO_2 nanoparticles, J. Phys. Chem. C 111 (2007) 16272–16277.

Madhavan J, Sathishkumar PS, Anandan S, Zhou M, Grieser F, Ashokkumar M, Ultrasound assisted photocatalytic degradation of diclofenac in an aqueous environment, Chemosphere 80 (2010) 747–752.

Malani RS, Khanna S, Chakma S, Moholkar VS, Mechanistic insight into sonoenzymatic degradation of organic pollutants with kinetic and thermodynamic analysis, Ultson. Sonochem. 21 (2014) 1400–1406.

Midathana VR, Moholkar VS, Mechanistic studies in ultrasound–assisted adsorption for removal of aromatic pollutants, Ind. Eng. Chem. Res. 48 (2009) 7368–7377.

Mills A, Stephen LH, An overview of semiconductor photocatalysis, J. Photochem. Photobiol, A: Chem. 108 (1997) 1–35.

Moholkar VS, Warmoeskerken MMCG, Integrated approach to optimization of an ultrasonic processor, AIChE J. 49 (2003) 2918–2932.

Moholkar VS, Warmoeskerken MMCG, Ohl CD, Prosperetti A, Mechanism of mass–transfer enhancement in textiles by ultrasound, AIChE J. 50 (2004) 58–64.

Ni M, Leung MKH, Leung DYC, Sumathy K, A review and recent developments in photocatalytic water–splitting using TiO_2 for hydrogen production, Renew. Sustain. Energ. Rev. 11 (2007) 401–425.

Ohl CD, Arora M, Dijkink R, Janve V, Lohse D, Surface cleaning from laser–induced cavitation bubbles, Appl. Phys. Lett. 89 (2006) 074102:1–3.

Pandiyarajan T, Udayabhaskar R, Karthikeyan B, Role of Fe doping on structural and vibrational properties of ZnO nanostructures, Appl. Phys. A 107 (2012) 411–419.

Parra–Palomino A, Perales–Perez O, Singhal R, Tomar M, Hwang J, Voyles PM, Structural, optical, and magnetic characterization of monodisperse Fe–doped ZnO nanocrystals, J. Appl. Phys. 103 (2008), 07D121:1–3.

Patidar R, Khanna S, Moholkar VS, Physical features of ultrasound assisted enzymatic degradation of recalcitrant organic pollutants, Ultrason. Sonochem. 19 (2012)104–118.

Saleh R, Djaja NF, Prakoso SP, The correlation between magnetic and structural properties of nanocrystalline transition metal–doped ZnO particles prepared by the co–precipitation method, J. Alloy. Comp. 546 (2013) 48–56.

Samadi M, Asghari Shivaee H, Zanetti M, Ali P, Moshfegh A, Visible light photocatalytic activity of novel MWCNT–doped ZnO electrospun nanofibers, J. Mol. Catal. A: Chem. 359 (2012) 42– 48.

Selli E, Bianchi CL, Pirola C, Cappelletti G, Ragaini V, Efficiency of 1,4–dichlorobenzene

degradation in water under photolysis, photocatalysis on TiO_2 and sonolysis, J. Hazard. Mater. 153 (2008) 1136–1141.

Shi Z, Liu D, Yan X, Gao Z, Bai S, Growth and properties analysis of metalorganic chemical vapor deposited $Mg_xZn_{1-x}O$ films on C–Al_2O_3 substrates, Front. Mech. Eng. China 3 (2008) 261–264.

Sivasankar T, Moholkar VS, Physical insights into the sonochemical degradation of recalcitrant organic pollutants with cavitation bubble dynamics, Ultrason. Sonochem. 16 (2009) 769–781.

Sivasankar T, Paunikar AW, Moholkar VS, Mechanistic approach to enhancement of the yield of a sonochemical reaction, AIChE J. 53 (2007) 1132–1143.

Suslick KS, Sonochemistry, Science 247 (1990) 1439–1445.

Tuziuti T, Yasui K, Sivakumar M, Iida Y, Correlation between acoustic cavitation noise and yield enhancement of sonochemical reaction by particle addition, J. Phys. Chem. A 109 (2005) 4869–4872.

Westmoreland PR, Harrision DP, Evaluation of candidate solids for high temperature desulfurization of low–Btu gases, Environ. Sci. Technol. 10 (1976) 659–661.

Xu L, Li X, Influence of Fe–doping on the structural and optical properties of ZnO thin films prepared by sol–gel method, J. Crystal Growth 312 (2010) 851–855.

Zhao ZW, Tay BK, Chen JS, Hu JF, Lim BC, Li GP, Large magnetic moment observed in Co–doped ZnO nanocluster–assembled thin films at room temperature, Appl. Phys. Lett. 90 (2007) 152502:1–3.

9

MECHANISTIC INVESTIGATIONS IN HETEROGENEOUS HYBRID AOPS: $ZrFe_2O_5$ CATALYST WITH DUEL (PHOTO AND FENTON) ACTIVITY

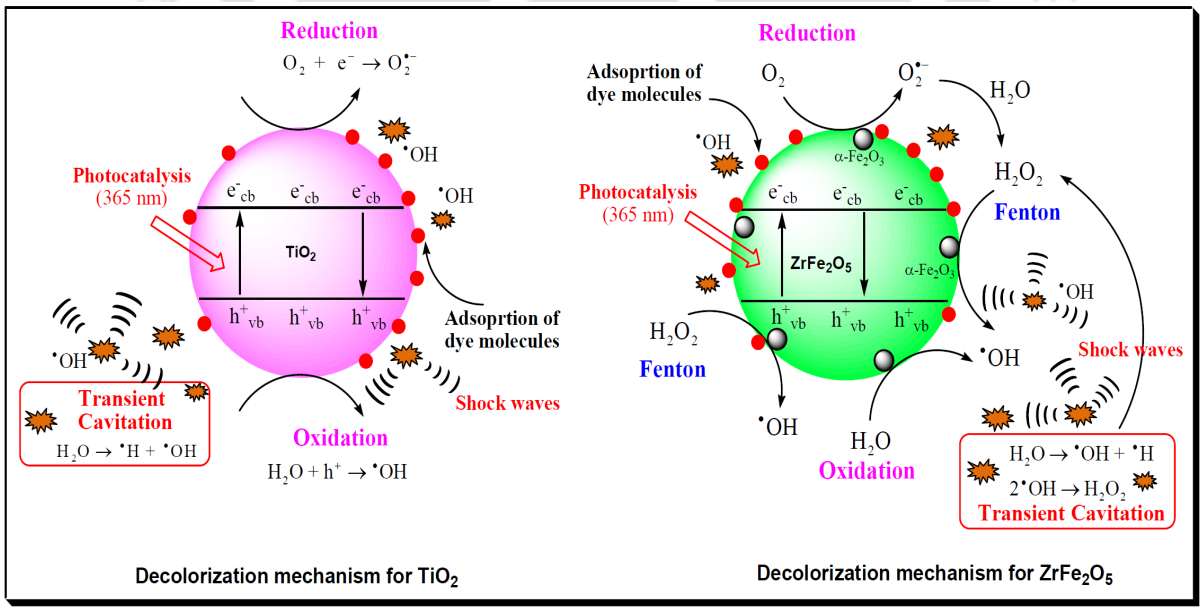

CHAPTER 9

MECHANISTIC INVESTIGATIONS IN HETEROGENEOUS HYBRID AOPS: $ZrFe_2O_5$ CATALYST WITH DUEL (PHOTO AND FENTON) ACTIVITY

9.1 INTRODUCTION

In the first three chapters, we presented investigations in hybrid advanced oxidation processes involving sonolysis and Fenton process, and variants of the Fenton process. In the last chapter, we presented investigations in mechanistic issues of sono-photocatalysis. In this chapter, we combine these approaches using a new catalyst that has both Fenton and photo-activity. Spinel compounds such as metal ferrites have high adsorption capacity for various dyes and can be used as catalyst during sonolysis (Suzuki et al., 2006; Nishimura et al., 2009; Ito et al., 2009). Metal ferrite in the form of nanoparticles can also be synthesized using sonochemical route (Sivakumar et al., 2006, 2012; Reddy et al., 2010). The studies reported by Choudhury et al. (2013) and Goswami et al. (2013) have indicated that the principle chemical mechanism in the synthesis is *in–situ* micro–calcination induced by physical and chemical effects of transient cavitation.

In this study, we have reported synthesis and characterization of zirconium ferrite ($ZrFe_2O_5$), and its use in concurrence with sonolysis for degradation of the textile dyes. On

the basis of the photo–activity of $ZrFe_2O_5$, we have also studied additional contribution of a UV source – which essentially gives the hybrid AOP of sono–photocatalysis, as noted earlier. $ZrFe_2O_5$ catalyst was also revealed to possess Fenton–activity, and hence, we have explored additional contributions of H_2O_2 addition to reaction mixture – which essentially gives the hybrid AOP of (heterogeneous) sono–Fenton. In order to emphasize efficacy of $ZrFe_2O_5$ in degradation of organic pollutants, we have also compared results with conventional TiO_2 catalyst. Both $ZrFe_2O_5$ and TiO_2 particles have been synthesized using sonochemical protocol and characterized with standard techniques. As explained in subsequent sections, our study has not only revealed special features of catalysts synthesized through sonochemical routes, but have also shed light on the exact synergies of the hybrid AOPs and the relative roles of individual mechanisms of adsorption, Fenton reactions, photocatalysis and transient cavitation. Synthesis of metal ferrites (for example zinc and manganese ferrites) through sonochemical route has been reported by earlier authors. Some distinct merits of sonochemical route for ferrite synthesis over convectional technique is one-pot synthesis with use of less hazardous chemicals, no need of additives and energy intensive step of calcination. However, to the best of our knowledge, this study is first report on sonochemical synthesis of $ZrFe_2O_5$ with dual activity (Photo– and Fenton– activity) and its application for degradation of textile dyes through diverse hybrid AOPs such as sonocatalysis, photocatalysis, sono–photocatalysis and heterogeneous sono–Fenton & sono–photo–Fenton.

9.2 EXPERIMENTAL SECTION

9.2.1 Materials

The following chemicals have been used for the present study: Titanium (IV) isopropoxide (Alfa Aesar), zirconium oxychloride (Merck), glacial acetic acid (Merck) and ammonium solution (30%, Merck), hydrogen peroxide (30%, Merck), ethanol (Merck) and

iron (II) acetate (Sigma–Aldrich). The model dye of Methylene Blue ($C_{16}H_{18}N_3SCl$) was purchased from Loba Chemie, while Acid Red B or Acid Red 14 ($C_{20}H_{12}N_2Na_2O_7S_2$) was procured from a.b. Chemicals and Instrument. Dye solutions in all experiments were prepared using ultrapure water (≥18 MΩ·cm resistivity at 25°C).

9.2.2 Synthesis of $ZrFe_2O_5$ and TiO_2 particles

***Protocol for sonochemical synthesis of zirconium ferrite* ($ZrFe_2O_5$):** In this protocol, an aqueous solution of 3.223 g (0.2 M) of zirconium oxychloride and 3.479 g (0.4 M) of iron (II) acetate was prepared in 50 mL of water. The molar ratio of zirconium chloride to iron acetate in this solution was 1:2. The pH of the solution was maintained at 6.5 using 30% ammonium solution. The reaction mixture was sonicated for 2 h with 5 s ON and 5 s OFF pulse mode. The temperature of the reaction mixture during sonication was maintained at 30°C using an ice bath. 2 h of sonication of this mixture resulted in brown colored solid suspension. The solid phase in the suspension was separated by centrifugation at 5000 rpm for 30 min (Remi Equipment, model: R–8C). Solid particles were further dried in a hot air oven (Navyug, model: 101) at 100°C for 12 h. The solid powder obtained after drying was ground and calcined at different temperatures in the range of 500° to 900°C.

***Protocol for sonochemical synthesis of TiO_2*:** An ultrasound–assisted sol–gel method was used for synthesis of TiO_2 particles. In this protocol, 2 mL of TTIP was added to 30 mL of ethanol and 1 mL of acetic acid mixture. The mixture was then sonicated for 10 min using 20 kHz ultrasonic probe with 40% amplitude (Sonics, model: VCX500, 500 W), which corresponded to theoretical power input of 200 W. Actual power input to the system and the pressure amplitude of the ultrasound waves generated by the probe was determined as 1.5 bar using calorimetric technique (Chakma and Moholkar, 2014). After 10 min sonication of the

mixture, 30 mL of water was added to the reaction mixture followed by sonication for another 30 min, which resulted in gel formation. The gel was dried in a hot air oven (Navyug, model: 101) at 100°C for 12 h. White powder obtained after drying was calcined at 300°C and 500°C to obtain TiO_2 in anatase form.

9.2.3 Assessment of catalytic activity of $ZrFe_2O_5$ and TiO_2 using dye decolorization

The catalytic activity of the as–synthesized TiO_2 and $ZrFe_2O_5$ was assessed using protocols of sonocatalysis, photo–catalysis, sonophotocatalysis and (heterogeneous) sono–Fenton. Decolorization/degradation of textile dyes was used as the model reaction. Two textile dyes, *viz.* Acid Red B (an azo dye, abbreviated hereafter as ARB), and Methylene Blue (non–azo dye, abbreviated hereafter as MB) were chosen as model recalcitrant organic pollutants. All experiments were carried out using 50 mL dye solutions with initial concentration of 20 ppm (corresponding molar concentration of 0.04 mM for ARB and 0.063 mM for MB). In each experiment, 25 mg of catalyst was added to the dye solution prior to experiment. All the experiments were conducted at neutral pH.

***Adsorption of dye onto catalyst*:** Both catalysts, *viz.* TiO_2 and $ZrFe_2O_5$ show tendency to adsorb dye molecules. The adsorbed dye molecules may be mistakenly counted as degraded molecules. In order to isolate this artifact, the adsorptive capacity of TiO_2 and $ZrFe_2O_5$ for both model dyes was assessed prior to main experiments. The protocol followed was as follows: 25 mg of catalyst was added in 50 mL of dye solution with initial concentration of 20 ppm. The progress of adsorption study was evaluated by withdrawing 1 mL sample of the dye solution at regular time interval. The residual concentration of the dyes in these samples was determined using UV–Visible spectrophotometer.

***Decolorization experiments*:** Ultrasound–assisted experiments (*viz.* protocols of sonocatalysis, sono–Fenton, sono–photocatalysis and sono–photo–Fenton) were carried out using an ultrasound bath (JeioTech, South Korea, Model: UC–10), which operates at a frequency of 40 kHz and a theoretical power of 200 W. For the photo–assisted experiments (*viz.* protocols of sono–photocatalysis, sono–photo–Fenton and photocatalysis with mechanical stirring), two UV sources, *viz.* a UVA lamp (11 W, Phillips) with maximum peak emission at 365 nm and a UVC lamp (11 W, Phillips) with maximum peak emission at 254 nm, were used. The experiments were conducted with either a single UV source (UVA) or a combination of two UV sources (UVA + UVC). The UV source was placed above the reaction beaker at a distance of 14 cm from the surface of dye solution in the beaker (greater details along with schematic of the experimental set up with all dimensions are given in Chapter 3).

In ultrasound–assisted experiments, the reaction beaker was placed exactly in the center of the bath. The UVA lamp was switched on for 15 min before the experiment so that the diffusion of UV light in the reaction solution is uniform. During the reaction, the temperature of the dye solution was maintained at 25±1^{o}C. In ultrasound–assisted experiments, the temperature of the reaction mixture increases during sonication. This temperature rise was controlled by circulating cooling water in the bath using a temperature controlled bath (Amkette Analytics, model: WB2000). The decolorization reaction was monitored by withdrawing aliquots of dye solution at regular intervals. These aliquots were centrifuged at 5000 rpm (Remi Equipment, model: R–8C) to separate the solid catalyst particles and the residual dye concentration in these samples was analyzed at 512 nm (for ARB dye) and 663 nm (for MB dye) using UV–Visible spectrophotometer (Perkin Elmer, Lambda 35). In addition, the removal of total organic carbon (TOC) in the dye solution with mineralization was analyzed using a TOC analyzer (O–I–Analytical, Model: Aurora 1030).

In view of experimental results of adsorption experiments (described in the next section), $ZrFe_2O_5$ catalyst was added to the ARB dye solution just before the commencement of main treatment. For consistency, the same protocol was followed for the other dye of MB as well. On the basis of results of characterizations of catalysts, the decolorization experiments were devised in 7 different categories on the basis of the prevalent mechanism of decolorization. Each of these categories used either TiO_2 or $ZrFe_2O_5$ as the catalyst. In view of the Fenton active $\alpha - Fe_2O_3$ phase present in $ZrFe_2O_5$ (as described in greater detail in the next section), the experiments using $ZrFe_2O_5$ were also carried out with external addition of H_2O_2 (7.83 mM). Moreover, for experimental categories employing ultrasound, the saturation level of the liquid medium was also varied. In one category, liquid medium saturated with dissolved oxygen (9 ppm) was used, while in another category, the dissolved oxygen content of the medium was lowered to 2 ppm by application of vacuum and heating. With permutation–combination of different techniques, the following experimental protocols employing either individual AOP or hybrid AOP have been devised.

Individual AOPs: Sonolysis, photocatalysis (with either TiO_2 or $ZrFe_2O_5$) and heterogeneous Fenton (with $ZrFe_2O_5 + H_2O_2$)

Hybrid AOPs: Sonocatalysis (with either TiO_2 or $ZrFe_2O_5$), sono–photocatalysis (with either TiO_2 or $ZrFe_2O_5$ and UV source), sono–Fenton (with $ZrFe_2O_5$+H_2O_2) and sono–photo–Fenton (with $ZrFe_2O_5$+H_2O_2+UV source)

9.3 CHARACTERIZATION OF $ZrFe_2O_5$ AND TiO_2 PARTICLES: RESULTS AND DISCUSSION

9.3.1 Particle size distribution (PSD) analysis

The particles size distribution of $ZrFe_2O_5$ and TiO_2 powder was performed using Delsa™ Nano C (Beckman Coulter, model: A53878) particle size analyzer. The result of

particle size distribution is shown in Fig. 1. The particle distribution of synthesized catalysts was as follows:

TiO_2: D (10%): 308.60 nm, D (50%): 692.80 nm and D (90%): 1,736.50 nm

$ZrFe_2O_5$: D (10%): 159.60 nm, D (50%): 272.60 nm and D (90%): 560.40 nm

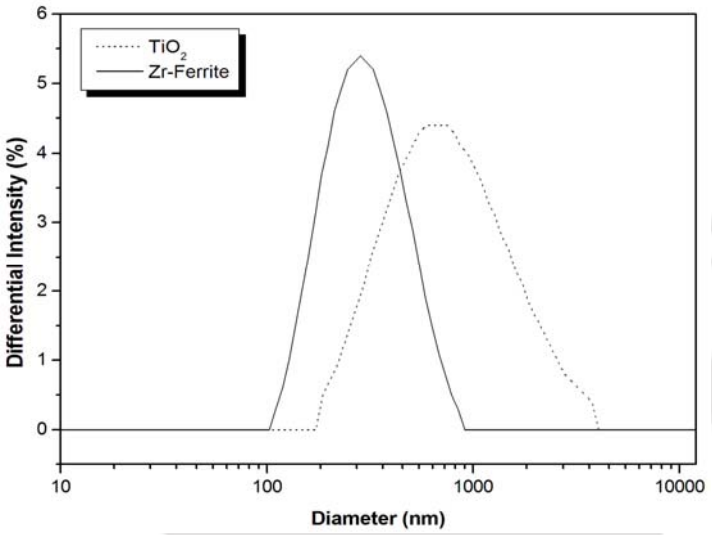

Figure 9.1: Particle size distribution of Zr–Ferrite ($ZrFe_2O_5$) and TiO_2 powders

9.3.2 X–ray diffraction (XRD) analysis

The structural characteristics of the catalysts were determined using X–ray powder diffractometer (Bruker, model: D8 Advance) with monochromatic Cu–K_α (λ = 1.5406 Å) radiation. Fig. 9.2 show the XRD spectrum of the catalyst particles in the range $2\theta = 10^o$–80^o. The strong peak in Fig. 9.2A at $2\theta = 25.4^o$ corresponds to the predominant (101) anatase phase of TiO_2 (Sathishkumar et al., 2014). The other peaks corresponding to lattice plane (004), (200), (105), (211), (204), (311), (112) and (103) also represented anatase phase of TiO_2 (Sathishkumar et al., 2008; Toyoda et al., 2004; He and Lin, 2007). As seen from Fig. 9.2A, the presence of above peaks in the XRD spectrum of TiO_2 prior to calcination is an evidence that titanium dioxide was formed during the sonochemical treatment.

Sonochemically synthesized TiO_2 has anatase phase, which remains unaltered even after calcination of the particles at a temperature of 500°C.

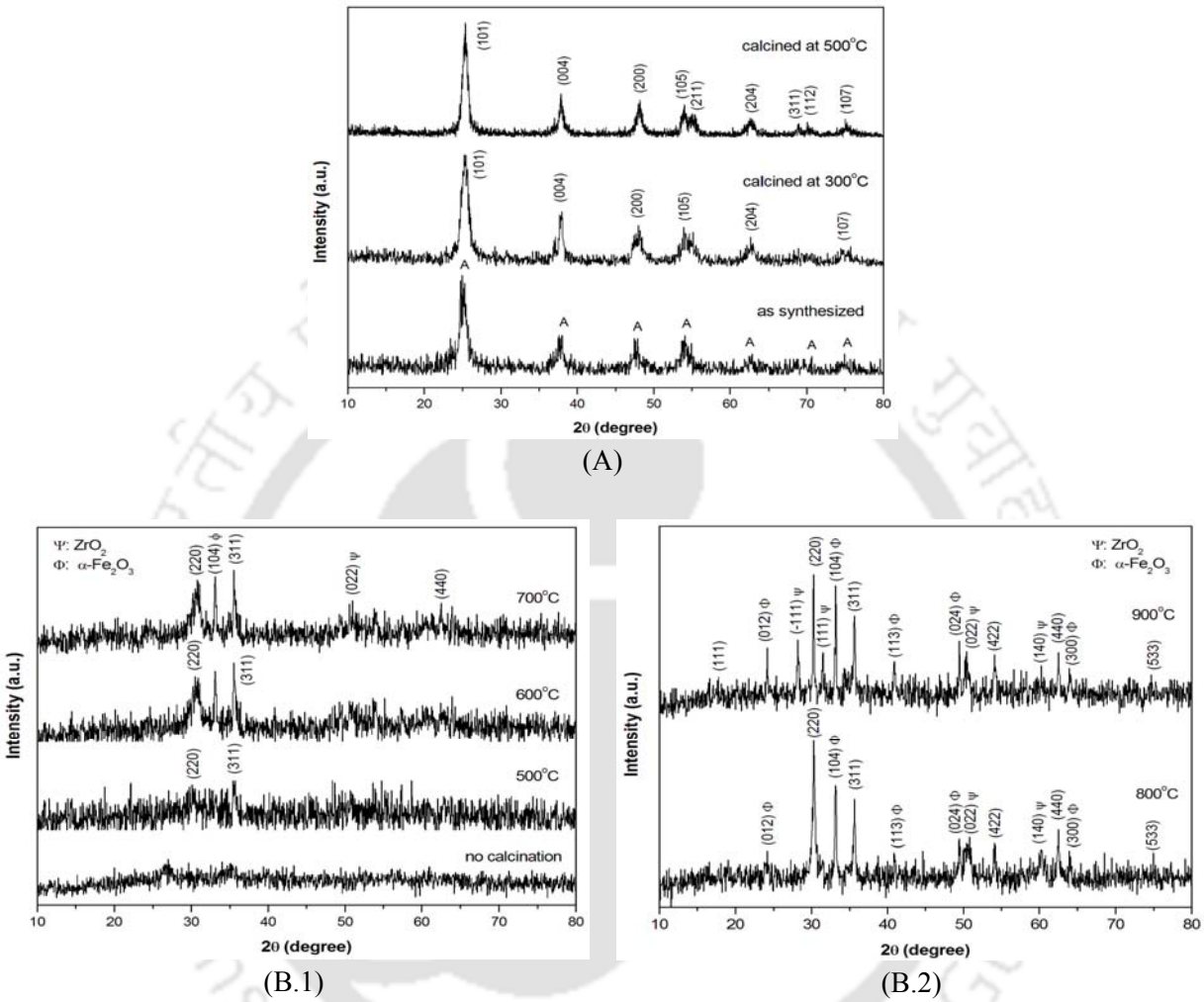

Figure 9.2: (A) Powder x–ray diffraction results of TiO_2 particles, (B) Powder x–ray diffraction results of $ZrFe_2O_5$ particles calcined at different temperatures

In case of $ZrFe_2O_5$, the solid particles obtained after sonochemical treatment did not show any peak corresponding spinel structure. This essentially means that synthesis of $ZrFe_2O_5$ is not complete after sonochemical treatment, and external calcination of the solid product is essential for formation of ferrite. As seen in Fig. 9.2(B.1), calcination of solid product from sonochemical treatment did not yield ferrite till calcination temperature of

600°C. Above this threshold temperature, peaks corresponding to the ferrite phase appeared in the XRD spectrum of calcined solids. The samples calcined at 700°C showed peaks at (220), (311) and (440) along with $\alpha-Fe_2O_3$ phase at (104) and tetragonal ZrO_2 at (022). The diffractograms of samples calcined at 800 and 900°C (shown in Fig. 9.2(B.2)) showed high intensity peaks at (111), (220), (311), (422), (440) and (533), which correspond to the spinel structure of ferrite particles (Shirsath et al., 2013; Sattar et al., 2007).

Some peaks at (012), (104), (113), (024) and (300) were also seen in Fig. 9.2(B.2), which correspond to the hematite phase ($\alpha-Fe_2O_3$) (Li et al., 2007; Lin et al., 2007). Solids calcined at 900°C also showed the presence of monoclinic phase (corresponding to peak at (–111, 111)) and tetragonal phase (corresponding to peak at (022, 140)) of ZrO_2 (Lin et al., 2007; De la Rosa et al., 2008). Reduction in the intensity of peak at (220) for solids calcined at 900°C (as compared to 800°C) could be attributed to agglomeration of particles (as observed in our previous study by Goswami et al. (2013). The increase in intensity of peak (104) for solids calcined at 900°C could be attributed to the formation of $\alpha-Fe_2O_3$ phase. It is noteworthy that this phase has Fenton activity, and this forms the basis of the experimental category with external H_2O_2 addition, as noted earlier.

9.3.3 FESEM and TEM analysis

The surface morphologies of the prepared $ZrFe_2O_5$ and TiO_2 particles were performed using Field Emission Scanning Electron Microscopy (Carl Zeiss GmbH, model: SIGMA VP, Germany) and Transmission Electron Microscope (JEOL, model: JEM 2100, USA). Figs. 9.3 & 9.4 represent the FESEM and TEM images of as–synthesized TiO_2 and $ZrFe_2O_5$ particles. It could be seen from these pictures that both $ZrFe_2O_5$ and TiO_2 particles are isotropic in shape and uniform in terms of size distribution.

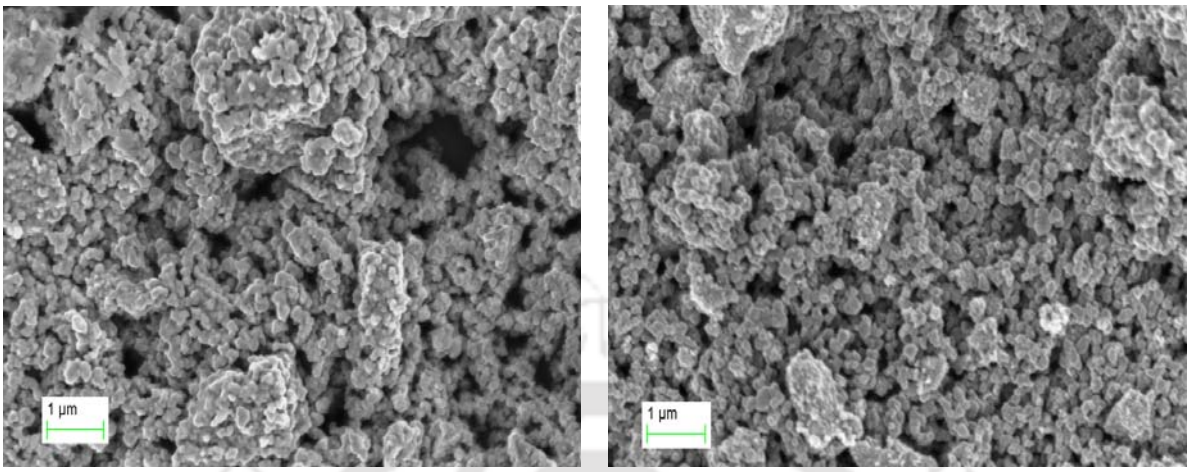

(A) (B)

Figure 9.3: FESEM images for surface morphology of (A) $ZrFe_2O_5$ and (B) TiO_2 at 30 KX

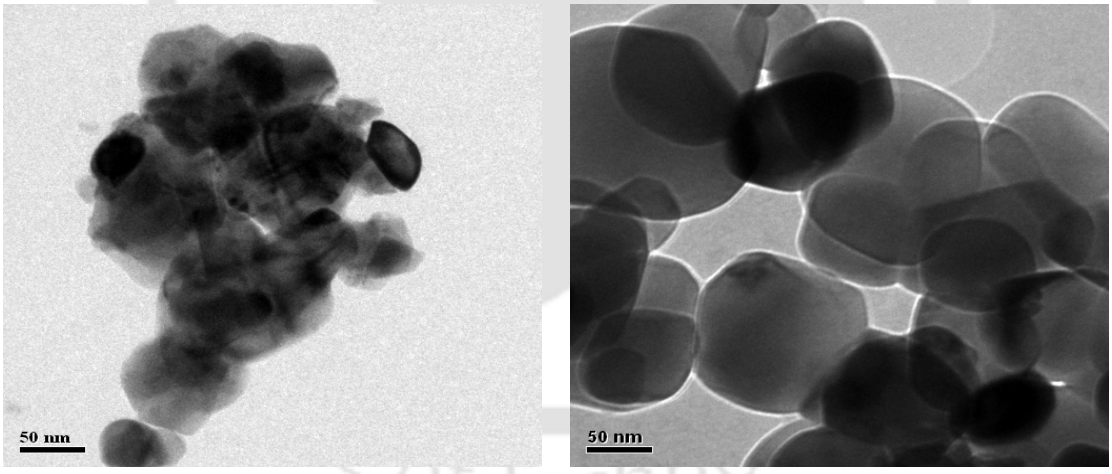

(A) (B)

Figure 9.4: TEM images of sonochemically synthesized (A) $ZrFe_2O_5$ and (B) TiO_2

9.3.4 Diffuse reflectance spectra (DRS) analysis

Fig. 9.5 shows the diffuse reflectance spectra (DRS) of $ZrFe_2O_5$ and TiO_2 powder. The band gap energies for both the catalysts have been determined by plotting $\left[F(R)\cdot h\nu\right]^{0.5}$ against photon energy hν (eV); and extrapolating the linear portion of $\left[F(R)\cdot h\nu\right]^{0.5}$ to 0 (zero). Here, F(R) is the Kubelka–Munk function, which is defined as (Chakma and Moholkar, 2004; Aydin et al., 2013): $F(R)=(1-R)^2/2R$, where R is the reflectance. The DRS results showed that sonochemically synthesized $ZrFe_2O_5$ has lower band gap energy than TiO_2. With this analysis, the band gap energies for $ZrFe_2O_5$ and TiO_2 have been estimated as 2.05 and 3.1 eV, respectively.

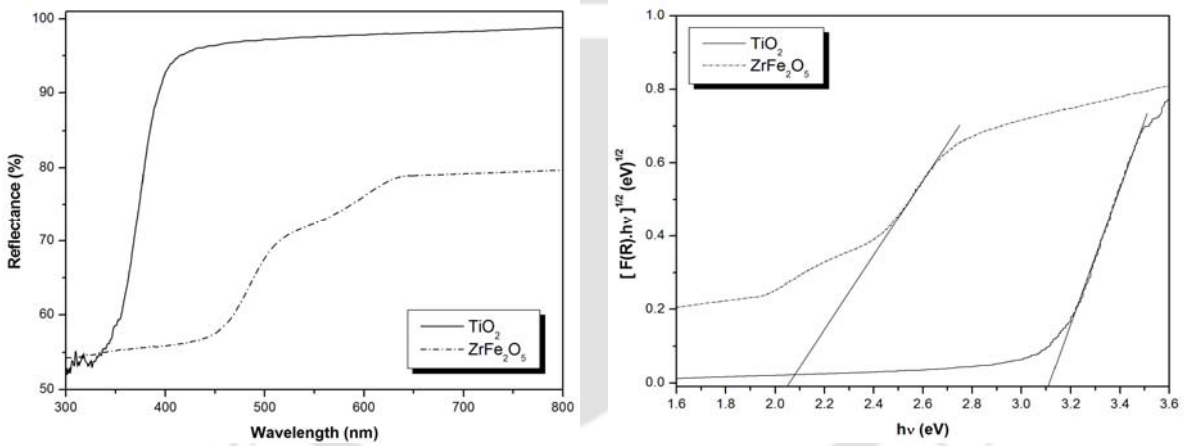

(A) (B)

Figure 9.5: (A) UV–Visible diffuse reflectance spectra of $ZrFe_2O_5$ and TiO_2, and (B) Estimated band gap energy of $ZrFe_2O_5$ and TiO_2

9.3.5 BET surface area analysis

The surface area of $ZrFe_2O_5$ and TiO_2 was analyzed using BET surface area analyzer (Beckman Coulter, Model: SA3100). The N_2 adsorption–desorption isotherms and the corresponding BJH pore size distribution curve for $ZrFe_2O_5$ and TiO_2 are shown in Fig. 9.6. The adsorption – desorption isotherms showed a large hysteresis loop above the relative

pressure of 0.4. These types of isotherm characteristic curves belong to type VI, which indicate the presence of mesoporosity due to the capillary condensation in the open mesoporous channels (Kim et al., 2009; Cho et al., 2012). The BET surface areas for $ZrFe_2O_5$ and TiO_2 were 97.13 and 152.39 m^2/g, respective, while the pore volumes of $ZrFe_2O_5$ and TiO_2 were 0.2808 and 0.3465 cm^3/g, respectively.

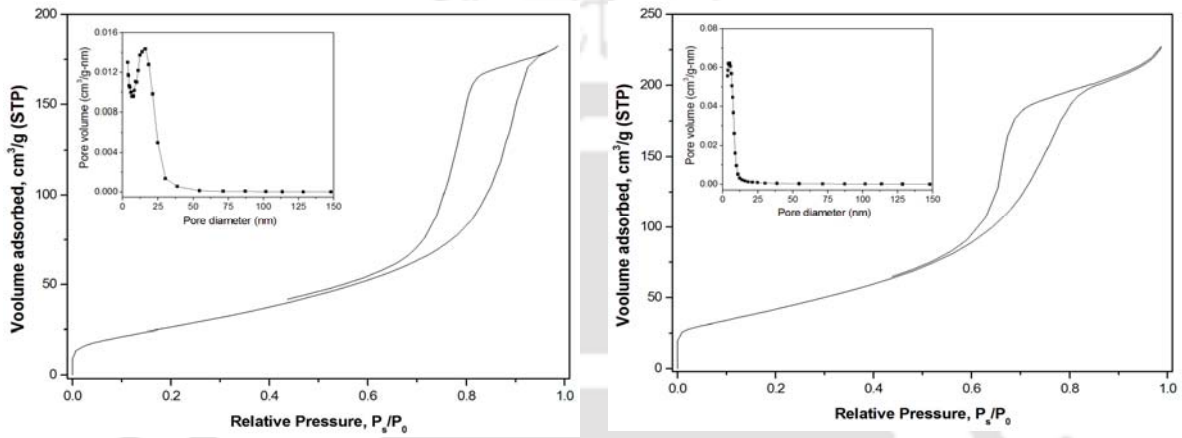

(A) $ZrFe_2O_5$ (B) TiO_2

Figure 9.6: Results of BET surface area analysis. N_2 adsorption–desorption isotherms of catalysts and the corresponding BJH pore size distribution curves (inset). (A) $ZrFe_2O_5$ and (B) TiO_2

9.3.6 Thermogravimetric analysis (TGA)

In order to determine the thermal characteristics of $ZrFe_2O_5$ and TiO_2, TG/DTG analysis was performed using thermo–gravimetric analyzer (TG 209 F1 Libra, NETZSCH) under N_2 environment with a flow rate of 40 mL/min. The analyses were conducted using heating rates of 10°C/min and the temperature range from 30°C to 900°C. The thermo–gravimetric analysis results of $ZrFe_2O_5$ calcined at 800°C and TiO_2 calcined at 500°C are shown in Fig. 9.7. The TGA results showed two stages of weight loss. The major weight loss of 2.20% and 0.41% for TiO_2 and $ZrFe_2O_5$, respectively, was observed from room temperature to 150°C, which corresponds to dehydration of physically adsorbed water. The

second and minor weight loss of 1.8% and 0.04% for TiO_2 and $ZrFe_2O_5$, respectively, was observed in the range of 150°–900°C. This could be attributed to the decomposition of residual contaminants from the reaction mixture present in the solid products after synthesis.

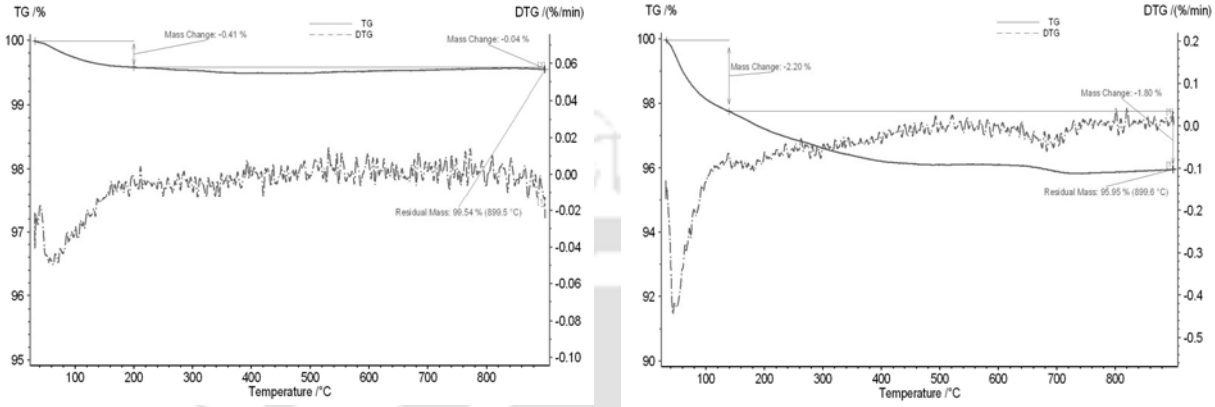

(A) $ZrFe_2O_5$ (B) TiO_2

Figure 9.7: Thermo–gravimetric analysis (TGA) results of (A) $ZrFe_2O_5$ and (B) TiO_2.

9.4 DYE DECOLORIZATION: RESULTS AND DISCUSSION

9.4.1 Dye adsorption

The results of dye adsorption on $ZrFe_2O_5$ and TiO_2 catalyst particles are given in Fig. 9.8. As stated earlier, the BET surface area analysis revealed much higher surface area for TiO_2 than $ZrFe_2O_5$. The adsorption of MB dye on both catalysts was ~5.5%, while the adsorption percentage of ARB dye was 6.6 and 19.4% on TiO_2 and $ZrFe_2O_5$, respectively. An explanation for higher adsorption of ARB on $ZrFe_2O_5$ could be given in terms of presence of $\alpha - Fe_2O_3$ phase on as–synthesized $ZrFe_2O_5$. This phase helps produce cationic sites around the particles of $ZrFe_2O_5$ after addition to water. ARB being an acidic dye, it always has the tendency for ionic bonding with the cationic sites of the particles. The attraction of anionic dye molecule to a cationic site on the $ZrFe_2O_5$ essentially results in higher extent of adsorption of ARB. In view of large adsorption of ARB dye, $ZrFe_2O_5$ particles were added to

dye solution just before the treatment so as to reduce the artifacts due to dye adsorption.

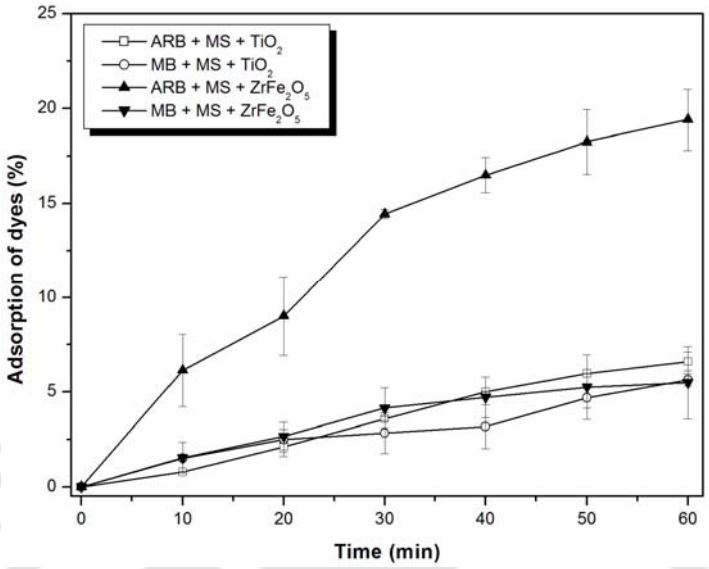

Figure 9.8: Adsorption study of ARB and MB dyes onto $ZrFe_2O_5$ and TiO_2 powders

9.4.2 Decolorization experiments

The summary of the experimental results of dye decolorization is given in Table 9.1 (for the ARB dye) and Table 9.2 (for the MB dye). The time trends of dye decolorization in different experimental categories employing either individual or hybrid AOP are shown in Figs. 9.9 & 9.10 for ARB and MB dye, respectively. The TOC removal in experiments employing with both ARB and MB dye is shown in Fig. 9.11 (individual as well as hybrid AOPs). Tables 9.1 & 9.2 also depict the pseudo 1st order kinetic constant fitted to the decolorization data. It should be noted, however, that the decolorization is non–uniform in time. Hence, the kinetic constant has been determined on the basis of decolorization obtained in first 30 min of treatment (although the total treatment time was 60 min), during which almost of the total decolorization was obtained. The degradation of the dye with the two catalysts can have different mechanisms on the basis of the properties of the catalysts. For

TiO_2, the possible mechanisms could be adsorption and photocatalysis. For $ZrFe_2O_5$, the possible mechanisms are adsorption, photocatalysis and Fenton reactions due to the presence of $\alpha - Fe_2O_3$ phase. The net decolorization obtained in any protocol is a manifestation of the above mechanisms that can occur simultaneously as shown in Scheme–I.

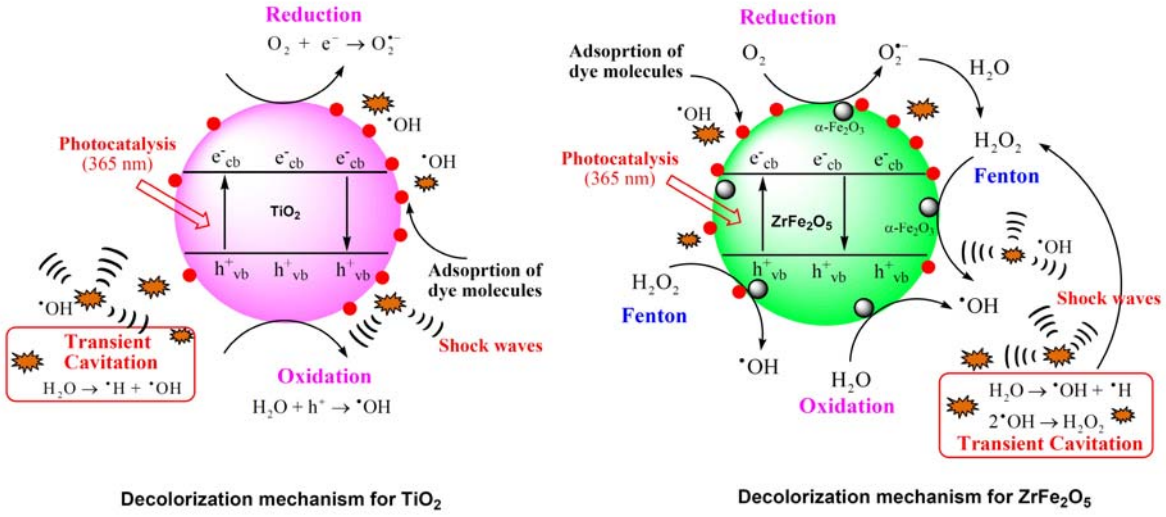

Scheme I: Schematic depicting the decolorization/ degradation mechanisms with TiO_2 and $ZrFe_2O_5$ catalysts

Some peculiar trends of decolorization could be identified from Tables 9.1 & 9.2 and Figs. 9.9 & 9.10. Given below are these trends along with discussion of possible underlying mechanism.

(1) Least decolorization for both dyes is seen for the AOP of sonolysis. In this case, the dye decolorization occurs through the •OH radicals generated by cavitation bubbles. Due to rather low concentration of the dye solution, the probability of interaction between dye molecules and radicals is low, which is essentially reflected in lower decolorization. Comparing among the two dyes, sonolysis yields higher decolorization for the azo ARB dye. We attribute this result to the chemical structure of the ARB dye, in which the azo group (-

N=N- linking the azo dye), which is susceptible to •OH radicals attack.

(2) $ZrFe_2O_5$ under Fenton treatment yields much higher decolorization for the ARB dye than MB dye. This result is a consequence of greater adsorption of the ARB dye on $ZrFe_2O_5$. Radicals generated through Fenton reaction of $\alpha-Fe_2O_3$ phase in ferrite have high probability of interaction with the adsorbed dye molecules. Being extremely unstable, these radicals do not diffuse into the medium. Hence, the extent of adsorption of dye onto the catalyst surface is also a crucial mechanism in overall decolorization. Consequently, higher decolorization was seen for the ARB dye that has higher extent of adsorption.

(3) Under the individual AOP of photocatalysis, TiO_2 yields higher decolorization for both dyes than $ZrFe_2O_5$. This is an anomaly as the band gap for $ZrFe_2O_5$ is much lower than TiO_2, as revealed in the DRS analysis, and hence, the photoactivity of $ZrFe_2O_5$ is expected to be higher. We explain this anomaly as follows on the basis of a similar study by Xia and Yin on photocatalytic activity of core−shell structured $\alpha-Fe_2O_3-TiO_2$ nanocomposites (Xia et al., 2013): Under the UV light irradiation, electron–hole pairs are produced in the conduction and valence bands of $ZrFe_2O_5$ and as a result, a heterojunction is formed between $ZrFe_2O_5$ and $\alpha-Fe_2O_3$. The $\alpha-Fe_2O_3$ present in the $ZrFe_2O_5$ powders could act as a recombination center of the photogenerated electrons and holes. Also, $\alpha-Fe_2O_3$ present in $ZrFe_2O_5$ may absorb most of the electromagnetic irradiation and promote favorable conditions for the presence of hole–electron recombination centers, so that $ZrFe_2O_5$ catalyst exhibits lower photocatalytic activity even after having the lower band gap energy than the TiO_2.

It should be noted that photo–chemically generated radicals are utilized mainly for the decolorization of adsorbed dye molecules. Thus, the extent of dye adsorption on catalyst surface also contributes to overall mechanism of decolorization. Although $ZrFe_2O_5$ is a stronger adsorbent than TiO_2, the net decolorization with $ZrFe_2O_5$ is lower as a consequence of its inferior photocatalytic activity.

Table 9.1: Summary of experimental results on decolorization/ degradation of Acid red B (ARB)

Experimental Category	**Decolorization of ARB (η %)**					
1. Sonolysis (US)	13.74 ± 2.23		$k = 3.94 \times 10^{-5}$			
	TiO_2		**$ZrFe_2O_5$**		**($ZrFe_2O_5$ + H_2O_2)**	
	60 min	k (s^{-1})	60 min	k (s^{-1})	60 min	k (s^{-1})
2. Fenton (MS)	–	–	–	–	60.19 ± 4.16	3.12×10^{-4}
3. Photocatalysis (MS + UVA)	55.38 ± 2.47	2.28×10^{-4}	32.80 ± 1.91	1.58×10^{-4}	–	–
4. US + Sat.	34.83 ± 0.99	1.34×10^{-4}	51.86 ± 1.35	2.28×10^{-4}	67.57 ± 0.48	6.14×10^{-4}
5. US + Unsat.	37.52 ± 1.23	1.59×10^{-4}	46.53 ± 1.66	1.56×10^{-4}	70.46 ± 0.67	4.25×10^{-4}
6. US + UVA + Sat.	80.58 ± 0.69	4.80×10^{-4}	59.10 ± 1.70	3.36×10^{-4}	90.54 ± 2.28	1.40×10^{-3}
7. US + UVA + Unsat.	78.15 ± 0.94	4.01×10^{-4}	53.73 ± 1.68	2.27×10^{-4}	82.07 ± 0.59	5.46×10^{-4}

Note: US – ultrasound assisted, MS – assisted with mechanical stirring, η – decolorization efficiency (%), k – pseudo 1st order kinetic constant (sec^{-1}) calculated on the basis of initial 30 min of decolorization reaction data.

Table 9.2: Summary of experimental results on decolorization/ degradation of Methylene Blue (MB)

Experimental Category	**Decolorization of MB (η %)**					
1. Sonolysis (US)	8.35 ± 1.24		$k = 2.39 \times 10^{-5}$			
	TiO_2		**$ZrFe_2O_5$**		**($ZrFe_2O_5$ + H_2O_2)**	
	60 min	k (s^{-1})	60 min	k (s^{-1})	60 min	k (s^{-1})
2. Fenton (MS)	–	–	–	–	40.76 ± 2.01	4.73×10^{-4}
3. Photocatalysis (MS + UVA)	34.07 ± 3.44	1.98×10^{-4}	31.30 ± 3.61	2.77×10^{-4}	–	–
4. US + Sat.	32.12 ± 2.83	2.16×10^{-4}	50.34 ± 1.35	4.65×10^{-4}	53.19 ± 1.51	5.35×10^{-4}
5. US + Unsat.	32.49 ± 2.82	1.16×10^{-4}	51.11 ± 1.16	4.68×10^{-4}	51.69 ± 2.95	7.18×10^{-4}
6. US + UVA + Sat.	60.96 ± 2.14	2.31×10^{-4}	57.78 ± 1.08	6.03×10^{-4}	87.62 ± 1.21	6.75×10^{-4}
7. US + UVA + Unsat.	49.45 ± 2.79	1.85×10^{-4}	49.30 ± 1.50	6.02×10^{-4}	62.17 ± 2.52	5.88×10^{-4}

Note: US – ultrasound assisted, MS – assisted with mechanical stirring, η – decolorization efficiency (%), k – pseudo 1st order kinetic constant (sec^{-1}) calculated on the basis of initial 30 min of decolorization reaction data

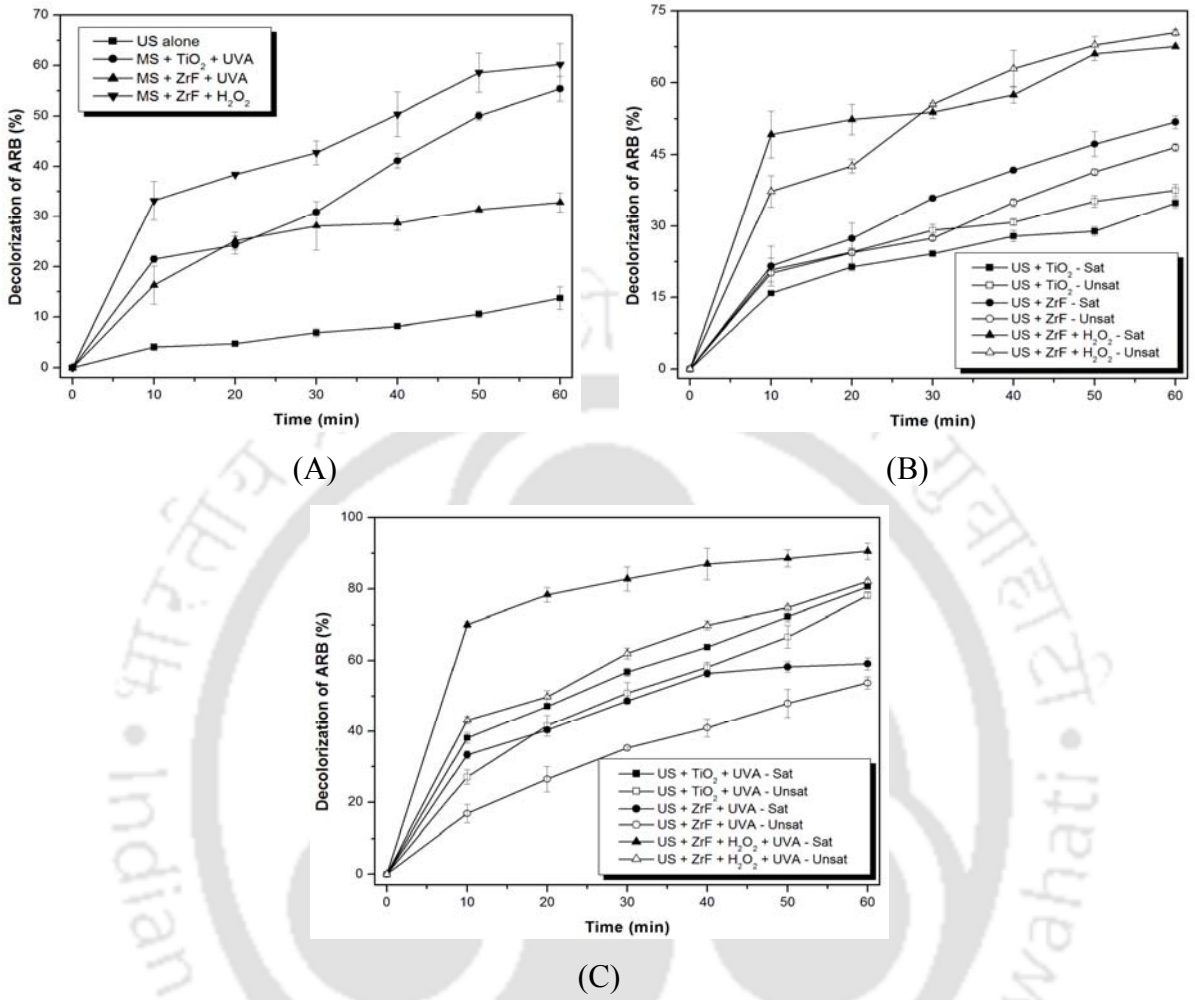

Figure 9.9: Time history of decolorization of ARB with various operating conditions: (A) Individual AOPs, (B) Hybrid AOPs (sonocatalysis and sono–Fenton), and (C) Hybrid AOPs (sono–photocatalysis and sono–photo–Fenton process). Note: US – ultrasound, MS – mechanical stirring, ZrF – zirconium ferrite.

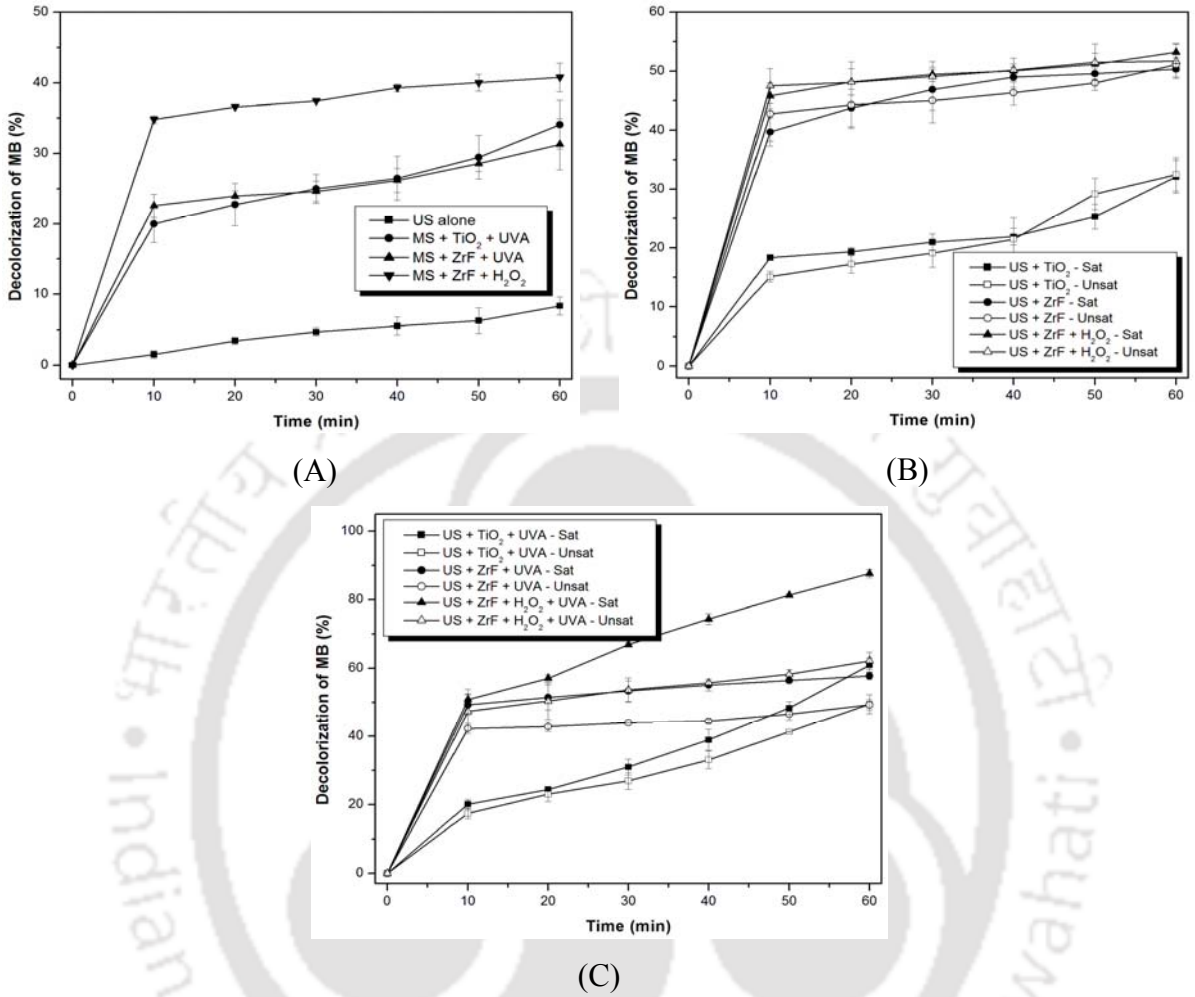

Figure 9.10: Time history of decolorization of MB with various operating conditions: (A) Individual AOPs, (B) Hybrid AOP (sonocatalysis and sono–Fenton), and (C) Hybrid AOPs (sono–photocatalysis and sono–photo–Fenton process). Note: US – ultrasound, MS – mechanical stirring, ZrF – zirconium ferrite.

(4) The saturation level of the medium has no effect on dye decolorization for both dyes under the protocol of sonocatalysis, as almost similar decolorization has been obtained for both dyes, with saturated as well as unsaturated medium.

(5) Under the protocol of sonocatalysis (in which the catalyst is added to the dye solution but no external UV source is provided), an interesting manifestation of Fenton active $\alpha - Fe_2O_3$ phase of $ZrFe_2O_5$ is seen. In this case, the role of catalyst is merely that of an adsorbent that creates higher local concentration of dye on its surface. Although the adsorption of MB dye on both TiO_2 & $ZrFe_2O_5$ is similar, higher decolorization is seen for $ZrFe_2O_5$. We attribute this result to Fenton – reactions occurring in the solution due to the H_2O_2 generated *in–situ* by the recombination of •OH radicals generated from transient cavitation. A similar trend is also seen for the ARB dye, however, contribution of higher adsorption of the ARB dye to higher extent of decolorization cannot be ruled out. Addition of external H_2O_2 to the medium further enhances the Fenton reactions and extent of dye decolorization. We would like to point out that there are many possible routes through which H_2O_2 can degrade the dyes. One mechanism is evaporation of H_2O_2 in cavitation bubbles and decomposition of this H_2O_2 to produce higher •OH radicals during transient collapse of bubbles, which can degrade the dye. Alternately, H_2O_2 itself is an oxidant which can degrade the dyes. However, results of our previous study have clearly distinguished the relative contributions of these mechanisms in comparison to the Fenton–mechanism [50] (Chakma and Moholkar, 2013). Our previous results confirm that contribution of first two mechanisms is relatively trivial and the oxidation of the textile dye in presence of H_2O_2 is predominantly affected through the Fenton mechanism. Therefore, rise in extent of decolorization of dyes with addition of H_2O_2 is attributed to Fenton type reactions induced by the $\alpha - Fe_2O_3$ (or hematite phase) of the ferrite catalyst.

The contribution of adsorption in overall decolorization is more pronounced in this

protocol. Significantly higher decolorization with external addition of H_2O_2 is seen for the ARB dye than MB dye. Due to higher adsorption, the probability of interaction of the ARB dye molecules with the •OH radicals generated through heterogeneous Fenton reaction is higher, which essentially results in greater decolorization.

(6) Under the protocol of sono–photocatalysis, where an external UV source is employed, marked enhancement in decolorization is seen. TiO_2 yields high decolorization (~80%) for ARB, while relatively lesser decolorization is seen for MB. The decolorization for the $ZrFe_2O_5$ catalyst is relatively lesser as a result of reduced photoactivity due to presence of $\alpha - Fe_2O_3$ phase. However, with addition of H_2O_2 initiates the Fenton activity of the $\alpha - Fe_2O_3$ phase of the catalyst to give the hybrid AOP of sono–photo–Fenton, and the extent of decolorization shows marked rise.

In the protocols of sono–photocatalysis and sono–photo–Fenton, the negative effect of unsaturation of the medium is evident. For both dyes, the decolorization reduces by ~10–15% with unsaturation. We attribute this result to intensification of the transient cavitation with unsaturation of the medium (Moholkar and Warmoeskerken, 2004). As a result, the intensity of the shock waves generated by bubbles also increases these shock waves are responsible for desorption of the dye molecules from the surface of $ZrFe_2O_5$ (Chakma and Moholkar, 2015). This phenomenon reduces the probability of interaction of dye molecules with •OH radicals generated either through heterogeneous Fenton reaction between H_2O_2 and $\alpha - Fe_2O_3$ phase of $ZrFe_2O_5$ or through the photocatalysis.

The reduction in total organic carbon (TOC) of the reaction solution with individual as well as hybrid AOPs employed in this study is depicted in Fig. 9.11. The typical trends in TOC removal are essentially same as that for the decolorization. Among the individual AOPs, highest TOC removal is seen for sono–Fenton ($ZrFe_2O_5$ + H_2O_2), while among the hybrid AOPs, highest TOC removal is seen for sono–photo–Fenton with $ZrFe_2O_5$. If we

compare the performance of two catalysts for TOC removal in individual and hybrid AOPs, we find that TiO_2 gives better performance in AOPs where external UV source was used (sono–photocatalysis). $ZrFe_2O_5$, on the other hand, gives better performance in protocols where H_2O_2 was added to the medium (*viz.* sono–Fenton or sono–photo–Fenton). The former result is a consequence of higher photo–activity of TiO_2 (which overwhelms the moderate adsorption capacity), while the latter result is a consequence of utilization both photo as well as Fenton activity of the $ZrFe_2O_5$ catalyst.

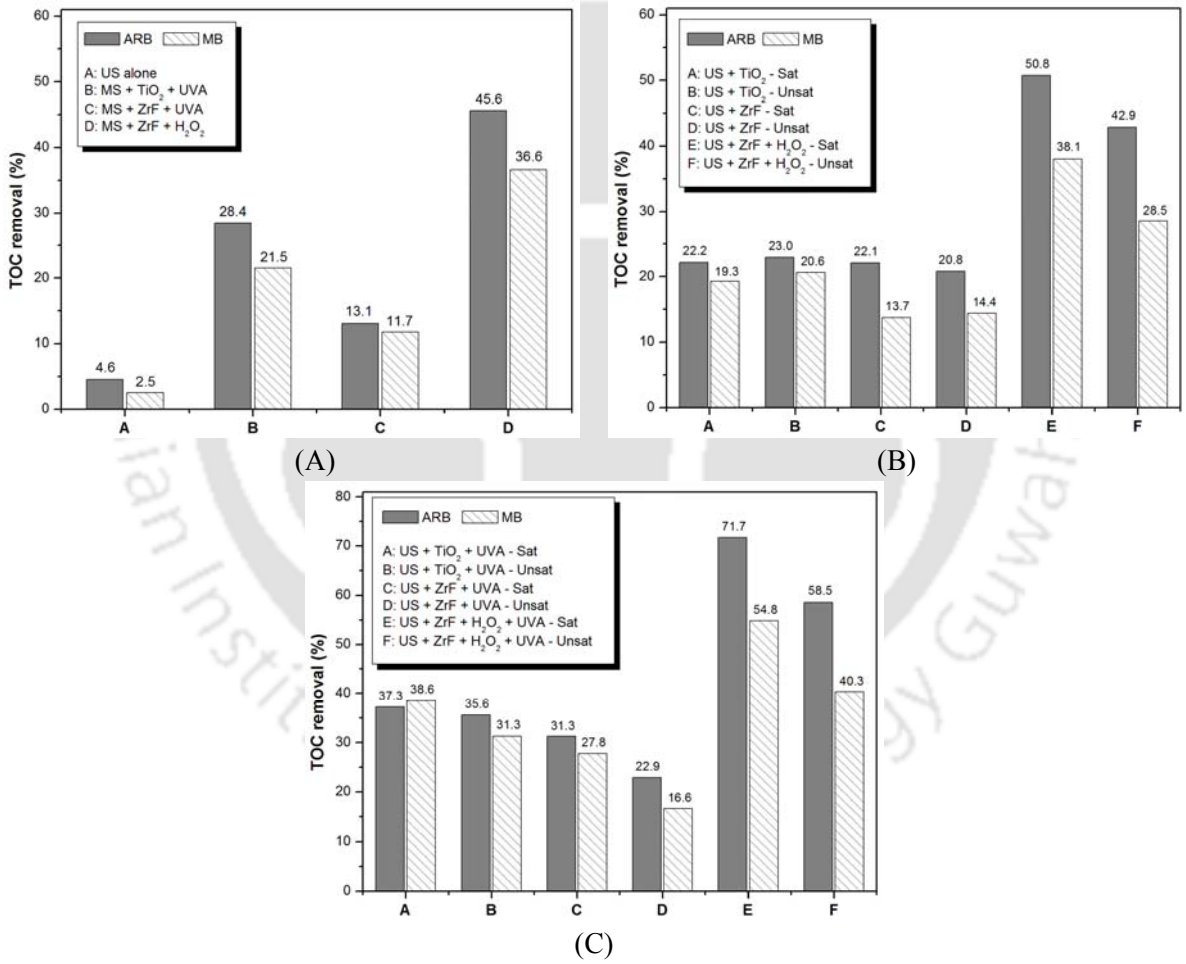

Figure 9.11: Total organic carbon (TOC) removal after 60 min of treatment of ARB and MB dyes with various operating conditions: (A) Individual AOPs, (B) Hybrid AOPs (sonocatalysis and sono–Fenton), and (C) Hybrid AOPs (sono–photocatalysis and sono–photo–Fenton process). Note: US – ultrasound, MS – mechanical stirring, ZrF – zirconium ferrite.

9.4.3 Effect of UV source for mineralization

In order to assess the effect of UV light sources, we have conducted experiments under with either UVA or combined with UVA + UVC light. Fig. 9.12 shows the result of this study. Comparison of the decolorization results with single UV source of UVA and combined source UVA+UVC revealed that extent of dye decolorization does not change appreciably with application of UVC source in addition of UVA. However, the extent of TOC removal shows marked enhancement with simultaneous application of UVC with UVA (~ 40% enhancement for ARB dye and ~ 65% enhancement for MB dye). This essentially means that UVC photo emission (with peak emission at 254 nm which assists photolysis of H_2O_2 to generate •OH radicals) mainly contributes to further degradation of the intermediates/ byproducts of dye degradation, which results in higher mineralization of the organic carbon.

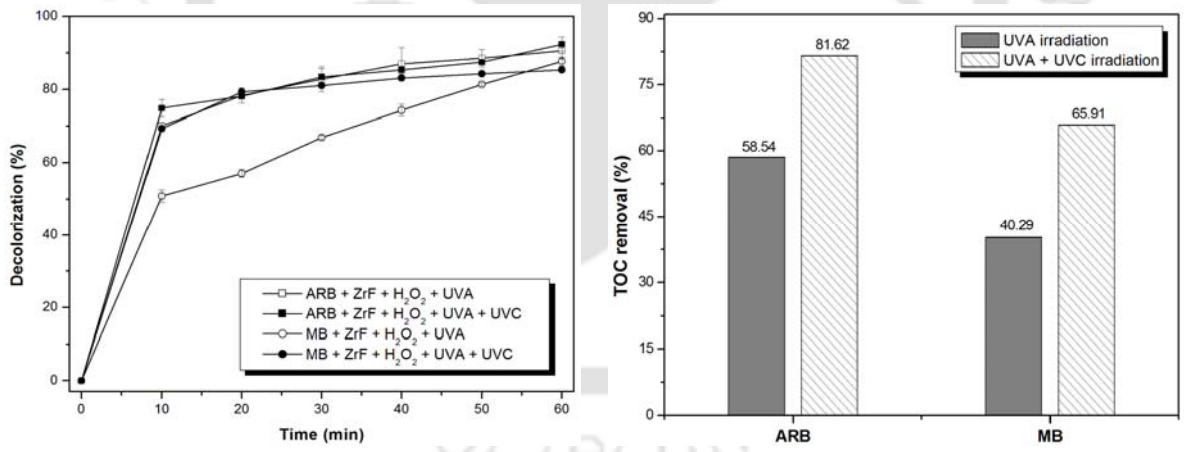

(A) (B)

Figure 9.12: (A) Time history of decolorization under hybrid AOP (sono–photo–Fenton reaction) assisted with different UV light sources. (B) Effect of UV irradiation sources for TOC removal with hybrid AOP (sono–photo–Fenton reaction).

9.4.4 Synergy effect

As noted earlier, for any particular protocol, several mechanisms occur

simultaneously which contribute to the overall decolorization. The positive/ negative synergies between these mechanisms result in enhanced/ reduced decolorization in any hybrid AOP. Fig. 9.13 depicts the synergies in the hybrid AOPs. In this section, we have attempted to determine the synergy between these mechanisms. The synergy effect in hybrid advanced oxidation processes (HAOPs) has been calculated with following formula:

$$\text{Synergy Factor } (S_F) = \frac{\left[\begin{matrix}\text{Decolorization with}\\ \text{Hybrid AOP}\end{matrix}\right] - \left[\left(\begin{matrix}\text{Decolorization with}\\ \text{individual AOP}\end{matrix}\right) + \left(\begin{matrix}\text{Decolorization due to}\\ \text{Adsorption}\end{matrix}\right)\right]}{\left[\left(\text{Decolorization with individual AOP}\right) + \left(\text{Decolorization due to Adsorption}\right)\right]}$$

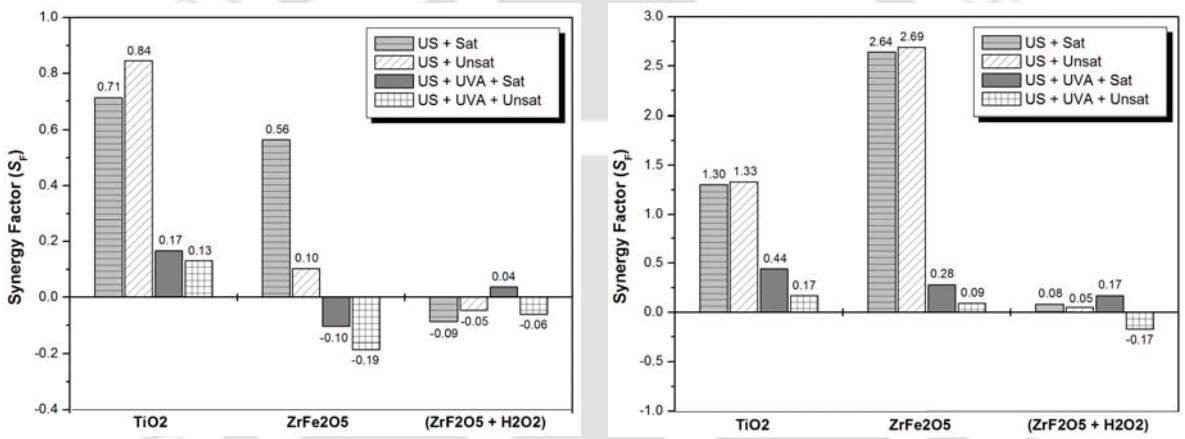

(A) (B)

Figure 9.13: Synergism of hybrid AOPs: (A) synergistic effect for decolorization of ARB (azo dye), and (B) synergistic effect for decolorization of MB (non−azo dye). *Note*: While calculation of the synergies, the extent of adsorption of the dye onto the photocatalyst (after total reaction time of the advanced oxidation treatment) has been accounted.

The highest synergies are seen for both catalysts and both dyes in the hybrid AOP of sonocatalysis. As noted earlier, in sonocatalysis protocols, the catalyst mainly acts as an adsorbent that creates high localized concentration of dye molecules, which essentially increases the probability of interaction between dye molecules and •OH radicals generated through transient cavitation bubbles. Small negative synergies are seen for $ZrFe_2O_5$ catalyst

in protocol of sono–photocatalysis and sono–photo–Fenton. In both of these protocols, the •OH radicals generated at the surface of catalyst either photo–chemically or through heterogeneous Fenton reaction (of $\alpha-Fe_2O_3$ phase) interaction with dye molecules adsorbed on the catalyst surface. The acoustic waves generated by transient cavitation cause desorption of the dye molecules which hampers their interaction probability with radicals. This phenomenon renders negative synergy between individual mechanism of sonolysis, photocatalysis and Fenton reactions.

9.5 CONCLUSION

In this chapter, we have reported sonochemical synthesis and characterization of zirconium ferrite ($ZrFe_2O_5$), which has potential application as catalyst in AOPs. The efficacy of $ZrFe_2O_5$ in degradation of the recalcitrant organic pollutants has been assessed with decolorization/ degradation of azo and non–azo textile dyes as yardstick using various individual and hybrid AOPs. The characterization of $ZrFe_2O_5$ reveals that it has lower band gap than conventional photocatalyst TiO_2. However, it also possesses $\alpha-Fe_2O_3$ (hematite) phase. This phase has adverse effect on the photo−activity of the $ZrFe_2O_5$ due to which the effective photo−activity of $ZrFe_2O_5$ reduces despite the lower band gap energy. However, in the context of degradation of recalcitrant pollutants, this adverse effect is compensated by the Fenton activity of $\alpha-Fe_2O_3$ (hematite) phase. Moreover, sonochemically synthesized $ZrFe_2O_5$ also has high adsorption capacity that promotes the Fenton– and photo–activity. As a result of these facets, $ZrFe_2O_5$ is revealed to be a better catalyst for hybrid AOPs than TiO_2. Experimental results of dye decolorization have revealed that Fenton–activity of $ZrFe_2O_5$ has higher contribution to decolorization than photo–activity. The most efficient protocol for dye decolorization is revealed to be sono–photo–Fenton, in which both photo– and Fenton–activities of $ZrFe_2O_5$ are utilized. The analysis of decolorization experiments has also

provided interesting mechanistic insight into interactions between different competing mechanisms of hybrid AOPs, which could be useful for further research in hybrid advanced oxidation processes.

ACKNOWLEDGEMENT

Authors acknowledge the analytical facilities provided by Central Instruments Facility (CIF), I.I.T. Guwahati. The use of XRD facility (procured through FIST grant No. SR/FST/ETII–028/2010 from Department of Science and Technology, Government of India) at Department of Chemical Engineering, I.I.T. Guwahati is also acknowledged.

REFERENCES

Aydın C, El–sadek MSA, Zheng K, Yahia IS, Yakuphanoglu F, Synthesis, diffused reflectance and electrical properties of nanocrystalline Fe–doped ZnO via sol–gel calcination technique, Optic. Laser Technol. 48 (2013) 447–452.

Chakma S, Moholkar VS, Investigation in mechanistic issues of sonocatalysis and sonophotocatalysis using pure and doped photocatalysts, Ultrason. Sonochem. 22 (2015) 287−299.

Chakma S, Moholkar VS, Investigations in synergism of hybrid advanced oxidation processes with combinations of sonolysis + Fenton process + UV for degradation of bisphenol–A, Ind. Eng. Chem. Res. 53 (2014) 6855–6865.

Chakma S, Moholkar VS, Physical mechanism of sono–Fenton process, AIChE J. 59 (2013) 4303 – 4313.

Cho JY, Nam WH, Lim YS, Seo W−S, Park H−H, Lee JY, Bulky mesoporous TiO_2 structure, RSC Adv. 2 (2012) 2449–2453.

Choudhury HA, Choudhary A, Sivakumar M, Moholkar VS, Mechanistic investigation of the

sonochemical synthesis of zinc ferrite, Ultrason. Sonochem. 20 (2013) 294−302.

De la Rosa JR, Hernandez A, Rojas F, Ledezma JJ, Sol–gel synthesis and characterization of novel La, Mn and Fe doped zirconia: Catalytic combustion activity of trichloroethylene, Colloids and Surfaces A: Physicochem. Eng. Aspects 315 (2008) 147–155.

Goswami PP, Choudhury HA, Chakma S, Moholkar VS, Sonochemical synthesis and characterization of manganese ferrite nanoparticles, Ind. Eng. Chem. Res. 52 (2013) 17848−17855.

He D, Lin F, Preparation and photocatalytic activity of anatase TiO_2 nanocrystallites with high thermal stability, Mater. Lett. 61 (2007) 3385–3387.

Ito D, Nishimura K, Miura O, Removal and recycle of phosphate from treated water of sewage plants with zirconium ferrite adsorbent by high gradient magnetic separation, J. Phys. Conf. Ser. 156 (2009) 012033.

Kim E−Y, Kim DS, Ahn B−T, Synthesis of mesoporous TiO_2 and its application to photocatalytic activation of methylene blue and E. coli, Bull. Korean Chem. Soc. 30 (2009) 193−196.

Li FB, Li XZ, Liu CS, Liu TX, Effect of alumina on photocatalytic activity of iron oxides for bisphenol A degradation, J. Hazard. Mater. 149 (2007) 199–207.

Lin C, Zhang C, Lin J, Phase transformation and photoluminescence properties of nanocrystalline ZrO_2 powders prepared via the pechini−type sol−gel process, J. Phys. Chem. C 111 (2007) 3300−3307.

Moholkar VS, Warmoeskerken MMCG, Investigations in mass transfer enhancement in textiles with ultrasound, Chem. Eng. Sci. 59 (2004) 299−311.

Nishimura K, Miura O, Ito D, Tsunasima T, Wada Y, Removal of radioactive heavy metal ions from solution by superconducting high–gradient magnetic separation with schwertmannite and zirconium–ferrite adsorbents, IEEE Trans. Appl. Supercond. 19

(2009) 2162−2164.

Qin H, Li W, Xia Y, He T, Photocatalytic activity of heterostructures based on ZnO and N−doped ZnO, ACS Appl. Mater. Interfaces 3 (2011) 3152–3156.

Reddy BR, Sivasankar T, Sivakumar M, Moholkar VS, Physical facets of ultrasonic cavitational synthesis of zinc ferrite particles, Ultrason. Sonochem. 17 (2010) 416−426.

Sathishkumar PS, Mangalaraja RV, Mansilla HD, Gracia−Pinilla MA, Anandan S, Sonophotocatalytic (42 kHz) degradation of Simazine in the presence of Au–TiO_2 nanocatalysts, Appl. Catal. B Environ. 160–161 (2014) 692–700.

Sathishkumar PS, Sivakumar R, Anandan S, Madhavan J, Maruthamuthu P, Ashokkumar M, Photocatalytic degradation of Acid Red 88 using Au–TiO_2 nanoparticles in aqueous solutions, Water Res. 42 (2008) 4878−4884.

Sattar AA, El−Sayed HM, Agami WR, Ghani AA, Magnetic properties and electrical resistivity of Zr^{4+} substituted Li−Zn ferrite, Am. J. Appl. Sci. 4 (2007) 89−93

Shirsath SR, Pinjari DV, Gogate PR, Sonawane SH, Pandit AB, Ultrasound assisted synthesis of doped TiO_2 nano−particles: Characterization and comparison of effectiveness for photocatalytic oxidation of dyestuff effluent, Ultrason. Sonochem. 20 (2013) 277–286.

Sivakumar M, Towata A, Yasui K, Tuziuti T, Iida Y, A new ultrasonic cavitation approach for the synthesis of zinc ferrite nanocrystals, Curr. Appl. Phys. 6 (2006) 591−593.

Sivakumar M, Towata A, Yasui K, Tuziuti T, Kozuka T, Iida Y, Maiorov MM, Blums E, Bhattacharya D, Sivakumar N, Ashok M, Ultrasonic cavitation induced water in vegetable oil emulsion droplets – A simple and easy technique to synthesize manganese zinc ferrite nanocrystals with improved magnetization, Ultrason. Sonochem. 19 (2012) 652–658.

Suzuki Y, Kondo T, Nakagawa K, Tsuneda S, Hirata A, Shimizu Y, Inamori Y, Evaluation of sludge reduction and phosphorus recovery efficiencies in a new advanced wastewater

treatment system using denitrifying polyphosphate accumulating organisms, Water Sci. Technol. 53 (2006) 107–113

Toyoda M, Nanbu Y, Nakazawa Y, Hirano M, Inagaki M, Effect of crystallinity of anatase on photoactivity for methyleneblue decomposition in water, Appl. Catal. B Environ. 49 (2004) 227–232.

Xia Y, Yin L, Core–shell structured $\alpha-Fe_2O_3@TiO_2$ nanocomposites with improved photocatalytic activity in the visible light region, Phys. Chem. Chem. Phys. 15 (2013) 18627−18634.

Zhu L−P, Wang L−L, Bing N−C, Huang C, Wang L−J, Liao G−H, Porous fluorine−doped $\gamma-Fe_2O_3$ hollow spheres: synthesis, growth mechanism, and their application in photocatalysis, ACS Appl. Mater. Interfaces 5 (2013) 12478−12487.

10

OVERVIEW AND SCOPE FOR FUTURE WORK

CHAPTER 10

OVERVIEW AND SCOPE FOR FUTURE WORK

This thesis has addressed an important and fundamental issue in degradation of recalcitrant organic pollutants using hybrid advanced oxidation processes – i.e. establishment of the physical mechanism of such processes and finding the mechanistic interlinks and synergy between individual AOPs involved in the process. Using sonolysis as the base AOP, numerous other AOPs have been coupled to it. The degradation as well as mineralization of various recalcitrant organic pollutants appearing in wastewater discharge from various process industries has been analyzed. The pollutants, whose degradation behavior under hybrid AOP has been studied, include azo and non–azo textile dyes, plastic intermediates such as BPA and pharmaceutical drugs such as ibuprofen. In all studies, the methodology of concurrent analysis of experimental results with results of simulations of cavitation bubble dynamics has been adopted. A total of seven sono-hybrid AOPs have been studied, viz. (1) sono-Fenton & sono-photo-Fenton, (2) sono-ferrioxalate, (3) sono-photolysis, (4) sono-persulfate, (5) sono-enzymatic, (6) sono-photocatalysis with doped ZnO, and (7) sono-photocatalysis (using Zr-ferrite with heterogeneous Fenton activity). The synergy between the individual AOPs involved in the hybrid AOPs was defined either on the basis of the total decolorization obtained with hybrid AOP, in comparison with the individual AOP or in terms

of the ratio of pseudo 1st order kinetic constants of degradation for individual and hybrid AOP. Given below is a summary the major results/conclusions of all studies included in this thesis work.

Sono-Fenton: H_2O_2 added to the medium as one of the Fenton reagent scavenges the $^{\bullet}OH$ radicals produced by cavitation bubbles, which nullifies their effect, giving a negative synergy between sonolysis and Fenton process. Mere addition of H_2O_2 to the medium during sonolysis does not give much enhancement to decolorization, which is attributed to lower vapor pressure of H_2O_2 due to which it does not evaporate and dissociate inside the bubble (to generate additional $^{\bullet}OH$ radicals). Fenton reagent (Fe^{2+} + H_2O_2), on the other hand, gives volumetrically more uniform production of $^{\bullet}OH$ radicals in the solution, and hence, has a dominating contribution to decolorization in the hybrid process. The role of ultrasound and cavitation in the hybrid sono–Fenton process is simply physical, i.e. causing intense mixing in the medium. Radical conservation due to dissolved oxygen is also revealed to play a major role in effective utilization of $^{\bullet}OH$ radicals for decolorization.

Sono-Photo-Fenton: This process used combinations of sonolysis, Fenton process and UV irradiation. The categories for which positive synergies between the individual AOPs are obtained are: (1) sonolysis alone and sonolysis+Fe^{2+}, (2) sonolysis & sono–Fenton, (3) Fenton & sono–Fenton. The static pressure on the reaction mixture (which influences the transient behavior of the cavitation bubble dynamics) in sono–Fenton process did not show any influence on the extent of degradation. Variation in degradation with de-aeration of the medium (or variation in dissolved oxygen content of the medium) was also negligible. The categories with no synergy were: Fenton and Fenton+UV. The categories with negative synergy were: Fenton process and sono–Fenton+UV. The role of ultrasound and cavitation in the hybrid AOP is more or less physical nature with oxidizing radicals generated through Fenton process contributing mostly to BPA degradation.

Sono-Photo-Ferrioxalate: This study made an attempt to gain insight into physical mechanism of binary and ternary hybrid AOPs with combination of sonolysis, Fenton–like system and photo–ferrioxalate system. The decolorization profiles of the two model dyes, viz. Acid Red B (azo dye) and Methylene Blue (no–azo dye), essentially reveal same trends in all experimental categories. This result points at similarities in the physical mechanism of decolorization/ degradation of the two dyes despite significant dissimilarity in the chemical structure. Among the individual AOPs, sonolysis is revealed to have least decolorization efficiency, which is attributed to highly sporadic nature of transient cavitation events and low probability of interception of the radicals generated from transient cavitation with dye molecules. Even for an unsaturated medium, in which the cavitation bubble undergoes more intense collapse, contribution of sonolysis to decolorization is interior compared to other two systems. The contribution of ultrasound and cavitation in hybrid AOP is, thus, mostly of physical nature. Coupling of sonolysis with either Fenton – like system or photo–ferrioxalate system resulted in enhanced decolorization due to positive energy. However, coupling of all three AOPs resulted in negative synergy due to interaction of the chemical mechanisms of Fenton–like and photo–ferrioxalate system. Dissolved oxygen in the reaction system is also revealed to have a crucial role. For unsaturated reaction systems with depleted dissolved oxygen, the pathway of photo–ferrioxalate was further hindered resulting in reduced in decolorization efficiency.

Sono-Photolysis: Mechanistic investigation of sono-photolysis using decolorization/ mineralization of the azo textile dye Acid Red B revealed following features: In sono-photolysis, $^{\bullet}OH$ radicals generated through photolytic dissociation of H_2O_2 contribute mostly to the decolorization reactions. Role of ultrasound and cavitation in the hybrid AOP is rather subordinate. The total decolorization obtained with photolysis shows negligible change with simultaneous application of ultrasound. However, ultrasound causes enhancement in the

kinetics of decolorization as well as extent of mineralization, as compared to photolysis. Intermediates of dye degradation generated through photolysis possibly undergo mineralization via either thermal decomposition at the interfacial region of transient cavitation bubbles or hydroxylation/oxidation induced by radicals produced from transient collapse of cavitation bubbles. The physical effect of intense and random micro-convection induced by transient cavitation has adverse effect on the decolorization reactions induced by photolysis. Both kinetics of decolorization and extent of TOC removal (or mineralization) in sono-photolysis can be enhanced by addition of salt to the reaction medium. Increase in ionic strength of the reaction mixture with salt addition increases the hydrophobic interactions between dye molecules (and also degradation intermediates) and water that results in greater partitioning of these species at the bubble interface, where they undergo further degradation either through hydroxylation/ oxidation or thermal decomposition.

Sono-Persulfate treatment: This study explored the physical mechanism of persulfate-based decolorization of azo dyes using different activators for generation of sulfate radicals. Three techniques, *viz*. transition metal ion (Fe^{2+} ions), sonolysis and UV-C light, were applied, either individually or in binary or ternary combinations, for activation of persulfate ions. UV-C is revealed to be the most efficient technique for activation. Among the other two techniques, *viz*. sonolysis and Fe^{2+} ions, the former is found to have almost independent mechanism (thermal decomposition of persulfate in bubble-bulk interfacial region) than UV-C. Thus, decolorization as well as mineralization obtained with simultaneous application of sonolysis and UV-C is almost addition of individual effects. Fe^{2+} ions have been revealed to have adverse impact on the UV-C based activation, due to scavenging of $SO_4^{\bullet-}$ radicals. Among all techniques (single/binary/ternary) attempted for activation of persulfate and decolorization, the binary technique of (US + PS + UVC) is found to yield maximum decolorization as well as mineralization.

Sono-Enzymatic treatment: This study explored the physical mechanism of hybrid technique of sono–enzymatic treatment for degradation of inflammatory drug ibuprofen using Arrhenius and thermodynamic analysis of the experimental data. This technique has been found to be an effective tool for degradation as well as mineralization of the IBP. At low ultrasound frequency and atmospheric static pressure, sono-enzymatic treatment is revealed to be more effective than the individual techniques of sonolysis and enzyme treatment. The positive synergy between sonolysis and enzyme treatment is a consequence of formation of hydrophilic intermediates due to hydroxylation induced by radicals generated by transient cavitation. These intermediates are rapidly degraded by the enzyme action through decarboxylation. The activation energy of sono–enzymatic treatment is lesser than enzyme treatment (due to spontaneity of reactions induced by radicals produced by transient cavitation), while the frequency factor of sono–enzymatic treatment is greater than sonolysis (due to volumetrically uniform enzymatic reactions).

Sono-Photocatalysis (with doped ZnO catalyst): This study investigated the mechanistic issues of the hybrid AOPs of sonocatalysis and sonophotocatalysis. Three photocatalysts, viz. pure ZnO and Fe–doped ZnO (synthesized with two protocols) were used. Decolorization of two textile dyes (azo and non–azo) was used as model reaction. Characterization of doped ZnO catalyst indicated that Fe–doping increased the absorption band width in visible region, in addition to reducing the hole–electron recombination, due to which $^{\bullet}OH$ radical generation potential of the catalyst increases. However, experiments in 6 different protocols that alter the characteristics of ultrasound and cavitation events in the medium have clearly revealed a negative synergy between individual AOPs of sonolysis and photocatalysis. A major cause leading to this effect are the shock waves generated by cavitation bubbles, which desorbs the dye molecules adsorbed on the surface of photocatalyst, thus reducing the probability of radical–dye molecule interaction. The sonoluminescence light emitted during transient

cavitation is also unable to activate the photocatalyst, in absence of an external UV source. These results have been found to be almost consistent for all three photocatalysts and for both dyes. The Fe–doping of ZnO could increase the extent of decolorization with respect to pure ZnO, but the synergy between two AOPs remains unaltered in the hybrid AOPs employing all three catalysts.

Sono-(heterogeneous) Fenton-Photocatalysis (using Zr-Ferrite): This study reported sonochemical synthesis and characterization of zirconium ferrite ($ZrFe_2O_5$), which has potential application as catalyst in AOPs. The characterization of $ZrFe_2O_5$ reveals that it has lower band gap than conventional photocatalyst TiO_2. However, it also possesses $\alpha - Fe_2O_3$ (hematite) phase. This phase has adverse effect on the photo−activity of the $ZrFe_2O_5$ due to which the effective photo−activity of $ZrFe_2O_5$ reduces despite the lower band gap energy. However, in the context of degradation of recalcitrant pollutants, this adverse effect is compensated by the Fenton activity of $\alpha - Fe_2O_3$ (hematite) phase. Moreover, sonochemically synthesized $ZrFe_2O_5$ also has high adsorption capacity that promotes the Fenton– and photo–activity. As a result of these facets, $ZrFe_2O_5$ is revealed to be a better catalyst for hybrid AOPs than TiO_2. Experimental results of dye decolorization have revealed that Fenton–activity of $ZrFe_2O_5$ has higher contribution to decolorization than photo–activity. The most efficient protocol for dye decolorization is revealed to be sono–photo–Fenton, in which both photo– and Fenton– activities of $ZrFe_2O_5$ are utilized.

10.1 OVERVIEW

An overview of results of all studies reveals interesting physical facets of sono–hybrid advanced oxidation processes as discussed below:

For all sono–hybrid processes, major contribution of ultrasound and cavitation seems to be physical. The chemical effect of cavitation, i.e. production of oxidizing radicals, does

not make significant contribution. As stated earlier, the main cause leading to the effect is sporadic nature of cavitation events in time as well as in space, due to which the net utilization of $^{\bullet}OH$ radicals generated during cavitation for pollutant degradation is severely hampered. Thus, in all hybrid AOPs, the chemical contribution of the coupling AOP overwhelms that of sonolysis. It is for this reason that elimination of transient cavitation with application elevated static pressure does not make marked change in extent of decolorization/ degradation. Also, no significant variation in degradation is observed with dissolved oxygen content of the medium. In some cases, the adverse interaction between chemical effects of the AOPs should be taken into account. A vivid example of this is scavenging of radicals generated during sonolysis by H_2O_2 added as Fenton reagent. As far as positive synergy (or constructive or complementing interactions) is concerned, conservation of radicals is revealed to be an important mechanism. An example of this is regeneration of $^{\bullet}OH$ radicals by Fe^{2+} added to sonolysis system (though Fenton reaction) from H_2O_2 produced in–situ by recombination of $^{\bullet}OH$ radicals produced during transient cavitation.

The physical effects of cavitation are also revealed to have adverse impact on coupling AOP, and this effect is more pronounced in heterogeneous system such as sonocatalysis and sono–photocatalysis. Shock waves generated by transient cavitation, which cause desorption of pollutants from catalyst, reduce the influence of coupling AOP. Therefore, even the positive synergy due to physical effect of micro–mixing or micro–turbulence is concerned, the physical effect of ultrasound (micro–streaming) is found to have more constructive contribution towards hybrid AOP. The shock waves (or acoustic wave) component of micro–convection is a discrete and high energy phenomena and has adverse impact as far as degradation of pollutant is concerned. However, in many catalytic reactions, the shock waves render beneficial effect on the system, in that they contribute towards cleaning of surface of catalyst, prevention of catalyst poisoning and de–agglomeration of

catalyst particles that gives higher utilization of surface area and active sites. For homogeneous system, the micro-convection and micro-mixing generated by ultrasound an cavitation makes modest contribution. In some cases like decolorization/ degradation of the azo dye with sono-photolysis, random movement of dye molecules in the reaction mixture induced by shock waves emitted by the transient cavitation bubbles reduce the probability of interactions between dye molecules and the oxidizing radicals. The intermediates of the decolorization, however, can undergo further degradation either through thermal decomposition or hydroxylation at the interface of transient cavitation bubble. Similar arguments also hold true for the sono-persulfate oxidation process, in which activation of persulfate anion can occur in the interfacial region of the cavitation bubble.

On a whole, the results of all studies on several sono-hybrid AOPs have revealed that the positive synergy between the mechanisms of sonolysis and the coupling AOP is not always possible in a sono-hybrid AOP. Another marked observation in these studies is that despite significantly different chemical structure of the model pollutants used in study of different hybrid AOPs, the physical mechanism of the hybrid AOP (or mechanistic interlinks between individual AOPs) has been astonishingly similar. This essentially means that the physical mechanism of the sono-hybrid AOP is not influenced by the chemical pathway of degradation/ mineralization of the pollutant. This result also means that the nature of synergy (either positive or negative) among individual AOPs is independent of the chemical nature of pollutant. The crucial factor of mechanistic interaction between AOPs, resulting in either positive or negative synergy, needs to be accounted for in design and optimization of wastewater treatment processes using sono–hybrid techniques. We believe that the results presented in this thesis can form useful guidelines for such an endeavor.

The work presented in this thesis can be advanced through several approaches. Some suggestions for future work in the area of hybrid AOPs are given below.

10.2 SUGGESTIONS FOR FUTURE WORK

The work presented in this thesis can be advanced in several ways:

(1) All of the work carried out in this thesis is on laboratory scale. It would be worthwhile to apply the results of the lab–scale studies to large scale process.

(2) The ultrasound equipment used in this work has constant frequency and power input. For greater efficiency of the process, these parameters could be optimized using suitable instruments.

(3) The degradation process in this work has been mainly monitored through residual concentrations of original pollutant in the samples withdrawn from reaction mixture. The intermediates of degradation have been determined only at the end of the process. For deeper insight into the chemistry of degradation under different experimental conditions that alter the characteristics of the ultrasound and cavitation phenomena in the reaction mixture, it is essential that the time profiles of the degradation intermediates are also monitored throughout the treatment of reaction mixture.

(4) All intermediates formed during the degradation reaction have to be identified and analyzed individually for toxicity test in comparison with the parent compound.

(5) The photocatalysis process for degradation of recalcitrant pollutants can also be conducted with other metal ferrites possessing photo– and Fenton– activity.

(6) This thesis addressed only the Fe^{3+}–doped photocatalyst for degradation of organic pollutants using sonocatalysis and sono–photocatalysis advanced oxidation processes. The sono–hybrid degradation process can also be extended with rare earth metal doped photocatalyst.

भारतीय प्रौद्योगिकी संस्थान गुवाहाटी
Indian Institute of Technology Guwahati

ACKNOWLEDGMENTS

It is my great pleasure to thank each and everyone who helped directly or indirectly to complete my research work and made this thesis possible. I owe my deepest gratitude to all of them.

The first and foremost gratitude goes to my supervisor **Prof. V. S. Moholkar** for his valuable guidance throughout the research work. I thank him for his encouragement, patience towards research and support, which enabled me to develop a better understanding of the subject leading to the present this thesis. I would like to thank him for spending his precious time to discuss thoroughly on the topic and make me what I am today. I would also like to acknowledge my sincere gratitude to my doctoral committee members, **Prof. B. P. Mandal, Prof. M. Jawed** and **Dr. A. Kumar**, for their advices and suggestions throughout my research work.

My sincere thanks go to the faculty members of Department of Chemical Engineering, I.I.T. Guwahati, for their continuous suggestions and inspirations. I also like to express my thanks to the staff members for making a homely atmosphere. The analytical facilities from Central Instruments Facilities (CIF) of Indian Institute of Technology Guwahati are also acknowledged.

I am grateful to my senior members from our group, *Dr. A. Ranjan, Dr. H.A. Choudhury* and *Dr. S. Khanna,* for their co-operative assistance and suggestions in performing experiments. I also thank my lab members *Jaykumar, Pritam, Ritesh, Maneesh, Amit, Arup, Shyamali, Shuchi, Sachin and Mayank*. I must thank to my other senior *Dr. A. S.*

Giri and *Dr. M. K. Gagrai* for spending their valuable time to discuss on the topic and to help whenever I needed.

Finally, I express my gratitude to my beloved family members for supporting and encouraging me throughout my life. I extend my gratefulness to my brothers, who have been the motivation behind my hard work, patience and character.

Date: 06.08.2015 *Sankar Chakma*

RESEARCH OUTPUT

RESEARCH OUTPUT FROM THE THESIS

1. S. Chakma, V.S. Moholkar, Sonochemical synthesis of $ZrFe_2O_5$ and its application for degradation of recalcitrant pollutants, RSC Advances 5 (2015) 53529 – 53542.
2. S. Chakma, V.S. Moholkar, Investigation in mechanistic issues of sonocatalysis and sonophotocatalysis using pure and doped photocatalysts, Ultrasonics Sonochemistry 22 (2015) 287–299.
3. S. Chakma, V.S. Moholkar, Intensification of wastewater treatment using sono–hybrid processes: an overview of mechanistic synergism, Indian Chemical Engineer XX (2015) 1–23. DOI: 10.1080/00194506. 2015.1026948.
4. S. Chakma, V.S. Moholkar, Investigations in synergism of hybrid advanced oxidation processes with combinations of sonolysis + Fenton Process + UV for degradation of bisphenol–A, Industrial and Engineering Chemistry Research 53 (2014) 6855–6865.
5. S. Chakma, V.S. Moholkar, Physical mechanism of sono–Fenton process, AIChE Journal 59 (2013) 4303–4313.
6. S. Chakma, V.S. Moholkar, Mechanistic analysis of hybrid sono–photo–ferrioxalate system for decolorization of azo dye, Journal of the Taiwan Institute of Chemical Engineers (2015). (Under review)
7. S. Chakma, V.S. Moholkar, Dye decolorization with hybrid advanced oxidation processes comprising sonolysis/ Fenton–like/photo–ferrioxalate systems: A mechanistic investigation, Separation and Purification Technology (2015). (Under review)
8. S. Chakma, V.S. Moholkar, Mechanistic analysis of sono–photolysis process, Journal of

Industrial and Engineering Chemistry (2015). (Under review)

9. S. Chakma, V.S. Moholkar, Investigations in sono–enzymatic degradation of ibuprofen, Ultrasonics Sonochemistry (2015). (Under review)
10. S. Chakma, V.S. Moholkar, Mechanistic investigations in sono–persulfate oxidation process (2015). (To be communicated)

CONFERENCE PRESENTATIONS

1. S. Chakma, V.S. Moholkar, Additives free sonochemical synthesis of magnetic nanoparticles, 2nd International Conference on Nanotechnology (ICNT 2015), 19-22 February 2015, Haldia Institute of Technology, Haldia, India.
2. S. Chakma, V.S. Moholkar, Effects of process parameters in sono–photolysis process, The Annual Chemical Engineering Symposium: Reflux–2015, 27–29 March 2015, IIT Guwahati, India.
3. S. Chakma, V.S. Moholkar, Sonochemical synthesis of ferrite nanoparticles and their applications, International Conference on Emerging Materials: Characterization & Application (EMCA–2014), 04–06 December 2014, CSIR–Central Glass and Ceramic Research Institute, Kolkata, India.
4. S. Chakma, V.S. Moholkar, Kinetic and Thermodynamic Parameter Analysis in Sono–Enzymatic Degradation Process, Annual Chemical Engineering Symposium: Reflux 2014, 29–30 March 2014, IIT Guwahati, India.
5. S. Chakma, V.S. Moholkar, Sono–hybrid degradation of recalcitrant pollutant, International Conference on Frontiers in Chemical Engineering (ICFCE–2013), 09–11 December 2013, NIT Rourkela, India.
6. S. Chakma, V.S. Moholkar, Mechanistic study of ultrasound assisted degradation of dye using sonochemically synthesized photocatalyst, International Conference on Material

Science (ICMS–2013), 21–23 February 2013, Agartala, India.

7. S. Chakma, V.S. Moholkar, Mechanistic study of hybrid sono–Fenton process for degradation of azo dye, 2nd International Congress on Advanced Oxidation Process (AOP–2012), 5–8 October 2012, Kottayam, India.

CORRIGENDUM

Chapter 6

***Analysis of ARB degradation intermediates*:** The intermediates of ARB degradation were analyzed using a liquid chromatography mass spectrophotometer (Waters Q–Tof Premier & Aquity UPLC). The mass spectra of the aliquots of reaction mixtures drawn after 10 min of treatment are given in Fig. 1. The comparative analysis of this spectra vis–à–vis the spectra reported in published literature helps to identify some of the degradation intermediates of ARB dye (Gao et al., 2012; Xia et al., 2014; Thiam et al., 2015). Table 2 listed the degradation intermediates identified in the present study with chemical structures and molecular weights. On the basis identified intermediates, we have proposed the ARB dye degradation mechanism as shown in Schemes 1 & 2.

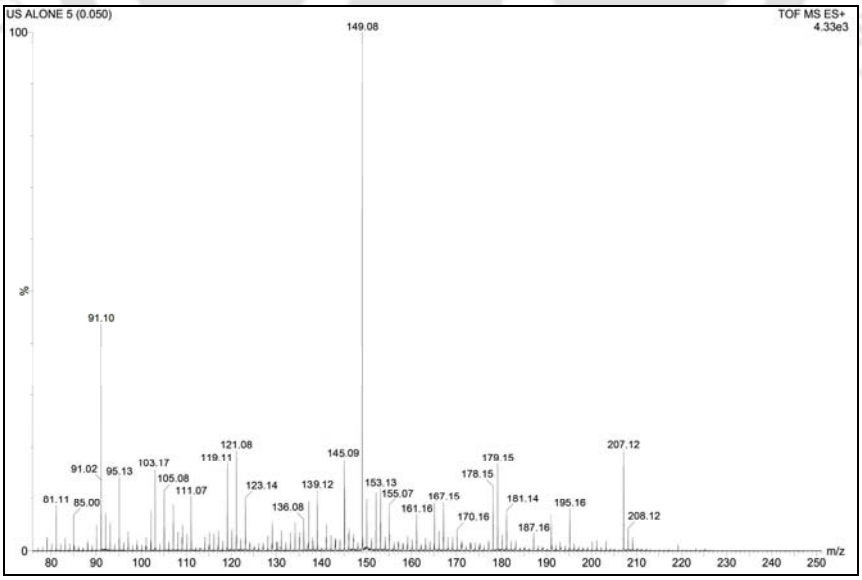

(A) US alone

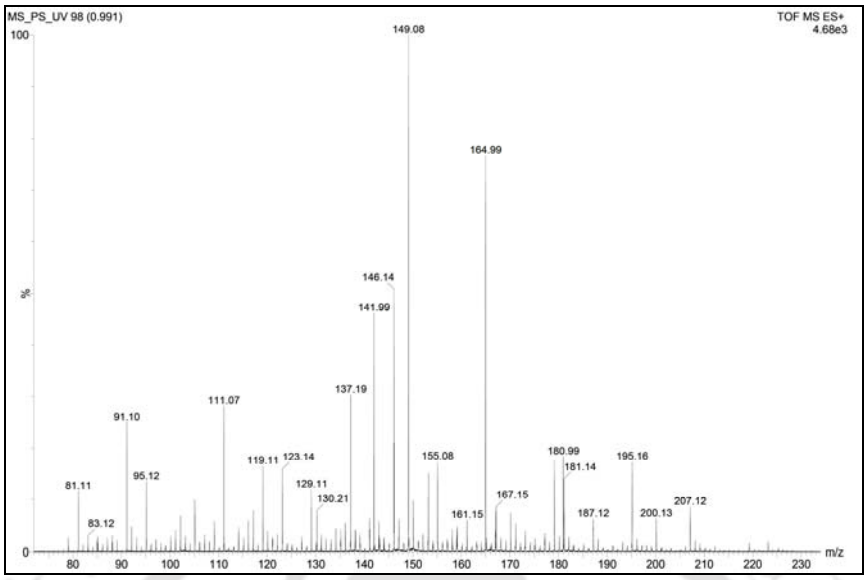

(B) MS + PS + UVC

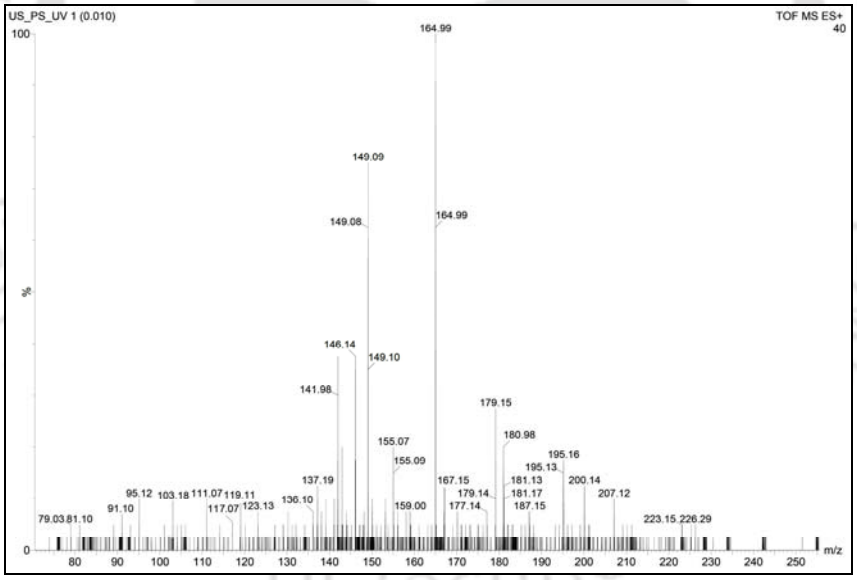

(C) US + PS + UVC

Figure 1: Mass spectrum (m/z in ES+ mode) of the reaction mixture after 10 min of treatment with (A) US alone, (B) (MS+PS+UVC), and (C) (US+PS+UVC).

Table 1: Intermediates of ARB degradation in individual and hybrid AOPs

Intermediates	ES Positive	Mol. Wt. (*M*)	Chemical Structure	Ref. in schemes
2–propionylbenzoic acid	179.15	178.18 [a,c]	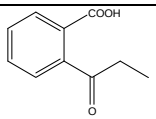	D1
2–hydroxynaphthalene–1,4(4a*H*,8a*H*)–dione	177.14	176.17 [c]	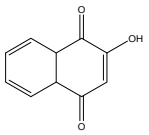	D2
Benzene–1,2–dicarboxylic acid (OR) Phthalic acid	167.15	166.13 [a,b,c]	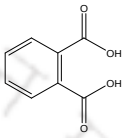	D3
1,4–dinaphthol (OR) Naphthalene–1,4–diol	161.16 161.15	160.17 [a,b]	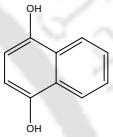	D4
1,4–Naphthoquinone (OR) Naphthalene–1,4–dione	159.00	158.15 [c]	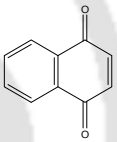	D5
2,3–dihydroxybenzoic acid	155.07	154.12 [a,c]	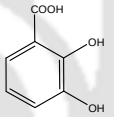	D6
Phthalic anhydride (OR) Isobenzofuran–1,3–dione (OR) 2–benzofuran–1,3–dione	149.08 149.09	148.12 [a,b,c]	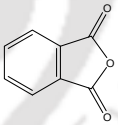	D7
1–Naphthol	145.09 146.14	144.17 [a, c]	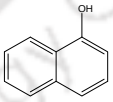	D8
2–hydroxybenzoicacid	139.12	138.12 [a]	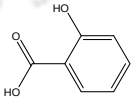	D9
Benzoic acid	123.13 123.14	122.12 [a,b,c]	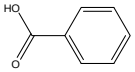	D10

Table 1: (*Continued…*)

Intermediates	ES Positive	Mol. Wt. (*M*)	Chemical Structure	Ref. in schemes
2–methylmalonic acid	119.11	118.09 [a,c]	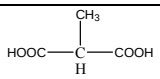	D11
Maleic acid	117.07	116.07 [c]	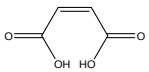	D12
Benzene–1,4–diol (OR) Hydroquinone	111.07	110.11 [a,b,c]		D13
Malonic acid	105.08	104.06 [a]	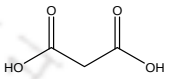	D14
2–methyl butyric acid	103.18	102.13 [c]	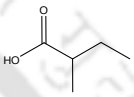	D15
Phenol	95.12 95.13	94.11 [a,b,c]	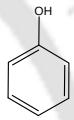	D16
Lactic acid	91.10	90.08 [a,b,c]	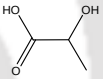	D17
Oxalic acid	91.02	90.03 [a]		D18

Intermediate detected in: [a] – US alone; [b] – [MS+PS+UVC]; [c] – [US+PS+UVC]

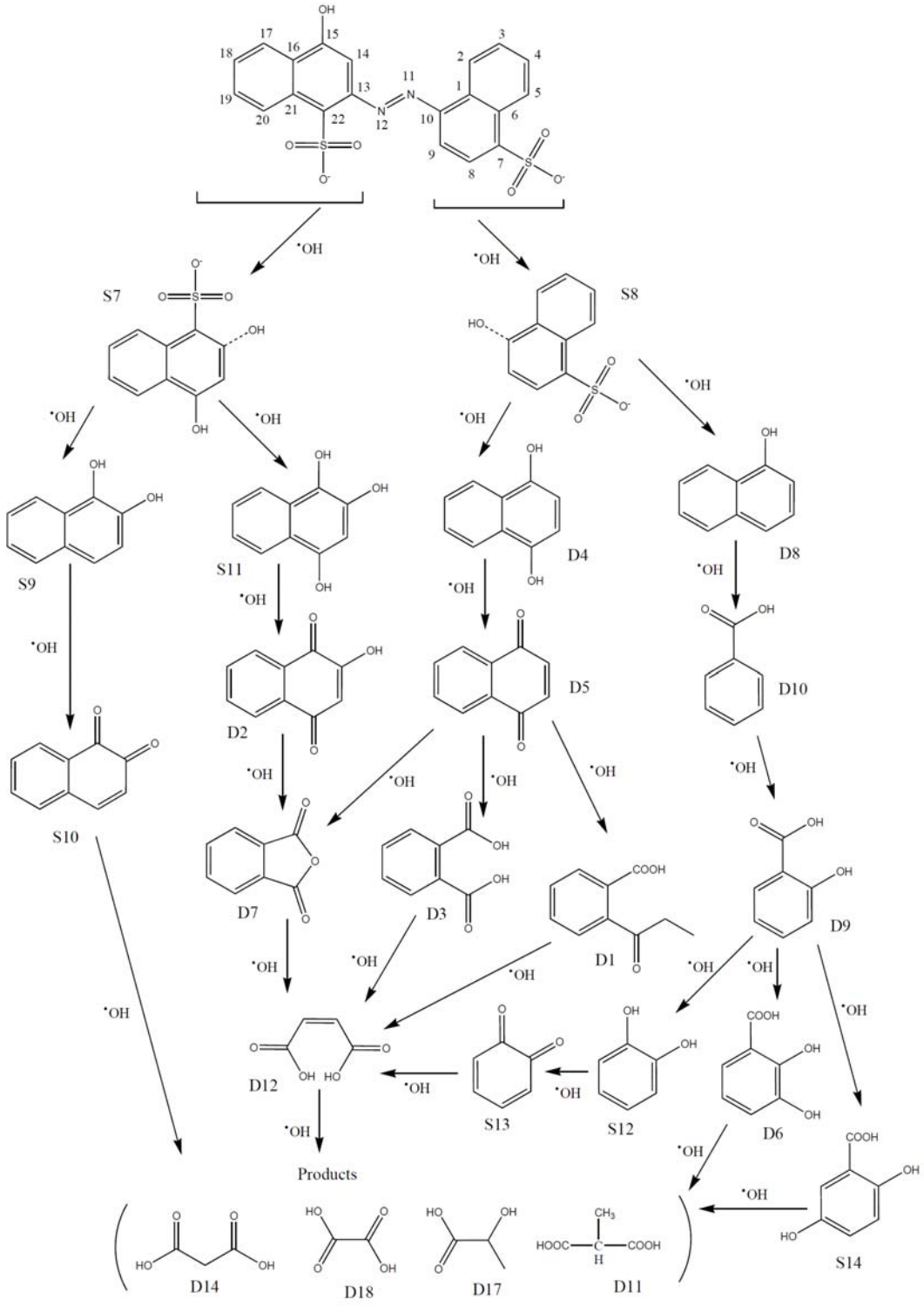

Scheme 1: Possible degradation pathways for ARB degradation in sonochemical treatment. D – intermediates detected by mass spectrophotometer (MS), S – tentative states

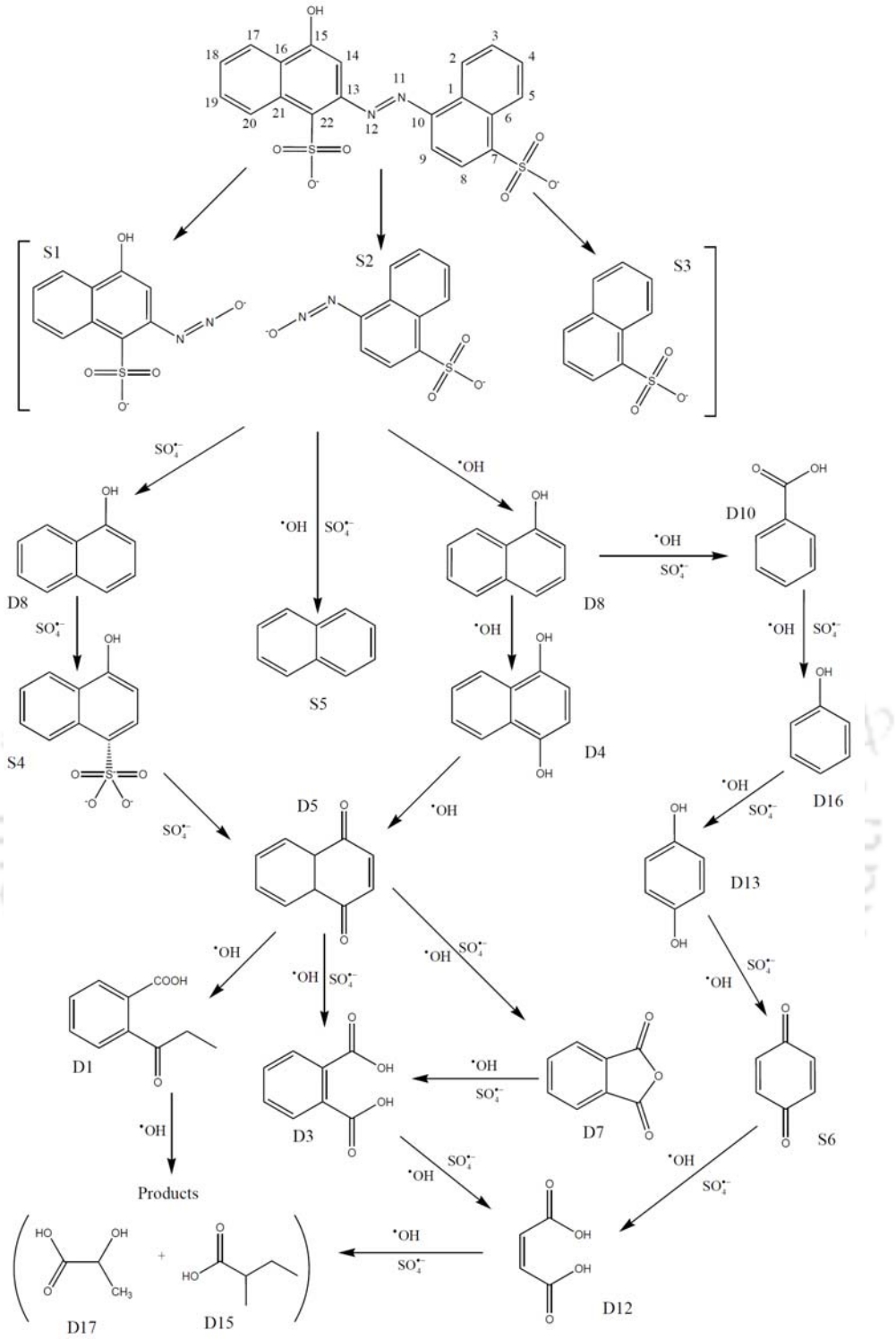

Scheme 2: Possible degradation pathways for ARB degradation in sono–hybrid persulfate treatment. D – intermediates detected in mass spectrophotometer (MS), S – tentative states

REFERENCES

M. Gao, Zeng Z, Sun B, Zou H, Chen J, Shao L, Ozonation of azo dye Acid Red 14 in a microporous tube–in–tube microchannel reactor: Decolorization and mechanism, Chemosphere 89 (2012) 190–197.

Thiam A, Sirés I, Garrido JA, Rodríguez RM, Brillas E, Effect of anions on electrochemical degradation of azo dye Carmoisine (Acid Red 14) using a BDD anode and air–diffusion cathode, Sep. Purif. Technol. 140 (2015) 43–52.

Xia S–J, Zhou X–B, Shi W, Pan G–X, Ni Z–M, Photocatalytic property and mechanism studies on acid red 14 by M_xO_y/ZnTi–layered double hydroxides (M = Fe, Sn, Ce), J. Mol. Catal. A Chem. 392 (2014) 270–277.

LIST OF ABBREVIATION USED IN THE THESIS

$C_{V,i}$ – Heat capacity at constant volume, J kg^{-1} K^{-1}

c_L – Velocity of sound in liquid medium, m s^{-1}

c_W – Velocity of sound in water, m s^{-1}

c_T – Velocity of sound in toluene, m s^{-1}

c_H – Velocity of sound in n–hexane, m s^{-1}

D_w – Diffusion coefficient of solvent vapor, m^2 s^{-1}

f – Frequency of ultrasound wave, Hz

f_i – Translational and rotational degrees of freedom

h – van der Waal's hard core radius, m

$I_{diff,w}$ – Instantaneous diffusive penetration depth for water molecules

k – Boltzmann constant, J K^{-1}

N_W – Number of water molecules trapped in the bubble

N_{N2} – Number of N_2 molecules in the bubble

N_{O2} – Number of oxygen molecules in the bubble

N_T – Number of toluene molecules in the bubble

N_H – Number of n–hexane molecules in the bubble

N_{Ar} – Number of Ar molecules in the bubble

N_{tot} – Total number of molecules (gas + vapor) in the bubble

P_o – Static pressure in the liquid medium, Pa

P_{max} – Pressure peak reached in the bubble at the time of first collapse, Pa

P_{AW} – Pressure amplitude of the acoustic wave generated by the cavitation bubble, Pa

Q – Heat conducted across bubble wall, J s^{-1}

R – Radius of the bubble, m

R_o – Initial radius of the cavitation bubble, m

dR/dt – Bubble wall velocity, m s^{-1}

t – Time, s

T – Temperature of the bubble contents, K

T_o – Ambient (or bulk liquid medium) temperature, K

T_{max} – Temperature peak reached in the bubble at the time of first collapse, K

V_{turb} – Average velocity of the micro–turbulence in the medium generated by ultrasound and cavitation in the medium (estimated at 1 mm distance from bubble center), m s^{-1}

ρ_L – Density of the liquid, kg m^{-3}

υ – Kinematic viscosity of liquid, m^2 s^{-1}

σ – Surface tension of liquid, N m^{-1}

κ – Thermal conductivity of bubble contents, W m^{-1} K^{-1}

λ – Thermal diffusivity of bubble contents, m^2 s^{-1}

θ – Characteristic vibrational temperature(s) of the species, K

η – Degradation efficiency (%)